Localization of generators of epileptic activity in the brain using multimodal data fusion of EEG and MEG data

Rasheda Arman Chowdhury

Doctor of Philosophy

Department of Biomedical Engineering, Faculty of Medicine
McGill University
Montreal, Quebec, Canada

November, 2016

A thesis submitted to McGill University in partial fulfillment of the requirements of the degree of PhD

DEDICATION

I dedicate this thesis to my parents for their unconditional love, for always believing in me and for their dedicated partnership for success in my life.

ABSTRACT

Detection and analysis of interictal epileptic discharges (IEDs) is widely used for the identification and localization of the epileptogenic focus during the pre-surgical evaluation of patients with intractable epilepsy. Electro-encephalography (EEG) and Magneto-encephalography (MEG) can measure the fast propagating IEDs, generated by spatially extended regions, thanks to their high temporal resolution (~1ms). Source localization methods, in particular the Maximum Entropy on the Mean (MEM) method, can provide reliable and accurate localization of the sources of EEG and MEG discharges together with their spatial extent along the cortical surface. However, EEG and MEG differ in their sensitivity to the orientation and location of neuronal sources, as a result of which some epileptic spikes are recorded only in EEG and some only in MEG. Therefore, this dissertation provides a new source analysis pipeline for combining the complementary information from EEG and MEG within a fusion framework in order to improve the localization of IEDs.

The goal of this dissertation was achieved through three main projects. The first project was to design and develop an optimal EEG/MEG fusion strategy using the MEM method (MEM-fusion), which was then quantitatively evaluated using realistic simulations. The originality of MEM framework lies in its ability to incorporate the complementary information brought by EEG and MEG data through a spatio-temporal prior model; which allows for an efficient integration of the two modalities. MEM-fusion proved to be more accurate and robust than monomodal EEG/MEG localizations and other standard source localization approaches. We also investigated the impact of the number of EEG electrodes required for an efficient EEG-MEG fusion, suggesting that only 20 EEG electrodes can bring sufficient information missed by MEG.

Performance of MEM algorithm has never been studied when dealing with high density EEG and MEG data on complex patterns of IEDs. In the second project, we used a realistic simulation pipeline that combined a biophysical distributed model

with a computational neural mass model to generate simultaneous high density EEG and MEG signals mimicking normal background and IEDs. The complex patterns of IEDs involved sources at different spatial extents, exhibiting propagation patterns and correlated activity. Comparing MEM with another source localization method also developed for its ability to recover spatially extended sources (4-ExSo-MUSIC), we showed their accuracy when localizing and characterizing complex patterns of IEDs using either EEG or MEG data.

Finally, a common practice in EEG/MEG source analysis of IEDs involves selecting reproducible transients of IEDs, averaging them to improve the signal-to-noise ratio before applying source localization. However, averaging effect is likely to filter out source activities, which vary slightly over each individual spike due to signal cancellation. Thus, single spike source localization seems appropriate for bringing important information carried by the individual spikes, more so when combining EEG and MEG data for source localization. To this end, the third project was to assess the clinical relevance of single spike source localization using MEM-fusion. To do so, we proposed and validated a new source analysis approach involving clustering of single spike source localization results to provide a consensus map for the most reproducible and clinically reliable source localization results. The combination of MEM-fusion and consensus map was applied on 26 patients with focal epilepsy, which yielded successful localization in all cases. This pipeline is able to overcome the limitations of averaged spike localization and offers an efficient way to characterize the most reproducible and reliable source results from clinical data, thus demonstrating the pertinence of MEM-fusion as a valuable non-invasive tool for pre-surgical evaluation of epilepsy.

ABRÉGÉ

Détecter et analyser les décharges épileptiques inter-ictales (DEI) contribuent à l'identification et la localisation du foyer épileptogène, lors de l'évaluation pré-chirurgicale des patients souffrant d'épilepsie réfractaire. L'Électroencéphalographie (EEG) et la Magnétoencéphalographie (MEG) permettent de mesurer les propagations rapides des DEI qui sont générées au niveau de régions spatialement étendues, et ce à l'aide d'une excellente résolution temporelle. Les méthodes de localisation de sources tels que le Maximum d'Entropie sur la Moyenne (MEM), autorisent la localisation précise des générateurs des signaux EEG et MEG, ainsi que leur extension spatiale le long de la surface corticale. Cependant, l'EEG et la MEG sont sensibles à différentes caractéristiques liées à l'orientation et la position des sources neuronales, de sorte que certaines DEI sont visibles seulement en EEG alors que d'autres seulement en MEG. L'objectif de cette thèse de doctorat est de proposer et valider une nouvelle méthode de fusion des informations complémentaires en EEG et MEG afin d'améliorer la localisation des DEI.

Trois projets principaux ont permis d'atteindre notre objectif. Le premier projet a consisté en la réalisation d'une stratégie optimale de fusion EEG/MEG dans le cadre du MEM (MEM-fusion). Les performances du MEM-fusion ont été évaluées à l'aide de simulations réalistes. L'originalité du modèle MEM réside dans sa capacité à incorporer, de manière optimale, les informations complémentaires EEG et MEG dans un modèle spatio-temporel a priori. Le MEM-fusion s'est avéré plus précis et robuste que le MEM monomodal EEG ou MEG ainsi que d'autres méthodes classiques de localisation. L'impact du nombre d'électrodes EEG nécessaire à une fusion optimale a aussi été étudié, concluant qu'il suffisait de 20 électrodes EEG pour apporter l'information additionnelle manquante en MEG.

Les performances du MEM n'ont jamais été étudiées en présence de données EEG haute densité et de MEG lors de profils de DEI complexes. Dans ce deuxième

projet, nous avons utilisé un modèle biophysique distribué couplé à un modèle de masses neurales afin de simuler des signaux EEG haute densité et MEG réalistes. Ces simulations consistaient en la génération de DEI complexes, impliquant des sources d'extensions spatiales différentes, associées à des activités corrélées ou se propageant. Le MEM a été comparé avec une autre méthode de localisation de sources précédemment développée dans le but de récupérer des sources étendues spatialement (4-ExSo-MUSIC).

Finalement, lors de l'analyse de sources des DEI en EEG ou MEG, il est courant de sélectionner des décharges reproductibles et de les moyenner afin d'améliorer le rapport signal/bruit avant de localiser les sources. Cependant, l'effet de moyennage a tendance à supprimer la variabilité inhérente des pointes individuelles. Ainsi, localiser des DEI non moyennées semble plus appropriée pour prendre en compte une telle variabilité, notamment lorsqu'il s'agit de combiner EEG et MEG dans le cadre d'un processus de fusion. Le troisième projet consistait en l'évaluation de la pertinence clinique des localisations de DEI individuelles non moyennées à l'aide de la fusion MEM. Nous avons proposé et validé une nouvelle approche basée sur la classification hiérarchique de résultats de localisations de sources de DEI individuelles, afin d'estimer une carte de consensus spatial des localisations les plus reproductibles. Appliquée à l'analyse de données de 26 patients atteints d'épilepsie focale, notre approche combinant fusion MEM et estimation d'une carte de consensus a permis la localisation du foyer épileptique dans tous les cas, surmontant ainsi les limitations inhérentes à la localisation de DEI moyennées. Notre méthode permet d'extraire des résultats cliniques reproductibles et fiables, démontrant ainsi la pertinence de la fusion MEM en tant qu'outil non invasif lors de l'évaluation pré-chirurgicale des patients épileptiques.

ACKNOWLEDGMENTS

This project was supported by studentship from Savoy foundation, Quebec Bio-Imaging Network (QBIN) PhD Foreign Student scholarship, BioMedical Engineering (BME) Excellence award, grants from Natural Sciences and Engineering Research Council of Canada (NSERC), Fonds de la recherche en santé du Québec (FRSQ), and Canadian Institutes of Health Research (CIHR) (MOP-133619).

First and foremost, I would like to extend my deepest gratitude to Dr. Christophe Grova, my supervisor. It has been my honor to be his first student. This thesis and my research were successful because of his dedicated guidance, support and for his trust in me. He has taught me the fundamentals of scientific research. His critical thinking, attention to details, the joy and enthusiasm he has for his research were awe-inspiring. I deeply appreciate all his contributions of time, ideas, and financial support to make my PhD experience productive and stimulating. I am thankful for his encouragement, his insightful comments and discussions. I am grateful for his emotional support during tough times in the PhD pursuit.

Thanks to Dr. Jean-Marc Lina for helping me through all the methodological aspects and for his regular guidance and useful comments when designing my projects and writing my articles. I have appreciated the camaraderie and local expertise of the students of Dr. Jean-Marc Lina.

I am grateful to Dr. Eliane Kobayashi for her advice and expertise in clinical matters. It is through her collaboration that I had access to the clinical EEG/MEG data.

I would like to thank the rest of my PhD thesis committee: Prof. Sylvain Baillet, and Prof. Louis Collins, for their insightful comments and encouragement, but also for the hard questions which incented me to widen my research from various perspectives.

Special thanks to my colleague Dr. Giovanni Pellegrino for his help in reviewing EEG/MEG data, his insightful ideas and for enriching my knowledge on epilepsy. I am also thankful to my colleagues Dr. Marcel Heers, Dr. Giovanni Pellegrino, and Tanguy Hedrich for their help in acquiring EEG/MEG data. I am grateful to all of them for their hard work, their passion for research, and their friendship.

My sincere thanks to Dr. Isabelle Merlet and her team for their collaboration on the project of my second manuscript. In this project we compared two source localization algorithms, one developed by their team and the other developed by our team. It is through this collaboration that I had access to the codes of their source localization algorithm. Dr. Merlet primarily helped generate realistic simulations of EEG and MEG data from neural mass model. She also contributed equally in preparing the results and the second manuscript. I am also grateful to Dr. François Dubeau for giving me access to the intracranial EEG findings required for my third manuscript.

Thanks to Pina Sorrini, Daniel Caron, Nancy Abate, I was able to navigate through the administrative maze. And thanks to the Biomedical Engineering Department for extending all its resources for my work.

Special thanks to my colleagues and friends for keeping me motivated and cheerful during the writing of this dissertation. A special mention to Atousa Assadi for her continuous help in formatting, editing and proof reading of this dissertation.

I would like to acknowledge all the love, patience, and moral support that my husband and family has endlessly given me over the years, and for keeping me motivated to achieve greater grounds.

CONTRIBUTION OF AUTHORS

Manuscript 1: MEG–EEG Information Fusion and Electromagnetic Source Imaging: From Theory to Clinical Application in Epilepsy

Authors: ***Rasheda Arman Chowdhury****, Younes Zerouali, Tanguy Hedrich, Marcel Heers, Eliane Kobayashi, Jean-Marc Lina, Christophe Grova*

Published in Brain Topography on May 28, 2015

Rasheda Arman Chowdhury designed and implemented the EEG-MEG fusion framework, performed the data analysis, interpreted the results and wrote the manuscript.

Younes Zerouali contributed to the interpretation of results and revision of the manuscript.

Tanguy Hedrich contributed to the implementation of some quantitative metrics and revision of the manuscript.

Marcel Heers visually identified the EEG and MEG interictal spikes and revised the manuscript.

Eliane Kobayashi helped in gathering clinical data and information, visually identified the EEG and MEG interictal spikes, and contributed to the interpretation of the results, redaction and revision of the manuscript.

Jean-Marc Lina contributed to the design of the study, interpretation of the results, redaction and revision of manuscript.

Christophe Grova supervised the project, contributed to the design of the study, interpretation of the results, redaction and revision of manuscript.

Manuscript 2: Complex patterns of spatially extended generators of epileptic activity: Comparison of source localization methods cMEM and 4-ExSo-MUSIC on High Resolution EEG and MEG data

Authors: ***Rasheda Arman Chowdhury****, Isabelle Merlet, Gwenael Birot, Eliane Kobayashi, Anca Nica, Arnaud Biraben, Fabrice Wendling, Jean-Marc Lina, Laurent Albera, Christophe Grova*

Published in NeuroImage on August 22, 2016

Rasheda Arman Chowdhury designed the study, implemented the simulation and source localization pipeline for data analysis, participated in the data acquisition of clinical data, interpreted the results and wrote the manuscript.

Isabelle Merlet participated in the designing of the study, initiated with C. Grova the collaboration leading to the idea of comparing cMEM with 4-ExSo-MUSIC algorithm, generated the simulations using neural mass model, visually marked the interictal spikes for clinical data application, contributed to the data analysis, interpretation of the results, redaction and revision of the manuscript.

Gwenael Birot provided the code for 4-ExSo-MUSIC algorithm and revised the manuscript.

Eliane Kobayashi helped gathering clinical data and information, visually marked the interictal spikes from the clinical data and contributed to the interpretation of clinical MEG results.

Anca Nica was involved in the data acquisition and interpretation of the results regarding clinical EEG data.

Arnaud Biraben was involved in the data acquisition and interpretation of the results regarding clinical EEG data.

Fabrice Wendling provided the environment for neural mass simulations and revised the manuscript.

J.M. Lina contributed to the design of the study, interpretation of the results, redaction and revision of manuscript.

Laurent Albera contributed to the design of the study, interpretation of the results, redaction and revision of manuscript.

Christophe Grova supervised the project, initiated the collaboration with Isabelle Merlet, contributed to the design of the study, interpretation of the results, redaction and revision of manuscript.

Manuscript 3: Reproducibility of EEG-MEG fusion source analysis of interictal spikes - relevance in pre-surgical evaluation of epilepsy

Authors: ***Rasheda Arman Chowdhury****, Giovanni Pellegrino, Umit Aydin, Jean-Marc Lina, François Dubeau, Eliane Kobayashi, Christophe Grova*

In preparation

Rasheda Arman Chowdhury designed the whole study, implemented the method to estimate the consensus maps, performed the data acquisition, selection and analysis, interpretation of the results and wrote the manuscript.

Giovanni Pellegrino contributed to the design of the study, data selection, visual identification the EEG and MEG interictal spikes, delineation of the gold standard irritative zone from clinical data, interpretation of the results, and revised the manuscript.

Umit Aydin contributed in the interpretation of the results and revised the manuscript.

Jean Marc Lina proposed the idea of consensus map approach, contributed to the design of the study, interpretation of the results, redaction and revision of the manuscript.

Francois Dubeau helped gathering clinical data and information and revised the manuscript.

Eliane Kobayashi contributed to the design of the study, helped gathering clinical data and information, contributed to the visual identification the EEG and MEG

interictal spikes, delineation of the gold standard irritative zone from clinical data , interpretation of the results, redaction and revision of the manuscript.

Christophe Grova supervised the project, contributed to the design of the study, interpretation of the results, redaction and revision of manuscript.

Table of Contents

LIST OF TABLE

LIST OF FIGURES

Introduction

Epilepsy is a neurological disorder characterized by the tendency to have recurrent seizures. Approximately 50 million people worldwide have epilepsy ("WHO | Epilepsy," 2016). Treatment options include antiepileptic drugs, surgery, vagus nerve stimulation, and ketogenic diet (usually in children) (Banerji and Pauranik, 2011). Most patients (about 70%) have their seizures controlled with drug therapy but about 20-30% patients are refractory to all forms of drug therapy. An approximate estimate is that one half of patients with medically intractable epilepsy are potential candidates for epilepsy surgery (Engel, 1996). Epilepsy surgery allows to reduce or even stop the occurrence of seizures. Candidates for epilepsy surgery undergo an extensive pre-surgical evaluation, which aims at localizing the areas in the brain called the epileptogenic focus where the epileptic discharges are generated, and to determine whether surgical treatment can be considered. The evaluation also helps to precisely identify important structures in the brain, so that epileptogenic focus may be removed without causing damage to important nearby brain regions or causing only minimal functional loss.

The state during which the seizure takes place is called the ictal state. Between seizures, abnormal neuronal discharges, the so-called interictal epileptic discharges (IEDs) may take place; they usually occur more frequently than the seizures. They are generated without any clinical manifestations, originating partially from brain regions similar to the ones involved during the seizures, i.e. from the epileptogenic focus. Analysis of IEDs is widely used as a marker of epilepsy (Ebersole, 1997a, 1997b; Noachtar and Rémi, 2009). *The overall goal of this PhD dissertation consists in improving the localization of the epileptogenic focus using these markers, which is a crucial task during the pre-surgical evaluation of epilepsy surgery* (Lüders and Awad, 1992; Chauvel et al., 1996).

During such a pre-surgical investigation, several anatomical or functional neuroimaging techniques are considered, for instance, scalp Electroencephalography (EEG), video-EEG monitoring, Magnetic Resonance Imaging (MRI), Single Photon Emission Computed Tomography (SPECT), Positron Emission Tomography (PET), functional MRI (fMRI), Magneto-encephalography (MEG) and Intracranial EEG (iEEG) when available (Engel, 1993, 1996; Jette and Wiebe, 2013). Each of these modalities brings complementary information to circumscribe the patient-specific underlying epileptogenic focus. For instance, an MRI scan can reveal structural abnormalities of the brain such as developmental malformation, tumor growths, scars, or other physical conditions that may be cause seizures. SPECT and PET, which monitor brain hemodynamic and metabolic processes, can identify brain regions exhibiting functional abnormalities associated with the epileptic tissues (e.g., glucose hypometabolism). EEG and MEG, which measure the bio-electrical and bio-magnetic neuronal activity, respectively, can detect abnormal epileptic discharges non-invasively. iEEG which records bioelectrical activity can detect abnormal epileptic discharges from the cerebral cortex using electrodes placed directly on the exposed surface or inside the brain. *In the present PhD dissertation, we focused on pre-surgical evaluation involving noninvasive techniques (EEG and MEG) to recover with high temporal resolution the generators of neuronal epileptic discharges.*

EEG and MEG are non-invasive electro-physiological techniques, which measure on the scalp the electric and magnetic fields generated by synchronous neuronal currents, respectively. The postsynaptic currents generated within the large pyramidal neurons of the cortical layer V, which are oriented perpendicularly to the cortical surface of the brain, are the main generators of EEG and MEG (Speckmann et al., 2004). Epileptic activity originates from abnormal excitability and synchronization of neurons. Because of their high temporal resolution (~1ms), EEG and MEG are the only non-invasive techniques that are able to directly detect and follow the fast propagating epileptic discharges (Stefan, 2009; Ebersole and

Ebersole, 2010; Lopes da Silva, 2013). To be detected from scalp EEG or MEG recording, the generators of epileptic discharges should be synchronized over a spatially extended region of several square centimeters, in order to result in a signal of sufficient amplitude visually distinguishable from the ongoing background activity (Cooper et al., 1965; Ebersole, 1997a; Mikuni et al., 1997; Merlet and Gotman, 1999; Oishi et al., 2002; Tao, Baldwin, Hawes-Ebersole, et al., 2007; von Ellenrieder et al., 2014a; Ramantani et al., 2014).

Source localization methods using EEG and MEG data aim at locating within the brain the generators of EEG and MEG data measured from the scalp. In the context of epilepsy, an additional challenge lies in localizing the generators of transient epileptic discharges while recovering their spatial extension. In this regard, the teams of Dr. Grova and Dr. J.M. Lina work in close collaboration to develop and evaluate source localization methods within the Maximum Entropy on the Mean (MEM) framework. These methods provide reliable and accurate localization of the sources of EEG and MEG discharges together with their spatial extent along the cortical surface (Amblard et al., 2004; Grova et al., 2006, 2016, Chowdhury et al., 2013, 2015; Lina et al., 2014; Heers et al., 2016). Although EEG and MEG are generated by the same neurophysiological processes, there are important differences concerning the way signals are generated. As a result, scalp EEG and MEG provide complementary information and different sensitivity to epileptic discharges. This means not all epileptic MEG discharges are accompanied by simultaneous EEG discharges, and conversely not all EEG discharges are accompanied by MEG discharges. Integrating these two modalities within the same framework can therefore bring in complementary information, thereby allowing better accuracy in source localization (Cohen and Cuffin, 1983; Sharon et al., 2007; Molins et al., 2008; Ebersole and Ebersole, 2010; Tanaka et al., 2010).

The aim of this PhD dissertation project is to develop and carefully validate an optimal EEG-MEG fusion strategy using simultaneous EEG-MEG recordings to accurately localize the generators of IEDs, their spatial extent and propagation patterns. This, in turn, is expected to demonstrate the clinical relevance of source

localization from EEG-MEG fusion as a valuable non-invasive clinical tool during the pre-surgical investigation of patients with epilepsy.

We hypothesized that the differences in sensitivity of the two modalities, the increased number of recording channels considered when fusing them, and the ability of MEM method to localize spatially extended sources, will provide an accurate localization of epileptic generators.

This thesis is organized in the following way. Chapters 1, 2 and 3 will provide the necessary background. Chapter 1 will present the fundamental mechanisms underlying epilepsy and pre-surgical evaluation of epilepsy. It consists of a brief introduction to epilepsy, types and treatment of epilepsy, and pre-surgical evaluation. In Chapter 2, the reader will be introduced to the non-invasive electrophysiological techniques (EEG and MEG) by presenting their technical and biological basis. This chapter will first review the history of EEG and MEG. Then, there will be a discussion about the generators of electromagnetic activities, i.e. neurons, their anatomy, mechanisms involved in producing electric and magnetic fields, followed by differences in the sensitivities of EEG and MEG and their instrumentation. Chapter 3 will summarize the concept of source localization, describing some of the common source localization methods used to analyze the electric and magnetic fields. This will also include a detailed description of the MEM method, followed by a discussion on the validation of source localization methods. Then, a brief literature review on EEG/MEG source localization of IEDs will be presented, before reviewing the importance of combining EEG and MEG data in the context of localizing interictal spikes. Original contributions and details of the studies leading to the development, validation and application of the proposed EEG-MEG fusion strategy will be presented in Chapters 4, 5, and 6. Chapter 4 will present the first published manuscript (Chowdhury et al., 2015), which describes the developed MEM-based EEG-MEG fusion source localization method, its quantitative evaluation using realistic simulations, and its comparison with other standard source localization methods. This paper also investigates the impact of the number of EEG electrodes required when combining EEG with the

high density MEG within a fusion framework. Chapter 5 will present the second published manuscript (Chowdhury et al., 2016) involving a quantitative assessment of the MEM algorithm on complex patterns of IEDs using realistic simulations of EEG and MEG data generated from a neural mass model. In this study, the MEM algorithm was compared with an advanced source localization algorithm called the 4-ExSo-MUSIC (4^{th} order extended source multiple signal classification), which has also been developed for its sensitivity to the spatial extent of the generators of epileptic discharges. This was a collaborative study with the research team UMR INSERM U1099, Laboratoire de Traitement du Signal et de l'Image (Université de Rennes 1, France) who developed the 4-ExSo-MUSIC method. Chapter 6 will present the third manuscript, which studied the application of MEM-based fusion on clinical data, and an investigation of the impact of the number of EEG electrodes required during fusion on clinical data. Finally, Chapter 7 will conclude the thesis with a summary and a discussion of the findings, the contributions of this work, and conclusion.

Chapter 1 Fundamentals and pre-surgical evaluation of epilepsy

This chapter will provide a brief overview on epilepsy, classification of seizures and epilepsy, treatment of epilepsy mainly focusing on epilepsy surgery and finally details on pre-surgical evaluation of intractable epilepsy.

1.1. Epilepsy

Epilepsy is among the most serious primary disorders of the brain and accounts for 1% of the global burden of disease. Seizures are the primary manifestations of epilepsy, which occur when a population of nerve cells, or neurons, in the brain fire abnormally. This can lead to many symptoms such as a person's consciousness or actions are altered for a short period of time (seconds to minutes in general). Epileptic seizures can be caused by a wide variety of factors such as brain lesions, tumors, central nervous system disease, post-traumatic scar, family history (genetic component), or other abnormalities (whose cause may be not known).

In ancient times, epileptic attacks were thought to be the result of invasion and possession of the body by supernatural forces, usually malign or evil influences, requiring exorcism, incantations or other religious or social approaches (Global Campaign against Epilepsy et al., 2005). Although first suggested by Hippocrates in the 5th century B.C., the concept of epilepsy as a brain disorder only began to take root in the 17th and 18th centuries. Until the middle of the 19th century, epilepsy was widely assumed to be a vascular disease, but in 1849 Robert Bentley Todd, who was influenced by Michael Faraday's contemporary work on electromagnetism, came up with a new explanation to epilepsy that is based on the electromagnetic theory. Today it is known that epileptic seizures are due to

abnormal, synchronous and excessive electrical activity in the brain (Reynolds and Trimble, 2009). A wide range of different types of seizures and epilepsy syndromes have been identified. Patients are now treated with pharmacotherapy, with neurosurgical techniques, as well as with psychological and social support.

1.2. Types of seizures and epilepsy syndrome

The classification of seizures and epilepsy can be important for prognosis and treatment. The type of seizure depends upon several factors. One of the most important factors is the site of the abnormal electrical discharges. The 1981 International league against Epilepsy (ILAE) seizure classification ("Proposal for revised clinical and electroencephalographic classification of epileptic seizures.," 1981) is the most widely accepted classification system, despite revisions in terminology and classification of seizures and epilepsy by the ILAE ("Proposal for revised classification of epilepsies and epileptic syndromes.," 1989; Berg et al., 2010; Fisher et al., 2016). It is based on clinical features, interictal and ictal EEG, and neuroimaging. It divides known epilepsy seizures into partial and generalized seizures, depending on their site of origin and propagation pattern **Figure 1.1**. When the seizures have onset on one region of the brain they are defined as focal seizures while the generalized seizures may rapidly involve a large portion of both hemispheres (Fisher and Saul, 2010).

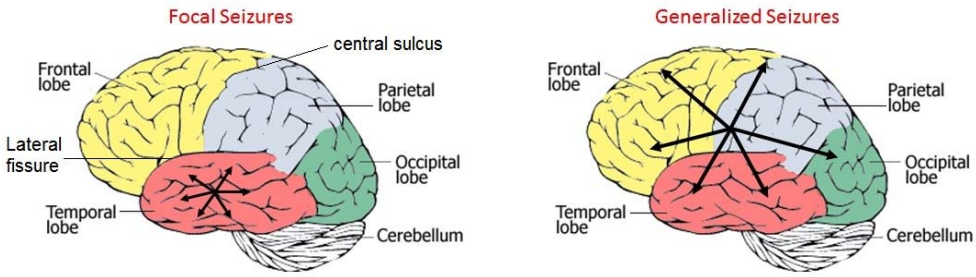

Figure 1.1. The cerebrum is the largest part of the brain. The outermost layer of the cerebrum is the cerebral cortex, the gray matter. Each hemisphere of the brain is divided into: Frontal, Parietal, Temporal and Occipital lobes. Focal seizures have onset on one lobe or region of the brain. Generalized seizures may involve several lobes of both hemispheres. Modified from https://www.epilepsy.org.au/about-epilepsy/understanding-epilepsy/human-brain-seizures.

Epilepsy syndromes can be classified according to etiology (cause) and type of seizure. Based on etiology, epilepsy can be symptomatic, idiopathic, or cryptogenic. Symptomatic means that a cause of the disease has been identified as, for instance, head injury, cerebrovascular disorders, brain infections, cortical malformations, or brain tumors. Idiopathic denotes a presumed genetic origin without any visible structural brain lesion or other neurological signs or symptoms. Cryptogenic means that no cause has been identified but a structural rather than genetic cause is suspected. The number of cases falling in the cryptogenic category is actually decreasing with recent progress in genetic and neuroimaging studies, identifying more and more possible causes of the disease. If the seizures are focal, the epilepsy is said localization-related, whereas if the seizures are generalized, the epilepsy may be either generalized or localization-related. Most of the localization-related epilepsies are the results of a suspected structural brain abnormality, even though it cannot always be identified. Localization-related epilepsies are usually divided into mesio-temporal and neocortical based on electroclinical semiology. Depending on which part of the cortex is affected, neocortical epilepsies can be frontal, parietal, occipital or neocortical temporal lobe epilepsy [1].

1.3. Treatment of epilepsy

The main clinical procedure when diagnosing epilepsy is a careful medical history with as much information as possible about what the seizures looked like and what

[1] https://www.uptodate.com/contents/localization-related-focal-epilepsy-causes-and-clinical-features#H10

happened just before they began, i.e. the initial seizure semiology. A second major diagnostic test in evaluating a patient with possible epilepsy is scalp EEG. Neuronal electrical activity, measured using scalp EEG, shows specific patterns that can assist the identification and classification of epileptic activity. Moreover, video-EEG recording of the seizure episodes allows synchronous recording and display of EEG patterns and video-recorded seizure semiology, thus assisting the epileptologists in diagnosis and classification of the seizures and epilepsy syndrome. Treatment of epilepsy consists in controlling the occurrence and severity of the seizures using anti-epileptic drugs (AED). Generally, long-term drug therapy helps about 70% of the epileptic population to either become seizure free or reduces the occurrence of seizures, while the remaining 30% who are resistant to the drug therapy are considered for other forms of treatment (Berg, 2004). However, the type of treatment prescribed depends on several factors including the frequency and severity of the seizures, localization of the epileptogenic focus as well as the person's age, overall health and medical history.

1.3.1. Epilepsy surgery

Epilepsy surgery, which involves surgical resection of the epileptogenic zone (brain region that is responsible for the generation of the seizures), is one form of treatment (Genow et al., 2004). It is considered to be an appropriate solution to help patients who are in critical condition. Besides, surgically remediable epilepsies can be diagnosed using non-invasive procedures in most patients, and early surgical intervention is not only associated with seizure freedom in these patients but can prevent the development of irreversible psychological and social disabilities (Global Campaign against Epilepsy et al., 2005). Depending on the epilepsy syndrome and the ability to define clearly and resect completely the epileptogenic zone, 30–85% of epilepsy patients who underwent epilepsy surgery remain seizure-free (Stippich, 2007). Some of the large epilepsy centers reported average seizure-free rates of ~60% (Engel, 1993, 1996).

Sir Victor Horsley, recognized as pioneer of Neurological surgery, performed his first craniotomy in 1886 to effect a cure of epilepsy (Horsley, 1886; Feindel et al., 2009). Until the invention of EEG in 1929 by Hans Berger (Niedermeyer and Lopes da Silva, 2005; Cacioppo et al., 2007), the main source of information for the surgery was the seizure semiology observed by the physician (Global Campaign against Epilepsy et al., 2005). The introduction of EEG into epilepsy diagnosis was important in the development of surgical techniques. Herbert Jasper's work with Wilder Penfield at Montreal Neurological Institute (MNI) from 1937 led to increasing recognition of role of EEG in localization for epilepsy surgery (Feindel et al., 2009). They refined surgical techniques and developed diagnostic and localization techniques that included EEG, cortical stimulation, neuroradiology, Wada test, and neuropsychology. In recent years, the number of epilepsy surgeries is increasing especially in the developed countries due to important advancements in neuroimaging techniques and in pre-surgical epilepsy diagnosis with the help of interdisciplinary teams involving neurologists, neurosurgeons, radiologists, neurophysiologists, engineers, and mathematicians (Global Campaign against Epilepsy et al., 2005).

A patient having refractory epilepsy (pharmaco-resistant epilepsy) whose quality of life is significantly impaired by epilepsy, may become an epilepsy surgery candidate if seizures are of focal origin. Focal epilepsy arises as a result of epileptic activity in a localized portion of the brain or epileptogenic focus. In those cases, the surgical resection of this focus can help eliminate the incidences of epileptic seizures. However, care must be taken to minimize the effects of the surgical procedure on potentially healthy brain regions surrounding the epileptogenic focus. Therefore, before surgery is considered, a comprehensive pre-surgical evaluation, aiming at mapping both the patient specific epileptogenic focus and surrounding eloquent areas is necessary.

1.3.2. Pre-surgical evaluation of epilepsy - diagnostic techniques

The main goal of the pre-surgical evaluation of patients with intractable epilepsy is to determine the location of the epileptogenic zone. The evaluation requires prolonged video-EEG monitoring and other available exams, for instance, scalp EEG, MEG, Magnetic Resonance Imaging (MRI), Positron Emission Tomography (PET), Single Photon Emission Computed Tomography (SPECT), functional MRI (fMRI) in combination with EEG, and neuropsychological tests to pinpoint the exact location of the injured brain cells causing the seizures (Engel, 1993, 1996; Jette and Wiebe, 2013).

The location of the damaged cells determines whether the surgery can be performed and what technique should be used. For example, scalp EEG is a non-invasive electrophysiological technique used to record the electric potentials produced by the neuronal activity related to the epileptiform discharges. MEG is also a non-invasive electrophysiological technique used to record the magnetic fields produced by the same neuronal sources. MRI provides a structural estimate of the location of scar tissue or malformations of cortical development, which are major causes of intractable epileptic seizures. PET images reveal relative uptake of radioactively labeled glucose or neurotransmitters. They show areas of the brain with increased or decreased metabolism or neurotransmitter binding during a period of time shortly after the seizure. SPECT scans are images of cerebral blood flow averaged over the course of 40 s following the injection, made by measuring the distribution of a radioactively labeled tracer material as it travels though the blood vessels. When the injection is performed just at the beginning of the seizure, SPECT can depict the initial blood flow increase at the initiation of a seizure, this is the so-called ictal SPECT (la Fougère et al., 2009). fMRI provides an indirect estimate of the location of active brain tissue by measuring the changes in venous blood oxygen levels produced by neuronal activity. EEG can be recorded simultaneously with fMRI to identify the timing of interictal events on EEG at millisecond resolution and spatially localize with fMRI at millimeter resolution (Gotman and Pittau, 2011). Neuropsychology exam allows to evaluate areas exhibiting impairments in

specific cognitive functions in relation with the presumed epileptogenic focus, as well as medication effects, and emotional/psychological issues that may come up.

Most epilepsy centers employ implantation of intracranial electrodes to complement the non-invasive evaluations in guiding surgical resections by providing precise localization of an epileptogenic zone and functional cortex (Jayakar et al., 2016). Intracranial EEG (iEEG) records the electrical potentials directly within the cortical layers by implanting electrodes surgicallyon or into the brain tissue (either on the surface using subdural grid/strips or in the depths of the brain using depth electrodes). The techniques and types of recordings used by the centers vary greatly. For instance, most major epilepsy centers in North America and Japan employ subdural electrodes or combination of subdural and depth electrodes while European epilepsy centers rely primarily on stereotactically inserted depth electrodes (sEEG), which were introduced by Bancaud and Talairach in the 1950s (Enatsu and Mikuni, 2016).

Brain cells send and receive signals in a time span less than 10 milliseconds and multiple communications between several brain regions can occur in 200 to 300 milliseconds. PET, SPECT and fMRI measure indirectly the brain activity through metabolism and hemodynamic processes respectively. Therefore, they offer an excellent spatial resolution but low temporal resolution. The high temporal resolution of MEG and EEG allows tracking communications between brain regions occurring in one hundredth to one third of a second. This excellent temporal resolution of EEG and MEG is similar to that of iEEG as both are almost directly measuring the activity of the neurons (**Figure 1.2**). However, implanted electrodes can only detect brain activity occurring within a few millimeters from the electrodes, therefore implantation should be targeted towards presumed regions where epileptic activity should be assessed. In addition, iEEG requires a neurosurgical procedure to implant electrodes on the surface or in the depths of the brain (Jayakar et al., 2016). Therefore, the added value obtained in terms of better spatial and temporal resolution in iEEG is counter-balanced by the additional morbidity that is necessarily associated with invasive methods. The combination of

non-invasive and high temporal resolution of MEG and EEG measurements make them particularly interesting when compared to other brain functional imaging modalities. The millisecond temporal resolution of both EEG and MEG make them ideal for the study of spontaneous, evoked, and induced oscillatory processes at different frequency bands such as analysis of interictal spikes (Hamandi et al., 2016; Heers et al., 2016), ictal discharges (Pellegrino et al. 2016a), high gamma oscillations (Rampp et al., 2010; Jeong et al., 2013), high frequency oscillations (von Ellenrieder et al., 2016), functional connectivity and network analysis (Pittau and Vulliemoz, 2015) .

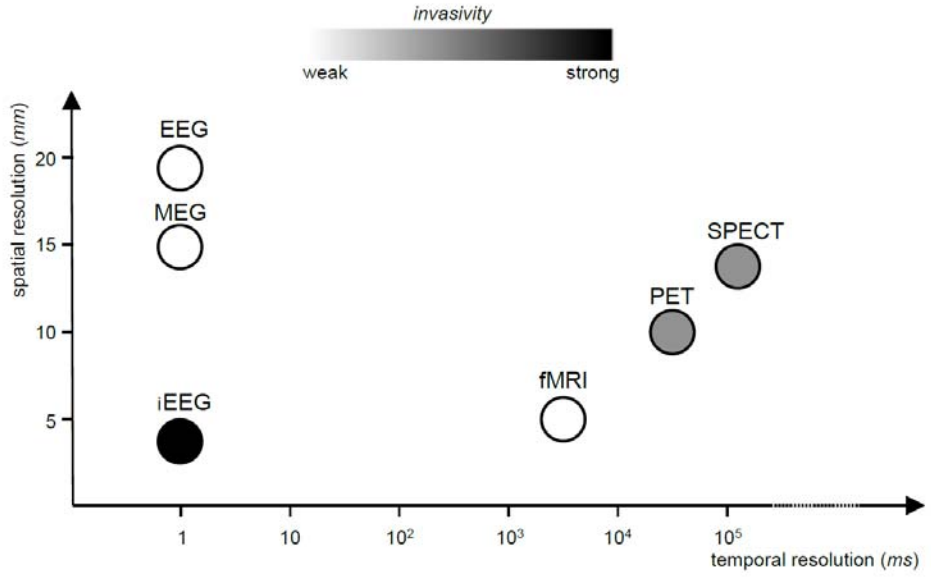

Figure 1.2. Spatial and temporal resolution of the different diagnostic techniques along with their level of invasiveness. Extracted from (Gramfort, 2009).

1.3.3. Pre-surgical evaluation of epilepsy - cortical zones

Success of epilepsy surgery depends profoundly on the correct determination of the epileptogenic zone. This zone is defined as the minimum amount of cortex that has to be resected (inactivated or completely disconnected) to produce seizure freedom (Chauvel et al., 1996; Luders et al., 2006). This zone is estimated prior to surgery based on information available from initial seizure semiology, lesions seen in MRI images, video EEG long term monitoring, MEG, SPECT, PET, EEG-fMRI and

neuropsychological examination. The epileptogenic zone cannot be identified directly. It is a theoretical zone that can be estimated by a number of other "zones" (**Figure 1.3**). The following five zones have been determined as the standard cortical zones that can be measured during the pre-surgical evaluation using different diagnostic techniques (Rosenow and Lüders, 2001):

1) Ictal onset zone: is the zone in which seizures are originating. This zone is always contained in the epileptogenic zone, but may be smaller than the epileptogenic zone. This area is determined primarily by EEG (invasive and non-invasive), but can also be defined by ictal SPECT and to a lesser degree by EEG-fMRI and MEG;

2) Epileptogenic lesional zone: lesion (scar, tumor or malformation) causing epilepsy. This brain area is usually defined by anatomical imaging such as high resolution MRI.

3) Symptomatogenic zone: zone that produces the first clinical manifestations of seizures. This area is determined by analyzing the initial seizure symptomatology.

4) Irritative zone: is defined as the brain area producing abnormal transient synchronous discharges of nerve cell clusters between seizures (interictal discharges). The irritative zone or the generator of interictal epileptic discharges (IEDs), is one of the most important zones for locating the epileptogenic zone, since it can be non-invasively detected and localized using EEG and/or MEG. It is believed that the interictal spiking emanates from an area larger than that responsible for ictal onset (Hauf et al., 2012). Several studies (Agirre-Arrizubieta et al., 2009; Brodbeck et al., 2011; Jung et al., 2013) validated EEG with electric source imaging and MEG with magnetic source imaging to show that the generator of IEDs had high spatial concordance with the epileptogenic zone, defined using either iEEG or surgical resection, and that the greater the overlap between the IEDs and the resected brain region the better was the seizure outcome. Therefore, an

accurate identification of the irritative zone can therefore be of crucial importance during pre-surgical evaluation (Bautista et al., 1999; Hufnagel et al., 2000; Ryvlin et al., 2014).

5) Functional deficit zone: zone responsible for functional deficits. This area is usually larger than the seizure onset and the irritative zone. The increased or decreased metabolism observed in PET can be used to assess this area. In addition to neuroimaging methods, neuropsychological examinations and seizure semiology are also used for evaluation of this zone.

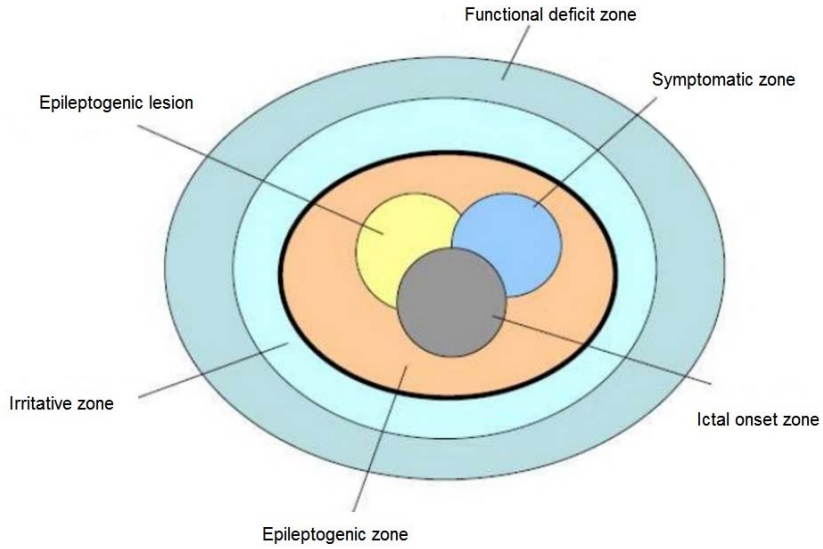

Figure 1.3. Different cortical zones described in (Rosenow and Lüders, 2001). Taken from presentation on slideshare.net: http://www.slideshare.net/yashika54/paroxysmal-dyskinesias.

Pre-surgical evaluation consists in combining many sources of information from different diagnostic techniques to define the epileptogenic zone as precisely as possible. A number of techniques have been developed to enhance understanding of the dynamics of the underlying generators of epilepsy. For instance, source localization of the generators of epileptic activity using EEG, MEG or combined EEG-fMRI (Agirre-Arrizubieta et al., 2009; Brodbeck et al., 2011; Jung et al., 2013). Also, EEG and/or MEG source imaging results are co-registered with

anatomical images from MRI and are reconstructed three dimensionally to show the exact region of activity. Furthermore, today it is widely accepted that epilepsy is a network disease, in which different parts of the brain are involved (Wilke et al., 2011; Kramer and Cash, 2012; Dansereau et al., 2014; Pittau and Vulliemoz, 2015), and thus, understanding the networks causing epilepsy requires the evaluation of the information from the whole brain, which is only possible with noninvasive methods like EEG/MEG, EEG/fMRI, etc. It has also been recently shown that there is a good agreement between noninvasive EEG and MEG source reconstructions and fMRI responses (Heers et al., 2014).

1.4. Interictal Epileptiform Discharges

Seizures are infrequent events in the majority of patients, making recording of ictal EEG or MEG time-consuming and labor intensive. Although it is possible to observe ictal EEG in long term EEG recordings it is rare to record ictal MEG during the short duration of MEG recording. IEDs are spontaneous abnormal paroxysmal events occurring in between the seizures. In 1936, Gibbs and Jasper independently reported the interictal events as the focal signature of epilepsy which means IEDs arise from a network of distributed anatomical brain regions closely related to the epileptogenic zone. These events are generated by the brain without any clinical signs. They do not induce any patient movement and occur more frequently than the ictal discharges (seizures). This suggests IEDs as the hallmarks of epilepsy that can be easily recorded noninvasively using EEG or MEG. This leads to the possibility to study their signatures using other modalities, as for instance simultaneous EEG-fMRI recordings (Gotman and Pittau, 2011). As a result, investigation of interictal activity is an important aspect of pre-surgical evaluation of patients who are candidates for epilepsy surgery (Lüders and Awad, 1992; Chauvel et al., 1996).

The following EEG/MEG patterns are classified as epileptiform discharges: spikes, sharp waves, spike–wave complexes, slow spike–wave complexes, polyspikes, and

seizure patterns (Noachtar and Rémi, 2009). To qualify as an IED, discharges should meet the following criteria as outlined for EEG by Walczak et. al in (Engel et al., 2008):

1. They must be paroxysmal and distinct from the patient's normal background activity.
2. They must include an abrupt change in polarity occurring over several milliseconds.
3. The duration of each transient should be less than 200 ms. A spike has a duration of less than 70 ms; sharp waves have a duration between 70 and 200 ms (**Figure 1.4**).
4. The discharge must have a physiological field, with the discharge recorded from more than one electrode and a voltage gradient should be present.

This definition of an EEG spike is based on its amplitude, duration, sharpness, and emergence from background. However, spikes in MEG have not yet been formally defined. In practice spikes are identified in MEG recording by using EEG as a guide, or by looking at EEG and MEG together and deciding on some general aspects of transients, or even by directly applying EEG spike criteria. Results from several studies showed that interictal epileptiform spikes recorded in EEG and MEG share some properties but differ in other characteristics, such as duration, sharpness, and shape (Merlet et al., 1997; Fernandes et al., 2005). Overall, identification of spikes by observers with EEG experience leads to reproducible and clinically valid results in MEG (Zijlmans et al., 2002).

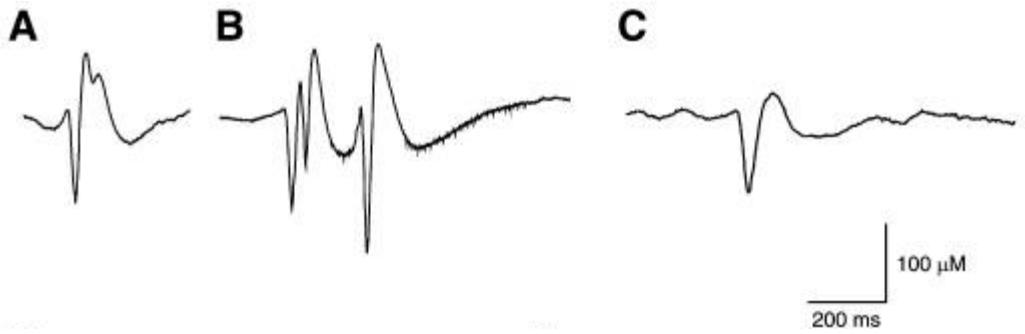

Figure 1.4. Interictal epileptic discharge patterns recorded in human partial epilepsies with intracranial electrodes. (**A**) interictal spike; (**B**) group of interictal spikes from neocortical dysplasia; (**C**) sharp wave from a lesional partial epilepsy. Modified from (de Curtis et al., 2012).

1.5. Conclusion

In summary, the non-invasive electrophysiological techniques, EEG and MEG can track the underlying dynamics of IEDs at a high temporal resolution. This makes them particularly interesting, and complementary to other diagnostic techniques. The detection and analysis of the IEDs is crucial for the identification and localization of the epileptogenic zone, since their generators usually overlap with the region involved in the seizure onset. The irritative zone is one of the most important zones for locating the epileptogenic zone, since it can be non-invasively detected and localized using EEG and/or MEG and identification of the irritative zone correlates with better seizure outcome.

Chapter 2 Non-invasive electrophysiological investigation using EEG and MEG

This chapter will elaborate further on the non-invasive EEG and MEG techniques. After reviewing their historical background, we will present the neuronal mechanisms involved in the generation of EEG and MEG signals, with specific emphasis on the generators of IEDs. The details describing the recording techniques for EEG and MEG will follow. Finally, the factors affecting the detectability of epileptic events in EEG and MEG will be discussed.

2.1. History of EEG and MEG

The recording of the electrical activity of the brain has a long history. In 1875, a British neuropsychologist, Richard Caton, was the first to measure the neural electrical phenomena in rabbits and monkeys (Caton, 1875; Swartz and Godensohn, 1998; Niedermeyer and Lopes da Silva, 2005). A German neuropsychiatrist, Hans Berger, was the first to record electric potentials generated by the human brain (**Figure 2.1**), first reported in 1929 (Berger, 1969; Haas, 2003). Initially, Berger recorded EEG using one electrode placed on the frontal and one on the occipital part of the patient's scalp, an electrocardiogram (ECG) channel and a time marker. He is also credited for inventing the word electroencephalogram as a graphic representation of the difference in voltage between two different cerebral locations plotted over time. With this early work as the foundation, EEG became the standard in clinical diagnostics of brain disorders from mid-1930s through the mid-1970s.

Epileptiform spikes were first recorded by Fisher and Lowenback in 1934 and then in 1935 Frederick Gibbs, Hallowell Davis and William G. Lennox described

interictal spike waves (Lüders and Comair, 2001). Later in 1936 Gibbs and Jasper reported the interictal spike to be a marker of epilepsy. During the same year, Frederick Gibbs, Lennox and Erna Gibbs showed focal spikes and a localized seizure pattern during clinical focal seizure (Lüders and Comair, 2001). In 1950s, William Grey Walter developed an adjunct to EEG called EEG topography, which allowed for the mapping of electrical activity across the surface of the head. To obtain congruence among different laboratories, a standard electrode placement scheme called the 10-20 electrode placement system was proposed by Jasper in 1958, basing the positioning on head anatomical landmarks. This standardization marked the beginning of modern electroencephalography. The number of electrodes used in research has increased over the years from around 19 of Jasper's time to as many as 256 to 512 today (Gevins, 1993; Holmes, 2008). However, the 10-20 system with 19 electrodes is still the dominant standard in routine clinical settings. Studies have shown the merit of dense-array EEG system consisting of more than 64 electrodes in improving the spatial resolution especially when source localization is applied, therefore, most current research is carried out with 64 to 128 electrodes (Ryynänen et al., 2004; Lopes da Silva, 2013).

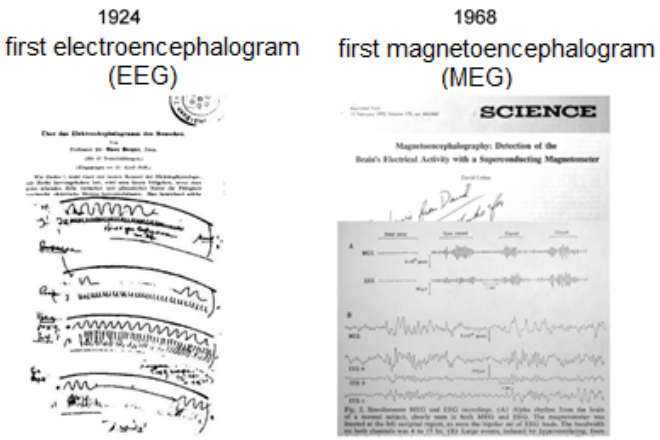

Figure 2.1. First measure of EEG in 1924 that was reported in 1929 by a German neurophysicist, Hans Berger. First measure of MEG in 1968 measured by David Cohen, a physicist in University of Illinois. (Courtesy: Teaching slides on megcommunity.org).

In 1819, Hans Christian Orsted discovered that electric currents create magnetic fields. Magnetic fields produced by cerebral currents in humans (**Figure 2.1**) were

first measured in 1968 by David Cohen, a physicist at the University of Illinois, using room-temperature copper induction coils (Cohen, 1968). The magnetic fields picked up by these coils had a very low signal to noise ratio due to low sensitivity of the device and the presence of magnetic background noise and thus were difficult to use. Under normal conditions the magnetic fields generated by human brain are very weak, in the range of 10^{-12} to 10^{-15} T, which is much weaker than the earth's magnetic field of 10^{-4} T or the one created by the 50/60 Hz current flowing in power lines (about 10^{-8} T). Other environmental sources of magnetic noise, for instance, any electrical devices or elevators also generate magnetic fields much larger than the ones produced by the human brain. The electrical activity in the heart and that associated with eye blinks and movements also create magnetic fields of at least an order of magnitude larger than the signals from the brain. Therefore, a magnetically shielded room was required to attenuate the magnetic noise from the environment. Cohen built a shielded room and used one of the first magnetometers employing SQUID (superconducting quantum interference device) sensors invented in 1962 by James E. Zimmerman to record MEG in real time. These superconducting devices are extremely sensitive magnetic flux to voltage converters. To benefit from superconductive properties, the SQUIDs need to be maintained at liquid helium temperature (-269 °C). Using the SQUID sensors, David Cohen significantly improved his MEG device to record the signals with lower noise level in 1971 (Cohen, 2004). This time the signals were almost as clear as those of EEG. Epileptic activity was detected by MEG for the first time in 1982 (Barth et al., 1982).

The first MEG device used a single SQUID sensor; to map the magnetic field it was necessary to repeat the measurement at a number of points around the head of the subject. This was cumbersome, so MEG manufacturers began to arrange multiple sensors into arrays to cover a larger area of the head such as a system with 5-7 coils in early 1980s, then system with about 20-40 sensors in the late 1980s. An important milestone was the introduction of the first helmet whole-head MEG system introduced in 1992 (Ahonen et al., 1993) that contained 122 sensors. It was

thus possible to study spontaneous activity of the brain and responses evoked by different kinds of stimuli simultaneously all over the cortex. At about the same time, CTF Systems Inc. introduced their whole-head system with 64 sensors (Vrba et al., 1993). Today's whole-head MEG systems can contain more than 300 SQUIDS connected to sensor coils in a configuration following the curvature of the head. Due to several theoretical analyses that showed a higher density would not lead to an increasing spatial resolution, the technological development in terms of increasing the number of sensors reached a stable stage (Preissl, 2005). The whole-head system of CTF Systems Inc. was later upgraded to 143, 151 and 275 sensors, along with other manufacturers such as Elekta Neuromag TRIUX (with 306 sensors), 4D Neuroimaging (with 148 or 248 sensors) and MEGvision (with 160 sensors).

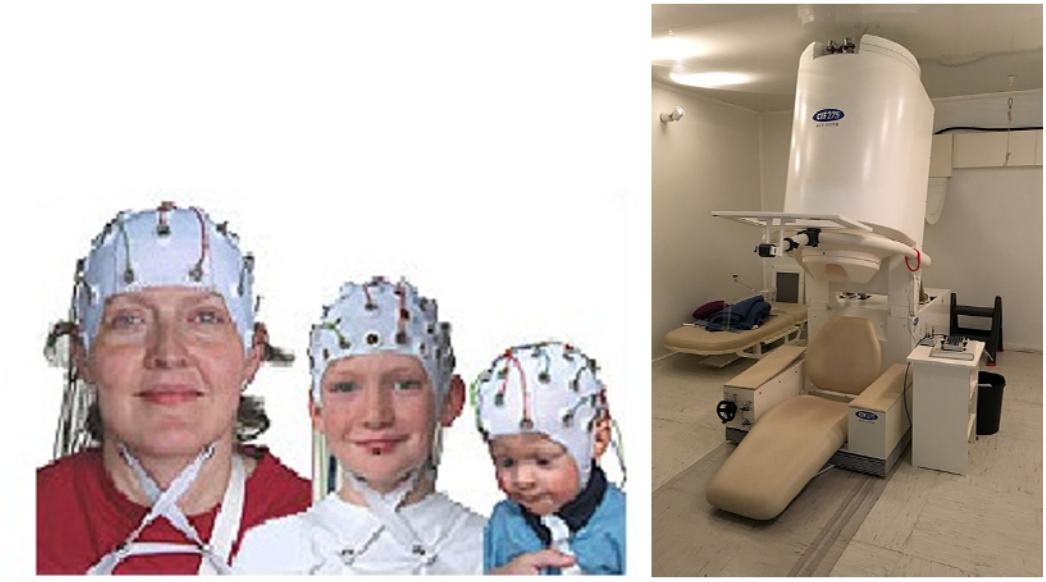

Figure 2.2. For this thesis, simultaneous EEG-MEG recordings were performed using a 56 channel EEG easycap (left) and 275 channel CTF MEG system (right). Extracted from http://www.easycap.de/e/products/products.htm and http://www.ctfmeg.com/ respectively.

2.2. Neuronal generators of EEG and MEG signals

In this section, we will discuss the underlying electrophysiological phenomena recorded with EEG and MEG. While EEG measures the differences of electric

potentials on the scalp, MEG measures the magnetic fields around the scalp. The EEG or MEG signal arises from temporally synchronized and spatially aligned postsynaptic electrical currents in populations of cortical neurons. Mainly pyramidal cells located in layer V that are organized along cortical columns are involved in the generation of EEG and MEG signals (Hämäläinen et al., 1993).

2.2.1. Anatomy

An average human brain is composed of around 100 billion neurons (nerve cells), among which approximately 10 billion are the cortical pyramidal neurons. Each neuron may be connected to up to 10,000 other neurons, passing signals to each other via as many as 1,000 trillion synaptic connections.

A typical neuron (see **Figure 2.3**) consists of a cell body or soma where the nucleus resides, a tree of dendrites that receive information from other neurons to the cell body, and an axon (a long extension of the nerve cell) that carries nerve signals away from the soma, ensuring distant communication with other neurons. The part of the axon where it emerges from the soma is called the axon hillock. All these portions of the neuron are contained within the neural membrane that separates the cytoplasm from the extra-cellular fluid. The axon of one neuron communicates with the dendrites of another neuron via the synapses present in the axon terminal. The cell body and the dendrites of the neuron are concentrated in the gray matter of the brain, the largest part of which is the cerebral cortex forming the surface of the brain (Hämäläinen et al., 1993). The cerebral cortex includes two main classes of neurons. The projection or principal neurons (e.g., pyramidal neurons) are cells that "project" or send information to neurons located in distant areas. Interneurons (e.g., basket cells) are generally considered to be local-circuit cells which influence the activity of nearby neurons. Most principal neurons form excitatory synapses on post-synaptic neurons, while most interneurons form inhibitory synapses on principal cells or other interneurons neurons (**Figure2.3**).

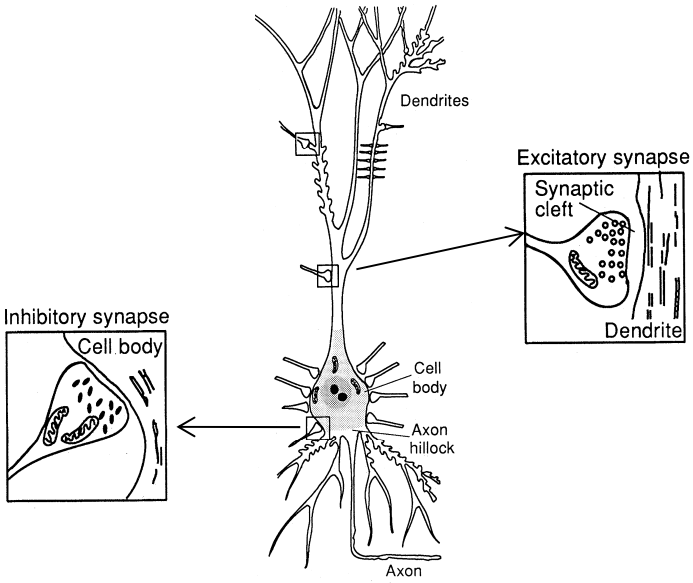

Figure 2.3. Cortical neuron. Schematic illustrations of a pyramidal neuron and magnified Excitatory and Inhibitory synapses. Modified from (Hämäläinen et al., 1993).

2.2.2. Physiological mechanisms of neuronal activity

Transmission of information is done uni-directionally within and between neurons, first along the axon and then across the synapse to the next nerve cell. The part of the synapse that is on the side of the axon is called the presynaptic terminal; the part on the side of the adjacent nerve cell is called the postsynaptic terminal. Between these terminals there is a gap called the synaptic cleft. When an action potential travelling along the axon reaches the pre-synaptic terminal, a chemical substance called a neurotransmitter is released in the synaptic cleft. This neurotransmitter will then activate the post synaptic terminal: the permeability of the membrane changes locally and specifically to different ions. Every cell has a voltage (difference in electrical potential) across its membrane called a membrane potential. Neuronal messages are transmitted through local changes in membrane potential. When a neuron is not sending any signal, the membrane potential of the neuron at rest is typically estimated to be -70 mV. Active mechanisms involving ion pumps and ion channels maintain the resting potential of a neuron. During chemical signaling the membrane potential of the post synaptic cell is altered temporarily by moving charges (mainly Na^+, Cl^- and K^+ ions) across the cell

membrane. A synapse can be excitatory (generating an excitatory post-synaptic potential, EPSP) or inhibitory (generating an inhibitory post-synaptic potential, IPSP). The distributions of excitatory and inhibitory synapses within the dendritic tree are different; most inhibitory synapses are located close to the soma where they influence the electric potential of the soma more than the excitatory synapses which are concentrated further away, at dendritic spine (Hämäläinen et al., 1993) (**Figure 2.3**). During an EPSP, the cell membrane becomes more permeable to Na^+ ions, a high influx of positive charges results in an increased membrane potential causing depolarization. This potential change drives the polarity of a neuron closer to the generation of an action potential. On the other hand, during an IPSP, negative Cl^- ions flood into the cell, which causes a decrease in membrane potential, or membrane hyper-polarization. This potential drives the polarity of a neuron further away from the generation of an action potential. Integration of EPSP's and IPSP's establishes the probability that the post-synaptic cell will fire, i.e. will trigger the generation of an action potential. An action potential is initiated at the axon hillock when enough depolarization accumulates to bring the membrane potential up to a threshold of around -55mV. The action potential (or a spike[2]) is a short duration (1ms) impulse exhibiting a positive difference of potential, travelling along the length of the axon, therefore ensuring distant transmission of information between neurons (Sherwood, 2008).

a. Integration of postsynaptic potentials

Both EPSPs and IPSPs are low-amplitude potentials. They are "graded" potentials, i.e. their amplitude reflects the intensity and duration of the interaction between the neurotransmitter and its receptor complex. Postsynaptic potentials do not regenerate as they spread along the membrane of a cell; they become smaller with distance from the synapse. A single EPSP would be too small to trigger an action potential in a postsynaptic cell. Temporal or spatial summation of the neighboring

[2] which is different from interictal spikes that are generated by synchronized postsynaptic potentials

post synaptic potentials are actually needed to reach a specific depolarization level that can trigger the generation of an action potential in the postsynaptic cell. The duration of a post-synaptic potential (around 10 ms, in comparison to 1 ms for an action potential) allows temporal summation of several post synaptic potentials that are synchronized in time. Then, similar geometrical arrangements of the dendrites of a pyramidal cell and its neighbors allows summation of post synaptic potential in space. These summations apply to IPSP as well. Although, through summation, an IPSP can also counter the effect of an EPSP by favoring more hyperpolarization, thus preventing the occurrence of action potential. Therefore, if the neurons all have a similar orientation and all receive the same type of input, their PSPs will summate and may be measurable around the scalp. This is most likely to occur in cortical pyramidal cells located in the layer V of the cortex. In the pyramidal cells, their apical dendrites are oriented in parallel along the cortical sheet; therefore, the ionic current flowing in the dendrites towards the soma is also perpendicular to the cortical surface. Pyramidal neurons located in the layer V of the cortex, therefore, play an important role in the measurement of electric and magnetic fields around the scalp.

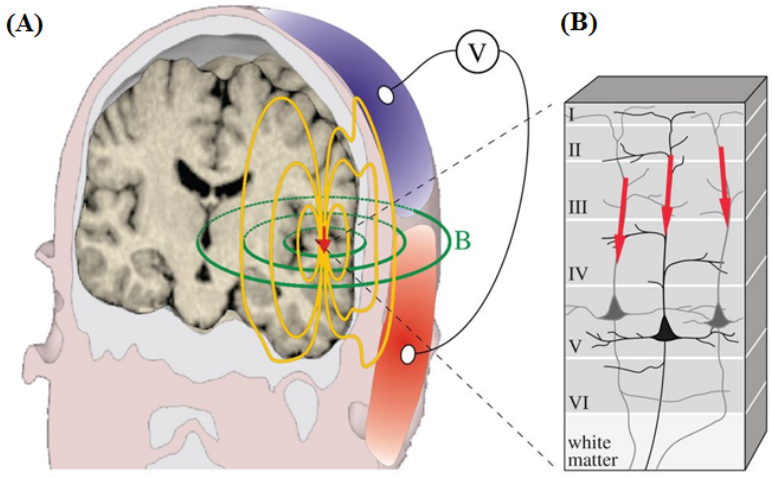

Figure 2.4. Generation of EEG and MEG signals. (**A**) Electric currents (red arrow) in active neurons drive extracellular (volume) currents (yellow lines) within the head, which gives rise to a potential distribution (V) on the scalp. The currents also generate a magnetic field (green lines; B) outside of the head; here the direction of the magnetic field follows (according to the right-hand rule) the direction of the net intracellular currents (red arrow). (**B**) The main contribution to EEG and MEG signals comes from

post-synaptic currents (red arrows) in the apical dendrites of pyramidal neurons. Extracted from (Hari and Parkkonen, 2015).

b. Intracellular and Extracellular currents

Both action potentials and post-synaptic potentials are associated with movements of ions, resulting in currents occurring within the cell: the so-called intracellular currents. They are accompanied by passive extracellular currents, which close the electric circuit and thus prevent the accumulation of electric charge (**Figure 2.4 B**). For instance, when an EPSP is generated in the dendrites of a neuron an extracellular voltage is created that is more negative than elsewhere along the neuron, resulting from Na^+ currents flowing inside the neuron's cytoplasm. The current completes a loop further away from the excitatory input (Na^+ flows outside the cell), to create as a positive voltage. This process can last hundreds of milliseconds. On a macroscopic scale, this situation can be modeled as a *current dipole* exhibiting a region of positive flux of ions (current) which is referred to as a *source*, and at a small distance a region of negative flux of ions referred to as a *sink*. The macroscopic ohmic return currents closing the current loop are commonly referred to as volume currents while the current dipole equivalent to the primary source is called the primary current.

The patterns of the electric potentials on the scalp and magnetic field components are orthogonal, under the assumption of a spherically symmetric head conductivity. The "right-hand rule" can be used to estimate the orientation of the magnetic field generated by neuronal currents (see **Figure 2.4**). The electric potential measured by EEG and the volume currents set forth by the primary currents are directly related by the Ohm's law (Jackson and Bolger, 2014). In conclusion, EEG and MEG quantify the same neuronal processes but providing complementary information regarding the underlying generators. EEG and MEG measurements are, therefore, more informative when they are combined during data acquisition and analysis (Pflieger et al., 2000).

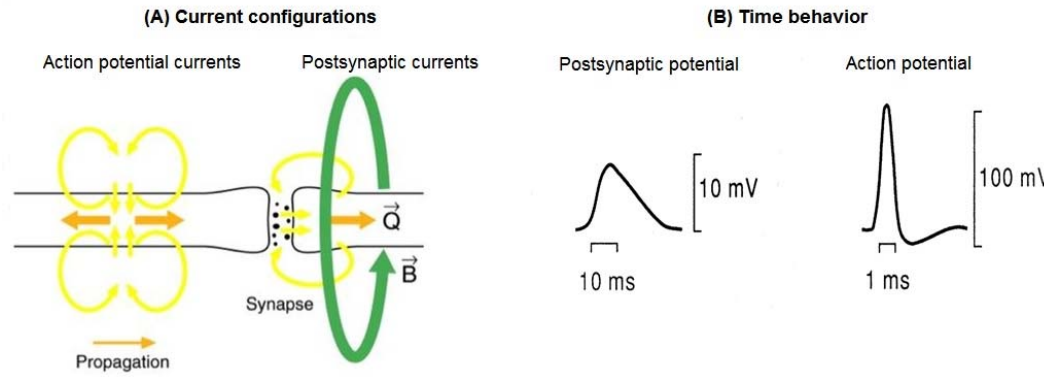

Figure 2.5. Action potential versus Postsynaptic potential. (**A**) Currents involved in the generation and propagation of action potential in the pre-synaptic neuron are bi-directional forming two opposing dipoles; post-synaptic currents have uni-directional currents forming only one dipole. (**B**) Time behavior a postsynaptic potential and an action potential. Modified from (Hämäläinen et al., 1993).

2.3. Action potential vs postsynaptic potential

As illustrated in **Figure 2.5**, two kinds of bioelectrical signals are generated at the neuronal level: (i) the action potential propagating along the axon and (ii) the post-synaptic potentials. An action potential is generated when the sum of all postsynaptic potentials reaches a threshold of -55 mV. Because a propagating depolarization wave is quickly followed by hyperpolarization of the membrane, an action potential can be modeled as two opposing current dipoles, therefore resulting in a quadrupolar structure producing electrical potentials and magnetic fields decreasing at $1/r^3$ with the distance (Milstein and Koch, 2008). On the other hand, post-synaptic currents can be modeled by a single current dipole, therefore producing electrical potentials and magnetic fields decreasing as $1/r^2$. Consequently, the contribution of action potentials on scalp EEG and MEG can be neglected since the decrease of the magnetic or electric fields with the distance is faster than that of dipoles. Moreover, the action potentials only last for a duration of 1ms, while the post synaptic potentials last for about 10ms; which is slow enough to allow temporal integration of the contribution from nearby neurons (**Figure 2.5**). Thus, EEG and MEG signals are produced in large parts by the post synaptic potentials.

2.4. EEG recordings

An EEG recording system comprises several electrodes (recording electrodes as well as a reference and a ground electrode), an amplifier with filters, analog to digital converter, the acquisition computer and dedicated softwares allowing visualization and analysis of the recorded waveforms. Abrasive gel followed by the application of conductive paste is generally needed to ensure good electrical conductivity between electrodes and the skin.

During an EEG recording session, the electric potential is recorded simultaneously from several sites. The combination of all electrodes together with the reference and the ground electrode compose the channels. The electrode configuration is called a montage. A typical montage would include at least 21 channels, or more, with some system allowing up to 512 channels. The choice of the reference electrode varies for different systems and applications such as vertex electrode (Cz), linked-ears, linked-mastoids, ipsilateral-ear, contralateral-ear and tip of the nose. For the ground electrode, forehead (Fpz) or an ear location are usually preferred, but sometimes the wrist or the leg can also be considered.

The international 10-20 system (Jasper, 1958) standardized physical placement and designations of electrodes on the scalp (**Figure 2.6**). The head is divided into proportional distances from prominent skull landmarks that are the nasion, peri-auricular points (left and right ear), and the inion, thus providing adequate coverage of most regions of the brain. The nasion is located at the bridge of the nose immediately beneath the forehead, and the inion is the lowest point of the skull from the back of the head, normally indicated by a bony. The distance from the anatomical landmark to the electrode positions were at 10% distance while the electrodes are separated at a distance of 20% from each other. Each electrode is specified by a letter name related to the general underlying cortical region or lobe (Frontopolar - F_p; Frontal - F; Temporal - T; Central – C; Occipital - O; Parietal - P) and a subscript reflecting its position relative to the midline. Therefore, even and

odd numbers refer to the right and to the left hemispheres respectively, while *z (zero)* refers to an electrode placed on the midline. More detailed EEG montage can also be considered by notably adding extra electrodes within the spaces between the existing 10-20 systems, leading to the so-called 10-10 system (Chatrian et al., 1985) (see **Figure 2.6C** for an example) or 10-5 system (Oostenveld and Praamstra, 2001).

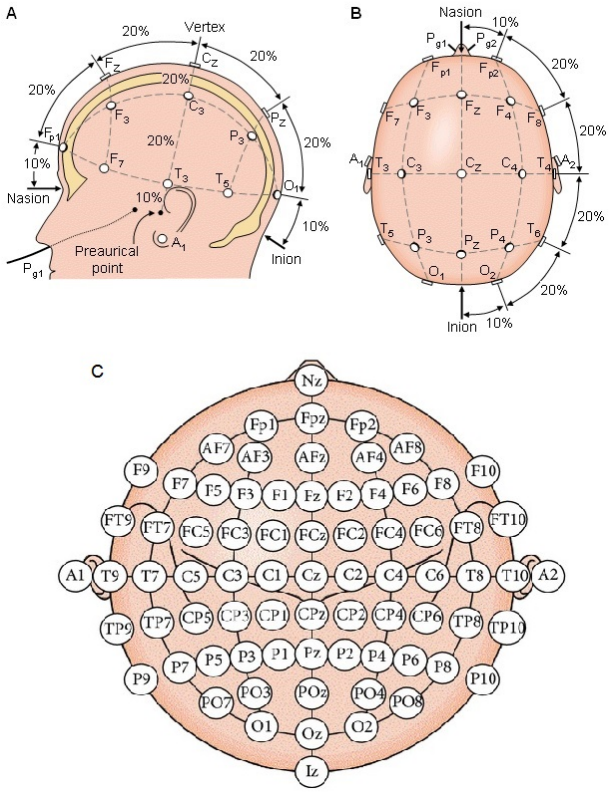

Figure 2.6. The international 10-20 system seen from (A) left and (B) above the head. A = Ear lobe, C = central, Pg = nasopharyngeal, P = parietal, F = frontal, Fp = frontal polar, O = occipital. (C) Location and nomenclature of the intermediate 10% electrodes, as standardized by the American Electroencephalographic Society. AF - intermediate between Fp and F, FT - between F and T, TP - between T and P, CP - between C and P, PO - between P and O. Modified from Sharbrough et al., (1991).

Duration of EEG data collection can vary depending on the application, as long as the electrical contact can be maintained. Typically, EEG is recorded with person in supine position for only 30 minutes (routine EEG), but data can be collected over the course of a day to examine brain function during normal daily activity (24-h

EEG or ambulatory EEG), during sleep (polysomnography) or even for several days in hospital settings in an epilepsy monitoring unit (video-EEG monitoring).

2.5. MEG Recordings

As mentioned in **Section 2.1**, MEG records very weak magnetic fields of the brain which are in the range of 10^{-12} to 10^{-15} T. For instance, they are much weaker than the earth's magnetic field of 10^{-4} T. The challenge of MEG recording is mainly to measure the magnetic fields produced by neuronal activity, while attenuating the influence of external magnetic noise. A typical MEG device is composed of the magnetic field sensors (SQUID), detection coils connected to the SQUIDs, a cryostat, and a magnetically shielded room.

The SQUID (superconducting quantum interference device) is a superconducting ring interrupted by one or two "weak links" called Josephson junctions (Josephson, 1962). By applying a suitable bias to the voltage across (or the current through) the junction, the SQUID becomes a periodic function of the magnetic flux going through the SQUID loop. The high sensitivity of the SQUID stems from the fact that the period of this function is very small; this value is called a flux quantum (Körber et al., 2016). In practical, contemporary MEG magnetometers have a typical magnetic field noise at frequencies higher than a few Hz is 2 - 3 fT/sqrt(Hz) (Hämäläinen et al., 1993).

In practice the SQUID loop is small and magnetic field containing relatively low spatial frequencies are recorded by integrating the field over a larger spatial scale with help of a superconducting flux transformer connected to the SQUID. Due to superconductivity, frequency response of a SQUID magnetometer extends down to dc, unlike in a traditional resistive induction-coil magnetometer. The simplest type of a flux-transformer is the magnetometer (**Figure 2.7**), which comprises a single superconducting pickup coil (or a few turns), situated as close as possible to the subject's head. Magnetometer measures some component of the magnetic field directly. Such devices are extremely sensitive but also pick up all environmental

changes in magnetic field. When the pickup coil configuration includes two coils connected in series but wound in opposite directions, the sensor is then called a gradiometer. If the magnetometers are next to each other in a horizontal plane, the sensor is called a planar gradiometer, and if the coils are one above the other, the sensor is called an axial gradiometer. Gradiometers are used to measure spatial gradient of magnetic field in a specific direction (in fT/cm). Magnetic interference from distant sources (in the form of noise source) will be relatively uniform across the two coils, thus resulting in dampening of the disturbance. Conversely, nearby cerebral sources will produce different fields at the two coil sites and brain signals thus not significantly dampened.

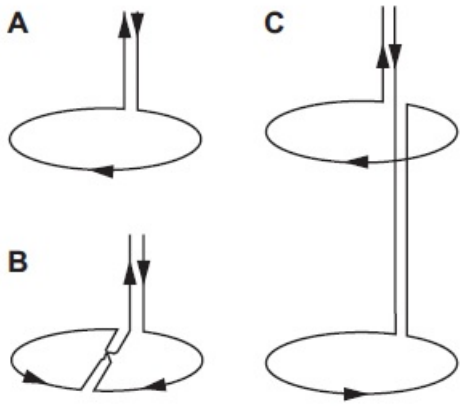

Figure 2.7. Common pick up coil geometries. (A) magnetometer, (**B**) planar gradiometer, (**C**) axial gradiometer. Modified from (Hämäläinen et al., 1993).

As the systems incorporate superconducting materials, they must be operated at liquid helium temperature (4 K= -269° C). To maintain the cryogenic conditions, the sensor array is immersed in a large container (Dewar) of liquid Helium. Heat conduction is eliminated by two-wall structure with a vacuum in between while heat radiation losses are minimized by a radiation shield in the vacuum space.

The need for helium for cooling is a major maintenance cost factor for MEG systems. Finally, MEG recordings require a magnetically shielded room in order to dampen the environmental magnetic fields. Some MEG devices, such as the CTF

system installed in our institution, are also equipped with additional reference sensors to pick up environmental noise to further correct for their influence MEG brain sensors.

Since MEG acquisition consists in placing the head in a helmet and MEG sensors are not attached to the head of the subject, immobility during the acquisition is absolutely needed. Consequently, in the context of epilepsy, MEG acquisitions are usually limited to a maximum of 1 or 2 hours of acquisition and are therefore generally confined to interictal state recordings. To track the head movements, the location and orientation of the head with respect to the MEG sensor array are monitored based on three-dimensional digitization of several anatomical landmarks (nasion and pre-auricular point), and by head position indication (HPI) coils that are affixed on the scalp (Uutela et al., 2001). The MEG system used for the studies in this thesis is the CTF system with 275 sensors (SQUIDs) coupled with axial gradiometers (**Figure 2.8**).

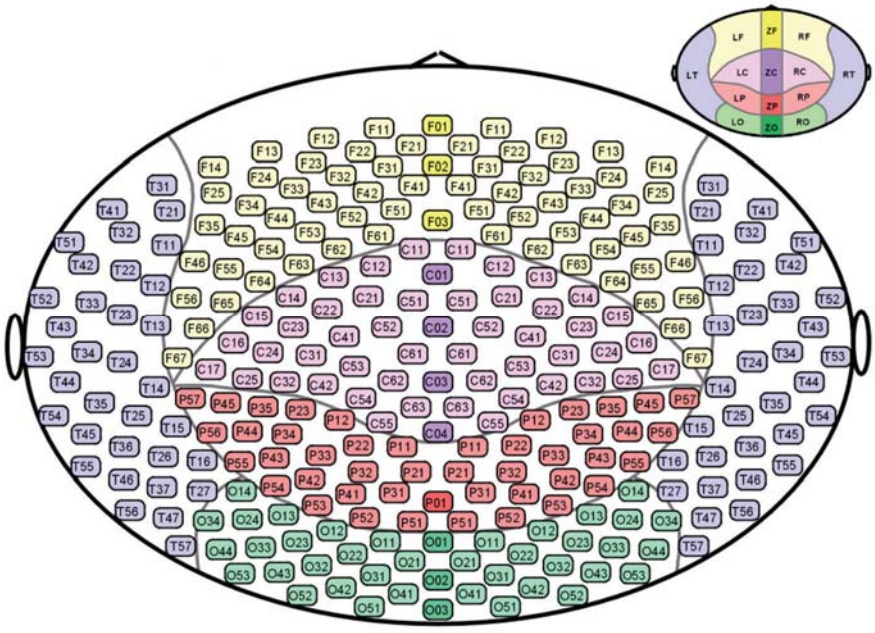

Figure 2.8. Schematic representation of the whole head coverage with 275 MEG sensors in a CTF system. Each sensor is named with 5 digits and the first is always M for MEG. The small figure on the upper right corner shows the second and the third characters and the bigger figure shows the last three digits of the sensor name. Taken from Aydin (2015).

2.6. EEG and MEG in epilepsy

There are several factors determining if and how the transient epileptic discharges are detectable in EEG or MEG scalp recordings: the spatial extent of the underlying activated cortex, its depth from the surface, the amplitude of the activity and the orientations of the dipoles, conductivity of intervening tissues as well as the density of the recording channels. This section will discuss some of these factors. The key differences between EEG and MEG have also been presented in **Table 2.1**.

2.6.1. Spatial extent of the generators of IEDs recorded using EEG and MEG

To allow sufficient signal amplitude to be distinguishable from ongoing EEG and MEG background traces, the generators of epileptic discharges should be spatially extended on the cortex. Several studies addressed this important issue specifically and showed that the extent of the involved cortex is different for MEG and EEG.

In MEG and EEG, the current generator is described by an equivalent current dipole $\boldsymbol{Q}$. The current dipole density q is defined as $q = Q / \theta$ in units of nA.m/mm^2, where Q is the dipole moment expressed in units of nA.m and θ is the surface area of the active cortical volume. Since the current density q is independent of the size of active tissue, it is expected to be more uniform than Q and may serve as an effective physiological constraint when solving the inverse problem. Recently, it has been shown that the maximum value of current dipole moment density q associated with synchronous population activity is uniform (1-2 nA.m/mm^2) across a wide range of brain structures (Murakami and Okada, 2015). Considering this, if the maximum value of q is constrained to be 1 nA.m/mm^2, the epileptiform response reported by (Oishi et al., 2002) as a mean Q value of 137 and 275 nA.m for two patients would imply that the minimum size of active tissue was actually 137-275 mm^2. Thus, these results confirm the fact that the size of epileptiform tissue is not a point source as assumed by the equivalent current dipole representation of the generator.

The earliest study (Cooper et al., 1965) that compared subdural and scalp EEG recordings showed that only widely synchronized components of the cortical activity could be observed on scalp recording. In this study that was based on a simple phantom model involving a large piece of fresh wet skull, Cooper and colleagues proposed that 6 cm^2 area of cortical activity was necessary to produce scalp-recordable electrical potentials. However, this value can be arguable given that the in vitro design of their study was hardly comparable to the generation of human EEG. Ebersole and colleagues studied simultaneous recordings from intracranial (subdural electrodes) and scalp electrodes on temporal lobe epilepsy patients and he suggested that a minimal cortical activation area of 6-8 cm^2 was required to produce discernible scalp EEG potentials (Ebersole, 1997a). Accordingly, from the analysis of simultaneous intracranial depth EEG and scalp EEG recordings, Merlet and Gotman never observed very focal activity, occurring only at one intracranial contact, when a spike was present at the surface of the scalp. At least 8 intracranial contacts needed to be able to detect a interictal discharge on scalp EEG traces (Merlet and Gotman, 1999), therefore confirming previous findings of Ebersole and Cooper.

These earlier studies were followed by several others involving simultaneous intracranial subdural and scalp EEG recordings to further assess the scalp EEG detectability of cortical source in Temporal Lobe Epilepsy (TLE) (Tao et al., 2005; Tao, Baldwin, Ray, et al., 2007) and Frontal Lobe Epilepsy (FLE) (Ramantani et al., 2014). While Ramantani and colleagues showed that cortical sources generating scalp-detectable spikes presented a median of 6cm^2 of activated cortical surface in FLE patients, Tao and colleagues demonstrated that at least 10 cm^2 of synchronous or temporally overlapping cortical activity was usually necessary to produce scalp-recordable EEG spikes in TLE. Tao and colleagues also suggested that much larger cortical source areas, involving 20 to 30 cm^2, are often associated with spikes detected on scalp EEG, while mentioning that intracranial spikes involving extent less than 6 cm^2 were never detected on scalp EEG traces. However, these studies did not take into consideration the effect of the non-conducting substrate of the

subdural grid on the scalp EEG. This important issue was carefully addressed using realistic simulations models by von Ellenrieder and colleagues, who showed how the amplification/attenuation associated with the subdural grid and skull holes may affect the results of simultaneous scalp and subdural measurements (von Ellenrieder et al., 2014a). Their results suggest that the minimum extent of cortical generators needed to obtain epileptic discharges visible on the scalp is lower than the usually accepted values of 10 to 20 cm^2, with a high probability of generators in the range from 4 to 8 cm^2 able to produce visible scalp activity. The difference is explained by the attenuation of the scalp potential by the non-conducting substrate of the cortical grid in simultaneous scalp and cortical recordings, that resulted in an overestimation of the underlying required extent.

From simultaneously recorded MEG and electrocorticography (ECoG) analysis, Mikuni et al. and Oishi et al. showed that an area of at least 3 cm^2 for frontal regions and 4 cm^2 for temporal regions must be synchronously active to be detectable in MEG (Hari, 1990; Mikuni et al., 1997; Oishi et al., 2002). From temporal lobe studies of simultaneous intracranial EEG, it has been estimated that at least 6 to 8 cm^2 of basal lateral cortex is necessary for MEG detection of spikes (Mikuni et al., 1997; Baumgartner et al., 2000; Oishi et al., 2002).

2.6.2. Effect of source orientation in EEG and MEG measurements

Visibility of the EEG and MEG signal sources is largely determined by the orientation of the anatomical sources (Haueisen et al., 2012). Since the generators of these anatomical sources are essentially the pyramidal cells (Hari, 1990), they are oriented parallel to each other and mainly perpendicular to the circumvoluted cortical surface. Therefore, cell assemblies along the crest of a cortical gyrus are considered as mainly radial when approximating the shape of the head as a sphere and represents about 30% of the cortex cell assemblies. Cell assemblies within the wall of a sulcus or from basal cortex are considered as tangential sources (i.e. parallel to the spherical head surface) and constitute around 70% of the cortex. This

anatomical approximation is extended to the physiology assuming that pyramidal cells and their dendrites are evenly distributed along the cortex. Research indicates differential sensitivities of MEG and EEG to the sources along the cell assemblies (**Figure 2.9**). EEG and MEG measurement at any position on the scalp will consist of the sum of influences from many sources of electric and magentic fields considering the brain consists of many dipoles. MEG favors the tangential sources (Hämäläinen et al., 1993; Ahlfors et al., 2010). Magnetic fields created by tangential sources spread outside of the "spherical" head towards sensors. On the other hand, magnetic fields generated by radial sources do not spread outward towards sensors. EEG is sensitive to both tangential and radial sources but EEG spikes are usually obscured by the radially oriented background brain noise coming from deep regions in the brain (Ahlfors et al., 2010). For large patches of cortical activations extending over a region where the surface normal changes, and therefore, also the orientation of the source elements changes, cancellation of the EEG and MEG signals occurs. In particular, cancellation occurs when the activation involves opposing walls of a sulcus or a gyrus, which can lead to loss in signal magnitude thus affecting the relative signal-to-noise ratio of EEG and MEG (Ahlfors et al., 2009; Goldenholz et al., 2009; Huiskamp et al., 2010).

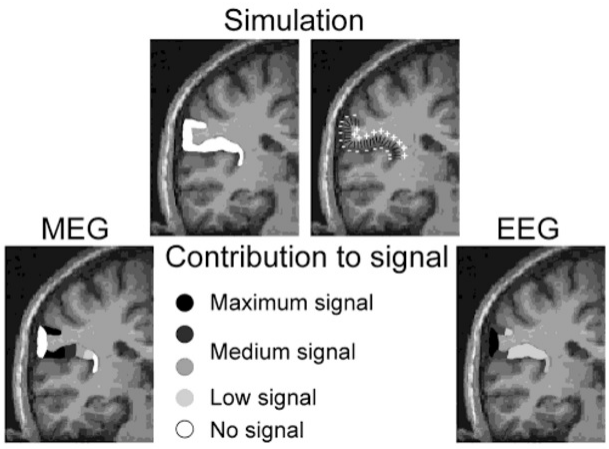

Figure 2.9. Contribution of different cortical areas to EEG and MEG signals. Top left: Simulation of a cortical activation. Top right: simulation of dipolar currents. Bottom left: Only pyramidal neurons with tangential and oblique orientation relative to the head surface contribute to MEG signal. Bottom right: EEG signal is dominated by activities from

radially oriented sources. Tangential sources contribute to the signal, but in a smaller extent. Extracted from (Wyllie et al., 2012).

2.6.3. Effect of volume conduction on EEG and MEG measurements

The electric potential distribution generated by the synchronized neural activity is attenuated and distorted by resistive layers of tissue such as the cerebro-spinal fluid (CSF), dura, skull, and scalp. This provides, at scalp level, a distorted view of the underlying brain activities. In particular, those various layers, and especially the combination of a poorly conducting skull layer followed by the conducting skin layer, results in a significant spatial blurring effect at scalp level. Such volume–conduction-induced blurring effect is the main cause of the poor spatial resolution of scalp EEG (Srinivasan et al., 1996; Nunez and Srinivasan, 2006; Jackson and Bolger, 2014).

On the contrary, MEG is largely insensitive to the uncertainty and variations in skull conductivities (Vorwerk et al., 2014). For example, changes in the thickness of the skull over different regions of the cortex do not affect the MEG measurements. Therefore, spatial resolution of MEG is better than EEG (Barkley, 2004; Baumgartner and Pataraia, 2006). It is important to note that this difference between EEG and MEG due to volume conduction has a more important role in regard to head modeling accuracy than sensitivity per se, this issue will be discussed in the next chapter.

2.6.4. Detection rates of EEG and MEG epileptic discharges

Several studies have compared the spike detection rates in simultaneously recorded EEG and MEG (Hillebrand and Barnes, 2002; Yoshinaga, 2002; Lin et al., 2003; Iwasaki et al., 2005; Ramantani et al., 2006; Ossenblok et al., 2007; Scheler et al., 2007). MEG generally showed larger spike detection rates than scalp EEG. Scheler and colleagues studied 100 patients with both temporal and extra-temporal lobe

epilepsy and found spikes in MEG only in 22%, spikes in EEG only in 7%, but 71% of spikes were found in both EEG and MEG (Scheler et al., 2007). Haueisen and colleagues suggested that the ratio between the number of tangential and radial sources were approximately 3:1 (Haueisen et al., 2012). Therefore, since MEG favors tangential sources, for sources in realistic heads it is rare that MEG will be completely blind to a source due to the orientation (Cohen and Cuffin, 1983). Another possible cause of higher MEG spike detection rates in these studies is the higher number of MEG sensors considered when compared to surface EEG. Only few studies compared spike detection rate in MEG with high density EEG (70, 71). Knake and colleagues studied 70 candidates for epilepsy surgery who underwent simultaneous 70-channels EEG and 306-channels MEG recordings (Knake et al., 2006). They reported that interictal spikes were detected in 72% of the patients for MEG and 61% for EEG. Spikes were identified by both modalities in 55.7% of the patients and combined sensitivity of EEG and MEG was found to be 75%. MEG-only spikes occurred in 13% and EEG-only spikes in 3% of the patients. Their study overall suggested that not all epileptic MEG discharges are accompanied by simultaneous EEG spikes, while, conversely, not all EEG spikes are accompanied by MEG spikes. This can be attributed to the influence of the complementary sensitivities of the two techniques and to the characteristic of the generator of the discharge such as spatial extent, amplitude of the activity, orientations and distance to the sensors. They finally concluded that epileptic spike detection can be improved by analyzing a combination of EEG and MEG data.

Several authors have investigated the sensitivity of MEG versus EEG to the type of epilepsy. While MEG detected more spikes compared to EEG in neocortical epilepsies (Nakasato et al., 1994), EEG was superior in the detection of spikes in mesio-temporal epilepsies (Yamazaki et al., 2012). Detecting epileptic activity in the mesial temporal cortex and deep orbitofrontal cortices directly by MEG was difficult because gradiometers are relatively insensitive to deep sources (Mikuni et al., 1997; Oishi et al., 2002; Huiskamp et al., 2010). Detection rates of epileptic activity in anterior temporal epilepsies were comparable for EEG and MEG. MEG

seems to have better sensitivity than EEG to sources in posterior lateral cortex (Lin et al., 2003).

2.7. Conclusion

This chapter discussed the key differences between EEG and MEG, summarized in **Table 2.1**. IEDs represent the summation of postsynaptic potentials from abnormal hypersynchronous pyramidal neurons located perpendicular to the cortical surface. Furthermore, to be visible in EEG and MEG the generators of IEDs have to be spatially extended.

Table 2.1. Differences between EEG and MEG (modified from (Wyllie et al., 2012))

EEG	**MEG**
Signals result from differences in surface potentials by secondary extracellular volume currents	Signals result from extracranial magnetic fields produced directly by intracellular neuronal currents
Dominated by radial sources (predominantly pyramidal neurons in gyral crowns)	Mainly generated by tangential sources (sulcal and/or basal pyramidal neurons)
Tangential sources contribute to the signal in a smaller extent	Discards any information in a radial direction
Conductivity information needed for accurate modeling.	Little information about electrical conductivities are usually needed for accurate modeling.
Detectable on scalp when at least 4-8 cm^2 of the cortex is synchronously active	Requires activation of 3-4 cm^2 of cortex to be detected on scalp
Widely available	Limited availability
Cheap	Expensive
Usually limited to 30 (max. 64) electrodes in clinical routine and up to 512 in research	High number of sensors (up to >300)
Long preparation time	Short preparation time
Electrodes fixed on scalp	Sensitive to head movements since sensors are not fixed to the head, therefore immobility is required during recording
Mobile/portable	Acquisition limited within the shielded room
Suitable for long-term recordings	Recording time is limited
Interictal and ictal recordings	Mainly interictal, ictal recordings rare

Chapter 3 Source localization of IEDs using EEG and MEG

Source localization or source imaging of EEG or MEG data employs scalp measurements to estimate brain current sources, that are generating those scalp signals, during a specific physiological or pathological process. The problem of EEG/MEG source localization requires two steps: (i) the forward problem consists in estimating EEG and MEG signals from the knowledge of the underlying neuronal current sources within a given volume conductor head model (Hallez et al., 2007), (ii) the inverse problem refers to the estimation of the neural source strength, location and time course from the measured EEG and MEG signal (Grech et al., 2008).

The main difficulty when solving the EEG or MEG inverse problem, which is our overall objective, arises from the fact that more than one source configuration within the brain can account for the observed signals measured on the scalp. Therefore, the inverse problem is a so-called ill-posed problem that does not admit a unique solution (Hadamard, 1902). To limit the number of possible solutions to provide relevant or "possible" source configurations, assumptions must be made on the organization of those underlying generators (source model) and its surrounding environment (the volume conductor model or head model). Consequently, before proposing strategies to solve the inverse problem, one needs to solve the forward problem, which is well-posed (i.e. it admits a unique solution) built upon the specification of a source model and a head model.

The overall structure of this chapter is: (i) forward problem, (ii) inverse problem, (iii) validation, and (iv) source localization of epileptic activity.

Notations

All matrices and vectors are written in bold letters. Deterministic matrices, such as ***G***, are written in *italics* upper case, whereas deterministic vectors, such as ***m***, are in *italics* lower case. Deterministic scalar quantities, such as *r*, are in *italics* lower case. When describing algorithms in the statistical framework, a random vector, such as **m,** is written in non-italics bold lower case. The matrix ***I*** stands for the identity matrix. Estimator of ***A*** is represented by $\widehat{\boldsymbol{A}}$. $\|\boldsymbol{A}\|_F$ stands for Frobenius norm of ***A***. The transpose of ***A*** is indicated by $\boldsymbol{A}^{\boldsymbol{T}}$.

3.1. Forward problem: from neural currents to EEG and MEG distributions

Given a known current source distribution within the brain, the forward model computes corresponding EEG and MEG signals, given specific source and head models. The forward problem is a well-posed problem. However, the accuracy of the solution depends on the accuracy of the so-called source and head models. The next sections will describe the most frequently used source and head models before describing methods to solve the forward problem.

3.1.1. Source model

The source model specifies the underlying organization of the generator of current sources giving rise to EEG and MEG signals. The most common approach consists in modeling neuronal current sources using the equivalent current dipole (ECD) model (Henderson et al., 1975). Each dipole represents a current source and sink of equal amplitude separated by a small distance. A piece of active cortex is assumed to behave as a dipole layer representing a focal area of the cortex with a large number (i.e. at least 10^5 cells) of parallel-oriented pyramidal neurons that are simultaneously active. A macro-column of cortex actually forms a current dipole layer, which can be considered as a single equivalent current dipole, modeling the

activity of the whole region, when observed at a distance much larger than the dimensions of the area of active cortex. Assuming that only a few restricted areas are active simultaneously, brain activity can then be modeled by modeling the sources using a small set of ECDs, representing the activity within few well localized brain regions, thus defining a so-called discrete source model (Koles, 1998).

In contrast to those models assuming brain activity to be generated by few discrete ECDs (less than 5 in general), more realistic source models have been proposed. Guided by some knowledge regarding cortical anatomical organizations, they consist in the so-called distributed source models, for which a large number (usually several thousands) of ECDs with fixed positions are considered. These anatomical constraints might consist in distributed dipolar sources within the gray matter volume or along a tessellated mesh of the cortical surface, whereas dipole orientations might either be free or constrained to be normal to the cortical surface (Dale and Sereno, 1993).

3.1.2. Volume conductor model (head model)

The volume conductor model plays a critical role in source localization since this is the essential part of the modeling that aims at mimicking in a realistic manner the way neuronal sources give rise to the signals recorded outside of the head. The head model actually takes into account mathematically both the electromagnetic (e.g., conductivity values for the brain, skull and scalp) and geometrical (e.g., shape) properties of the solution space. Specifying the head or volume conductor model consists in introducing a set of simplification hypothesis regarding the geometry and conductivity properties of the different head tissues, in order to solve the forward problem by solving Maxwell's equation (as described in the next section).

Several head models involving different levels of realism and complexity have been proposed and can be broadly categorized into three categories: 1) spherically

symmetric model; 2) boundary element model (BEM) and 3) finite element model (FEM). In terms of complexity and computational burden, the spherical model represents the simplest, the BEM the intermediate and the FEM the most complex model (Hallez et al., 2007). BEM and FEM models are typically developed from high resolution structural MRI scans of individual subjects and can better account for individual anatomical differences, providing therefore more realistic head models.

The oldest and simplest model is the spherical model, which assumes that the head can be represented as one or a series of homogenous concentric spheres with one sphere per major category of head tissue (scalp, skull, cerebrospinal fluid and brain). Such head models consisting of simple geometrical shapes allow the calculation of surface electrical potentials and magnetic field (i.e. solving Maxwell's equations) using an analytical solution (Rush and Driscoll, 1969). The first proposed volume conductor model of the human head consisted of a homogeneous sphere (Frank, 1952). However, it was soon noticed that the skull tissue had a conductivity which was significantly lower than the conductivity of other scalp and brain tissues. Therefore, the volume conductor model of the head needed further refinement and a three-shell concentric spherical head model was introduced. The three-spherical head model (de Munck and Peters, 1993; Zhang, 1995; Mosher, Leahy, et al., 1999), which has been most frequently used, approximates the head as a set of nested concentric and homogenous spheres, in which the skull, scalp and brain are modeled as different layers with different conductivities. These models can be generated and solved very efficiently, but their accuracy is limited especially for EEG data whereas they can be considered as sufficiently accurate for MEG (Hämäläinen and Sarvas, 1989; Mosher, Leahy, et al., 1999). Note that for MEG an intermediate modeling approach has been proposed: the overlapping spherical model (Huang et al., 1999). In this model, a best fit spherical model of the brain is estimated iteratively for each individual sensor.

In the boundary element methods, only tissue boundaries between regions exhibiting different conductivity values are modeled (Mosher, Leahy, et al., 1999), typically the scalp, the outer skull and the inner skull surfaces. The realistic boundaries or surfaces are segmented from an anatomical MRI and then discretized into a finite number of surface elements. The volume between two adjacent surfaces is then assumed to be characterized by one homogeneous and isotropic (i.e. identical throughout the region and in every direction) conductivity value. Solving the forward model using BEM requires calculating electrical potentials and magnetic field on every surface, i.e. at every vertex or centroid of the discretization elements (e.g., triangles or quadrilaterals). Although the BEM clearly represents an improvement and more realistic model than the three-spherical head model, it is not capable of modeling anisotropic[3] conductivities or discontinuous boundaries, such as holes in the skull. Additional geometrical constraints are imposed by BEM models, as every surface should actually correspond to a closed surface and adjacent surfaces should not be connected or too close from each other. The numerical accuracy of the BEM deteriorates when surfaces are too close together. This numerical inaccuracy can be mitigated using the OpenMEEG[4] (Gramfort et al., 2010) approach called the Symmetric BEM method (Kybic et al., 2006; Gramfort et al., 2011) which has been shown to be the most accurate than other implementations of BEM.

The FEM, unlike the other methods, can account for the actual head shape and tissue discontinuities, and accommodate anisotropic tissue in the conductivity model of the head volume, allowing detailed 3-D information on tissue conductivity for every region (Pruis et al., 1993). For instance, FEM methods allow modeling the impact of the different hard bone and soft bone components of the skull (Dannhauer et al., 2011). For the FEM model, the electrical potentials or magnetic

[3] Anisotropy refers to the property of having different values when measured in different directions.

[4] http://openmeeg.github.io/

fields are calculated throughout the entire volume, which leads to a larger number of calculations, when compared to BEM. The advantages of the volume-based methods include the possibility of introducing a nearly unlimited number of conducting regions and potentially incorporating anisotropy (Vorwerk et al., 2014).

Any approach proposed to solve the forward problem relies on assumptions regarding the geometrical shape and the conductivity profiles of the volume conductor. Whereas significant improvements have been made using MRI-based segmentation to model accurately the geometry, an important difficulty still relies on the fact that accurate measurements of electrical conductivities and magnetic permeability values for all biological tissues are generally unknown. This issue is quite problematic for BEM and even more for FEM models.

As mentioned in **Section 2.6.3,** EEG scalp potentials are highly attenuated and spatially smeared by the combination of the very low conductivity of the skull followed by a conductive skin layer; whereas MEG is less distorted by the resistive properties of the skull. This leads to higher sensitivity of EEG to errors in forward problem while MEG forward solutions are more robust. In general, modeling only the inner skull surface, assuming the skull to be an insulator, is sufficient to provide accurate solutions of the forward model in MEG (Hämäläinen and Sarvas, 1989; Mosher, Leahy, et al., 1999). In fact, even the single sphere or series of overlapping spheres models are often adequate for MEG head modeling (Huang et al., 1999). Those surfaces that are important for the degradation of scalp EEG signals, namely the inner and outer layers of the skull and outer layer of the scalp, should be segmented from three-dimensional MRI or CT to generate a realistic head model. In clinical practice, BEM model are most commonly used, particularly when the goal is to perform source localization within the "non-spherical" parts of the brain such as the base of the skull. For instance, the accuracy of correctly localizing sources of activity within the temporal lobe is improved considerably using more realistic models. Even without having access to a patient's individual MRI, the benefits of a realistic head model can be obtained by using one derived from standardized head models (Silva et al., 1999). Silva and colleagues compared

spherical, individual realistic, and standard realistic head models for localizing the source of epileptic EEG signals. They showed that realistic head models increased dipole localization accuracy compared to spherical model but the difference between individual and standard models was less than 1 cm (Silva et al., 1999), thus indicating the importance of realistic head model in EEG. Henson and colleagues compared a single sphere, an overlapping sphere and a BEM forward model to find the solution to MEG inverse problem (Henson et al., 2009a). This study suggested that BEM was superior to both single sphere and overlapping sphere in terms of localization accuracy, clearly justifying the need for the extra computation.

Finally, another important consideration in head modeling, especially for EEG, is the conductivity values of the different head tissues. Indeed, it is critical to assign as accurate conductivity values as possible. In many cases, conductivity values are introduced using values reported from previous literature studies, providing estimates through several experimental studies, such as in-vivo (e.g. electrical impedance tomography) (Oostendorp and Delbeke, 1999; Lew et al., 2009), intracranial and scalp recordings (Lai et al., 2005; Zhang et al., 2006) and in-vitro (such as a piece of skull in saline) (Oostendorp and Delbeke, 1999) measures. These studies have reported consistent and similar conductivity values for the brain and scalp (ranging from 0.12 to 0.48 S/m), reporting consistently conductivity value significantly larger than the skull conductivity value. However accurate estimation of the skull conductivity is less straightforward and several studies have reported more inconsistent skull conductivity values ranging between 0.006 and 0.080 S/m (Oostendorp and Delbeke, 1999; Malmivuo and Suihko, 2001; Hoekema et al., 2003; Lai et al., 2005; Zhang et al., 2006; Huiskamp, 2008; Lew et al., 2009; Vallaghé and Clerc, 2009; Fangmin Chen, 2010). Studies with patients (Huppertz et al. 2001; Ossenblok et al. 2007; Birot et al. 2014; Heers et al. 2016; Pellegrino et al. 2016a) have shown that using approximate conductivity ratios (such as brain-to-skull conductivity ratio) with an accurate geometrical description of the head might yield reasonable, verifiable results for both cortical and deep EEG sources.

The brain-to-skull conductivity ratio has long been accepted as being 1:80 (Geddes and Baker, 1967; Rush and Driscoll, 1969). This was largely based on extrapolations from measurements reported by Rush and Driscoll demonstrating that the skull conductivity was 1:80 times that of saline solution (Rush and Driscoll, 1969). Most recent papers suggest that the commonly accepted 1:80 brain-to-skull conductivity ratio is not recommended anymore and a range of between 1:10 to 1:50 ratios should rather be considered. In this thesis, we have used the BEM model with the inner skull, outer skull and the scalp surfaces and adopted the corresponding conductivity values of 0.33:0.0165:0.33 S/m respectively (Ferree et al., 2000; Hoekema et al., 2003; Lai et al., 2005), and we used the OpenMEEG BEM implementation available in the Brainstorm software[5] (Tadel et al., 2011) to solve the EEG and MEG forward model.

3.1.3. Electric potential and magnetic field computation

Given a source model of the generators of currents within the brain, a volume conductor model providing the geometry and conductivity properties of the different head tissues and sensors positions (and orientations, accurately co-registered with the head) (Schwartz et al., 1996), the forward model is solved using Maxwell's equations of the propagation of electric and magnetic fields in non-homogeneous tissues. For biological sources, the electric and magnetic fields are calculated on the basis of a "quasi-static approximation of Maxwell's equations (Plonsey and Heppner, 1967). Based on the quasi-static condition, magnetic and electric fields become independent from each other and all fields and currents behave as if they were stationary at each instant. They are actually not static because the neural activity changes with time. But these changes are slow compared to the electromagnetic propagation effects. Therefore, under this approximation the

[5]

potential and electric field expressions are exactly the same as those used in the presence of steady-state or non-time-varying currents.

Under those quasi-static approximations, the time derivatives of the electric field and magnetic fields are close to zero, resulting in the following set of governing equations:

1) According to the integral equations, Gauss' law for electricity states that the electric flux (***E***) out of any closed surface is proportional to the total charge enclosed within the surface. The corresponding differential equation for Gauss' law for electricity therefore states that the divergence of the electric field (***E***) is

$$\nabla . \boldsymbol{E} = \frac{\rho}{\varepsilon_0} \tag{3-1}$$

where $\nabla .$ is the divergence operator, ρ is the charge density, ε_0 are the electric permittivity of free space

2) According to the integral equations, Gauss' law for magnetism states that the net magnetic flux (***B***) out of any closed surface is zero. The corresponding differential equation for Gauss' law for magnetism therefore states that the divergence of the magnetic field (***B***) is null

$$\nabla . \boldsymbol{B} = 0 \tag{3-2}$$

3) According to the integral equations, Faraday's law of induction states that the line integral of the electric field around a closed loop is equal to the negative of the rate of change of magnetic flux through the area enclosed by the loop. In the static state, it becomes zero. The corresponding differential equation therefore states that the curl of the electric field (***E***) is

$$\nabla \times \boldsymbol{E} = -\frac{\boldsymbol{\partial B}}{\boldsymbol{\partial} t} \approx 0 \tag{3-3}$$

where $\nabla \times$ is the curl operator and t is the time

4) According to the integral equation, Ampère's law states that in case of static electric field, the line integral of magnetic field around a closed loop is proportional to the electric current flowing through the loop. The corresponding differential equation therefore states that the curl of the magnetic field is

$$\nabla \times \boldsymbol{B} = \mu_0 \boldsymbol{J} + \mu_0 \varepsilon_0 \frac{\partial \boldsymbol{E}}{\partial t} \approx \mu_0 \boldsymbol{J} \tag{3-4}$$

where μ_0 is the magnetic permeability of free space, $\boldsymbol{J}$ is the current density

In the quasi-static approximation, since $\nabla \times \boldsymbol{E} = 0$, electric field ($\boldsymbol{E}$) can then be expressed as a gradient field from a scalar quantity, therefore introducing the notion of scalar electrical potential V as $\boldsymbol{E} = -\nabla V$ [6]. Then, the total current density $\boldsymbol{J}$ can be expressed as the sum of the primary current ($\boldsymbol{J}^{\mathrm{P}}$) (the actual generators we aim at localizing) with the macroscopic volume currents ($\sigma \boldsymbol{E}$) (ohmic currents):

$$\boldsymbol{J} = \boldsymbol{J}^{\mathrm{P}} + \sigma \boldsymbol{E} = \boldsymbol{J}^{\mathrm{P}} - \sigma \nabla V \tag{3-5}$$

where σ is the conductivity of the medium. From equation (3-4) and the vector identity that divergence of a curl is zero ($\nabla . \nabla \times \boldsymbol{B} = 0$), it follows that $\nabla . \boldsymbol{J} = 0$. Thus, equation (3-5) can be re-written as $\nabla . (\sigma \nabla V) = \nabla . \boldsymbol{J}^{P}$, which yields (assuming constant σ) the following Poisson's equation

$$\Delta V = \frac{1}{\sigma} \boldsymbol{J}^{\mathrm{P}} \tag{3-6}$$

where Δ denotes the Laplacian operator, which is the divergence of a gradient (∇V). This Poisson's equation connects the electric potential (coming from the volume current distribution) to the primary current distribution. As a solution to equation (3-4), in free space, the magnetic field is given by the Biot-Savart law,

$$\boldsymbol{B}(\boldsymbol{x}) = \frac{\mu_0}{4\pi} \int \frac{\boldsymbol{J}(\boldsymbol{x}') \times \boldsymbol{X}}{\|\boldsymbol{X}\|^3} d\boldsymbol{x}' \tag{3-7}$$

where $\boldsymbol{X} = \boldsymbol{x} - \boldsymbol{x}'$, and $\boldsymbol{x}$ is the location where the field is computed and $\boldsymbol{x}'$ is the location of the source and $\times$ denotes the vector cross product. From this equation,

[6] The minus sign indicates that the electric field is actually oriented from an area with a high potential to an area with a low potential

we can see that the magnetic field is inversely proportional to the square of the distance between the source and the detector.

However, within the head, one cannot assume the conductivity sigma to be constant and therefore the original equation $\nabla.(\sigma\nabla V) = \nabla.\boldsymbol{J}^{P}$ should be solved. Under specific simplification hypothesis, such as assuming that the head consists of a set of contiguous regions (representing the brain, skull and scalp for instance) each characterized of constant isotropic conductivity σ, then the Biot-Savart law can be re-written as a sum of contributions of the primary and volume conduction currents (Hämäläinen et al., 1993):

$$\boldsymbol{B}(\boldsymbol{x}) = \boldsymbol{B}_0(\boldsymbol{x}) + \frac{\mu_0}{4\pi}\sum_{ij}(\sigma_i - \sigma_j) \oiint V(\boldsymbol{x}') \frac{\boldsymbol{X}}{\|\boldsymbol{X}\|^3} dS_{ij}' \quad \text{with } \boldsymbol{B}_0(\boldsymbol{x}) = \frac{\mu_0}{4\pi}\int \frac{\boldsymbol{J}^{\mathrm{P}}(\boldsymbol{x}')\times\boldsymbol{X}}{\|\boldsymbol{X}\|^3} d\boldsymbol{x}' \tag{3-8}$$

where $\boldsymbol{B}_0(\boldsymbol{x})$ is the magnetic field due to the primary current only. The second term is the volume conduction current contribution to the magnetic field formed as a sum of surface integrals (S_{ij}), typically over the brain-skull, skull-scalp, and scalp-air boundaries (when considering a multiple sphere or BEM volume conduction models). A similar equation can be used to compute the electric potential,

$$(\sigma_i + \sigma_j)\, V(\boldsymbol{x}) = 2\sigma_0 V_0(\boldsymbol{x}) - \frac{1}{2\pi}\sum_{ij}(\sigma_i - \sigma_j) \oiint V(\boldsymbol{x}') \frac{\boldsymbol{X}}{\|\boldsymbol{X}\|^3} dS_{ij}' \quad \text{where } V_0(\boldsymbol{x}) = \frac{1}{4\pi\sigma_0}\int \frac{\mathbf{J}^{\mathrm{P}}(\boldsymbol{x}').\boldsymbol{X}}{\|\boldsymbol{X}\|^3} d\boldsymbol{x}' \tag{3-9}$$

where $V_0(\boldsymbol{x})$ is the electrical potential at the 3D location $\boldsymbol{x}$ created by the primary current distribution $\boldsymbol{J}^{\mathrm{P}}(\boldsymbol{x}')$, and the operator "." denotes the dot product. These above two general equations states that the electric potentials and magnetic fields can be calculated if we know the primary current distribution $\boldsymbol{J}^{\mathrm{P}}(\boldsymbol{x}')$ and the potential $V(\boldsymbol{x}')$ on all surfaces of the volume conduction model. Therefore, equations (3-8) and (3-9) represent the integral solution of the forward problem,

which can be solved either analytically for certain symmetries such as spherical symmetry, or numerically with BEM or FEM approaches. Detailed reviews on forward solutions with mathematical emphasis can be found in the cited papers (Hämäläinen et al., 1993; Pruis et al., 1993; Kybic et al., 2006; Hallez et al., 2007; Gramfort et al., 2011).

Basically, the EEG and MEG forward problems consist in solving the Poisson's equations to find $V(\boldsymbol{x})$ and $\boldsymbol{B}(\boldsymbol{x})$ at a sensor positioned outside the head at $\boldsymbol{x}$, elicited by a single current dipole source, with dipole moment $\boldsymbol{u}$ and positioned at $\boldsymbol{x}'$. The single equivalent current dipole, as described in **Section 3.1.1**, is the most widely used source model in EEG/MEG forward problem. In mathematical terms, it comprises a current source and sink at infinitesimal distance apart. A current dipole is characterized by position $\boldsymbol{x}'$ and moment $\boldsymbol{u}$, which incorporates the orientation ϕ and strength u of the current.

$$\boldsymbol{J}(\boldsymbol{x}) = \boldsymbol{u}\,\delta(\boldsymbol{x} - \boldsymbol{x}') \tag{3-10}$$

where $\delta(\boldsymbol{x})$ is the Dirac delta function. The total neuronal current is then viewed as the superposition of thousands of such current dipoles. Thanks to superposition principle, this leads to solving the Poisson's equation to find the electric potential and the magnetic field on the measurement points for different configurations of $\boldsymbol{x}'$ and $\boldsymbol{u}$ within the source space Thus, for q sensors and r dipoles, $V(\boldsymbol{x})$ can be discretized in a matrix $\boldsymbol{G}$ of size $q \times 3r$, where each column of the matrix represents the electric potential produced by a unit current dipole at a given position and oriented according to one of the three orthogonal directions. This matrix is usually referred to as the lead field matrix, which describes the sensitivity distribution of the sensors. The lead field matrix for the magnetic field $\boldsymbol{B}(\boldsymbol{x})$ can be obtained in a similar manner. As shown in equations (3-8) and (3-9), both $V(\boldsymbol{x})$ and $\boldsymbol{B}(\boldsymbol{x})$ are linearly related to the neural current sources when the position of the sources is fixed (note that the effect of the position of the sources is non-linear, since it is decreasing as the inverse of the square of the distance). Following this, the

relationship between the EEG/MEG measurements and the sources inside the brain is given by the linear model,

$$\begin{bmatrix} m_1 \\ \vdots \\ m_q \end{bmatrix} = \begin{bmatrix} g_1(\boldsymbol{x}'_1,\phi_1) & \cdots & g_1(\boldsymbol{x}'_r,\phi_r) \\ \vdots & \ddots & \vdots \\ g_q(\boldsymbol{x}'_1,\phi_1) & \cdots & g_q(\boldsymbol{x}'_r,\phi_r) \end{bmatrix} \begin{bmatrix} u_1 \\ \vdots \\ u_r \end{bmatrix} \tag{3-11}$$

$$\boldsymbol{m} = \boldsymbol{G}(\{\boldsymbol{x}'_i,\phi_i\})\,\boldsymbol{j} \quad \text{with } i = 1,\ldots,r$$

where the vector $\boldsymbol{m}$ is $q \times 1$ and contains the collection of data measured by all the q recording channels, while the vector $\boldsymbol{j} = [u_1, \ldots, u_r]^{\mathrm{T}}$ is $3r \times 1$ and contains the dipole strengths in the 3 orientations of the moments for the r equivalent current dipole sources located at fixed locations contained in the lead field $\boldsymbol{G}$. Thus, the predicted forward data $\boldsymbol{G}(\{\boldsymbol{x}'_i,\phi_i\})\,\boldsymbol{j}$, given by the linear generative model in equation (3-11) is further used in the inverse problem.

This model can be readily extended to include a time component t, when considering time evolving activities at every dipole location. Therefore, for q sensors, r dipoles, and τ discrete time samples, the spatio-temporal model can therefore be represented as,

$$\boldsymbol{M} = \boldsymbol{G}\,\boldsymbol{J} \tag{3-12}$$

where $\boldsymbol{M}$ is the matrix of data measurements of size $q \times \tau$, and $\boldsymbol{J}$ is the matrix of dipole moments of size $3r \times \tau$. Here the columns of the time series matrix $\boldsymbol{J}$ are the corresponding time series for each dipole in every orientation. $\boldsymbol{G}$ is a $q \times 3r$ matrix that does not dependent on time.

3.2. Inverse problem: From EEG and MEG signal to neural currents

Solving the EEG or MEG inverse problem, given the forward model is an ill-posed problem that does not admit a unique solution unless further assumptions are made.

However, based on the existing knowledge about the anatomical and neuro-physiological basis of the brain signals, *a priori* assumptions or constraints regarding the underlying sources can be considered to solve the inverse problem and identify one solution. These prior assumptions are essential, since they determine whether the solution is limited to only explaining the data or if the solution actually supports neuro-physiological information about where the signals were generated in the brain. Consequently, any source localization method solving the inverse problem depends on these *a priori* assumptions.

To estimate the EEG and MEG neuronal sources, three types of general approaches based on different *a priori* assumptions on sources have been proposed: 1) dipole fitting approaches, 2) dipole scanning approaches, and 3) distributed source imaging approaches. For a review, we are referring the reader to (Baillet and Mosher, 2001; Grech et al., 2008).

Before introducing the different inverse solutions, let us define the generative model

$$\boldsymbol{M} = \boldsymbol{G}\,\boldsymbol{J} + \boldsymbol{E} \tag{3-13}$$

as the $q \times \tau$ spatio-temporal matrix containing the measurement data under analysis in the presence of measurement noise $\boldsymbol{E}$ (dimension $q \times \tau$). The objective of the inverse solutions is then to estimate $\boldsymbol{J}$ from the measured data $\boldsymbol{M}$ and the estimated lead field matrix $\boldsymbol{G}$, while taking into account the influence of the noise $\boldsymbol{E}$.

3.2.1. Dipole fitting approach

One approach to EEG/MEG inverse problem is to assume that neuronal activity of interest is generated by an individual or few ECDs of unknown locations, orientations and amplitudes (Scherg and Von Cramon, 1986; Ebersole, 1997a; Wendel et al., 2009). Several types of dipole models can be considered: moving dipoles (with unknown position, orientation and amplitude), rotating dipoles (with fixed position and unknown orientation and amplitude) or fixed dipoles (with fixed

position and orientation but unknown amplitude). While orientation and amplitude can be estimated using a least square approach, estimating the location of those ECDs consist in solving iteratively a non-linear problem (Mosher et al., 1992; Huang et al., 1998; Uutela et al., 1998). The locations and orientations of these dipoles can then be represented and mapped on the anatomical MRI. The dipole fitting approach can be applied for fitting a single dipole at a single time sample of the measurements or it can be performed over a time period of several time samples (Michel et al., 2004; Hara et al., 2007).

Although, dipole fitting approach is a well-established procedure and has been widely used for source localization of epileptic spikes for decades, few important issues and limitations should be pointed out. One main limitation of dipole fitting approaches when applied to epileptic discharges is that they are modeling the activity of point-like source, whereas we have already mentioned that the generators of epileptic spikes are spatially extended over several square centimeter of cortex (see **Section 2.6.1)**. Moreover, several studies also pointed out that dipole fitting approaches might be inaccurate when applied in low SNR conditions (Shiraishi, Ahlfors, et al., 2005; Hara et al., 2007). Another difficult aspect with these methods is to decide the number of sources that can be identified from the data.

Several indicators of the quality of the fit, such as the goodness of fit (GOF) or the residual variance are used, to quantify the concordance between the potentials or fields estimated from the ECD and the actual measurements. Generally, single ECD do not provide a GOF of 100%, i.e. 100% of the measured data cannot be explained by a single ECD due to the oversimplification of this source model. A threshold is thus set for these indicators to choose the best fitting ECDs and discard the ECDs below the threshold. This threshold is set subjectively and can vary from user to user. Finally, one should be aware that when localizing EEG or MEG data with dipole fitting approaches in cases where the underlying assumption are not fully respected (few very focal generators), source localization might be completely

misleading even when showing good quality indices (GOF) (Kobayashi et al., 2005).

3.2.2. Dipole scanning approaches

Dipole scanning approach (Mosher et al., 1992; Bénar et al., 2006; Gaetz and Cheyne, 2006) are actually an extension of the single dipole fitting approach, particularly addressing the difficult issue of the number of dipoles to be considered in a standard dipole fitting approach. The idea of dipole scanning approaches is to test the relevance of fitting a fixed or rotating dipole on every point of a 3D grid within the source space and estimate a metric showing how likely such dipole could explain EEG and or MEG data. Dipole scanning approaches results in 3D maps for which only local maxima should be considered since they represent the most relevant dipoles. As a dipole model estimated iteratively for each point of the grid, it will suffer from the same modeling limitation as the dipole fitting approach in presence of a spatially extended generator. Some of the known dipole scanning approaches are the beam-forming approach (Baillet and Mosher, 2001), Multiple Signal Classification approach (MUSIC) (Mosher et al., 1992), its extension recursive MUSIC (R-MUSIC) and recursively applied and projected MUSIC (RAP-MUSIC) (Mosher and Leahy, 1998).

The beamforming approach consists in estimating, iteratively for each point of the grid, a spatial filter to enhance only the signal coming from this specific location, while removing signals from other sources. A widely used beamformer approach actually consists in the so-called linearly constrained minimum variance (LCMV) method (Van Veen et al., 1997), which attempts to minimize the beamformer output power subject to a unity gain constraint for the grid location of interest,

$$\min_{\boldsymbol{W_d}} tr(\boldsymbol{W_d}^{\mathrm{T}} \boldsymbol{C_m} \boldsymbol{W_d}) \text{ subject to } \boldsymbol{W_d}^{\mathrm{T}} \boldsymbol{G_d} = \boldsymbol{I} \qquad (3\text{-}14)$$

where $\boldsymbol{C_m} = [\boldsymbol{M}\boldsymbol{M}^{\mathrm{T}}]$ is the data covariance matrix (dimension $q \times q$), $\boldsymbol{G_d}$ is the $q \times 3$ lead field matrix at source location $\boldsymbol{x}'$ considering the three orientations for each

source location, *tr* stands for trace The solution of this optimization problem is given by $\boldsymbol{W_d} = (\boldsymbol{G_d}^{\mathrm{T}}\boldsymbol{C_m}^{-1}\boldsymbol{G_d})^{-1}\boldsymbol{G_d}^{\mathrm{T}}\boldsymbol{C_m}^{-1}$, thus providing for every source location $\boldsymbol{x}'$ on a grid the $q \times 3$ spatial filter matrix. Consequently, by applying this spatial filter on the data $\boldsymbol{W_d}^{\mathrm{T}}\boldsymbol{M}$, we obtain the parametric source activity at source location $\boldsymbol{x}'$. LCMV beamformer quantifies the contribution of a source localized at $\boldsymbol{x}'$ to the data. Finally, by simply changing the location $\boldsymbol{x}'$ iteratively, we can produce a 3D map of beamformer estimates of the neuronal activity at any location.

The synthetic aperture magnetometry (SAM) approach (Vrba and Robinson, 2001) is an extension of the LCMV beamformer with the exception that an optimal dipole orientation vector for each location on the grid is estimated in order to maximize the power-to-noise output ratio (thus providing "pseudo-Z" score maps). A frequency domain extension of these beamformer approaches is entitled dynamic imaging of coherent sources (DICS) (Gross et al., 2001). DICS actually consists in estimating a spatial filter matrix optimized for some specific frequency band, using a cross-spectral density matrix for the data covariance matrix.

By construction beamformer approaches are not appropriate when dealing with correlated sources, since the spatial filter aims at focusing on the activity on one source while removing the influence of the others (Sekihara et al., 2002). Moreover, beamformer spatial filter being only computed from the lead field and data covariance matrices, beamformer approaches are sensitive to errors in the head model (Wax and Anu, 1996) and to the number of independent data samples that are necessary for the robust and stable estimation of data covariance statistics (Cheyne et al., 2006; Oswal et al., 2014). Therefore, beamformers ideally require long, stationary episodes of data. This can be an issue when dealing with epilepsy data as it cannot be guaranteed that such long segment of data without epileptic events will be present from the short duration of EEG/MEG recordings.

MUSIC is another dipole scanning approach which assumes that there are fewer sources than sensors, that the sources are uncorrelated and that the noise is white. Based on singular value decomposition (SVD) of the data time series $\boldsymbol{M} = \boldsymbol{U}\boldsymbol{\Sigma}\boldsymbol{V}^{\mathrm{T}}$,

a signal subspace $\boldsymbol{U_d}$ is first identified from the noise subspace. $\boldsymbol{U_d}$ is the signal subspace spanned by the $\boldsymbol{d}$ first left singular vectors of $\boldsymbol{U}$, while the noise subspace is spanned by the remaining left singular vectors. The whole brain volume is then scanned in order to assess which source locations actually contribute to the signal subspace (Mosher et al., 1992), which is equivalent to contributing the least to the noise subspace. Therefore, the MUSIC cost function to be minimized is,

$$\mathcal{M}_{\mathbf{d}} = \frac{\left\|(\boldsymbol{I} - \boldsymbol{U_d}\boldsymbol{U_d}^{\mathrm{T}})\boldsymbol{G_d}\right\|_2^2}{\|\boldsymbol{G_d}\|_2^2} = \frac{\left\|\mathbf{P}_{\boldsymbol{U_d}}^{\perp}\boldsymbol{G_d}\right\|_2^2}{\|\boldsymbol{G_d}\|_2^2} \qquad (3\text{-}15)$$

where $\mathbf{P}_{\boldsymbol{U_d}}^{\perp}$ is the orthogonal of the signal subspace projection operator $\mathbf{P}_{\boldsymbol{U_d}}$, which therefore results in a projection onto the noise subspace. This cost function is minimal when $\boldsymbol{G_d}$ corresponds to one of the most likely source locations and orientations. Other MUSIC strategies, such as RAP-MUSIC, iterates the MUSIC cost function after each source is found by projecting the signal subspace away from the lead fields corresponding to the sources already found (Mosher and Leahy, 1998; Mosher, Baillet, et al., 1999). However, the practical aspects of MUSIC and its variations remain limited by their sensitivity in the accurate definition of the respective signal and noise subspaces.

Localization of extended sources using dipole scanning approaches: Whereas most dipole scanning approach exhibits same limitation as dipole fitting method when assuming an ECD model for every point on the grid, some attempts have been made to allow reconstruction of spatially extended generators, for instance, beamforming using cortical patches(Limpiti et al., 2006; Hillebrand and Barnes, 2011) or the 2q-ExSo-MUSIC (2q-th order extended source MUSIC) algorithm (Birot et al., 2011). Yet these methods make it difficult and computationally very demanding to localize several correlated, simultaneously active extended source regions, which are subsequently referred to as patches. We have used the 2q-ExSo-MUSIC algorithm for the study in chapter 5, therefore, details on this method can be found in **Section 5.4.1c** of chapter 5.

3.2.3. Distributed source imaging (dSI) approach

Whereas previous methods consisted in estimating the contribution of every source within a grid iteratively, distributed source imaging techniques are imaging approaches, attempting to estimate a 3D distribution of the underlying current density for every time sample of the recorded EEG or MEG signals. These approaches are considering distributed source models (**Section 3.1.1**), consisting either in ECD dipole distributed within the entire brain or just along the cortex (Dale and Sereno, 1993; Daunizeau et al., 2006; Grova et al., 2006). Anatomical constraints can therefore be introduced by defining the source space within the gray matter volume or along the cortical surface. Triangular lattices are generally used to represent the cortical surface, while tetrahedral or hexahedral lattices are used to represent the interior of the head, such as the gray matter volume. The typical lattice spacing ranges from 1 mm to 1 cm. Each lattice point represents a single ECD for which the orientation could either be fixed perpendicular to the cortical surface, or kept completely free. Since the position of all the dipoles is now fixed, the localization problem becomes linear since only amplitude (and eventually orientations) should be estimated from the data. Mathematically, these models are linear but largely underdetermined problems, because the number of observation points (usually a few hundreds) is much less than the number of source coefficients that must be identified (usually several thousands). Consequently, additional constraints on the sources amplitudes should be incorporated in order to find a unique solution for these distributed inverse problems.

Two main approaches have been proposed to handle these issues: 1) regularization which favors features consistent with the available *a priori* knowledge on the solution, and 2) probabilistic approaches which makes statistical inferences (Bayesian or entropic) about the real source configuration based on the information given by the measurements and some *a priori* knowledge about the sources. In most cases, the same methods can generally be described within both frameworks.

a. Regularization techniques

All regularization methods actually consist in estimating a stable solution to the inverse problem by tuning a trade-off between the quality of data fit and the regularizing function (*a priori* constraint). One such regularization method commonly used is the Tikhonov regularization to find the estimate of $\boldsymbol{J}$ (i.e. $\hat{\boldsymbol{J}}$) that minimizes the following cost function,

$$\hat{\boldsymbol{J}} = \underset{\boldsymbol{J}}{\operatorname{argmin}}\left\{((\boldsymbol{M}-\boldsymbol{G}\boldsymbol{J})^T\boldsymbol{L}_m(\boldsymbol{M}-\boldsymbol{G}\boldsymbol{J}))^p+\lambda\left(\boldsymbol{J}^T\boldsymbol{L}_j\boldsymbol{J}\right)^p\right\} \qquad (3\text{-}16)$$

Here, the first term on the right hand side is a data fit term that expresses the deviation of the estimate from the measurements. The last term is the regularizing term that describes the *a priori* constraints on the sources, thus promoting solutions with certain properties while penalizing others. In equation (3-16), Tikhonov regularization is defined by a p-norm formulation, where, $p = 1$ or 2 would therefore correspond to L-1 norm or L-2 norm versions of the regularization. λ is the regularization hyperparameter that controls the trade-off between the data fit and the *a priori* constraint. This regularization hyperparameter can be chosen by the user through various methods such as the Morozov discrepancy principle (Morozov, 1966) or the L-curve approach. In this thesis, we considered the L-curve method (Hansen, 2000), which consists in choosing the regularization hyperparameter by plotting the data fit against the regularizing term for different values of λ. Then, the L-shaped corner of this L-curve provides the optimal trade-off value for λ that minimizes the two terms. $\boldsymbol{L}_m$ and $\boldsymbol{L}_j$ are weighting matrices for the data and the regularizing term, respectively. Different choices of those weighting matrices lead to different variants of the distributed inverse solutions.

Here we described some of the well-known inverse solutions based on Tikhonov regularization principle:

- **Classical regularized minimum-norm estimate (MNE)** (Hämäläinen and Ilmoniemi, 1994): assumes the current density distribution of the solution

to exhibit minimum energy property. The minimum norm solution is obtained when choosing a L-2 norm Tikhonov regularization. Considering the weighting matrices $\boldsymbol{L}_m = \boldsymbol{\Sigma}_e$ and $\boldsymbol{L}_j = \boldsymbol{\Sigma}_s$ in equation (3-16) as the inverse covariance matrices of the sensor noise and sources respectively, the estimated MNE solution is,

$$\begin{aligned} \hat{\boldsymbol{J}}_{MNE} &= \underset{\boldsymbol{J}}{\operatorname{argmin}}\{\|\boldsymbol{\Sigma}_e(\boldsymbol{M}-\boldsymbol{G}\boldsymbol{J})\|^2+\lambda\|\boldsymbol{\Sigma}_s\boldsymbol{J}\|^2\} \\ &= (\boldsymbol{G}\boldsymbol{\Sigma}_e\boldsymbol{G}^{\mathrm{T}}+\lambda\boldsymbol{\Sigma}_s)^{-1}\,\boldsymbol{G}^{\mathrm{T}}\boldsymbol{\Sigma}_e\boldsymbol{M} = \boldsymbol{W}_{MNE}\boldsymbol{M} \end{aligned} \tag{3-17}$$

In standard MNE, the covariance of the sources is set to be the identity.

$\boldsymbol{W}_{MNE}$ is the MNE linear inverse operator. By estimating a minimum energy solution, this approach will then naturally tend to bias source localization results towards more superficial sources, as they have the strongest coupling to the sensors and will require less amplitude. MNE has been used as a standard approach for model comparison and performance evaluation throughout this thesis.

- **Weighted minimum norm (wMNE)** (Ioannides et al., 1990; Lin et al., 2006): In order to compensate for the tendency of MNE to favor superficial sources, in wMNE the inverse of the source covariance matrix $\boldsymbol{L}_j = \boldsymbol{\Sigma}_s$ is no longer proportional to the identity matrix; instead, the source covariance matrix contains a weighting factor for each source, aiming to remove the bias towards superficial sources. $\boldsymbol{\Sigma}_s$ can have different forms but the simplest one is based on the norm of the columns of the matrix $\boldsymbol{G}$, also known as lead field normalization. This results in the general weighted MNE solution ($\hat{\boldsymbol{J}}_{wMNE}$). Other forms of weighting includes spatial smoothness constraint (described below), fMRI priors or information from other imaging modalities (Liu et al., 1998; Phillips et al., 2002).

- **LORETA** (low-resolution electromagnetic tomography) (Pascual-Marqui et al., 1994): This is another form of weighting which combines the lead

field normalization of wMNE with Laplacian operator to introduce a constraint of spatial smoothness between neighboring sources. LORETA is then based on the search for solution with maximum spatial smoothness, while normalizing the columns of $\boldsymbol{G}$ to give all sources (close to the surface and deeper ones) the same opportunity of being reconstructed. Originally, LORETA was proposed for volumetric source localization, but it is also referred to as **cLORETA** (cortical LORETA) when it is applied on cortical surface grid (Wagner et al., 1996).

- **dSPM** (dynamic statistical parametric mapping) (Dale et al., 2000): has been proposed as another approach to compensate for depth bias, through noise-normalization procedure. The output of dSPM is, therefore, no longer an estimate of the neural current distribution, but rather a statistical measure of brain activity. Here, the estimated current at each source location is divided by an estimate of the noise at that location, which can be obtained by applying $\boldsymbol{W_{MNE}}$ to the noise covariance matrix $\boldsymbol{\Sigma_e}$.

$$\begin{aligned} \widetilde{\boldsymbol{W}}_{dSPM} &= \left(\sqrt{diag(\widetilde{\boldsymbol{W}}_{MNE} \boldsymbol{\Sigma}_e \widetilde{\boldsymbol{W}}_{MNE}^{\mathrm{T}})} \right)^{-1} \widetilde{\boldsymbol{W}}_{MNE} \\ \hat{\boldsymbol{J}}_{dSPM} &= \widetilde{\boldsymbol{W}}_{dSPM} \boldsymbol{M} \end{aligned} \tag{3-18}$$

- **sLORETA** (standardized LORETA) (Pascual-Marqui, 2002): is an alternative approach for depth-bias compensation of the minimum-norm solutions, using another noise-normalization procedure. Here, the estimated current at each source location is divided by the total variance of the estimated sources, instead of using just the variance due to noise.

$$\begin{aligned} \widetilde{\boldsymbol{W}}_{sLORETA} &= \left(\sqrt{diag(\widetilde{\boldsymbol{W}}_{MNE} (\boldsymbol{G}\boldsymbol{G}^{\mathrm{T}} + \boldsymbol{\Sigma}_e) \widetilde{\boldsymbol{W}}_{MNE}^{\mathrm{T}})} \right)^{-1} \widetilde{\boldsymbol{W}}_{MNE} \\ \hat{\boldsymbol{J}}_{sLORETA} &= \widetilde{\boldsymbol{W}}_{sLORETA} \boldsymbol{M} \end{aligned} \tag{3-19}$$

Note that this method has been shown to produce unbiased, zero-error localization of point sources, but in noise-free conditions only (Pascual-Marqui, 2002).

- **Sparse source imaging:** Due to the spatial blurring characteristic of L2-norm based solutions, sparse source imaging approaches have been introduced, with the objective of representing cortical current density distribution with minimal non-zero coefficients (sparseness). Spatial sparsity can be imposed directly on the sources by using L1-norm, thus favoring the localization of focal generators.

$$\hat{\boldsymbol{J}}_{MCE} = \underset{\boldsymbol{J}}{\operatorname{argmin}}\{\|\boldsymbol{\Sigma}_e(\boldsymbol{M}\text{-}\boldsymbol{G}\boldsymbol{J})\|^2+\lambda\|\boldsymbol{\Sigma}_s\boldsymbol{J}\|^1\} \tag{3-20}$$

These L1-norm based methods, also called minimum current estimate (**MCE**), were reported to produce over-focused inverse solutions, always shrinking to only few points of activated area. To overcome this, sparseness was explored in the transformed domain such as the variation-based sparse cortical current density (**VB-SCCD**). This approach is based on the so-called variational map that characterizes variations in amplitude between adjacent dipole sources (Ding, 2009a). Another approach that makes use of sparsity in a transformed domain considers a spatial wavelet transform that permits to compress the signals through a sparse representation. A combination of this wavelet-based prior and the variation-based prior has been considered in a recent method called the variation and wavelet based sparse source imaging (**VW-SSI**) (Zhu et al., 2014).

Note also that L1-norm based estimates usually provide very noisy unrealistic estimates of the time course of the underlying sources. Combination of L1 prior in space with L2 prior in time have been proposed to overcome this issue (Vega-Hernández et al., 2008; Gramfort et al., 2012).

b. Probabilistic approaches using Bayesian inference

An alternative statistical framework to handle the under-determined model of a distributed inverse problem is Bayesian inference. Within the Bayesian inference all forms of uncertainty are expressed in terms of probability distribution and all variables (measurements, sources and noise) are modeled as random variables. To this end, Bayes' theorem provides a flexible way for incorporating a-priori information (additional constraint on sources) into source estimation by means of probability distributions,

$$p(\mathbf{J}|\mathbf{M}) = \frac{p(\mathbf{M}|\mathbf{J})\, p(\mathbf{J})}{p(\mathbf{M})} \tag{3-21}$$

Here, $p(\mathbf{M}|\mathbf{J})$ is the data likelihood, i.e. a statistical distribution modeling data generation from the sources that depends mainly on the forward model and on the noise statistical distribution. $p(\mathbf{M})$ is the distribution characterizing the data. The term $p(\mathbf{M})$ is linked to the notion of *model evidence*, especially when assessing the influence of different models or parametrization within a hierarchical Bayesian framework, such as *Bayesian model averaging* or *model selection* (Trujillo-Barreto et al., 2004; Henson et al., 2009a). $p(\mathbf{J})$ is the distribution modeling the information we have on the sources without taking into account any measurements. This is the *a priori* knowledge or model of the sources. The left hand term $p(\mathbf{J}|\mathbf{M})$ is the conditional distribution of the sources knowing the data. This is also called the a posteriori distribution of the sources. Once known, it will provide the distribution of the intensities of the sources, conditioned by the measured data. In Bayesian inference, this distribution is considered the solution to the inverse problem. In practice, a good assumption is to assume that the sources **J** and noise **E** exhibit a Gaussian distribution and their respective covariances are known. A common way to exploit the information contained in the a posteriori distribution is to infer a point estimate for the value of **J**. Maximum a posteriori (MAP) estimate is one such way that finds the estimator $\hat{\mathbf{J}}_{\mathbf{MAP}}$ of **J** that maximizes the posterior distribution of **J** given the measurements **M**.

$$\hat{\mathbf{J}}_{\mathbf{MAP}} = \underset{\mathbf{J}}{\operatorname{argmax}}\ p(\mathbf{J}|\mathbf{M}) \tag{3-22}$$

Assuming different models on the covariance of the source prior in $p(\mathbf{J})$, it is possible to associated Bayesian approaches to standard solutions like MNE or LORETA as introduced in **Section 3.2.3a** (Grova et al., 2006). The concept of Tikhonov regularization technique and the Bayesian inference using MAP estimator are actually equivalent and often lead to similar algorithms and solutions. For example, the MAP estimate with Gaussian noise and a priori source amplitudes, and identity matrix for the source covariance model is equivalent to the Tikhonov regularized minimum norm solution. A detailed derivation of this equivalence has been shown in Kaipio and Somersalo (2005).

Note that hierarchical Bayesian approach provides a very flexible way to develop several models and to assess the relevance according to the data using model evidence (Friston et al., 2002; Phillips et al., 2005; Friston et al., 2008). These models may consist in setting source covariance model as a linear combination of several components, while the hyperparameters tuning the contribution of every component could be estimated from the data using Restricted Maximum Likelihood techniques. In this context, methods like Multiple Sparse Prior model, Minimum norm model called "IID" and a LORETA-like model called "COH" within a Hierarchical Bayesian framework have been proposed (Friston et al., 2008). These methods will not be further pursued in this thesis but we have studied them extensively in the context of source localization of epileptic discharges, as demonstrated in (Chowdhury et al., 2013).

c. Probabilistic approaches using entropic inferences

The solution of inverse problem can also be addressed within the framework of Maximum Entropy on the Mean (MEM) (Jaynes, 1957; Amblard et al., 2004). In the context of EEG/MEG inverse problem, the idea of the MEM framework is to formalize hypothesis using *a priori* model and then further correct such a model using additional information from EEG/MEG measurements, while entropy

maximization will ensure regularization of the problem. MEM not only provides a promising alternative to the Bayesian probabilistic methodology, but also proposes an improvement to the distributed source model by incorporating flexible prior models, introducing the notion of regions of activation controlled by hidden random variables that tunes the state of activation. One of the key property of the MEM approach is its ability to recover spatially extended sources, while exhibiting very little distant spurious sources (Chowdhury et al., 2013; Grova et al., 2016; Heers et al., 2016). These topics are central to this thesis and will be further developed in the next chapters.

Mathematical formulation of the MEM framework: Within a probabilistic approach, $\mathbf{j}$ is the r-dimensional continuous random variable that describes the dipole current intensities. This random variable is associated with the probability distribution $dp(\mathbf{j})=p(\mathbf{j})d\mathbf{j}$ where $\mathbf{j} \in \mathbb{R}^r$.

With the objective to estimate the probability distribution $dp(\mathbf{j})=p(\mathbf{j})d\mathbf{j}$, the MEM framework regularizes the inverse problem by incorporating prior information on $\mathbf{j}$ in the form of a reference distribution $dv(\mathbf{j})$. Then, the Kullback Leibler divergence or ν-entropy defined by:

$$S_\nu(dp) = -\int_{\mathbf{j}} \log\left(\frac{dp(\mathbf{j})}{dv(\mathbf{j})}\right) dp(\mathbf{j}) = -\int_{\mathbf{j}} f(\mathbf{j}) \log(f(\mathbf{j}))\, dv(\mathbf{j}) \qquad (3\text{-}23)$$

measures the amount of information brought by the data with respect to the prior dv, where f is a ν-density of dp defined as, $dp(\mathbf{j})=f(\mathbf{j})d\nu(\mathbf{j})$. Being a pseudo-distance between the reference distribution dv and any ν-density dp, this entropy is always negative.

In order to introduce a data fit constraint, let us denote $\mathbb{C}_m$ as the set of probability distributions on $\mathbf{j}$ that explains the data on average:

$$dp \in \mathbb{C}_m:\ \mathbf{m} - \left[\boldsymbol{G} \mid \boldsymbol{I}_q\right]\begin{bmatrix} \mathrm{E}_{\mathrm{dp}}[\mathbf{j}] \\ \mathbf{e} \end{bmatrix} = 0 \tag{3-24}$$

where $\mathrm{E}_{dp}[\mathbf{j}] = \int_{\mathbb{R}} \mathbf{j}\, dp(\mathbf{j})$ is the mathematical expectation of $\mathbf{j}$ with respect to the probability distribution dp, $\boldsymbol{I}_q$ is a (qxq) identity matrix. Then, the MEM solution consists in selecting $d\hat{p}$ in $\mathbb{C}_m$ that maximizes the ν-entropy, thus choosing the distribution fulfilling the data fit constraint that is the closest (in terms of Kullback Leibler divergence) to the reference distribution dv:

$$d\hat{p} = \mathrm{argmax}_{dp \in \mathbb{C}_m} S_\nu(dp) \tag{3-25}$$

In the above MEM optimization, the ν-entropy is strictly a convex function that needs to be maximized under constraints, which is equivalent to minimizing an unconstrained strictly concave Lagrangian function. In this formulation, the Lagrangian parameters κ and $\boldsymbol{\lambda}$ are introduced to add constraints to the objective function $S_\nu(dp)$, as follows:

$$\begin{aligned} L(dp,\kappa,\boldsymbol{\lambda}) &= -S_\nu(dp) + \boldsymbol{\lambda}^T(\mathbf{m} - \boldsymbol{G}\mathrm{E}_{dp}[\mathbf{j}]) + \kappa(1 - \textstyle\int dp(\mathbf{j})) \\ L(dp,\kappa,\boldsymbol{\lambda}) &= \textstyle\int f(\mathbf{j}) \log f(\mathbf{j}) d\nu(\mathbf{j}) + \boldsymbol{\lambda}^T(\mathbf{m} - \boldsymbol{G}\mathrm{E}_{dp}[\mathbf{j}]) + \kappa(1 - \int dp(\mathbf{j})) \end{aligned} \tag{3-26}$$

where the first term is the ν-entropy, the second term is the data fit constraint, and the last term expresses the constraint that $dp(\mathbf{j})$ should be a probability distribution.

Therefore, the optimal solution $(d\hat{p}, \tilde{\kappa}, \tilde{\boldsymbol{\lambda}})$ of this optimization problem calculated via the Lagrangian formalism, i.e. $\arg\min_{dp,\kappa,\boldsymbol{\lambda}} L(dp,\kappa,\boldsymbol{\lambda})$, provides:

$$d\hat{p}(\mathbf{j}) = \frac{e^{\tilde{\boldsymbol{\lambda}}^T \boldsymbol{G}\,\mathbf{j}}}{Z(\tilde{\boldsymbol{\lambda}})} d\nu(\mathbf{j}) \tag{3-27}$$

where $\tilde{\boldsymbol{\lambda}}$ is the maximum of the non-linear optimization of a convex function $D(\boldsymbol{\lambda})$ in a q-dimensional space, thus accepting a unique solution. In practice, the optimization problem depends only on the parameter $\boldsymbol{\lambda}$ which is the same dimension as the number of sensors (q). Note that $D(\boldsymbol{\lambda})$ in equation (3-27) describes both the

prior knowledge encompassed in the reference measure *dv* and the measurements **m** that define the space $\mathbb{C}_m$ formalizing our data fit constraint (equation (3-23)).

$$\tilde{\boldsymbol{\lambda}} = \operatorname{argmax}_{\boldsymbol{\lambda}} D(\boldsymbol{\lambda}),$$
$$\text{where } D(\boldsymbol{\lambda}) = \boldsymbol{\lambda}^T \mathbf{m} - F_v(\boldsymbol{G}^T \boldsymbol{\lambda}) - \frac{1}{2}\boldsymbol{\lambda}^T \boldsymbol{\Sigma}_e \boldsymbol{\Sigma}_e{}^T \boldsymbol{\lambda} \tag{3-28}$$

The normalizing constant in equation (3-26), $Z(\tilde{\boldsymbol{\lambda}}) = e^{F_v(\boldsymbol{G}^T \tilde{\boldsymbol{\lambda}})}$ is the partition function and F_v is the free energy associated with the reference distribution *dv*, defined as the log of the partition function.

$$F_v(\xi) = \log \int e^{\xi^T \mathbf{j}} dv(\mathbf{j}) \text{ with } \xi = \boldsymbol{G}^T \tilde{\boldsymbol{\lambda}} \tag{3-29}$$

and $\boldsymbol{\Sigma}_e$ is the noise covariance matrix for noise measurement **E** which is estimated as a diagonal matrix with a different value for each channel; thus taking into account the noise levels of each individual channel.

The MEM estimate of the source amplitudes $\hat{\mathbf{j}}$ is then computed as the mathematical expected value of the distribution $d\hat{p}$:

$$\hat{\mathbf{j}}_{MEM} = \mathrm{E}_{d\hat{p}}[\mathbf{j}] = \int_{\mathbf{j}} \mathbf{j} d\hat{p}(\mathbf{j}) d\mathbf{j} = \int_{\mathbf{j}} \frac{e^{\tilde{\boldsymbol{\lambda}}^T \boldsymbol{G}\,\mathbf{j}}}{Z(\tilde{\boldsymbol{\lambda}})} dv(\mathbf{j}) d\mathbf{j} = \frac{d}{d\xi} F_v(\xi)\,|_{\xi = \boldsymbol{G}^T \tilde{\boldsymbol{\lambda}}} \tag{3-30}$$

Therefore, the MEM estimate of the sources' amplitudes **j** could then be re-written as the gradient of the free energy F_v:

$$\hat{\mathbf{j}}_{MEM} = \nabla F_v(\xi)\,|_{\xi = \boldsymbol{G}^T \tilde{\boldsymbol{\lambda}}} \tag{3-31}$$

Definition of the reference distribution within the MEM framework: MEM relies on its inherent flexibility of introducing constraints or knowledge about the sources through the definition of the reference distribution *dv*. To do so, brain activity was considered to be organized into *K* cortical parcels, each parcel showing a homogeneous activation state (Amblard et al., 2004). A Data Driven

Parcellization (DDP) method was used to perform full parceling of the tessellated cortical surface into non-overlapping parcels (Lapalme et al., 2006). This spatial parcelling is driven by the Multivariate Source Pre-localization (MSP) technique (Mattout et al., 2005), which is a projection method providing a probability-like coefficient (MSP score) between 0 and 1 for each dipolar source characterizing its contribution to the data. The key aspect of DDP lies in the pre-localization of the sources of brain activity using the MSP method followed by a region growing algorithm. To do so, seed points were iteratively selected among the dipoles showing the highest MSP coefficients. Region growing around each seed points was then iterated until a given spatial neighborhood order, resulting in a partition of the whole brain into *K* parcels. This way of choosing the seed points and parceling ensured dipoles contributing to the same underlying generator to be gathered within the same parcel, whereas dipoles contributing to distinct generators to be associated within distinct parcels. For more details on the DDP method please refer to Chowdhury et al. (2013). DDP is therefore providing a partition of the whole cortical surface into K non-overlapping parcels.

Each cortical parcel *k* is then characterized by an activation hidden state variable S_k, describing if the parcel is active or not. Assuming a collection of mutually independent parcels, the reference distribution *dv* is defined as a factorization of the joint probability distribution of the *K* parcels:

$$dv(\mathbf{j}) = \prod_{k=1}^{K} \left[\left(1-\alpha_k\right) \delta\left(\mathbf{j}_k\right) + \alpha_k \; \mathcal{N}\left(\boldsymbol{\mu}_k, \boldsymbol{\Sigma}_k\right)\left(\mathbf{j}_k\right) \right] d\mathbf{j} \qquad (3\text{-}32)$$

where $\alpha_k = Prob\left(\mathrm{S}_k = 1\right)$ is the probability of the k^{th} parcel to be active. $\mathbf{j}_k$ denotes the random vector modeling the intensities of the r_k sources in the k^{th} parcel. When the parcel is active $(\mathrm{S}_k = 1)$, the dipole intensities within the k^{th} parcel are modeled using a Gaussian distribution $\mathcal{N}\left(\boldsymbol{\mu}_k, \boldsymbol{\Sigma}_k\right)$, where $\boldsymbol{\mu}_k$ and $\boldsymbol{\Sigma}_k$ represent respectively the mean and the covariance of the r_k dipoles within the k^{th} parcel.

When the parcel is inactive $(S_k = 0)$, the dipole intensities are modeled using a Dirac distribution δ, thus allowing to "shut down" the corresponding parcel.

Incorporating the cortical parcels through reference distribution in the MEM framework: When equation (3-30) is applied to the reference distribution introduced in equation (3-31), the MEM estimate of the sources in each parcel *k* can be found to be:

$$\hat{\mathbf{j}}^{k}_{MEM} = \hat{\alpha}_k[\boldsymbol{\mu}_k + \boldsymbol{\Sigma}_k \boldsymbol{G}_k^T \tilde{\boldsymbol{\lambda}}]$$

$$\text{where } \hat{\alpha}_k = \frac{\alpha_k}{\alpha_k + (1-\alpha_k)\exp(-F_{v,k}(\boldsymbol{G}_k^T \tilde{\boldsymbol{\lambda}}))} \tag{3-33}$$

(A8)

where $F_{v,k}$ is the free energy corresponding to the k^{th} parcel when active (i.e. S_k = 1), given by:

$$F_{v,k}\left(\boldsymbol{G}_k{}^T \tilde{\boldsymbol{\lambda}}\right) = \boldsymbol{\mu}_k^T \boldsymbol{G}_k^T \tilde{\boldsymbol{\lambda}} + \frac{1}{2}\tilde{\boldsymbol{\lambda}}^T \boldsymbol{G}_k \boldsymbol{\Sigma}_k \boldsymbol{G}_k^T \tilde{\boldsymbol{\lambda}} \tag{3-34}$$

and $\boldsymbol{G}_k$ is the $(q \times r_k)$ submatrix of $\boldsymbol{G}$ for the k^{th} parcel.

When incorporating the cortical parcels through the reference distribution *dv* in the MEM framework, the first step was to define the parameters (α_k, $\boldsymbol{\mu}_k$, $\boldsymbol{\Sigma}_k$) of each cortical parcel. Based on the initialization of these parameters, different variants of MEM-based inverse methods have been proposed (Grova et al., 2006; Chowdhury et al., 2013). In this thesis, we will focus on coherent-MEM (cMEM) method which has been extensively studied and validated using simulated and clinical EEG/MEG data (Chowdhury et al., 2013; Grova et al., 2016; Heers et al., 2016; Pellegrino et al., 2016a). In the cMEM method, the parameters were initialized as follows:

- α_k was initialized as the median of the MSP scores of the dipoles within the corresponding parcel.

- Considering the Gaussian distribution of the active state to be a zero mean distribution, $\boldsymbol{\mu}_k$ of each parcel was initialized to zero.

- The source covariance $\boldsymbol{\Sigma}_k$ of each parcel was initialized with an additional constraint of local spatial smoothness in each parcel. This spatial smoothness model assumes that nearby dipoles are more likely to have similar intensities. In order to introduce local spatial smoothness over a geodesic surface, a diffusion-based spatial prior was used, as proposed by Harrison et al. (Harrison et al., 2007). This diffusion-based spatial prior was constructed using the Green's function of the adjacency or spatial connectivity matrix defined over the geodesic cortical surface. For further details the reader can refer to Chowdhury et al. (2013).

cMEM method was designed specifically for the localization of spatially extended generators of IEDs. Quantitative assessment of cMEM method, using simulations and clinical data, demonstrated the relevance of using cortical parcels with spatial smoothness prior in source localization methods to detect the spatial extent of the sources. Performance of cMEM method has been compared with multiple source localization approaches (dipole fitting, MNE, dSPM, sLORETA, IID, COH and Multiple Sparse Prior model) (Chowdhury et al., 2013; Grova et al., 2016; Heers et al., 2016; Pellegrino et al., 2016a; Pellegrino et al., 2016c) and it was shown that cMEM provided better localization accuracy and was able to recover the spatial extent of the sources better than the other source localization methods. More specifically, cMEM was sensitive to a large range of spatial extent (3 cm^2 to 30 cm^2), which is favorable when localizing the generators of IEDs. Although the parcellization was crucial in regularization of the inverse problem, the accuracy of the underlying parcels was not required to obtain an accurate cMEM solution i.e. the number or size of the parcels and the type of data used to obtain the spatial clustering did not affect the cMEM solution. These aspects of cMEM method clearly justify its use in this thesis for the localization of the generators of IEDs.

3.3. Validation of source localization methods using simulation models

Validation of EEG/MEG source localization approaches in the case of epileptic spontaneous events is a difficult task, especially since there is usually no gold standard available when analyzing EEG and MEG clinical data. Therefore, quantitative evaluation of source localization results are difficult to make and qualitative evaluation requires the expertise of a neurologist. A first solution consists in providing quantitative evaluation of the properties of the source localization approaches using simulation models that can mimic the generation of epileptic discharges. However, the organization of neural activity in the brain is complex and the relationship between the underlying generators and the recorded electro-magnetic signals, governed by Maxwell equations, might be difficult to model in a very realistic manner. It is accepted that simulations are providing a simplified configuration of what the reality might be. For instance, simple static simulation models commonly consider a single dipole (Fuchs et al., 1998; Pascual-Marqui, 2002) or an extended patch of uniform activity (Liu et al., 2002; Trujillo-Barreto et al., 2004; Grova et al., 2006; Chowdhury et al., 2013) as theoretical generators. A single dipole does not mimic the spatially extended epileptic generators, whereas the simulation model involving a single static patch of uniform activity can be extended to simulate different spatial extents of the source but does not model the temporal dynamics within the patch. However, sufficient level of realism can still be obtained by considering the set-up of real EEG or MEG recordings as well as real background signals to add noise to simulated data. Such an approach to validate the sensitivity of the source localization methods to recover spatially extended sources using the static patch model has been used in chapter 4 (more details on this model can be found in **Section 4.4.5a** of chapter 4). A variant of the single static patch mimicking the propagation of epileptic discharges between two regions has also been considered and is described in **Section 4.4.5a**.

Amongst the most realistic modeling approaches considered in simulations, neuronal computational models have been proposed to mimic the relationship

between the neuronal activity and the measured EEG/MEG data. Biologically inspired neuronal mass models (Wilson and Cowan, 1972; Lopes da Silva et al., 1976; Traub, 1979; Jansen and Rit, 1995; Wendling, 2005; Cosandier-Rimélé et al., 2007) have been widely used to study and model brain activity at the microscopic and macroscopic levels. In the particular context of modeling epileptic activity, Wendling and colleagues proposed a macroscopic model to simulate spatially extended epileptic discharges by coupling multiple populations of cells (Wendling et al., 2000). An extension of this model, using a spatio-temporal approach (Cosandier-Rimélé et al., 2007) combining a biophysical distributed source model with a computational neural mass model has been used in this thesis. More details on this model can be found in **Section 5.4.2** of chapter 5.

The problems and limitations that we face with data recorded in clinical practice have to be considered during the validation using simulation models. It is actually difficult to properly handle all possible sources of variability inherent to real data such as properties of the noise, variations in electrode/sensor placements, inhomogeneities of the head surface, contribution of artifacts to some channels, and many others. However, the eligibility of the source localization approaches for application on clinical data, can still be carefully evaluated with more reliability if the simulation environment takes into consideration various factors affecting the detection of IEDs on EEG and MEG. These factors include for instance the possibility for spatially extended generators and propagation patterns in IEDs, different types of physiological artifacts to be cleaned or removed, structural abnormalities that needs to be taken into account during head modeling or the coverage of the head with sufficient number of electrodes and sensors. Some of these factors have been already discussed in **Section 2.6**. When using simulations for validation, it is also important to avoid the so-called inverse crime i.e. one should not produce simulated data with the same lead-field matrix used for the inversion. This topic has been discussed in details in (Kaipio and Somersalo, 2005) and will be considered in chapters 4 and 5.

3.4. Application of EEG and MEG source localization to clinical data

Whereas detailed evaluation within a fully controlled simulation environment is the first thing to investigate when proposing a new source localization method, in this next section, we will review the various aspects of source analysis of IEDs when applied on clinical data.

3.4.1. Averaged or single spike source analysis

A first and most crucial step of source analysis of IEDs is the spike detection phase. Detecting spikes not only depends on the morphology and signal-to-noise ratio, but also of the training and experience of the observer. Subsequently, the population of spikes should be grouped into distinct categories, which is generally performed on the basis of visual inspection by an EEG/MEG reviewer. Each single epileptic spike might also exhibit a low SNR condition, since they might be highly contaminated by background noise. Therefore, a common practice in source analysis is to average the time-locked spike signals in each group to increase the SNR of spike field maps, thus, allow for more accurate reconstruction of the sources (Bast et al., 2004; Hara et al., 2007; Tanaka et al., 2010). However, averaging effect is also likely to filter out source activities which are slightly variable over each individual spike. For instance, interictal spikes do not remain confined to a single neuronal population in a single cortical patch; rather, they propagate within milliseconds to involve cortical areas away from the initial generator (Alarcon et al., 1994; Baumgartner, Lindinger, et al., 1995; Emerson et al., 1995; Gotman, 2003; Zumsteg et al., 2006). This entails spatio-temporal source analysis of EEG and MEG data to detect and characterize possible propagation patterns associated to IEDs (Tanaka et al., 2010). Averaging these spikes exhibiting propagation patterns may enhance the overall signal-to-noise ratio but the differences in the origin between single spikes may get lost in the averaging process. Therefore, source localization of the single spikes seems more appropriate for detecting the onset and propagation patterns of IEDs while

creating a balance between taking into account inherent spike variability and the SNR (Hong et al., 2010; Tanaka et al., 2014). For this purpose, we chose to deal with single spike localizations in this thesis, in order to fully benefit from the complementarity of EEG and MEG recordings (chapters 4 and 5), while proposing a new method to assess the reliability and reproducibility of single spike source localization results by estimating a consensus map in chapter 6.

3.4.2. Performance of source localization methods applied to clinical data

The overall objective is the application of source localization approaches to clinical data and to evaluate how they behave in realistic configurations. As listed and described in **Section 3.2**, there exists several source localization and imaging approaches that have their advantages and limitations when it comes to localizing IEDs. In a special issue of Journal of Clinical Neurophysiology from 1999, a number of research groups (Fuchs et al., 1999; Michel et al., 1999; Scherg et al., 1999) analyzed the same epileptic data set to validate different EEG source imaging (MNE, wMNE, LORETA) and source localization approaches (dipole fitting and MUSIC). This systematic comparison led to the conclusion that each source localization approach had its limitations and failed under certain conditions, and that several distinct solutions were possible (Ebersole, 1999). They finally suggested that the use of several approaches is probably required to obtain reliable results in clinical practice. From a review on 25 clinical studies (until year 2008) of electromagnetic source imaging targeting epilepsy surgery (Leijten and Huiskamp, 2008), it was reported that 21 out of 25 studies performed single dipole fitting, whereas, only 6 studies also included MUSIC and distributed source imaging approaches. While rather simple compared to other available methods, dipole fitting is effective as demonstrated by clinical studies; suggesting that focal epileptic networks mostly localized in a confined volume can be adequately described by a single center of gravity. However, it is clear from the **Section 3.2**

that there exists more complex methods that seem more appropriate for describing spatially extended and dynamic networks involved during epileptic activity. Moreover, dSI approaches recovering the extent of the generators of epileptic activity seem the most suitable when targeting epilepsy surgery, although their efficacy and validity within a clinical context have yet to evaluated. A recent review by Tanaka and Stufflebeam (Tanaka and Stufflebeam, 2014) discussed the benefits and feasibility of dSI approaches compared to dipole fitting approach in the evaluation of epilepsy. Based on a recent European survey, the use of dSI methods has become more common in the different epilepsy surgery centers (Mouthaan et al., 2016). Note the cMEM method which is central in this PhD thesis has been extensively validated for source localization of IEDs on clinical data and has been compared with various other dSI approaches (Heers et al., 2014; Grova et al., 2016; Heers et al., 2016; Pellegrino et al., 2016a). cMEM provides overall robust, accurate and reproducible results, with the advantage of being sensitive to the spatial extent of the generator, while being robust to spurious distant secondary sources. In a recent study from our group (Pellegrino et al., 2016c), cMEM has been compared extensively with dipole fitting approach on a large cohort of patient data (340 different spikes types from 49 patients) to further assess the superior performance of cMEM method. This indicates that MEM-based method should definitely complement or even completely substitute dipole fitting in the daily clinical practice.

3.4.3. Validation of non-invasive source localization results

In order to further assess the clinical relevance of EEG or MEG source localization, several approaches have been considered such as qualitative or quantitative comparison of source localization results with iEEG findings, with resected brain volume and post-operative outcome, with visible structural abnormalities in MRI and sometimes its influence on the implantation strategy for intracranial electrodes. Many studies compared MEG source localization with data from Electro-CorticoGraphy (ECoG) confirmed satisfactory accuracy (Nakasato et al., 1994;

Oishi et al., 2002). Lower values of concordance were rarely described. Knowlton and colleagues prospectively compared localization accuracy of noninvasive epilepsy workup, namely MEG localization, ictal SPECT and PET, at a sublobar level with invasive EEG recording in 72 patients (Knowlton et al., 2008a; Knowlton et al., 2008b). They reported MEG localization sensitivity and specificity consistently better than those obtained for PET and SPECT. In addition, localization concordance with seizure onset zone was found to be 78% in patients with lateral temporal lobe epilepsy, 76% in those with mesial temporal lobe and 45% in patients with extra-temporal lobe epilepsy. Direct clinical impact was demonstrated by high success of surgery in patients with non-localized iEEG findings, where the decision was actually based on a combination of MEG, SPECT, and PET findings. Agirre-Arrizubieta and colleagues reported concordant MEG localization in 90% of lateral temporal spikes, 80% of inter-hemispheric and peri-central spikes, 60% of superior frontal spikes, 40% of orbitofrontal spikes, and 0% of mesial temporal spikes (Agirre-Arrizubieta et al., 2009). These findings suggest that MEG localization performs significantly better when the epileptic focus is not in the mesial temporal lobe, owing to the difficulties of MEG in recording and localizing deep sources within the mesial temporal lobe. Brodbeck and colleagues compared the accuracy of EEG source localization with post-surgical outcome on 55 patients (Brodbeck et al., 2011). The sensitivity of EEG source localization was 84% and its specificity 88%, suggesting good performances for both patients with temporal lobe epilepsy and extra temporal lobe epilepsy. They also showed that EEG localization performed at least as well, and often better, than structural MRI, PET and SPECT.

3.4.4. Spatial resolution of EEG and MEG

Spatial resolution of the EEG sensors influences the accuracy of source localization. It has been widely acknowledged that the spatial resolution of the 10–20 system is not sufficient for modern brain research (Gevins et al., 1994; Michel et al., 2004; Babiloni et al., 2009; Brodbeck et al., 2011; Yamazaki et al., 2012;

Lopes da Silva, 2013); since including only 21 coarsely sampled measurement electrodes only covers the top half of the head. The first step to improve the spatial resolution of EEG is then to increase the number of EEG electrodes. Electrode arrays that approximate the 10-10 system actually allows more accurate results (Ryynänen et al., 2004). In a study in which 128 channels of scalp EEG were progressively down-sampled to 64-32-21 channel recordings, Lantz et al. documented an improvement in source localization accuracy for up to 64 channels (Lantz and Grave de Peralta, 2003). In fact, adding more electrodes provided little additional accuracy because of the influence of other factors, such as the widely debated value of the skull's relative conductivity, which has a great impact on the accuracy of source localization. Additionally, the spatial resolution of dense array EEG systems (128–512 electrodes) is extremely sensitive to measurement noise (Gevins et al., 1994; Ryynänen et al., 2004; Malmivuo, 2012; Lopes da Silva, 2013). Lastly, some sensors might measure more artifacts than others due to their location near active muscles. Thus, for different EEG measurements conducted in different environments, the appropriate number of electrodes may vary considerably.

Based on combined EEG and MEG data analysis, several studies (Fuchs et al., 1998; Sharon et al., 2007) have indicated that the coverage of the whole head using dense sampling of EEG and MEG channels is required for obtaining good source localization accuracy. Most clinical centers commonly use the conventional 10-20 EEG system or a 10-10 EEG system. When EEG and MEG are recorded simultaneously, the set-up of 64 electrodes requires a long preparation time and can be a great discomfort for the subject wearing the EEG cap inside the MEG helmet. On the other hand, the large number (~300) of MEG sensors uniformly distributed around the whole head provides a dense spatial sampling and requires no preparation time for placing the head inside the helmet. MEG provides a higher spatial resolution than EEG not only due to an inherently more accurate forward model but, also the typically greater number of sensors used in MEG relative to EEG (Ossenblok et al., 2007; Klamer et al., 2015). However, a clinically relevant

point is the risk of misinterpretation of MEG data when no simultaneous EEG is analyzed. MEG and EEG sources reflect the different anatomical aspects of the activated source because of the different sensitivities of both modalities to the orientation of underlying neuronal currents (**Section 2.6.2**). There is no doubt that by analyzing combined EEG and MEG data we can already achieve dense spatial sampling with the large number of MEG sensors; and the addition of an appropriate number of EEG electrodes can bring the additional complementary information to complete the picture of the activated source. These aspects were specifically explored in this thesis using both simulations (chapter 4) and clinical data (chapter 6).

3.5. Combined EEG and MEG source analysis

As discussed previously, fusion of EEG and MEG can bring additional information from either modality due to their differential properties. The key differential properties are the effect of volume conduction (**Section 2.6.3** and **Section 3.1.2**), the detection rate of spikes owing to their sensitivity to the source orientation (**Section 2.6.2** and **Section 2.6.4**), and their spatial resolution owing to the dense spatial sampling of recording channels (**Section 3.4.4**). In general, fusion of multimodal data can be achieved through three possible integration strategies: 1) **Comparative integration** – both modalities are analyzed independently and then the results are compared (Bast et al., 2007; Kirsch et al., 2007), 2) **Constrained integration** – one modality is used to analyze the other one (Grova et al., 2008; Henson, 2010; Ou et al., 2010), and 3) **Symmetrical integration** – Jointly analyze the data of different modalities using multimodal generative models (Fuchs et al., 1998; Molins et al., 2008; Ding and Yuan, 2013; Hong et al., 2013). In the context of this thesis, since EEG and MEG relate to the same neuronal dynamics when acquired simultaneously (Molins et al., 2008), we were interested in the symmetrical integration which allows for a full integration, or fusion of EEG and MEG data. This type of fusion entails inverting a single "generative" model that explains both types of data. This model must relate the same hypothetical neuronal

causes (e.g., time courses of neuronal activity in circumscribed brain regions) to each type of data, using modality-specific "forward models". Therefore, the fusion generative model can be written as,

$$\begin{bmatrix} \boldsymbol{M}^{s}_{EEG} \\ \boldsymbol{M}^{s}_{MEG} \end{bmatrix} = \begin{bmatrix} \boldsymbol{G}^{s}_{EEG} \\ \boldsymbol{G}^{s}_{MEG} \end{bmatrix} \boldsymbol{J} + \begin{bmatrix} \boldsymbol{E}^{s}_{EEG} \\ \boldsymbol{E}^{s}_{MEG} \end{bmatrix} \tag{3-35}$$

where the concatenation of $\boldsymbol{G}_{EEG}$ (the EEG lead field matrix) and $\boldsymbol{G}_{MEG}$ (the MEG lead field matrix) gives the combined EEG+MEG lead field matrix, $\boldsymbol{J}$ is the unknown current density matrix, $\boldsymbol{M}_{EEG}$ and $\boldsymbol{M}_{MEG}$ are the observed EEG data and MEG data, while $\boldsymbol{E}_{EEG}$ and $\boldsymbol{E}_{MEG}$ are the EEG and MEG additive measurement noise. The different measurement units and scales of EEG and MEG (Volts and Tesla respectively) and the different sensor noise levels require the normalization of the data before they may be used jointly for source estimation within a fusion framework. The different measures have to be transformed to a common basis and this can be done by referencing each sensor to its individual noise statistics (Baumgartner, Deecke, et al., 1995). One method to automatically determine the noise level of each sensor is to use the standard deviation of measurement noise (Fuchs et al., 1998; Henson, 2010; Ding and Yuan, 2013). This normalization method is named the SNR transformation (Pflieger et al., 2000). Note that the superscript "s" in equation (3-34) represents the normalized data, lead field matrices and noise.

Several studies have suggested the added value of combining EEG and MEG data during source analysis (Yoshinaga, 2002; Pataraia et al., 2005; Bast et al., 2007; Ebersole and Ebersole, 2010). It has also been shown that simultaneous EEG and MEG recordings are super additive, i.e. they provide more information that is relevant to source localization of combined EEG and MEG data than the sum of both monomodal information. Several fusion strategies have been proposed to evaluate the advantage of combining EEG and MEG data using different inverse operators such as the dipole fitting approach (Fuchs et al., 1998; Huang et al., 2007), LCMV beamformer approach (Hong et al., 2013), MNE and dSPM (Liu et al.,

2002; Sharon et al., 2007; Molins et al., 2008), VB-SCCD (Ding and Yuan, 2013) and Multiple Sparse Prior method (Henson et al., 2009b). Most of these EEG/MEG fusion approaches differed in the way data were normalized and concatenated before applying the inverse operator. Some of the proposed methods consist in channel-wise SNR transformation (Fuchs et al., 1998), incorporation of intermodal noise covariance (Ko and Jun, 2010), minimization of mutual information for channel selectivity (Baillet et al., 1999), row normalization of lead-field matrices, weighted normalization (Hong et al., 2013), and integration within a Bayesian framework (Henson et al., 2009b). It is important to emphasize that none of these fusion approaches were designed or evaluated for the localization of spatially extended generators of epileptic activity, which is the main purpose of this thesis.

In this thesis, we proposed to combine EEG and MEG data within cMEM framework to take advantage of its excellent localization accuracy and its sensitivity to the spatial extent of the generators of underlying epileptic activity. An originality of fusion within the MEM framework is that it has the flexibility to incorporate the complementary information provided by EEG and MEG through the prior model. Consequently, MEM fusion will be driven not only by the symmetrically concatenated EEG and MEG data, but also by the fusion prior model per se. More details on this fusion approach can be found in chapter 4.

3.6. Conclusion

In this chapter, the reader was introduced to the different aspects of source localization methods. In the context of source localization of IEDs, we will be focusing on distributed source imaging approaches, and specifically, cMEM method, which has been established for its ability to localize the spatially extended generators of epileptic activity. Since the main goal of this thesis is to propose and validate an EEG-MEG fusion approach within the MEM framework, we have compared its performance with other distributed source imaging approaches such as MNE, dSPM, sLORETA and 4-ExSo-MUSIC. We have also pointed out that

averaging spikes before source localization can lead to loss of information due to variability exhibited by individual spikes. In order to detect the onset and propagation patterns of IEDs, it is recommended to perform single spike localization. It is also important to emphasize that when combining EEG and MEG data, we can achieve whole head coverage with the densely sampled MEG sensors and addition of an appropriate number of EEG electrodes can bring additional complementary information relevant for promoting accurate source reconstructions.

Chapter 4 Manuscript 1: MEG-EEG information fusion and electromagnetic source imaging: from theory to clinical application in epilepsy

4.1. Context

Detection and source analysis of IEDs is widely used in pre-surgical evaluation of patients with intractable epilepsy. As outlined in the previous chapters, EEG and MEG records the same neuronal dynamics with high temporal resolution, but due to the differences in their sensitivity, to the orientations of the sources notably, some epileptic spikes are visible only on EEG and some only on MEG, in addition to the ones that are visible on both EEG and MEG. Following this, the added value of combining EEG and MEG data during source analysis has been suggested in several other studies, but none has been designed or evaluated for the localization of spatially extended generators of epileptic activity. As outlined in chapter 4, cMEM source localization algorithm has been well-established and carefully evaluated for its ability to recover these spatially extended generators with excellent accuracy. Therefore, in this dissertation, we proposed the development of an optimal EEG-MEG fusion approach using the cMEM framework to efficiently fuse the complementary information brought by EEG and MEG data, to reach dense sampling of recording channels, and to achieve sensitivity to the location and spatial extent of the sources. The following manuscript describes the development and validation of this fusion approach for its ability to localize the generators of IEDs, their spatial extent and propagation patterns. In case of epilepsy data, which are spontaneous events, usually there is no clear gold standard to validate the behavior of the source localization algorithm. Therefore, as a first step of this dissertation, this manuscript includes the evaluation of the properties of the fusion strategy using

well-controlled simulation models mimicking spatially extended generators and propagation patterns. This manuscript also investigated the impact of combining only few EEG electrodes with the whole head covered MEG sensors within the EEG-MEG fusion framework.

The manuscript was published as (Chowdhury R. A.**,** Zerouali Y., Hedrich T., Heers M., Kobayashi E., Lina J.M., Grova C. *MEG–EEG Information Fusion and Electromagnetic Source Imaging: From Theory to Clinical Application in Epilepsy*, Brain Topography, 2015 May 28, DOI: 10.1007/s10548–015–0437–3)

4.2. Abstract

The purpose of this study is to develop and quantitatively assess whether fusion of EEG and MEG (MEEG) data within the Maximum Entropy on the Mean (MEM) framework increases the spatial accuracy of source localization, by yielding better recovery of the spatial extent and propagation pathway of the underlying generators of Interictal Epileptic Discharges (IEDs). The key element in this study is the integration of the complementary information from EEG and MEG data within the MEM framework. MEEG was compared with EEG and MEG when localizing single transient IEDs.

The fusion approach was evaluated using realistic simulation models involving one or two spatially extended sources mimicking propagation patterns of IEDs. We also assessed the impact of the number of EEG electrodes required for an efficient EEG-MEG fusion. MEM was compared with Minimum Norm Estimate (MNE), dynamic Statistical Parametric Mapping (dSPM), and standardized low-resolution electromagnetic tomography (sLORETA). The fusion approach was finally assessed on real epileptic data recorded from two patients showing IEDs simultaneously in EEG and MEG.

Overall the localization of MEEG data using MEM provided better recovery of the source spatial extent, more sensitivity to the source depth and more accurate

detection of the onset and propagation of IEDs than EEG or MEG alone. MEM was more accurate than the other methods. MEEG proved more robust than EEG and MEG for single IED localization in low signal-to-noise ratio conditions. We also showed that only few EEG electrodes are required to bring additional relevant information to MEG during MEM fusion.

4.3. Introduction

A successful pre-surgical evaluation in epilepsy entails the accurate detection of the onset of epileptic discharges, their spatial extent and propagation patterns (Stefan, 2009; Tanaka and Stufflebeam, 2014). Interictal Epileptic Discharges (IEDs), occurring between seizures in epilepsy, are commonly used as markers of epilepsy (Staley and Dudek, 2006). These are spontaneous transient activities that are clearly distinguishable from background activity. The high temporal resolution of Electro-Encephalography (EEG) and Magneto-Encephalography (MEG) allows the detection of the fast propagating IEDs more efficiently than other imaging techniques (Stefan, 2009; Ebersole and Ebersole, 2010). MEG can detect epileptic activity from background activities when a cortical area greater than 4 cm^2 is synchronously involved (Mikuni et al., 1997). EEG requires the activation of a larger region of the cortex (at least 10 cm^2) to detect epileptic activity on the scalp recordings (Ebersole, 1997a; Tao, Baldwin, Hawes-Ebersole, et al., 2007; von Ellenrieder et al., 2014b). Source analysis of EEG and MEG data is commonly used to localize the generators of brain activities that are detectable on the scalp (Stefan et al., 2003; Knowlton and Shih, 2004; Noachtar and Rémi, 2009; Wendel et al., 2009). Spatio-temporal source analysis of EEG and MEG data may be useful for accurate detection and estimation of propagation patterns of epileptic discharges (Tanaka et al., 2010, 2014). In order to detect the onset and propagation patterns of IEDs, source localization of single spike is more appropriate than averaged spike. Indeed, averaging spikes may enhance the signal-to-noise ratio but the differences in the origin between single spikes may get lost in the averaging process (Bast et al., 2004, 2006). EEG and MEG are sensitive to different aspects of neuronal

activity (Cohen and Cuffin, 1983; Sutherling et al., 1987; Hämäläinen et al., 1993; Baumgartner and Pataraia, 2006; Funke et al., 2009; Yu et al., 2010; Haueisen et al., 2012). Integrating these two modalities can bring in complementary information thereby allowing better accuracy in source imaging. Symmetrical fusion of EEG and MEG data is possible since the two modalities can relate to the same neuronal dynamics (temporal information) when acquired simultaneously (Molins et al., 2008).

Several studies have reported the added value of combining the complementarities of EEG and MEG data when performing source localization. These so-called EEG-MEG fusion methods allow improving the spatial resolution of source analysis by increasing the number of recording channels (EEG electrodes + MEG sensors) and the overall head surface coverage. Using single Equivalent Current Dipole (ECD) approach on simulated EEG/MEG and electrical median nerve stimulation data, Fuchs et al., 1998 suggested that deep sources mainly contribute to EEG data while superficial and tangential sources contribute mainly to MEG data. (Baillet et al., 1999) proposed a joint EEG/MEG analysis, aiming at minimizing the mutual information between the two modalities, thus enhancing their respective complementarities. This EEG/MEG fusion strategy demonstrated reduced sensitivity to noise and improved localization accuracy. Using L2-based Minimum Norm Estimate (MNE) and its variants, such as dynamic Statistical Parametric Mapping (dSPM), several studies demonstrated the added value of fusing EEG/MEG data using either simulated data (Liu et al., 2002), visual evoked responses (Sharon et al., 2007) and electrical median nerve stimulation (Molins et al., 2008). The advantage of combining EEG and MEG data was also evaluated using other inverse operators, such as sparse source reconstruction (Ding and Yuan, 2013) on simulated data, linearly constrained minimum variance beamformer approach on simulated and auditory data (Hong et al., 2013) or Multiple Sparse Prior methods on face evoked responses (Henson et al., 2009b). However, to the best of our knowledge, there exists no prior study that performed source analysis

using EEG/MEG fusion data to optimize the source localization of spatially extended generators of propagating epileptic discharges.

ECD solutions have been extensively used for localizing the sources of focal interictal spikes but distributed source localization methods are ideal for estimating distributed network of brain activity seen during most IEDs (Barkley and Baumgartner, 2003; Kobayashi et al., 2005). Some of the well-known and widely used distributed methods are MNE (Hämäläinen and Ilmoniemi, 1994) and Low Resolution Electromagnetic Tomography (LORETA) (Pascual-Marqui et al., 1994). We proposed the Maximum Entropy on the Mean (MEM) (Amblard et al., 2004) as an interesting framework with good sensitivity in recovering the spatial extent of the sources, when using simulated EEG data (Grova et al., 2006), simulated MEG data (Chowdhury et al., 2013; Lina et al., 2014), when comparing EEG/MEG sources to fMRI BOLD responses to epileptic discharges (Grova et al., 2008; Heers et al., 2014) and when comparing EEG/MEG sources to intracranial EEG findings (Heers et al., 2015). When applied to EEG or MEG data, MEM proved to be more accurate in recovering the source spatial extent, than MNE, LORETA and their variants within the hierarchical Bayesian framework (Friston et al., 2008). Therefore, the purpose of this study is to assess whether symmetrical fusion of EEG and MEG data within the MEM framework increases the spatial accuracy of the localization, by yielding better recovery of the spatial extent and propagation patterns of the underlying generators of epileptic discharges.

4.4. Methods and Materials

4.4.1. EEG-MEG inverse problem using distributed sources

The EEG-MEG inverse solution presented in this study uses a distributed source model where a large number of dipolar sources are distributed along the cortical surface. Considering the anatomical constraint that the orientation of each dipole is fixed perpendicular to the local cortical surface (Dale and Sereno, 1993), the linear relationship between the source amplitude and the data is given by:

$$\boldsymbol{M} = \boldsymbol{GJ} + \boldsymbol{E} \qquad (4\text{-}1)$$

where $\boldsymbol{M}$ is the ($q \times \tau$) signal matrix acquired on q EEG or MEG channels at τ time samples. $\boldsymbol{E}$ models an additive measurement noise (($q \times \tau$) matrix). $\boldsymbol{J}$ is ($r \times \tau$) unknown matrix of the current intensity of the p dipolar sources along the tessellated cortical surface. $\boldsymbol{G}$ is the ($q \times r$) lead field matrix obtained by solving the forward problem i.e. by estimating the contribution of each unit dipolar source on the sensors (Hallez et al., 2007).

4.4.2. Maximum Entropy on the Mean (MEM) Framework

To regularize the ill-posed inverse problem, the MEM framework incorporates prior information on **J** in the form of a reference distribution $d\nu(\mathbf{j})$. This reference distribution is a realistic spatial model that assumes brain activity to be organized into K ($K << r$) cortical parcels showing homogenous activation states. This type of spatial clustering into K parcels (**Figure 4.1a**) was obtained using a Data Driven Parcellization (DDP) technique (Lapalme et al., 2006). To do so, first a projection method, namely the Multivariate Source Pre-localization (MSP) (Mattout et al., 2005) was applied to estimate a probability-like coefficient (MSP score) between 0 and 1 for each dipolar source on the cortical mesh, characterizing its contribution to the data. Then, using a region growing algorithm starting from the local optima of the MSP map, a parcellization of the full cortical surface into K non-overlapping parcels was estimated (see (Chowdhury et al., 2013) for further details).

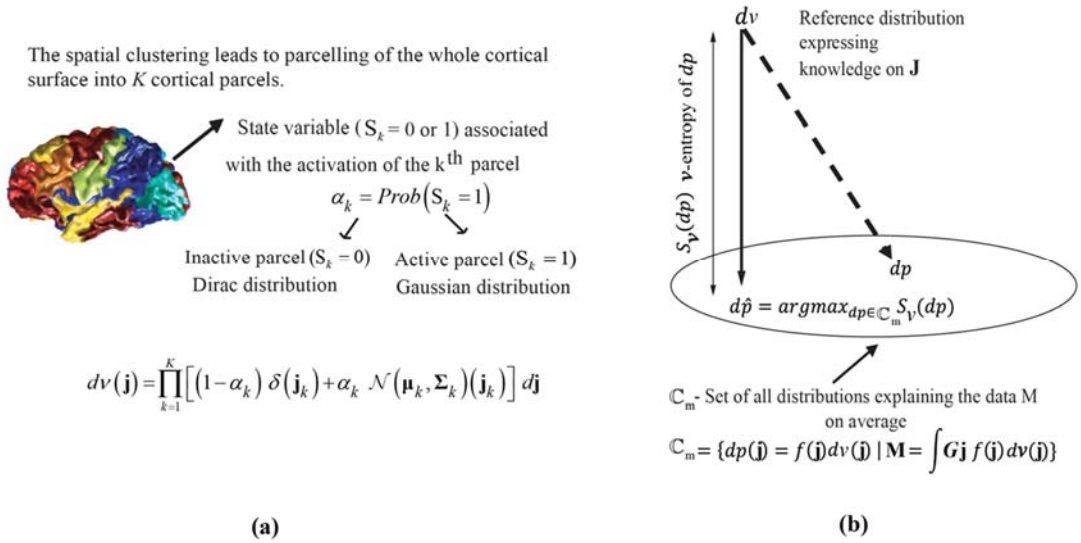

Figure 4.1. Maximum Entropy on the Mean (MEM) framework. (**a**) MEM initialization of the reference distribution dv: spatial clustering model that assumes brain activity to be organized into K cortical parcels showing homogenous activation state. This type of spatial clustering is obtained using data driven parcellization technique. After the definition of the state variable of the parcel, this dv will be used to regularize the inverse problem. (**b**) MEM regularization algorithm: $\mathbb{C}_m$ represents the set of all the probability densities dp that satisfy the data goodnes of fit . Given the prior information on $\mathbf{J}$ in the form of reference distribution dv , the relative ν-entropy ($S_V(dp)$) measures the amount of information brought by the data **M**, with respect to the reference distribution $dv(\mathbf{j})$.

Starting from this DDP, the reference distribution was modelled as follows:

$$dv(\mathbf{j}) = \prod_{k=1}^{K} \left[(1-\alpha_k)\, \delta(\mathbf{j}_k) + \alpha_k\, \mathcal{N}(\boldsymbol{\mu}_k, \boldsymbol{\Sigma}_k)(\mathbf{j}_k) \right] d\mathbf{j} \qquad (4\text{-}2)$$

Each cortical parcel *k*, assumed to be independent from the others, is characterized by an activation state S_k, describing if the parcel is active $(S_k = 1)$ or not $(S_k = 0)$. $\alpha_k = Prob(S_k = 1)$ is the probability of the k^{th} parcel to be active, which was initialized as the median of the MSP scores of the dipoles within the corresponding parcel. When the parcel is active $(S_k = 1)$, the dipole intensities within the k^{th} parcel are modeled using a Gaussian distribution $\mathcal{N}(\boldsymbol{\mu}_k, \boldsymbol{\Sigma}_k)$ where $\boldsymbol{\mu}_k$ and $\boldsymbol{\Sigma}_k$

represent respectively the mean and the covariance of the p_k dipoles within the k^{th} parcel. When the parcel is inactive $(S_k = 0)$, the dipole intensities are modeled using a Dirac distribution δ, thus allowing to "shut down" the corresponding parcel.

Within the MEM framework, we consider the amplitude of the sources $\mathbf{J}$ to be estimated as a multivariate random variable described by a probability distribution $dp(\mathbf{j}) = f(\mathbf{j})d\nu(\mathbf{j})$, where f is a ν-density of dp. Given the prior information on $\mathbf{J}$ in the form of reference distribution $d\nu$, the relative ν-entropy ($S_\nu(dp)$) measures the amount of information brought by the data, with respect to the reference distribution $d\nu(\mathbf{j})$ (Amblard et al., 2004). Defining $\mathbb{C}_m$ as the set of probability measures on $\mathbf{J}$ that explains the data, $\mathbf{M} = \int \boldsymbol{G}\mathbf{j}\, f(\mathbf{j})d\nu(\mathbf{j})$, on average (see **Figure 4.1b**), the MEM solution consists in selecting $d\hat{p}$ that maximizes the ν-entropy and is the closest distribution to the reference distribution $d\nu$:

$$d\hat{p} = \arg\max_{dp \in C_M} S_\nu(dp) \tag{4-3}$$

under the constraints: $\mathbf{M} - \boldsymbol{G}\mathrm{E}_{dp}[\mathbf{J}] = 0$ and $\int dp(\mathbf{j}) = 1$, where $\mathrm{E}_{dp}[\mathbf{J}] = \int \mathbf{j} dp(\mathbf{j})$.

The MEM estimate of the source intensities $\hat{\mathbf{J}}$ is then found to be the expected value of the distribution $d\hat{p}$:

$$\hat{\mathbf{J}} = \mathrm{E}_{d\hat{p}}[\mathbf{J}] \tag{4-4}$$

Such a regularization framework allows estimating the MEM solution through the optimization of a convex function within a q dimensional space, iteratively for each time sample. During the MEM optimization process, a noise covariance model is considered which is estimated as a diagonal matrix with a different value for each channel; thus taking into account the noise levels of each individual channel. For details on the MEM formulation, please refer to (Chowdhury et al., 2013).

In the present study, we will consider the coherent-MEM (cMEM) implementation, as described in (Chowdhury et al., 2013). In cMEM, additional constraint of local spatial smoothness in each parcel was introduced using diffusion-based spatial priors (Friston et al., 2008) in the initialization of the source covariance of every parcel ($\mathbf{\Sigma}_k$). The mean intensity of every parcel ($\boldsymbol{\mu}_k$) was initialized to zero. The spatial neighborhood order considered during the region growing procedure (cluster scale) has been fixed to a scale of 4, leading to approximately *K*=200 parcels of size ≈2.5 cm^2.

4.4.3. Multimodal EEG-MEG fusion within the MEM framework

The proposed EEG-MEG fusion within MEM framework consists of a 3-step fusion process, summarized in **Figure 4.2**:

Step 1. Normalization and concatenation of the data and lead field matrices from the two modalities. In order to integrate the two modalities, it is important to scale them to a common basis since they have different units and orders of magnitude. To do so, we applied a global mean signal to noise ratio (SNR) transformation of the data and the lead field, as described in (Fuchs et al., 1998) and (Ding and Yuan, 2013). This SNR transformation consisted in estimating normalized dimensionless measures of EEG and MEG, using the mean standard deviation of some baseline data. Baseline data ($\boldsymbol{E}_{EEG}$ and $\boldsymbol{E}_{MEG}$) consisted of real EEG and MEG background segments with the same duration (τ) as the data of interest ***M*** and exhibiting no epileptic discharges.

$$\sigma_*(i) = \sqrt{\frac{\sum_{t=1}^{\tau}(E_*(i,t) - \bar{E}_*(i))^2}{\tau - 1}} \text{ with } \bar{E}_*(i) = \frac{1}{\tau}\sum_{t=1}^{\tau} E_*(i,t) \tag{4-5}$$

where * refers to EEG or MEG, *i* is the index of the EEG or MEG channels, and *t* is the index of the τ time samples.

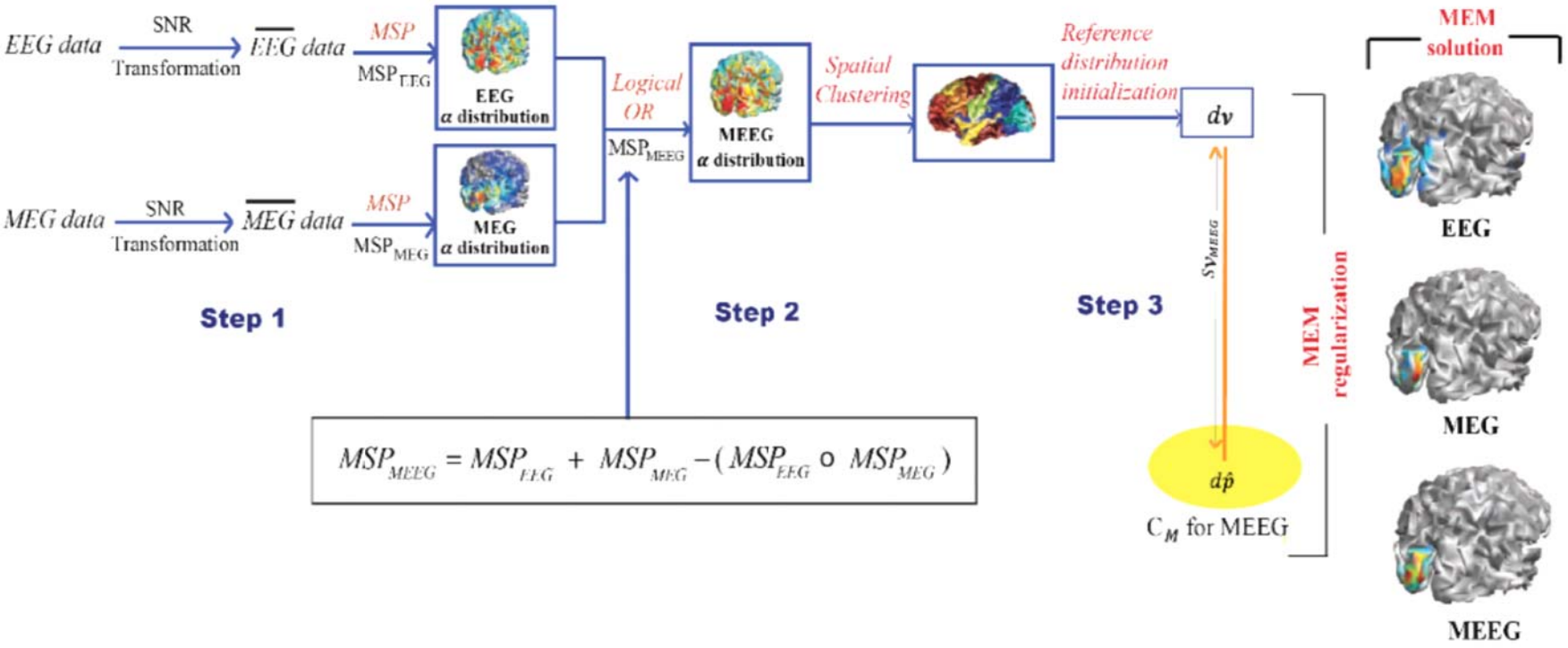

Figure 4.2. Multimodal EEG-MEG data fusion within the MEM framework. Step 1: Normalization and concatenation of the data and lead field matrices from the two modalities**.** Step 2: Parcellization of the cortical surface using the fusion of MSP scores (MSP_{MEEG}). Step 3: Initialization of the probability of activation of each parcel using MSP_{MEEG} and MEM regularization.

The mean standard deviation of the baseline over all sensors was then estimated as follows:

$$\overline{\sigma}_* = \frac{\sum_{i=1}^{q}(\sigma_*(i))}{q_*} \tag{4-6}$$

where q_* is the number of EEG or MEG channels. The SNR transformation consisted in scaling the data and lead field matrices as follows:

$$\mathbf{M}_*^S = \mathbf{M}_* \Big/ \overline{\sigma}_* \tag{4-7}$$

$$\mathbf{G}_*^S = \mathbf{G}_* \Big/ \overline{\sigma}_* \tag{4-8}$$

Based on the scaled data and lead field matrices, the EEG-MEG fusion could be formalized using the following concatenation along the rows of the matrices (Fuchs et al., 1998; Henson et al., 2009b; Ding and Yuan, 2013):

$$\begin{bmatrix} \boldsymbol{M}_{EEG}^s \\ \boldsymbol{M}_{MEG}^s \end{bmatrix} = \begin{bmatrix} \boldsymbol{G}_{EEG}^s \\ \boldsymbol{G}_{MEG}^s \end{bmatrix} \boldsymbol{J} + \begin{bmatrix} \boldsymbol{E}_{EEG}^s \\ \boldsymbol{E}_{MEG}^s \end{bmatrix} \tag{4-9}$$

Where ($\boldsymbol{E}_{EEG}^s$ and $\boldsymbol{E}_{MEG}^s$) refer to the scaled noise matrices. The symmetrical fusion of EEG and MEG will be further denoted by MEEG.

Step 2. Parcellization of the cortical surface using the fusion of MSP scores ($\boldsymbol{MSP}_{MEEG}$). An originality of the MEM framework is to incorporate the complementary information provided by EEG and MEG through the reference distribution *d*v. To do so, MSP scores were first computed from each modality separately ($\boldsymbol{MSP}_{EEG}$ and $\boldsymbol{MSP}_{MEG}$), to assign for each modality a coefficient of activation of the sources. MSP was actually applied on a singular value decomposition of the scaled data:

$$\boldsymbol{M}_*^s = \boldsymbol{U}_*\boldsymbol{Y}_*\boldsymbol{V}_*^{\mathrm{T}}, \text{ where } * = \text{EEG or MEG} \tag{4-10}$$

where $\boldsymbol{U}_*$ is an orthogonal $q \times q$ matrix in which the l^{th} column vector is the sensor signature of the l^{th} component. $\boldsymbol{V}_*$ is an orthogonal $\tau \times \tau$ matrix, $\boldsymbol{V}_*^{\mathrm{T}}$ denotes the transpose of $\boldsymbol{V}_*$. $\boldsymbol{Y}_*$ is an $q \times \tau$ matrix whose diagonal contains the singular values of $\boldsymbol{M}_*^{\mathrm{s}}$. With a selection of l functionally informed vectors $\boldsymbol{U}_*$, MSP scores were quantified by projecting the normalized lead field $\overline{\boldsymbol{G}}_*$ onto the normalized data $\overline{\boldsymbol{U}}_*$ (normalization by the norm of each column).

$$\boldsymbol{MSP}_* = \mathrm{diag}(\overline{\boldsymbol{G}}_*^{\mathrm{s}\,\mathrm{T}} \overline{\boldsymbol{U}}_* \overline{\boldsymbol{U}}_*^{\mathrm{T}} \overline{\boldsymbol{G}}_*^{\mathrm{s}}) \text{ where } * = \text{EEG or MEG} \tag{4-11}$$

With such a projection $\boldsymbol{MSP}_{EEG}$ or $\boldsymbol{MSP}_{MEG}$ scores estimated a probability-like coefficient assessing the contribution of each dipolar source to the corresponding EEG and MEG data. A second level of EEG/MEG fusion was then introduced, using a logical OR operation ($\vee$) on $\boldsymbol{MSP}_{EEG}$ and $\boldsymbol{MSP}_{MEG}$ scores, in order to taken into account the contribution of the dipolar sources either to EEG or MEG or both data.

$$\begin{aligned} \boldsymbol{MSP}_{MEEG} &= \boldsymbol{MSP}_{EEG} \vee \boldsymbol{MSP}_{MEG} \\ &= \boldsymbol{MSP}_{EEG} + \boldsymbol{MSP}_{MEG} - (\boldsymbol{MSP}_{EEG} \circ \boldsymbol{MSP}_{MEG}) \end{aligned} \tag{4-12}$$

where $\circ$ denotes the Schur (Hadamard) product of the two matrices leading to element-wise multiplication of their elements. DDP was then applied using these fused MSP scores ($\boldsymbol{MSP}_{MEEG}$) in order to obtain parcellization of the full cortical surface driven by information provided by MEEG fusion data.

Step 3. Initialization of the probability of activation of each parcel α_k using $\boldsymbol{MSP}_{MEEG}$. Given the parcellization obtained in **Step 2**, we then considered a 3rd level of the EEG/MEG fusion by using the median of the fused MSP scores ($\boldsymbol{MSP}_{MEEG}$) within the k^{th} parcel to initialize α_k i.e. the probability of each parcel to be active (cf. **Section 4.4.2**, equation (4-2)).

This three-level fusion scheme was proposed to integrate the complementary information provided by both modalities within the MEM framework. Then starting from the initialized reference model *dv* estimated from fused MEEG data, MEM regularization was used to find a solution from SNR-transformed concatenated MEEG data, as illustrated in **Figure 4.2**.

4.4.4. Minimum Norm Estimate and other variants with L-curve method

In the present study, we will compare the performance of cMEM with MNE method and two noise-normalized variants of MNE - dynamic statistical parametric mapping (dSPM) (Dale et al., 2000) and standardized low-resolution electromagnetic tomography (sLORETA) (Pascual-Marqui, 2002).

(a) MNE: With the assumption that all sources are independent and have same energy, MNE solution ($\hat{\boldsymbol{J}}_{MNE}$) provides the minimum energy of the current distribution $\boldsymbol{J}$ (Dale and Sereno, 1993; Hämäläinen and Ilmoniemi, 1994). The L-curve method (Hansen, 2000) was used to estimate the regularization hyper-parameter (λ), allowing the best balance between data fit ($\|\boldsymbol{M} - \boldsymbol{GJ}\|^2$) and the a priori constraint ($\|\boldsymbol{J}\|^2$), within the following optimization scheme:

$$\begin{aligned}\hat{\boldsymbol{J}}_{MNE} &= \operatorname{argmin}_J\left(\|\boldsymbol{M} - \boldsymbol{GJ}\|^2 + \lambda\|\boldsymbol{J}\|^2\right) \\ &= \left(\tilde{\boldsymbol{G}}^{\mathrm{T}}\boldsymbol{\Sigma}_d\tilde{\boldsymbol{G}} + \lambda\boldsymbol{\Sigma}_s\right)^{-1}\tilde{\boldsymbol{G}}^{\mathrm{T}}\boldsymbol{\Sigma}_d\tilde{\boldsymbol{M}} = \tilde{\boldsymbol{W}}_{MNE}\tilde{\boldsymbol{M}}\end{aligned} \tag{4-13}$$

where, $\tilde{\boldsymbol{M}} = \boldsymbol{\Sigma}_d^{-1/2}\tilde{\boldsymbol{M}}$ and $\tilde{\boldsymbol{G}} = \boldsymbol{\Sigma}_d^{-1/2}\boldsymbol{G}$ are the spatially whitened data and gain matrices, respectively. $\tilde{\boldsymbol{W}}_{MNE}$ is the classical MNE inverse operator with $\boldsymbol{\Sigma}_s$ as the identity source covariance matrix and $\boldsymbol{\Sigma}_d$ as the diagonal noise covariance matrix of the whitened data resulting in an identity matrix. In order to evaluate EEG/MEG fusion using MNE, data were normalized as in equation (4-7) and (4-8), spatially

pre-whitened and concatenated as in equation (4-9), and MNE was then directly applied to concatenated matrices.

Both dSPM and sLORETA are derived from $\widetilde{\boldsymbol{W}}_{MNE}$ by normalizing the rows of the inverse operator.

(b) dSPM (Dale et al., 2000): The estimated current at each source location is divided by an estimate of the noise at that location, which can be obtained by applying $\widetilde{\boldsymbol{W}}_{MNE}$ to the signal covariance matrix as follows:

$$\begin{aligned} \widetilde{\boldsymbol{W}}_{dSPM} &= \left(\sqrt{diag(\widetilde{\boldsymbol{W}}_{MNE} \boldsymbol{\Sigma}_d \widetilde{\boldsymbol{W}}_{MNE}^{\mathrm{T}})} \right)^{-1} \widetilde{\boldsymbol{W}}_{MNE} \\ \hat{\boldsymbol{J}}_{dSPM} &= \widetilde{\boldsymbol{W}}_{dSPM} \boldsymbol{M} \end{aligned} \tag{4-14}$$

(c) sLORETA (Pascual-Marqui, 2002): consists in a similar approach, but the normalization is obtained from the variance of the estimated sources, instead of using just the variance due to the noise component.

$$\begin{aligned} \widetilde{\boldsymbol{W}}_{sLORETA} &= \left(\sqrt{diag(\widetilde{\boldsymbol{W}}_{MNE} (\boldsymbol{G}\boldsymbol{G}^{\mathrm{T}} + \boldsymbol{\Sigma}_d) \widetilde{\boldsymbol{W}}_{MNE}^{\mathrm{T}})} \right)^{-1} \widetilde{\boldsymbol{W}}_{MNE} \\ \hat{\boldsymbol{J}}_{sLORETA} &= \widetilde{\boldsymbol{W}}_{sLORETA} \boldsymbol{M} \end{aligned} \tag{4-15}$$

Whereas MNE localization is biased towards more superficial sources, dSPM and sLORETA actually implicitly perform some "depth weighting" because of the noise normalization—sources with generally higher amplitude will be normalized by higher noise levels or source variances (Hauk et al., 2011).

4.4.5. Evaluation procedure

The proposed MEM fusion approach was evaluated in a well-controlled environment using realistic simulations of EEG and MEG interictal epileptic spikes. The geometry and the anatomy of our simulation environment were derived from a real patient's dataset.

a. Realistic simulations

Geometry dataset. Simultaneous EEG/MEG acquisition was performed on a patient with focal epilepsy using a 275 channel CTF-MEG system (272 active sensors) and a 54 channel EEG-cap (Easy-cap, Herrsching, Germany) at a sampling rate of 1200Hz. The 54 EEG electrodes were placed according to the 10-20 system with additional electrodes according to the 10-10 system especially covering the inferior temporal and parietal regions (FT9, P9, FT10, and P10). Written informed consent for this study was obtained from the patient. EEG and MEG data containing no traces of IEDs were recorded from this patient, which was used in the simulation model to create realistic noise.

Anatomy dataset. A high resolution T1-weighted anatomical MRI of the same patient was used to segment the surfaces of the brain to obtain a realistic head model. The distributed source model was obtained by segmenting the gray-white matter interface from the MRI using BrainVISA-4.2.1 software[7] (Mangin et al., 1995). The source model consisted in a realistic 3D mesh of the cortical surface (8000 vertices, 4mm resolution). Using the OpenMEEG (Gramfort et al., 2011) implementation in Brainstorm software (Tadel et al., 2011), we generated a 3-layer EEG Boundary Element Method (BEM) model consisting of the inner skull, outer skull and the scalp (conductivity values of 0.33:0.0165:0.33 S/m) and a 1-layer MEG BEM model consisting of the inner skull (conductivity value of 0.33 S/m).

Static simulation model. These simulations were similar to the ones considered in (Chowdhury et al., 2013). 100 simulation configurations involving one spatially extended source exhibiting spiking activity were randomly generated on the cortical mesh. The position of each source was selected by choosing a seed point randomly on the cortical surface mesh. The spatial extent of each source was obtained by region growing around the seed following the cortical surface using spatial

[7] http://www.brainvisa.info

neighborhood order s_e=3 (≈ 4 cm^2) and s_e =4 (≈ 12 cm^2). The time course of the simulated sources was the time course of an epileptic spike modeled with three Gamma functions, although only signal around the main peak of the spike was analyzed. Let us refer ***Jth*** as the simulated theoretical current distribution obtained from the spatial distribution of the simulated sources together with the corresponding time course. EEG and MEG data were then simulated by applying the forward model $\boldsymbol{G}_{\text{EEG}}$ and $\boldsymbol{G}_{\text{MEG}}$ to the simulated current density, respectively. Realistic physiological noise was extracted from a 3 mins segment of EEG/MEG background activity acquired on the selected patient and added to the simulated data. The amplitude of the background activity trials was scaled to ensure a signal-to-background ratio of 1 (0 dB) for most superficial sources when using reference source amplitude of 9.5 nA.m for each dipolar source along a patch of 6 cm^2. Consequently, the SNR of the realistic simulated data varied depending upon the location and extent of the underlying sources. In this set of 100 simulations, the SNR ranged approximately between 1 to 12. Note that as opposed to our previous study (Chowdhury et al., 2013), here only 1 trial of background EEG/MEG data was used in the simulations, thus mimicking the occurrence of single non-averaged spikes.

We considered the following indicators to characterize the simulations:

1. *Eccentricity* - Eccentricity is defined as the mean Euclidean distance between all vertices of the simulated patch and the center of the head model[8]. Most superficial sources had an eccentricity value higher than 80 mm. Sources with eccentricity ranging between 60 mm and 80 mm corresponded mainly to

[8] The center of head was defined with the fiducial points marked during EEG/MEG acquisition. It is the point which is equidistant to the left and right peri-auricular points, at the same height of the location of the nasion.

mesio-temporal sources and the ones with eccentricity lower than 60 mm corresponded to the sub-cortical sources.

2. *Cancellation index* - This index estimates the amount of overlap between signal patterns of individual sources within an active patch leading to signal cancellation (notably caused by dipolar sources oriented in opposite directions on both walls of a sulcus), as proposed by (Ahlfors et al., 2009).

$$Ic = 1 - \frac{\sqrt{\sum_{i=1}^{q}\left(\sum_{l\in\Phi} \boldsymbol{g}(i,l)\right)^2}}{\sum_{l\in\Phi}\sqrt{\sum_{i=1}^{q}\boldsymbol{g}^2(i,l)}} \qquad (4\text{-}16)$$

where i is the index of summation over all q sensors, l is the index of summation over all elements in the set of Φ active dipoles located within the simulated patch. $\boldsymbol{g}(i,l)$ is the value of the i^{th} row and l^{th} column of the lead field matrix $\boldsymbol{G}$. This index ranges between 0 and 1, Ic=1 indicates full cancellation and Ic=0 indicates no cancellation effect.

Spatio-temporal simulation model. 100 simulation configurations were randomly generated on the cortical mesh, involving activation of two spatially extended sources following the same time course but presenting a 15 ms delay between them. These simulations were proposed to mimic axonal propagation between two distant spike generators, with significant overlap between the time courses of the two generators. The sources were spatially separated by a fixed geodesic distance of 73 mm (i.e. a spatial neighborhood order of 10) and both sources were located in the same hemisphere. The velocity of this simulation model mimics the velocity of real propagating spikes (varying from 1 m/s to 40 m/s) (Emerson et al., 1995). This type of propagation is concordant with literature and can express a remote activation of a neural network connected to an active population by a fiber tract (Baumgartner, Lindinger, et al., 1995; Huppertz et al., 2001). For this set of 100 simulations, the spatial neighborhood order was s_e =3 consisting of sources with spatial extent ranging from 2 cm^2 to 6 cm^2. One trial of real background was added on noise-free simulated data. The amplitude of the background activity trials was scaled to ensure

a larger signal-to-background ratio (3 ≈ 4.7 dB) than the static simulations as the spatio-temporal simulations involve more complex source patterns to recover. Consequently, the SNR for this set of propagating spikes ranged approximately between 2 to 9.

b. Impact of the number of EEG electrodes considered during MEEG fusion

The static simulation model was considered to generate EEG and MEG data, while the impact of three different EEG configurations derived from the 10-10 electrode placement system was evaluated: A complete EEG setup involving 54 EEG electrodes (see **Figure 4.7a** EEG topography for the 54 EEG electrodes set-up), and two down-sampled montages involving respectively 32 and 20 EEG electrodes (see **Figure 4.9a** EEG topographies for the two down-sampled EEG electrodes set-up). Note that the 20 EEG electrodes set-up was similar to the conventional 10-20 EEG system used in most clinical centers.

c. Impact of Model-error

We are aware that the use of same head model during forward and inverse problem can lead to the best case scenario in any simulation study. In order to mimic real data scenario, one can introduce noise in the measurement through mis-modeling in simulations (Wang and Ren, 2013). We evaluated the robustness of cMEM method by varying the tissue conductivities in the EEG forward model during EEG and MEEG source localization. The correct modeling of head tissue conductivities, especially the conductivity ratio of the skull relative to brain and scalp is an important parameter that determines the accuracy of the forward and inverse solution especially in EEG. In the literature (Oostendorp and Delbeke, 1999; Lai et al., 2005; Zhang et al., 2006; Lew et al., 2009), similar conductivity values for the brain and scalp (ranging from 0.12 to 0.48 S/m) have been reported. However,

estimation of the skull conductivity has been reported to be more inconsistent with values ranging between 0.006 and 0.080 S/m (Hoekema et al., 2003). We extrapolated from past studies (Oostendorp and Delbeke, 1999; Malmivuo and Suihko, 2001; Lai et al., 2005; Zhang et al., 2006; Huiskamp, 2008; Vallaghé and Clerc, 2009; Fangmin Chen, 2010) a range of brain-to-skull conductivity ratio (that will be denoted Rbs) to be tested: Rbs ranging between 1:15 and 1:25 was found acceptable for the adult brain. For this test, we performed two sets of simulations. In the first set, we simulated EEG signals using different Rbs (randomized between 1:15 to 1:25 following a normal distribution with mean 1:20 and standard deviation of 1:3.3) of the EEG head model for 50 randomly placed sources and localized these sources using EEG head model at one Rbs (1:20). In the second set, we considered the same Rbs of 1:20 for both simulation and localization over the same 50 sources as the first set. Then we compared the localization accuracy (AUC) of cMEM on the two set of simulations for EEG and MEEG data.

d. Validation metrics

As the Ground Truth was fully controlled using simulated data, we considered the following validation metrics to evaluate the performances of MNE and cMEM source localization methods when applied on EEG, MEG or MEEG data. Some of the metrics have been described in further details in our previous studies, (Chowdhury et al., 2013) and (Grova et al., 2006).

1. Area Under the Receiver Operating Characteristic (ROC) curve, AUC - was used to assess the detection ability of the localization methods. The AUC index looks at the normalized energy of each source at a specific time sample. In case of static simulations, the energy at the main peak (τ_0) of the simulated spike was considered. For the 2-source spatio-temporal simulations, the AUC index was estimated separately at the peak of each source spike while removing the contribution of the vertices of the second source. Since the spatio-temporal simulation involved activation of two sources separated by a temporal delay of

15ms (with some temporal overlap), it was possible to estimate AUC for each source separately at the time of their peak.

This detection accuracy index (between 0 and 1) integrates sensitivity and specificity of the source localization methods to reconstruct the spatial extent of the source against the Ground Truth, by varying a detection threshold between 0 and the maximum of reconstructed current density. More details on AUC estimation can be found in APPENDIX A. An AUC value greater than 0.8 was considered good detection accuracy.

2. Spatial Dispersion (SD) - proposed in (Molins et al., 2008), measures both the spatial spread of the estimated source distribution around the true source location and the localization error between the estimated source distribution and the true source location. Let us denote by $\hat{\boldsymbol{J}}$ the result of the source localization method to be evaluated. Then, $\hat{\boldsymbol{j}}(i,\tau_0)$ represents the amplitude of the current density distribution estimated for a dipolar source *i* on the cortical surface at the main peak of IED (τ_0). To measure the SD of this solution, we weight the amplitude of all the *r* cortical sources by their minimum distances from the simulated patch using the following formula:

$$SD(\hat{\boldsymbol{j}}) = \sqrt{\frac{\sum_{i=1}^{r}\left(\min_{l\in\Phi}(\boldsymbol{D}^2(i,l))\hat{\boldsymbol{j}}^2(i,\tau_0)\right)}{\sum_{i=1}^{r}\hat{\boldsymbol{j}}^2(i,\tau_0)}} \qquad (4\text{-}17)$$

where $\min_{l\in\Phi}(\boldsymbol{D}(i,l))$ provides the minimum Euclidean distance between the source *i* and the sources *l* in the simulated patch. Φ denotes the set of indices of the dipoles in the simulated patch and this minimum distance is zero when the source *i* belongs to Φ. SD values close to zero means there is no active source outside the simulated patch. Large SD values could be caused either by the presence of sources far away from the true source that are contributing to

the estimated solution (spurious sources) or by the spatial spread of the reconstructed source around the true extent of the simulated patch.

3. Shape Error (SE) - In order to assess the accuracy of the reconstructed time courses within the simulated patch, we proposed the metric SE as the root mean square of the difference between the normalized theoretical source distribution (***Jth***) and the normalized estimated source distribution ($\hat{\boldsymbol{J}}$). Therefore, SE for a simulated source was estimated as follows:

   Let us consider $jth(i,t)$ and $\hat{j}(i,t)$, where $i \in \Theta$ and t is the time parameter.

$$SE = \sqrt{\frac{1}{\tau}\sum_{t}^{\tau}\left(\frac{m(jth(t))}{\max_t\left(\left|m(jth(t)\right|\right)} - \frac{m(\hat{j}(t))}{\max_t\left(\left|m(\hat{j}(t))\right|\right)}\right)^2} \qquad (4\text{-}18)$$

   with $m(jth(t)) = \frac{1}{card(\Phi)}\sum_{i\in\Phi} jth_n(i,t)$ and $m(\hat{j}(t)) = \frac{1}{card(\Phi)}\sum_{i\in\Phi}\hat{j}_n(i,t)$. The subscript "n" in jth_n or $\hat{j}_n$ denotes the normalization of the matrix $\hat{\boldsymbol{J}}$ so that its values are between -1 and 1, for example: $j_n(i,t) = \frac{|j(i,t)|}{\max_j\left(\left|j(i,t)\right|\right)}$. $\max_t$ is the maximum over t time samples.

e. Application of MEM fusion on clinical data

We evaluated our proposed MEEG fusion method on clinical data acquired from two patients with intractable focal epilepsy. We selected IEDs that occurred simultaneously in both EEG and MEG signals, while making sure that the individual IED on either EEG or MEG had high SNR (at least SNR of 1). SNR was estimated as the ratio between the maximum signal measured at the peak of the spike (over all channels) and the standard deviation of some baseline data (two seconds of data showing normal traces with no epileptic activity). We also carefully checked that the selected IEDs exhibited similar topographic maps.

Patient 1 is suffering from a cryptogenic focal epilepsy with a left fronto-temporal epileptic focus (defined by EEG telemetry and seizure semiology). In Patient 2 a Focal Cortical Dysplasia (FCD) was diagnosed based on the MRI in the left frontal opercular region. These patients participated as research subjects of the project entitled: "Application of magnetoencephalography in the assessment of the epileptic focus" (Dr. E. Kobayashi being the principal investigator for this project). Written informed consent for this study was obtained from the patients.

Analysis of the IEDs involved:

1. Data acquisition - Simultaneous EEG/MEG recordings were acquired using a 275 channel CTF-MEG-system using a 54 channel EEG-cap. EEG electrodes were placed according to the 10/20 system, with additional electrodes according to the 10/10 system covering the inferior temporal and parietal regions. EEG/MEG signals were recorded with patients at rest in a supine position. No filters were applied to the MEG recording and a hardware high pass filter of 0.03Hz was used for the EEG. The sampling rate was 2400Hz.
2. Pre-processing of EEG/MEG data – Standard CTF software was used to process the data offline. Data were down-sampled to 600 Hz and DC-offset was removed. Filtering included 0.3-70Hz bandpass filter (butterworth, 4th order) and 60Hz notch filter (and its harmonics). Any bad channels were removed.
3. Visual analysis and marking of EEG/MEG data - IEDs were visually marked by a clinical neurophysiologist (MH). Only simultaneous EEG and MEG spikes were analyzed.
4. Pre-processing of image data - Preprocessing of MRI data, co-registration and forward model estimation were done similarly to the simulated data in **Section 4.4.5a Anatomy dataset**.
5. Solving the inverse problem - We performed single spike localization of EEG, MEG and MEEG data using cMEM.

Single spike source localization was performed within a time window of 700 ms around the peak of the marked spike (200 ms before and 500 ms after). For each single spike, we identified (based on the SNR level), the first significant MEG peak and the first significant EEG peak, since these two peaks were not always synchronous.

4.5. Results

4.5.1. Performance of fusion approach on static simulation

We observed an overall good detection accuracy for cMEM on all modalities (median AUC>0.8) for sources with spatial extents s_e=3 and 4 (**Figure 4.3a and Figure 4.3b**). Similarly to our previous findings in Grova et al., (2006) and Chowdhury et al., (2013), MNE was less sensitive than cMEM to the spatial extent of the sources, showing overall lower AUC values. For the first time, we also clearly demonstrated that cMEM performed better than dSPM and sLORETA when recovering the spatial extent of the underlying generators. Notice the better performance for all the methods when using MEEG, as opposed to EEG or MEG alone. The validation metric SD exhibited clearly lower values for cMEM when compared to MNE, dSPM and sLORETA (**Figure 4.4**), suggesting less spatial spread around the true source and /or less distant spurious sources. From **Figure 4.4a and Figure 4.4b**, we observed that for all the methods the median of SD distribution for MEG was larger than for EEG and MEEG suggesting the presence of more spurious sources mis-localized outside the active region for MEG. The shape of the distribution for SD values when using MEG had long tails towards larger values. We checked that this was caused by misleading reconstructions for simulated mesial or deep generators. Interestingly, for all the methods, SD values for MEEG were the lowest indicating a more accurate estimation of the spatial extent of the generators and less spurious sources outside the simulated region, when compared to EEG and MEG localizations.

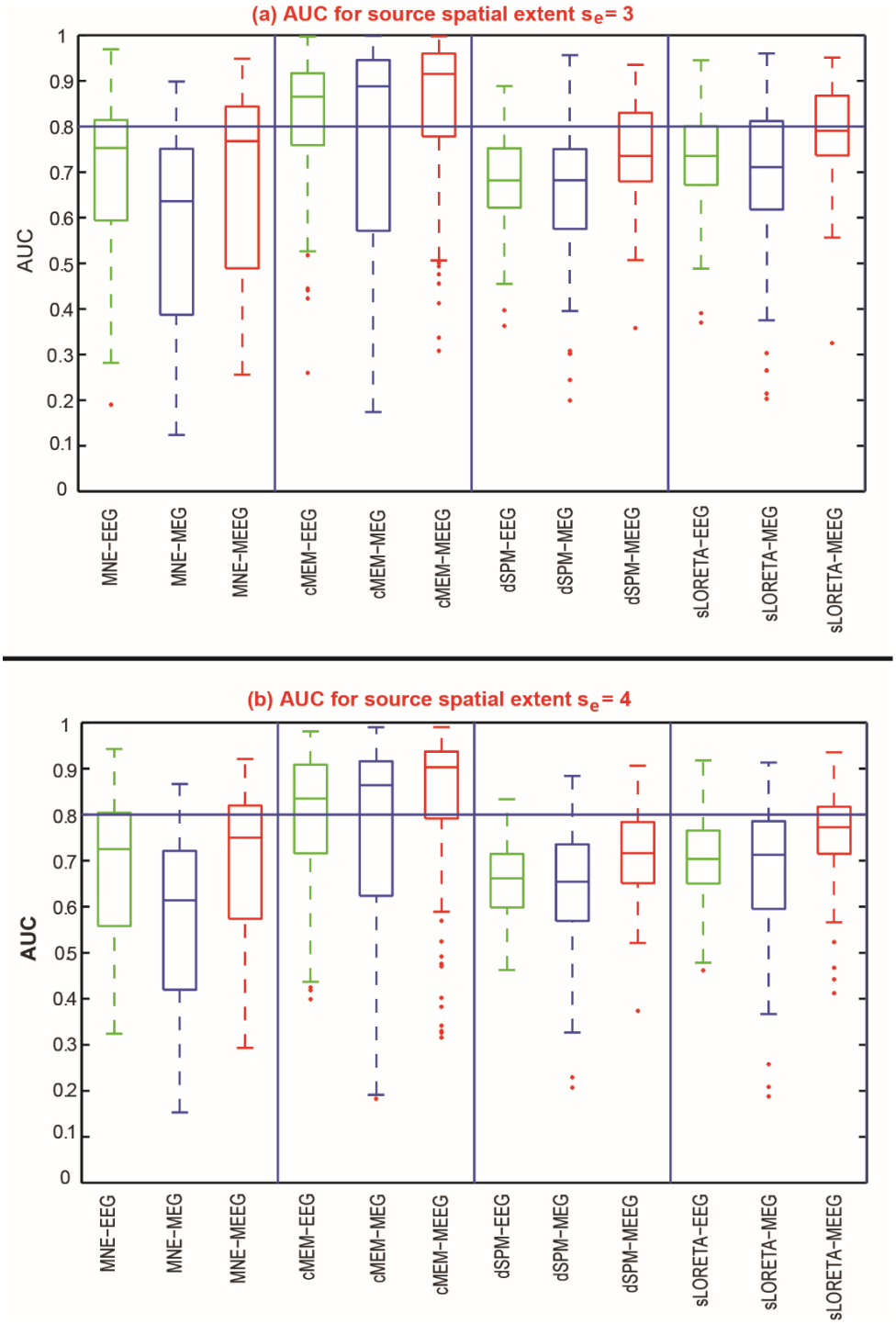

Figure 4.3. Distribution of AUC results over 100 simulations of randomly placed single static source for source localization methods, MNE, cMEM, dSPM and sLORETA on the three modalities (EEG, MEG and MEEG). (**a**) Boxplot representation of AUC values for simulated sources with spatial extent s_e=3, (**b**) Boxplot representation of AUC values for simulated sources with spatial extent s_e=4. (Horizontal line, AUC = 0.8). Color code for each modality: EEG in green, MEG in blue and MEEG in red.

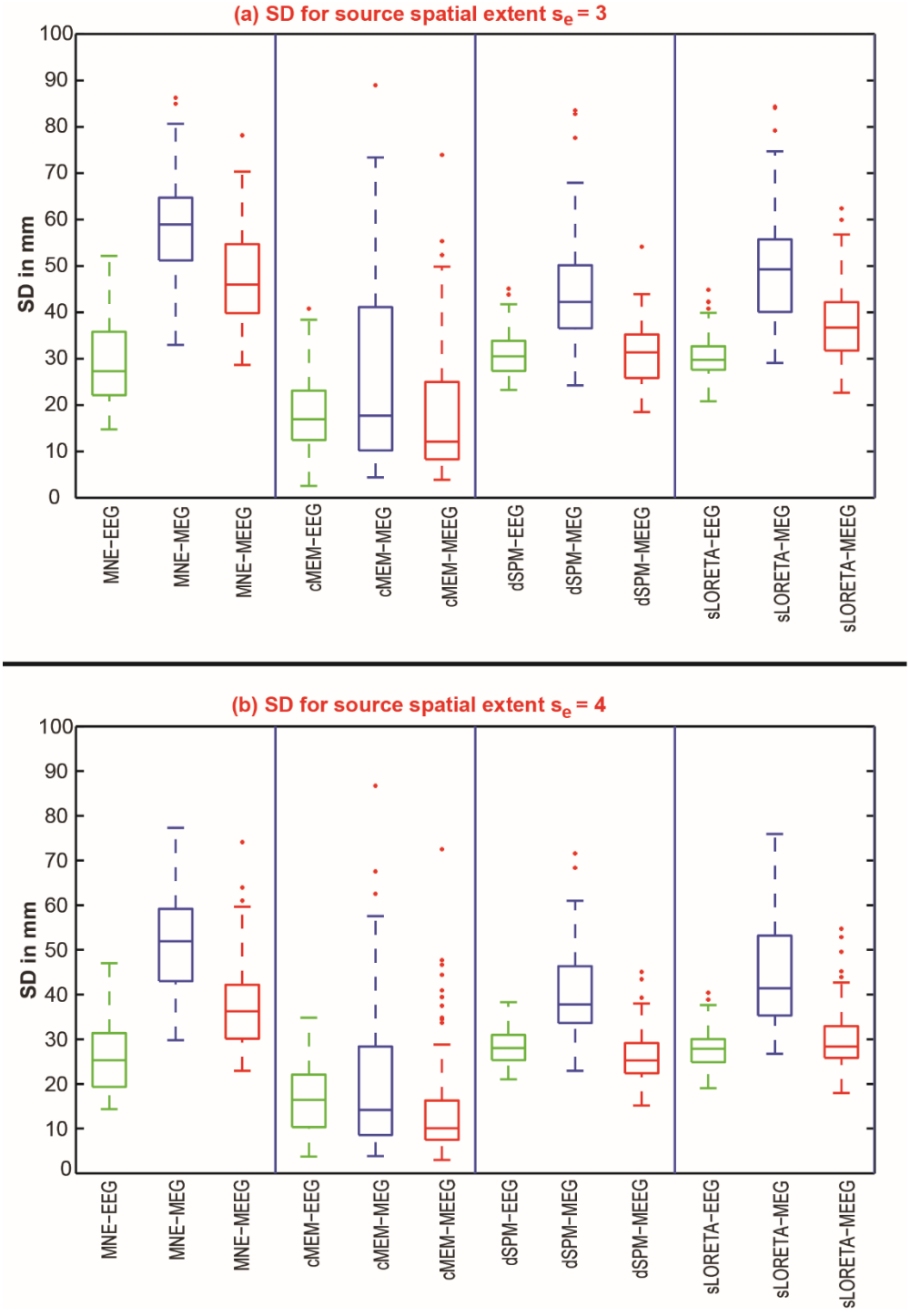

Figure 4.4. Distribution of SD results over 100 simulations of randomly placed single static source for source localization methods, MNE, cMEM, dSPM and sLORETA on the three modalities (EEG, MEG and MEEG). (**a**) Boxplot representation of SD values (in mm) for simulated sources with spatial extent s_e=3. (**b**) Boxplot representation of SD values (in mm) for simulated sources with spatial extent s_e=4. Color code for each modality: EEG in green, MEG in blue and MEEG in red.

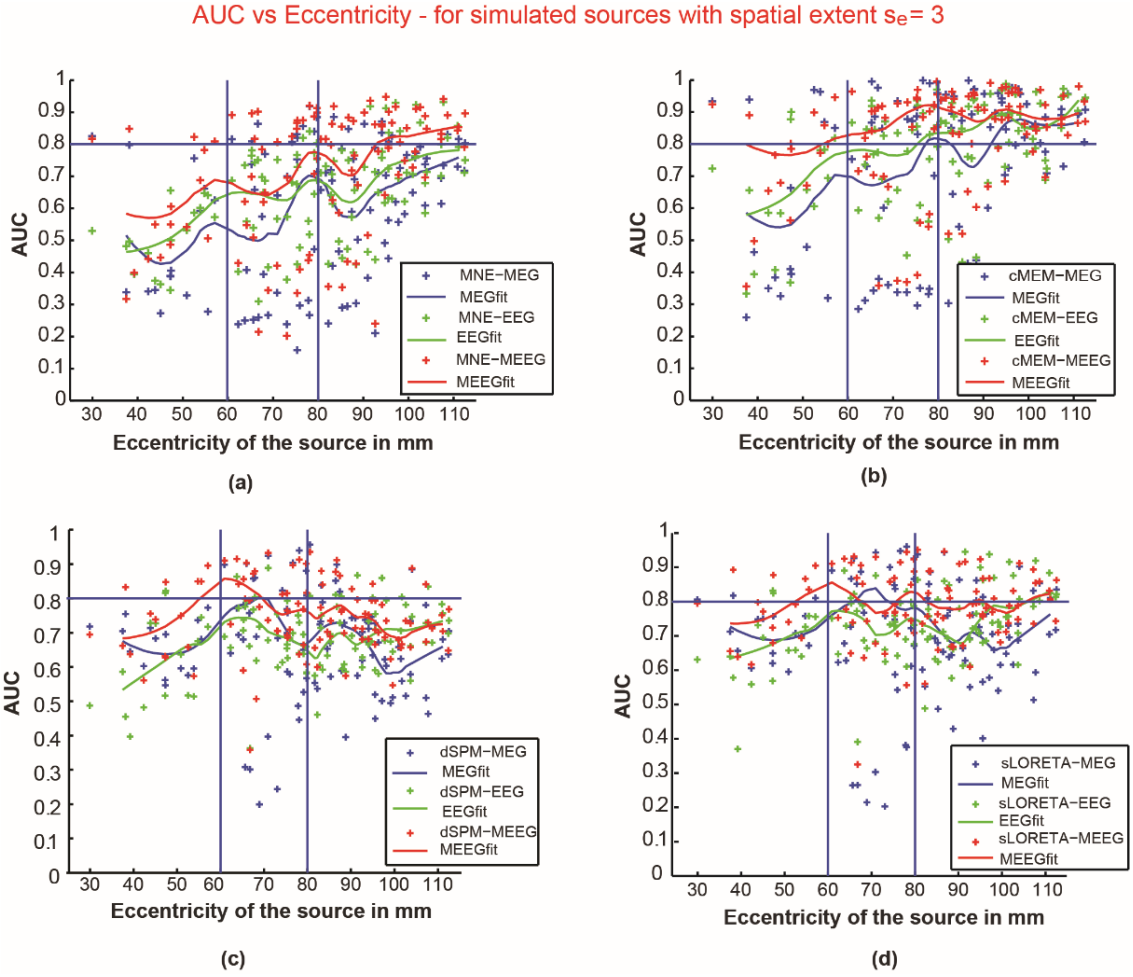

Figure 4.5. AUC as a function of eccentricity of the sources for 100 simulations involving randomly placed single static source at different locations for source localization methods MNE, cMEM, dSPM and sLORETA on the three modalities (EEG, MEG and MEEG). (**a**) AUC values obtained for MNE, (**b**) for cMEM, (**c**) for dSPM, and (**d**) for sLORETA when localizing simulated sources with spatial extent s_e=3. Solid lines are the moving average of the AUC values for the respective methods. Horizontal line, AUC = 0.8, Vertical lines: eccentricity = 60 mm and 80 mm. Color code for each modalities: EEG in green, MEG in blue and MEEG in red.

The behavior of AUC as a function of the eccentricity of the simulated sources is presented in **Figure 4.5**. As expected, for all the three modalities, we noticed better localization for superficial sources (eccentricity>80 mm, AUC>0.8 for cMEM) than for mesial and deeper sources (eccentricity<60 mm) for MNE and cMEM. EEG performed slightly better than MEG for most mesial sources (60 mm<eccentricity<80 mm). However, dSPM and sLORETA provided similar

localization accuracy for sources at all eccentricities; thus confirming that these methods are indeed less biased towards superficial sources. MEEG improved the detection accuracy of the methods for sources at all eccentricities. Overall, cMEM on MEEG data proved to be the most accurate (AUC>0.8) method showing good spatial accuracy for most sources, mainly superficial but also for some deeper ones. We also checked that the largest SD values in **Figure 4.4a and Figure 4.4b** were mainly due to mis-localized deep sources with low eccentricity (results not shown). As a particular example, **Figure 4.6** illustrates the ability of cMEM, MNE, dSPM, and sLORETA to localize a right superior frontal simulated source using EEG, MEG and MEEG data. Source localization results are presented over the inflated cortical surface, using Brainstorm software (Tadel et al., 2011). AUC and SD values were in agreement with visual inspection. We observed the largest AUC values (0.97) and smallest SD value (1.9) for cMEM when localizing MEEG data (**Figure 4.6b**). This result along with the findings from **Figure 4.3** and **Figure 4.4** suggests that MEEG localization using cMEM was the most accurate method in detecting the spatial extent of the source. SD for MNE was very large, especially for EEG and MEG localizations whereas for dSPM and sLORETA, SD was very large for all the three modalities. This corroborates with the visual analysis, showing an overestimation of the spatial extent and the presence of several spurious sources located far from the active region (in fronto-mesial and temporal regions notably), whereas the maximum of reconstructed activity was indeed accurately estimated. Overall, for all the methods, we noticed an improvement in spatial accuracy when localizing MEEG data, when compared to monomodal EEG and MEG localizations.

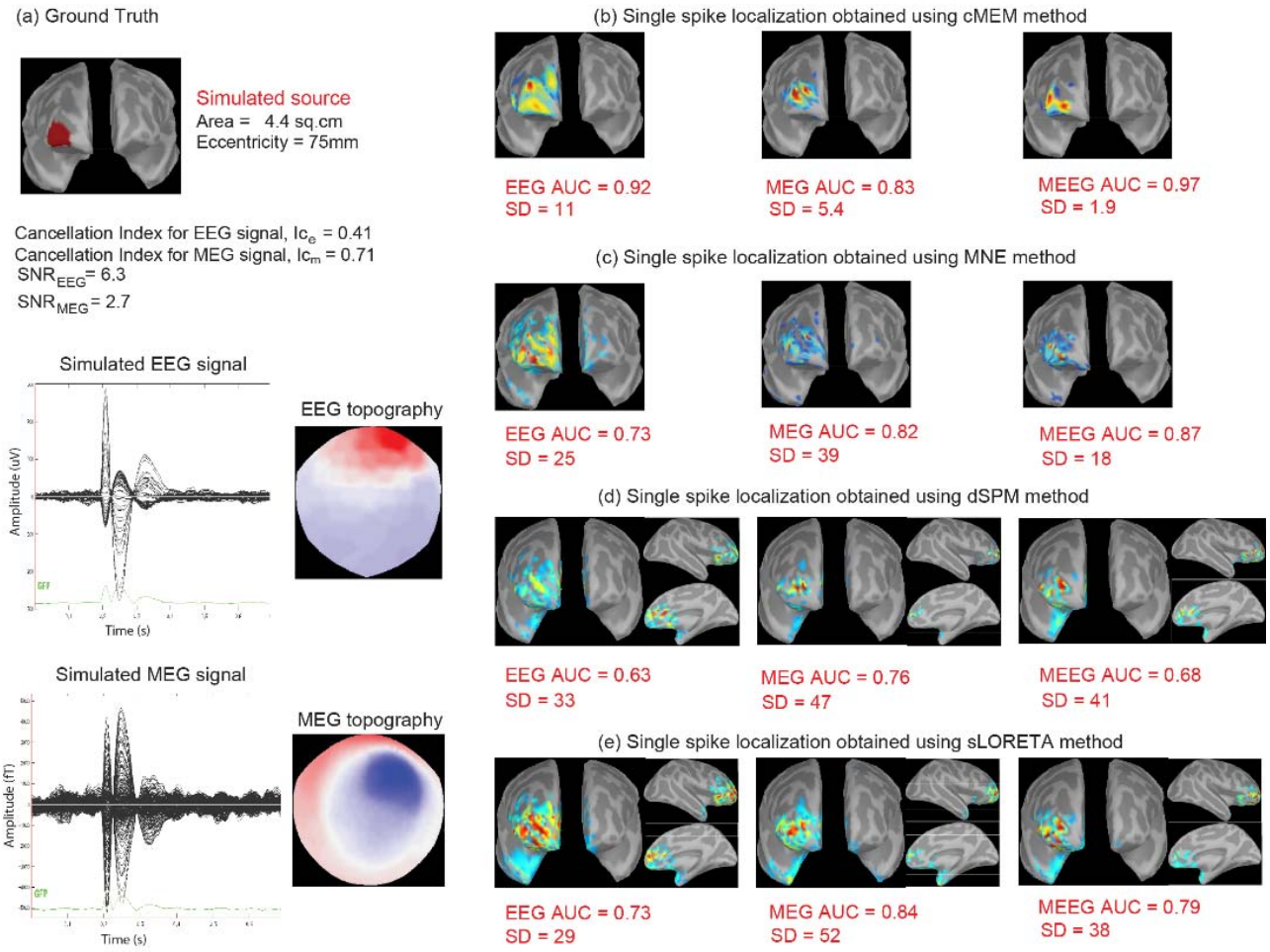

Figure 4.6. Qualitative assessment for example of static simulation. Visual analysis of source localization results together with AUC and SD values for a single static simulated source with area = 4.4 cm^2 and eccentricity 75 mm. All source localization results are presented as the absolute value of the current density at the peak of the spike, normalized to its maximum activity and thresholded upon the level of background activity. (**a**) Theoretical simulated source: area and eccentricity of the cortical source; associated simulated EEG and MEG signal and topography for all 54 EEG and 272 MEG channels respectively; Cancellation index for the simulated source in EEG, $Ic_e = 0.41$ and in MEG, $Ic_m = 0.71$; SNR for EEG signal, $SNR_{EEG} = 6.3$ and for MEG signal, $SNR_{MEG} = 2.7$. (**b**) Source localization results obtained using cMEM on EEG, MEG and MEEG data. (**c**) Source localization results obtained using MNE on EEG, MEG and MEEG data. (**d**) Source localization results obtained using dSPM on EEG, MEG and MEEG data. (**e**) Source localization results obtained using sLORETA on EEG, MEG and MEEG data.

Figure 4.7 illustrates the localization of a left deep cingulate simulated source with cMEM, MNE, dSPM, and sLORETA when considering EEG, MEG and MEEG

data. Overall, for all the methods, AUC and SD values showed that MEEG improved the localization, especially since fusion lead to higher AUC values and lower SD values than when considering MEG and EEG alone. MEEG localization using cMEM involved sources well localized on the left hemisphere, but with larger amplitudes towards the more superficial and fronto-polar vicinity of the generator. As expected, due to the implicit depth-weighting behavior of dSPM and sLORETA, these methods were able to recover the deeper aspects of the source (anterior cingulate sulcus) more accurately than cMEM or MNE. However, despite the fact that the main generator was found, both sLORETA and dSPM presented also spurious sources in the deeper regions of both hemispheres (including posterior cingulate gyrus and thalamus), resulting in misleading evaluation (i.e. high SD values and low AUC values). We noticed these spurious deep sources even in the previous example involving just a superficial source (**Figure 4.6d and Figure 4.6e**).

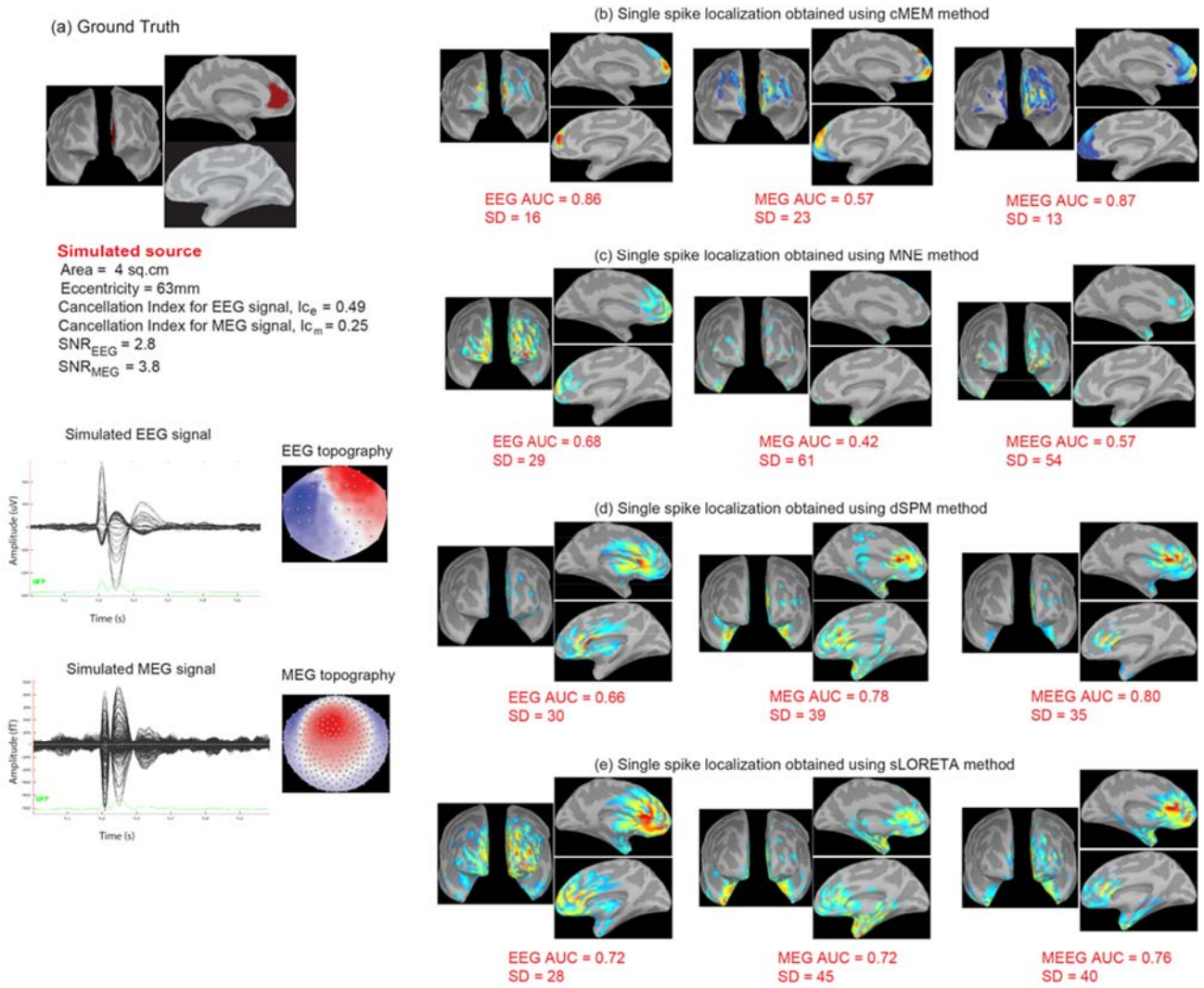

Figure 4.7. Qualitative assessment for an example of static simulation. Visual analysis of source localization results together with AUC and SD values for a single static simulated source with area = 4 cm^2 and eccentricity 63 mm. All source localization results are presented as the absolute value of the current density at the peak of the spike, normalized to its maximum activity and thresholded upon the level of background activity. (**a**) Theoretical simulated source: area and eccentricity of the cortical source; associated EEG and MEG topography; Cancellation index for the simulated source in EEG, Ic_e= 0.49 and in MEG, Ic_m= 0.25; SNR for EEG signal, SNR_{EEG} = 2.8 and for MEG signal, SNR_{MEG}= 3.8. (**b**) Source localization results obtained using cMEM on EEG, MEG and MEEG data. (**c**) Source localization results obtained using MNE on EEG, MEG and MEEG data. (**d**) Source localization results obtained using dSPM on EEG, MEG and MEEG data. (**e**) Source localization results obtained using sLORETA on EEG, MEG and MEEG data.

4.5.2. Impact of the number of EEG electrodes considered during MEEG fusion

Figure 4.8a presents the distribution of AUC values obtained on 100 static simulations, when decreasing the number of EEG electrodes. As expected, we observed a decrease of AUC for EEG source localization when reducing the number of EEG electrodes, for both MNE and cMEM methods (in green). However, the accuracy of MEEG localization (in red) using cMEM was quite robust to the number of EEG electrodes involved, reaching excellent performances (median AUC >0.8) even when only 20 EEG electrodes were added to the 272 MEG sensors. **Figure 4.8b** presents the distribution of SD values obtained on 100 static simulations, when decreasing the number of EEG electrodes. cMEM on MEEG showed the smallest SD values suggesting a more accurate sensitivity to the spatial extent, whatever was the number of EEG electrodes considered. These results are suggesting that the addition of only 20 EEG electrodes to the 272 MEG sensors will be sufficient to bring relevant information in the fusion, thus providing localization with good spatial accuracy.

Figure 4.9 illustrates cMEM localization for the left deep cingulate source presented in **Figure 4.7**, when considering two subsampled EEG electrodes configurations. Localization of this deep source was difficult as none of the configurations were able to recover accurately the deeper aspects of the source. The SD values showed that MEEG improved the localization, especially since any fusion configuration lead to lower SD values than EEG for the three EEG electrodes configurations (see **Figure 4.7b and Figure 4.9**). For EEG source localization, the maximum amplitude source was localized on the wrong hemisphere for all three EEG configurations. However, from **Figure 4.7b** for the 54 EEG electrodes configuration, EEG localization improved as it was indeed able to find a strong source within the simulated patch along with the strong source on the opposite hemisphere. MEEG localization for the three EEG configurations involved more accurately the deeper aspects of this anterior cingulate source, with sources well localized on the left hemisphere, but with larger amplitudes towards the more

superficial and fronto-polar vicinity of the generator. Note that some spurious sources in the left frontal neocortex were also localized.

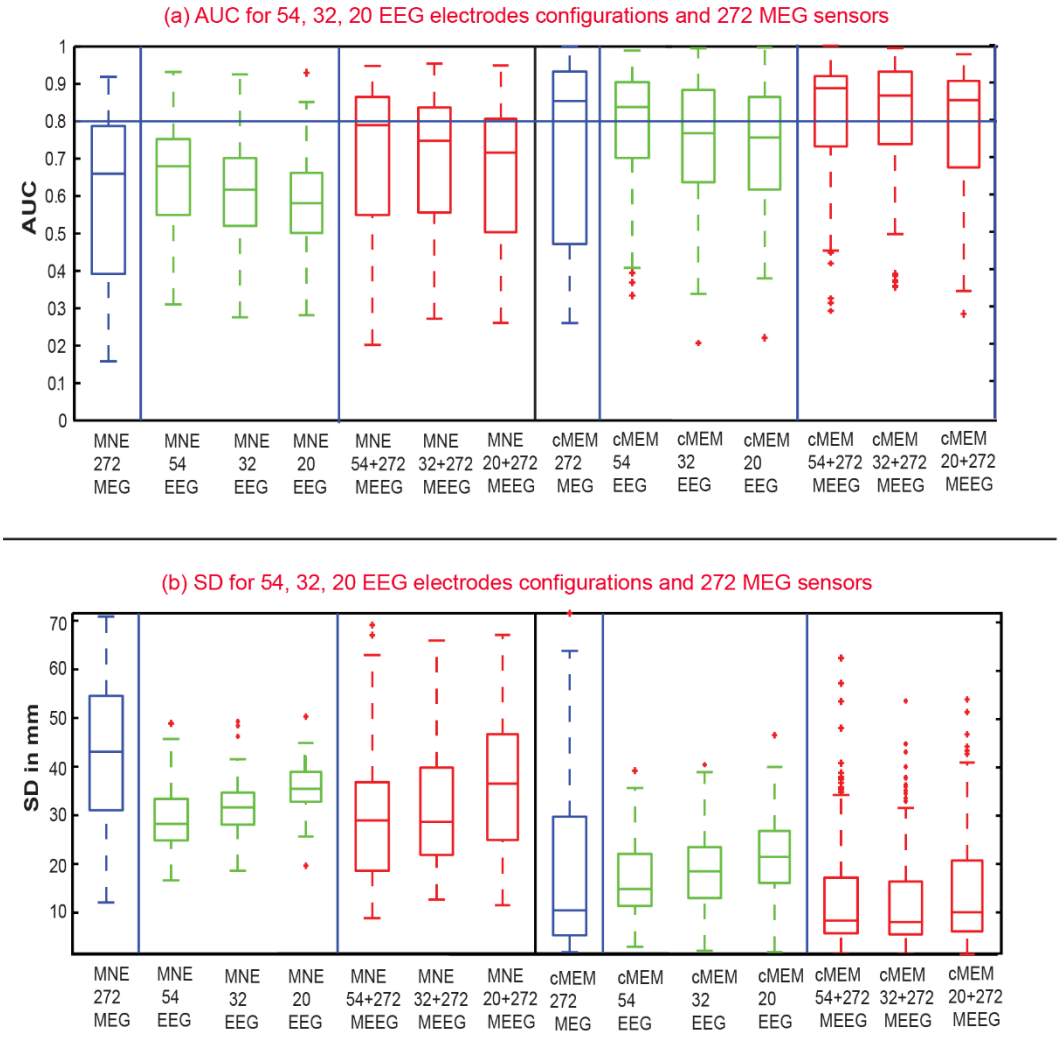

Figure 4.8. Evaluation of the source localization methods for three configurations of EEG electrodes using the detection accuracy index AUC and SD values. (**a**) Distribution of AUC values using boxplot representation over 100 simulated sources with spatial extent s_e=3 for MNE and cMEM methods applied on: (from left to right) 272 MEG sensors in blue, 54, 32, and 20 EEG channels in red and 272 MEG + 54 EEG, 272 MEG + 32 EEG, 272 MEG + 20 EEG channels in red. (**b**) Distribution of SD values using boxplot representation over 100 simulated sources with spatial extent s_e=3 for MNE and cMEM methods applied on: (from left to right) 272 MEG sensors in blue, 54, 32, and 20 EEG channels in red and 272 MEG + 54 EEG, 272 MEG + 32 EEG, 272 MEG + 20 EEG channels in red.

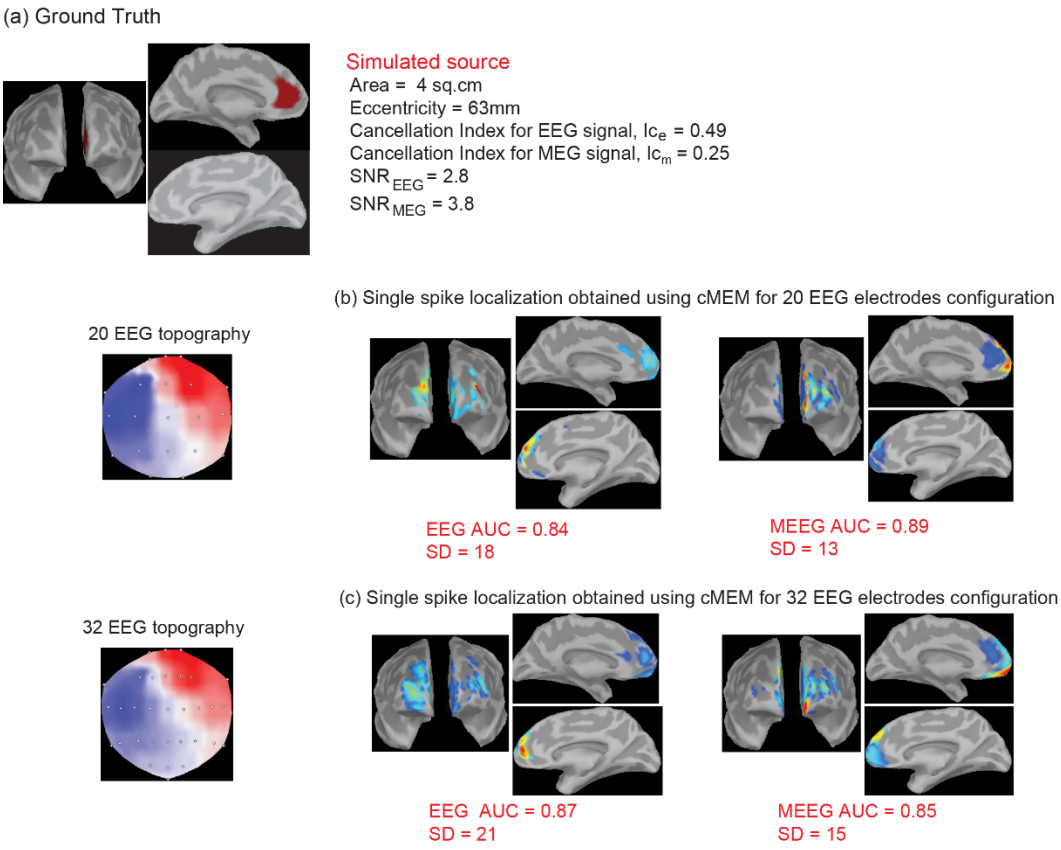

Figure 4.9. Qualitative assessment to evaluate the impact of the number of EEG electrodes using static simulation presented in Figure 7. Visual analysis of source localization results together with AUC and SD values for a single static simulated source with area = 4 cm^2 and eccentricity 63 mm. (**a**) Theoretical simulated source. (**b**) Source localization results obtained using cMEM method for 20 EEG electrode configuration on EEG and MEEG data. (**c**) Source localization results obtained using cMEM method for 32 EEG electrode configuration on EEG and MEEG data.

4.5.3. Performance of fusion on spatio-temporal simulations

Figure 4.10 reports the distribution of AUC values obtained for source 1 and source 2 (at their respective peak, separated by a 15ms delay) when using spatio-temporal simulations of propagating epileptic spikes. For each source, AUC distributions over 100 configurations are presented for cMEM and MNE methods and each modality. We observed that for all the modalities cMEM performed better than MNE in detecting the spatial extent of the propagating sources (higher AUC median

values for both the sources when using cMEM). MEEG localization using cMEM provided the highest AUC values for both source 1 and source 2. EEG source localization was found slightly less accurate for source 2 than for source 1 (lower AUC median value). For both MEG and MEEG, similar level of detection accuracy was found for both sources. This could be explained by the fact that the electrical potentials of the two sources will further mix because of larger overlap of the topographies of the two sources in EEG for the given sensor arrays, which is less the case with the magnetic fields measured in MEG. Consequently, MEG and the information from MEG provided in the fusion helped to separate the two sources.

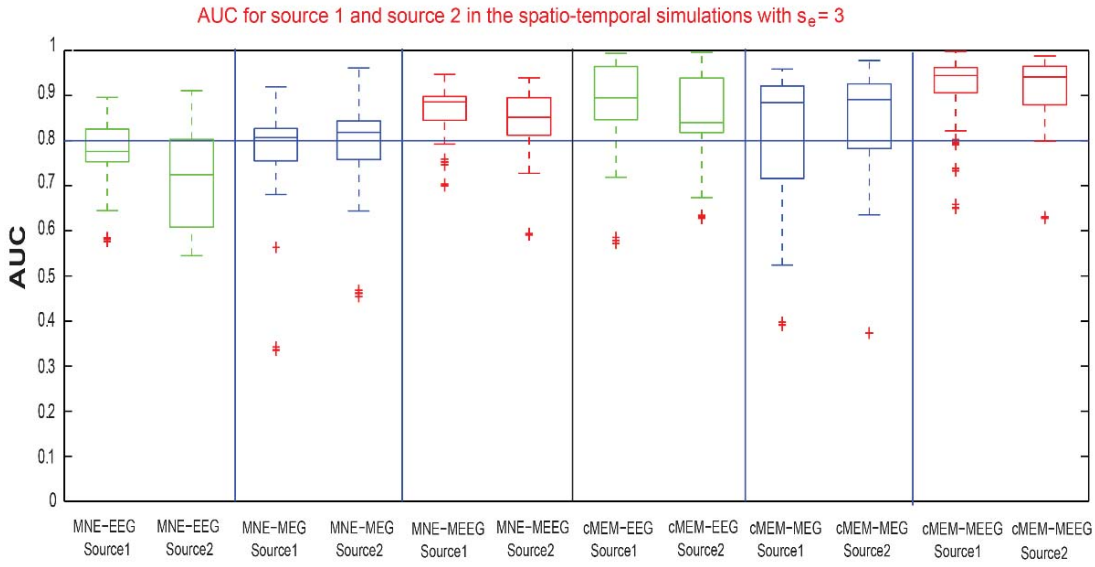

Figure 4.10. Evaluation of the source localization methods on the three modalities using AUC values over 100 spatio-temporal simulation configurations involving two randomly placed sources showing propagation within 15 ms duration between source 1 and source 2. Boxplot representation of AUC values for source 1 and source 2 with spatial extent s_e=3. Color code for each modalities: EEG in green, MEG in blue and MEEG in red for the methods MNE and cMEM.

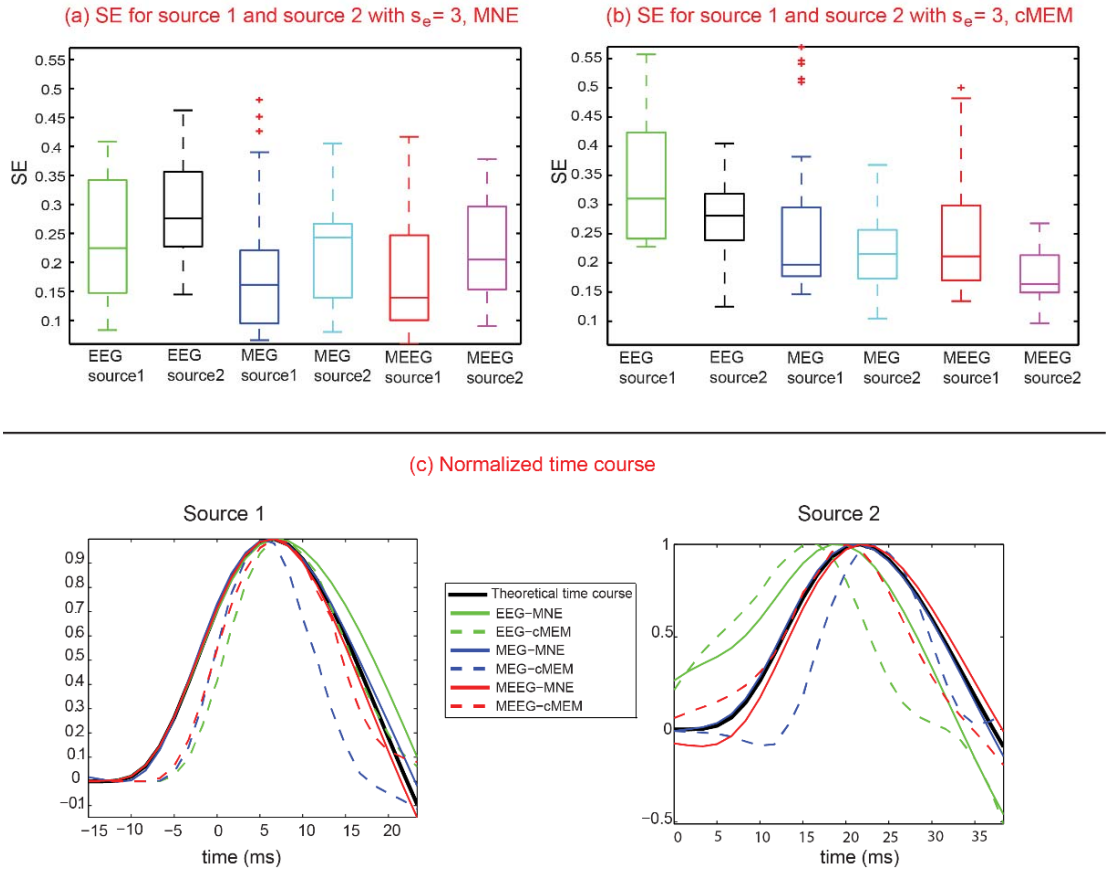

Figure 4.11. Evaluation of the source localization methods on the three modalities using SE estimates over 100 spatio-temporal simulation configurations involving two randomly placed sources showing propagation within 15 ms duration between source 1 and source 2. (**a**) Boxplot representation of SE values obtained for reconstruction of source 1 and source 2 using MNE method. (**b**) Boxplot representation of SE values obtained for reconstruction of source 1 and source 2 using cMEM method. Color code for each modalities: EEG in green for source 1 and black for source 2, MEG in blue for source 1 and cyan for source 2 and MEEG in red for source 1 and magenta for source 2. (**c**) Normalized mean time course of source reconstruction obtained for source 1 (left plot) and source 2 (right plot) using MNE and cMEM on EEG, MEG and MEEG data. Color code: black (solid line) for theoretical time course, EEG in green, MEG in blue, MEEG in red, solid line for MNE and dashed line for cMEM.

Analysis of the reconstructed time courses is shown in **Figure 4.11**. We observed that SE was clearly smaller for MNE (**Figure 4.11a**) than for cMEM (**Figure 4.11b**) for both sources in EEG localization. For MEG and MEEG localizations, SE for MNE was still slightly smaller than SE for cMEM, but we found a clear improvement on cMEM SE for MEG and MEEG when compared to EEG.

Moreover, MNE was able to reproduce the shape of the time course of first source better than the second source (larger SE for source 2). This could be explained by the fact that the SNR for source 1 was higher than source 2 since there was no mixing between the first and second source at the time of localization of source 1. The excellent performance of MNE in reconstructing the shape of the time course was rather expected, because MNE is a linear estimator. On the other hand, we provided here the first evaluation of the temporal behavior of cMEM localization. As cMEM sources consisted in non-linear estimates for each time sample independently, it was not obvious that it would reconstruct temporally smooth time courses. These first results are quite encouraging, especially for MEEG estimates providing almost similar temporal accuracy as MNE.

Figure 4.12 presents our results for a simulated spatio-temporal propagation from a left pre-frontal region to a left posterior superior frontal region. MNE and cMEM were able to localize accurately these two superficial sources, but with different sensitivity when recovering the spatial extents and the time courses. EEG localizations for both methods over-estimated the spatial extent by presenting large spatial spread around the true extent of the source (higher SD values than for MEG and MEEG). MEG localizations slightly under-estimated the spatial extent of the sources and also showed few distant spurious sources. This is probably due to the fact that the cancellation effect in MEG was very high (Ic_m = 0.78 for source 1 and 0.82 for source 2) and MEG was not able to recover the radial aspects of these generators. On the other hand, MEEG localizations provided a better estimation of the source spatial extent. From the visual inspection which is also in agreement with the metrics (Source 1: AUC = 0.97, SD = 4.7, and SE = 0.21; Source 2: AUC = 0.94, SD = 6.4, and SE = 0.15), MEEG localization using cMEM provided the most accurate detection of the sources with their respective spatial extents and time courses. The normalized mean time courses of source reconstruction for these two sources are presented in **Figure 4.11c**. We observed that MNE was the most accurate in reconstructing the time course of source 1 (in green, blue and red solid lines for EEG, MEG and MEEG respectively). This behavior is in agreement with

the lowest SE values (SE <0.15) estimated for source 1 when using MNE **Figure 4.12**. SE for source 2 using MNE and cMEM were the highest (SE >0.35) in EEG localization, which is also evident from the shape of the reconstructed time course in **Figure 4.11c**. Both MNE and cMEM were able to recover the time courses of the two sources better in MEEG than EEG or MEG (**Figure 4.11c**). Note that for MEEG, cMEM provided very accurate time course reconstructions around the peaks of source 1 and 2, whereas the amplitude decreased faster than MNE for lower SNR signals more distant from the peaks, illustrating the ability of cMEM to shut down the parcel.

4.5.3.1. Robustness to Model-error

Figure 4.13 presents the effect on localization accuracy when using correct Rbs versus incorrect Rbs on EEG (black plus signs) and MEEG (green circle) data using cMEM method. We found that the cMEM method is robust to this mis-modeling in the simulation protocol as the localization accuracy when using incorrect Rbs in the EEG head model does not differ much from results obtained when using correct Rbs. In a recent study, Wang and Ren tested the effect of correct and incorrect Rbs using simulations of EEG data when adding background noise or not (Wang and Ren, 2013). They showed that despite using the same Rbs in the EEG head model for simulation and localization there still exist localization errors in EEG source localization. This error was caused by contamination of the EEG data with background noise. This supports our simulation protocol where we added real background noise to both EEG and MEEG data.

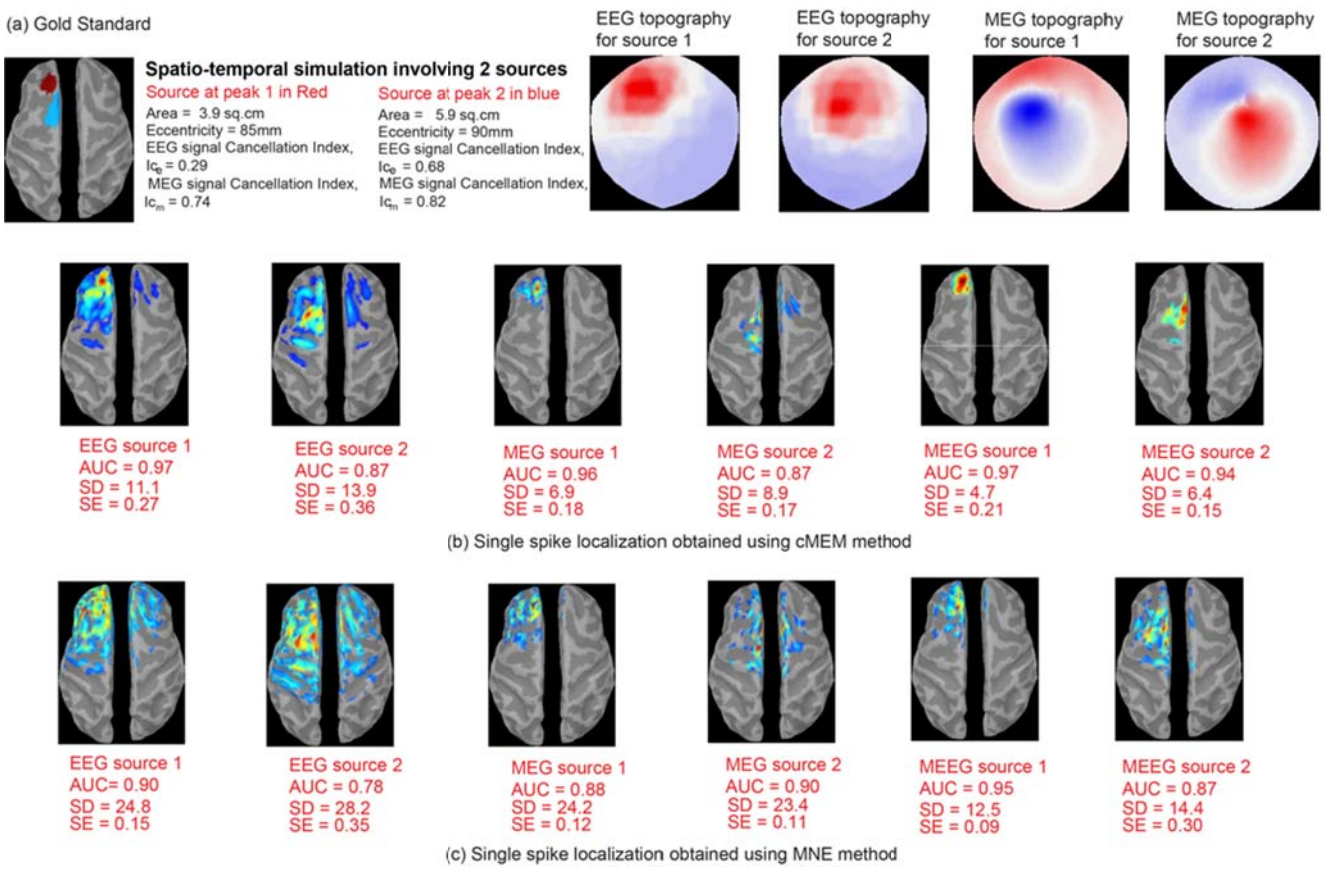

Figure 4.12. Qualitative assessment for example of spatio-temporal simulation. Visual analysis of source localization results together with AUC, SD, and SE values for an example of spatio-temporal simulation configuration. Source 1 with area = 3.9 cm^2 and eccentricity 85 mm and Source 2 with area = 5.9 cm^2 and eccentricity 90 mm. All source localization results are presented as the absolute value of the current density at the peak of the spike, normalized to its maximum activity and thresholded upon the level of background activity. (**a**) Theoretical simulated sources: area and eccentricity of the cortical source 1 and 2; associated EEG and MEG topography; Cancellation index for source 1 in EEG, Ic_e= 0.29 and in MEG, Ic_m = 0.74; Cancellation index for source 2 in EEG, Ic_e = 0.68 and in MEG, Ic_m= 0.82. (**b**) Source localization results obtained using cMEM on EEG, MEG and MEEG data. (**c**) Source localization results obtained using MNE on EEG, MEG and MEEG data.

121

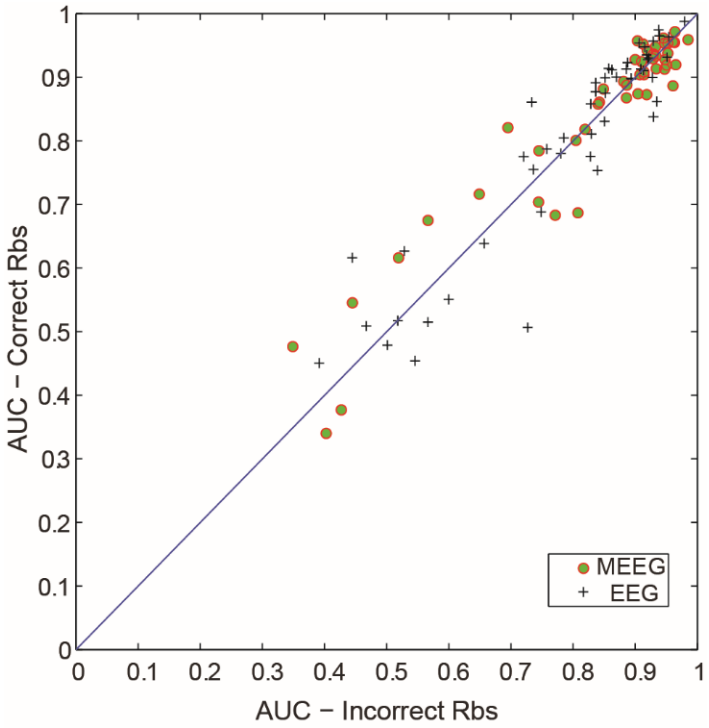

Figure 4.13. Test for robustness to model-error in simulation protocol. Plot showing the effect on localization accuracy when using correct Brain-to-skull conductivity (Rbs) ratio versus incorrect Rbs on EEG and MEEG data using cMEM method: EEG (black plus sign) and MEEG (green circle) (x-axis: AUC value for incorrect Rbs, y-axis: AUC value for correct Rbs).

4.5.4. Application of cMEM fusion approach on clinical data

For patient 1, we identified six left fronto-temporal spikes fulfilling our selection criteria. Source localization was performed on each of these single spikes and results from all the spikes were then averaged (supplementary **Figure S4.1**). **Figure 4.14** presents one of the single spike source localization results on EEG, MEG and MEEG data obtained using cMEM. For each spike, we identified two peaks in MEG (the first MEG peak occurring 26.7 ms before the second MEG peak) and one in EEG (second MEG peak was synchronous with the EEG peak). All single spike source localizations demonstrated propagation of activity from the left orbitofrontal region (at time point 1 = -26.7 ms, MEG peak) to the left temporal neocortex (time point 2 = 0 ms, EEG/MEG peak) in MEEG localizations. In MEG localizations, we observed the left orbitofrontal source along with a right fronto-mesial source at time

point 1. On the other hand, EEG localizations (at time point 2, EEG peak) found mainly a left temporo-polar source while presenting also a right temporal source. When averaging the localization of the six spikes (supplementary **Figure S4.1**), we found mainly the left orbito-frontal source in MEG at time peak 1, a left temporal neocortical source in EEG at time peak 2, while MEEG fusion described nicely the propagation between these two regions, suggesting the benefit of integrating EEG and MEG data using cMEM. The clinical seizure semiology of this patient suggested that the seizures originated from the left frontal lobe. Left fronto-temporal IEDs were recorded in EEG and MEG. This propagation from orbito-frontal to temporal neocortex identified by MEEG using cMEM is quite a plausible pattern of propagation for this type of epilepsy, following a well-known white-matter connection pathway.

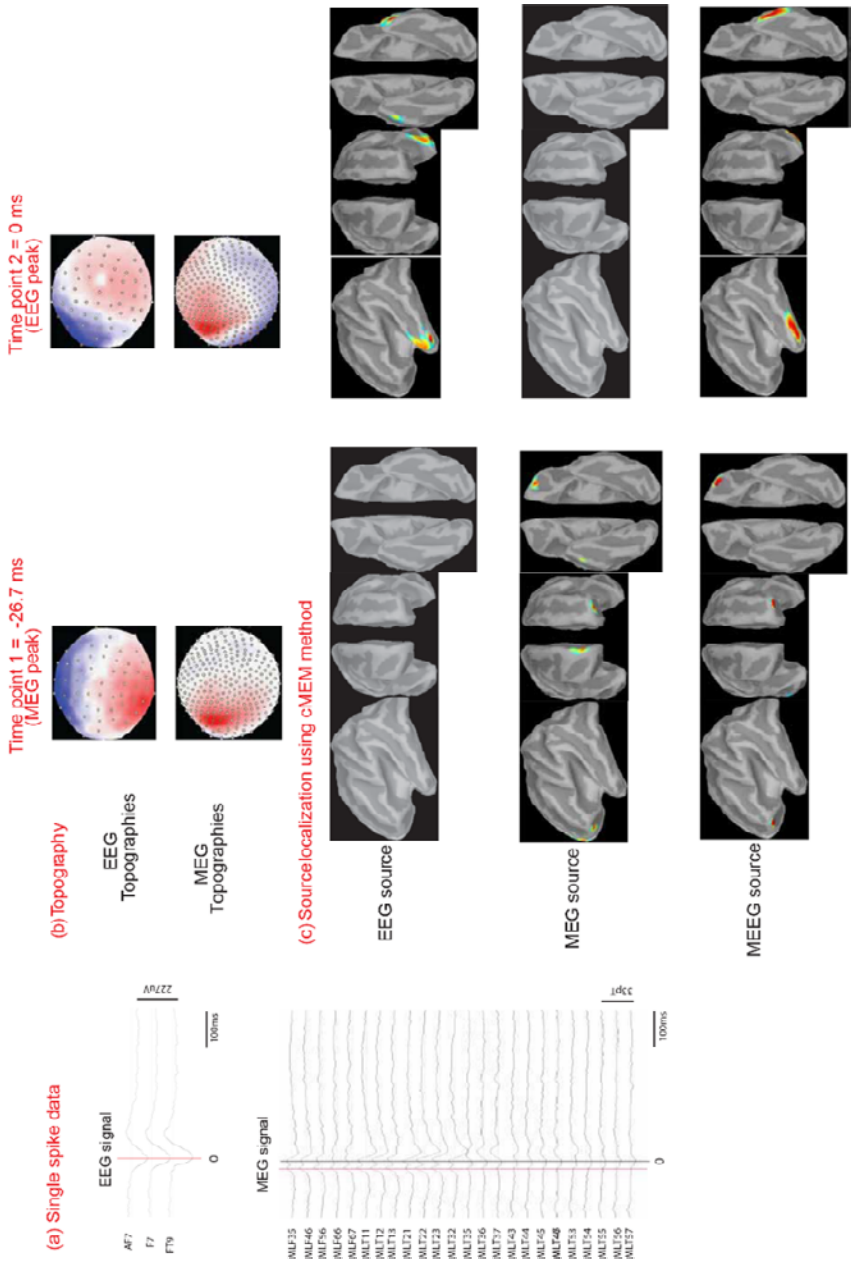

Figure 4.14. Patient 1 - Single spike localization. (**a**) EEG and MEG signal for the respective spike type (vertical black line = 0 ms in time, red line is the respective time point for selected EEG or MEG peaks)). (**b**) EEG and MEG topographies for time point T1 (MEG peak) and T2 (EEG peak). (**c**) Source localization results using cMEM method for EEG data, MEG data and MEEG data.

For Patient 2, we identified four left frontal spikes fulfilling our selection criteria. Single spike localizations were performed on these four spikes and then average of these four source localization results were obtained. In all the four single spike localization results (**Figure 4.15**), we noticed that EEG localization found a left frontopolar source, whereas, MEG localization presented mainly two sources: one

in the left inferior frontal gyrus and another in the inferior part of the left pre-central gyrus. However, MEEG fusion identified the main source in the inferior part of the left pre-central gyrus but with a slightly different spatial distribution than MEG pre-central source. The average of four single spikes localization (supplementary **Figure S4.2**) reproduced similar results as seen in each single spike, suggesting good reproducibility. These results are rather interesting, since MEEG identified mainly a source in the inferior part of left pre-central gyrus, that was in perfect overlap with the FCD of the patient, whereas sources identified by EEG or MEG did not overlap with the anatomical lesion. The clinical seizure semiology of this patient also suggested an involvement of the inferior central region.

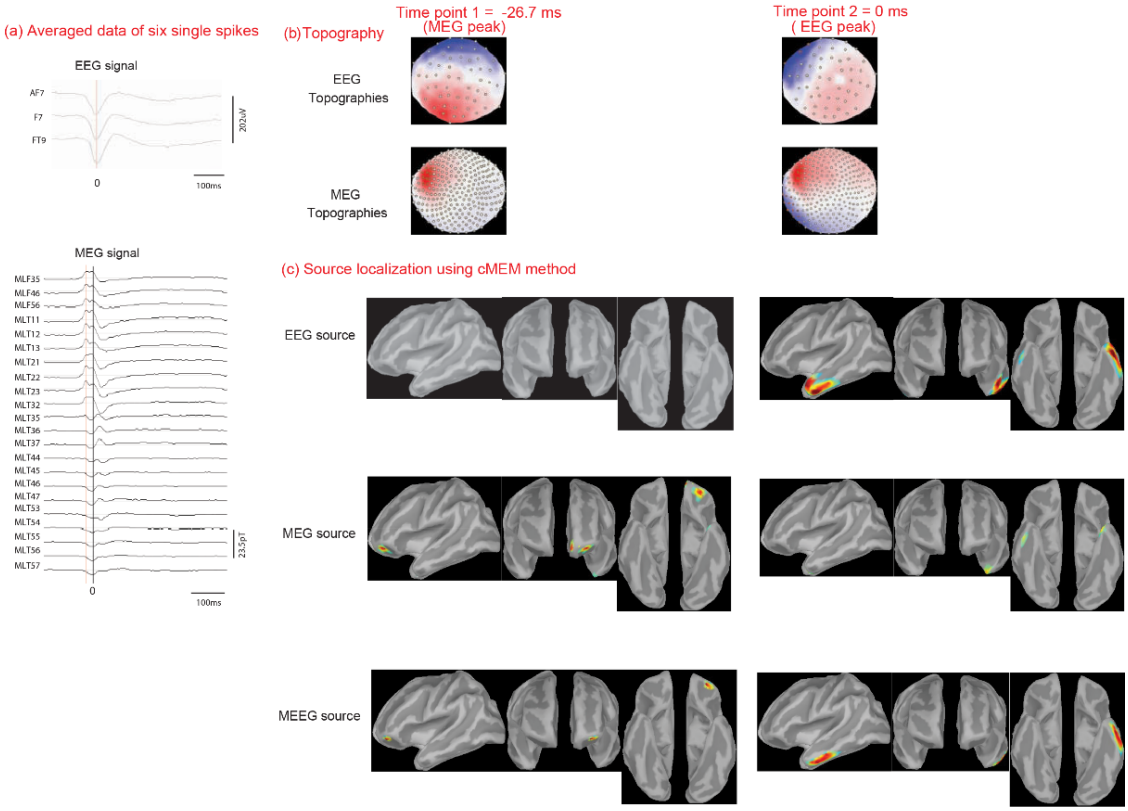

Figure S4.1. Patient 1 - Average of six single spike localizations. (**a**) EEG and MEG signal for the respective spike type (vertical black line = 0 ms in time, red line is the respective time point for selected EEG or MEG peaks)). (**b**) EEG and MEG topographies for time point 1 (MEG peak) and time point 2 (EEG peak). (**c**) Source localization results using cMEM method for EEG data, MEG data and MEEG data.

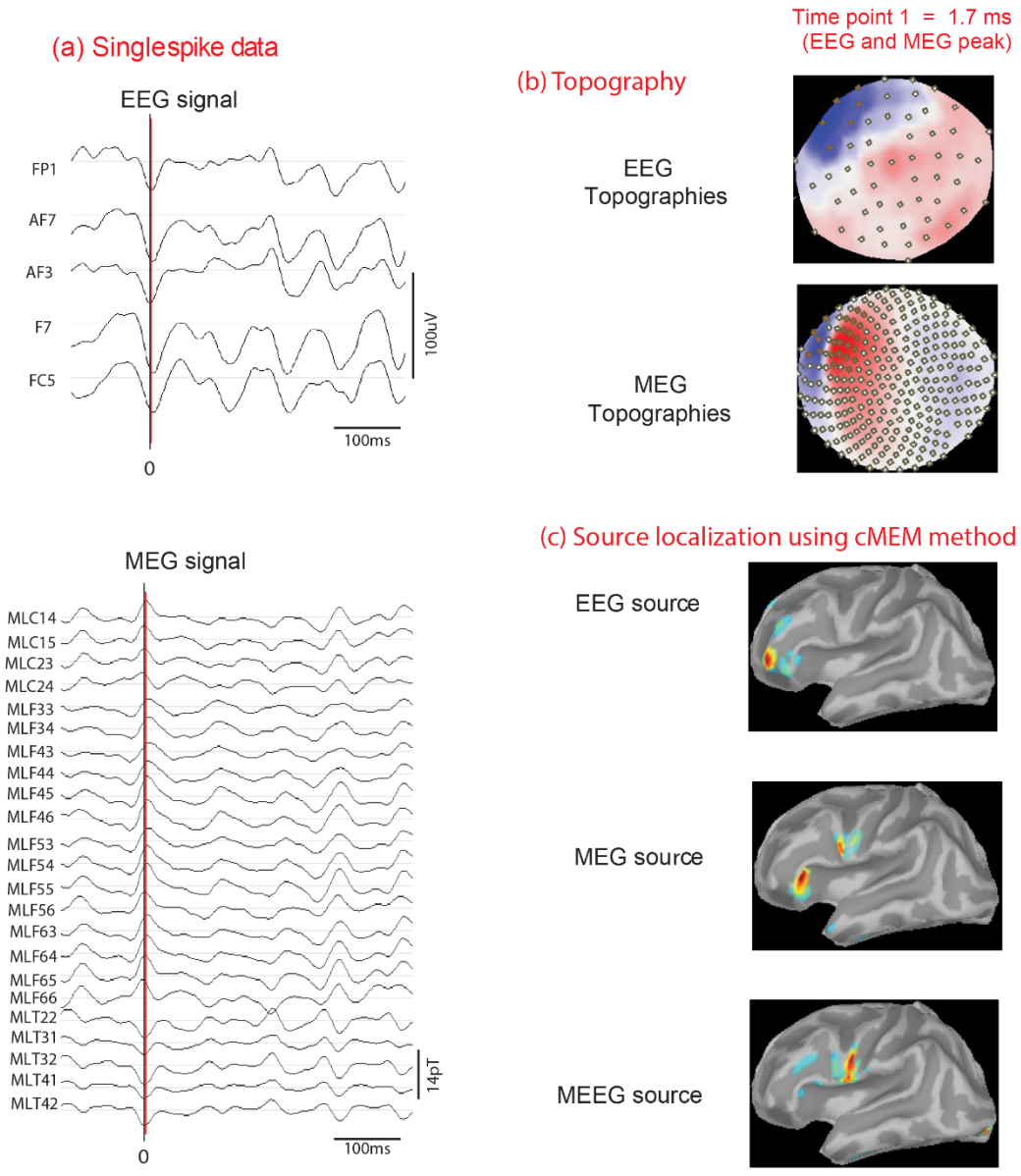

Figure 4.15. Patient 2 - Single spike localization. (**a**) EEG and MEG signal for the respective spike type (vertical black line = 0 ms in time, red line is the respective time point for selected EEG or MEG peaks)). (**b**) EEG and MEG topographies for time point 1 (EEG peak and MEG peak). (**c**) Source localization results using cMEM method for EEG data, MEG data and MEEG data.

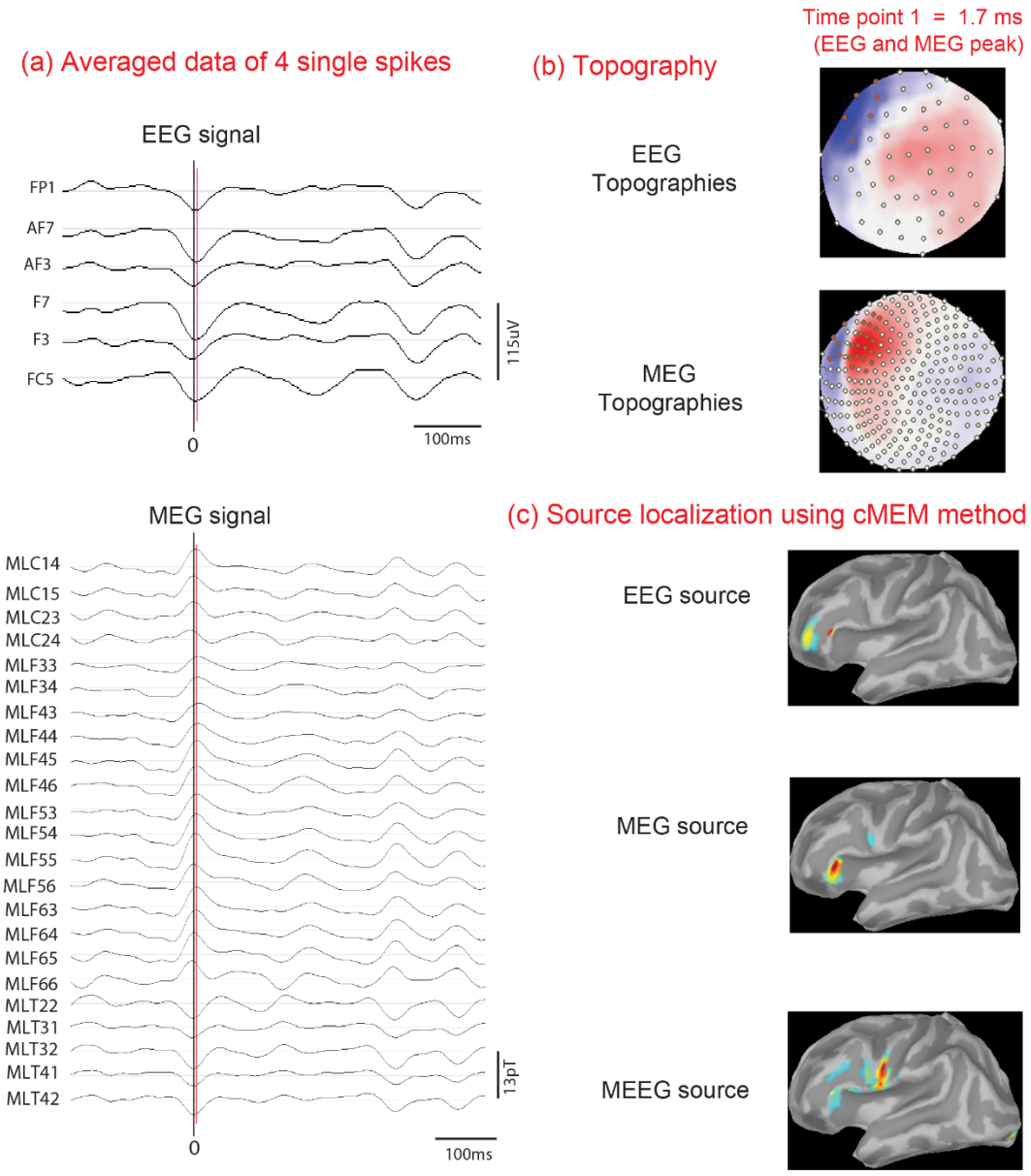

Figure S4.2. Patient 2 - Average of four single spike localizations. (**a**) EEG and MEG signal for the respective spike type (vertical black line = 0 ms in time, red line is the respective time point for selected EEG or MEG peaks)). (**b**) EEG and MEG topographies for time point T1 (EEG and MEG peak). (**c**) Source localization results using cMEM method for EEG data, MEG data and MEEG data.

4.6. Discussion

The purpose of this study was to propose and validate a new symmetrical EEG/MEG fusion strategy using the MEM framework. We provided an extensive evaluation of MEEG fusion when localizing single, non-averaged, epileptic spikes, using either realistic simulations or clinical data. Our results demonstrated the robustness of MEM-based fusion approaches to low SNR conditions of single spike localization and when recovering spatio-temporal propagations of epileptic discharges.

4.6.1. Why applying fusion to single spike localization?

For EEG and MEG to detect IEDs from background activity, the underlying generators should be spatially extended (Mikuni et al., 1997; Tao, Baldwin, Hawes-Ebersole, et al., 2007; Huiskamp et al., 2010). Although, single dipole fitting is currently the most common and clinically accepted method for the purpose of epileptic focus localization (Bast et al., 2004), distributed source models are more suitable for localizing the spatially extended generators of IED (Tanaka and Stufflebeam, 2014). When localizing IEDs, several epileptic spikes showing a similar morphology and field maps are usually averaged to improve the SNR and then source analysis is performed on the averaged spikes (Bast et al., 2004; Hara et al., 2007; Tanaka et al., 2010). Several studies (Bast et al., 2004, 2006) explored the pros and cons of averaging spikes and suggested that averaging will confound any important spatio-temporal information present in each individual spikes due to cancellation of signals. Therefore, spatio-temporal source analysis of single spike will be more appropriate to provide information on the spike onset and propagation pattern by creating a balance between increasing SNR and spike variability (Tanaka et al., 2014). Moreover, single spike analysis of combined EEG and MEG recordings is favorable to take full benefit of the complementarities between these two modalities (Pataraia et al., 2005).

4.6.2. Why cMEM based Fusion approach?

With the present study, we were able to show that single spike analysis using cMEM on EEG/MEG fusion data improved the spatial accuracy of spatially extended source reconstruction.

Symmetrical fusion of EEG and MEG within the MEM framework took place at three levels: 1) Normalization and concatenation of the data and lead field matrices, 2) data driven parcellization, and 3) initialization of the probability of activation of each parcels. As a first step, the data and the lead field matrices of each modality were normalized by the standard deviation of the respective background activity, using the SNR transformation method described in (Fuchs et al., 1998) and (Ding and Yuan, 2013). Different normalization methods have been proposed in previous works for combining EEG and MEG data. The motive behind using the SNR transformation method in our study was to account for the different physical units of MEG (Tesla) and EEG (Volt) and for their different noise content. Therefore, this modality-specific normalization seems appropriate for multimodal fusion of EEG and MEG. Most of other EEG/MEG fusion approaches differed in the way data were normalized and concatenated before applying the inverse operator. Some of the proposed methods consist in channel-wise SNR transformation (Fuchs et al., 1998), incorporation of intermodal noise covariance (Ko and Jun, 2010), minimization of mutual information for channel selectivity (Baillet et al., 1999), row normalization of lead-field matrices, weighted normalization (Hong et al., 2013), and integration within a Bayesian framework (Henson et al., 2009b). Note that we have tested our simulations with both global and channel-wise SNR transformation and there is no significant difference in the final result of fusion. However, it is important to mention that a more accurate noise covariance model was taken into account during the MEM optimization process, rather than starting by a pre-whitening of the data as it is usually considered. In the present study, the noise covariance model was estimated as diagonal but with a different value for each channel, thus taking into account the noise level of each individual channel.

However, the second and third levels described in the present MEM fusion framework are specific to our proposed method. We believe that using fusion MSP scores ($\boldsymbol{MSP}_{MEEG}$) for the whole cortex parcellization and for the initialization of the probability of each parcel to be active played an important role in combining the complementary information from EEG and MEG in the fusion process. In equation (4-12), we estimated $\boldsymbol{MSP}_{MEEG}$ using a logical OR operator to integrate $\boldsymbol{MSP}_{EEG}$ and $\boldsymbol{MSP}_{MEG}$ maps. Note that other fusion strategies could have been investigated at this level as well, as for instance using minimized mutual information for each source (proposed in (Baillet et al., 1999)) to reduce the redundancy between the two modalities.

4.6.3. Static simulations of realistic IEDs

Using AUC metric to assess the detection accuracy of the source localization methods, we have demonstrated an overall higher spatial accuracy of MEEG localization when compared to the mono-modal localizations for all the evaluated methods (cMEM, MNE, dSPM and sLORETA). We also observed that the single spike localization of MEEG data improved the detection accuracy of the sources at all eccentricities when compared to EEG or MEG localizations (**Figure 4.5**). This suggests that deeper sources can be localized more accurately with the fusion due to the increase in the number of recording channels and fusion of complementary information from EEG and MEG. We indeed showed that EEG data were likely to be more sensitive to deeper sources than MEG data measured using gradiometers, whereas MEEG fusion provided most accurate results.

SD seems an interesting metric for the evaluation of EEG, MEG and MEEG localizations. SD is influenced by both the spatial spread around the source and the presence of spurious sources. In **Figure 4.4a, Figure 4.4b and Figure 4.8b**, we noticed that all the methods provided overall lower SD values for MEEG localization when compared to MEG and EEG localizations while cMEM performed better than MNE, dSPM and sLORETA for all modalities. This indicates

that MEEG localizations presented less spatial spread of the solution around the true extent of the source or less spurious activities distant from the true source than EEG or MEG localizations. The simulation model used in this study involves a static patch of uniform activity, which has been extended to simulate different spatial extents of the source. In this model, the patch extends in all direction with uniform intensity, which is not fully realistic. This can indeed be a drawback, especially for MEG, when the patch included two opposing walls of sulcus leading to an increased amount of signal cancellation and low SNR signal. EEG simulated signals showed overall higher SNR due to the contribution of gyral sources. Therefore, most of the sources simulated in this study provided lower SNR for MEG simulated signals than for EEG simulated signals. This simulation bias explains the large variance observed in the distribution of SD values in MEG localizations; especially showing long tails towards large SD values (See one example in **Figure 4.6**). We also checked that most results involving large SD values corresponded to simulations exhibiting a low SNR (deep sources or large cancellation effect).

4.6.4. Impact of the number of EEG electrodes for fusion

Scalp EEG is sensitive to both radial and tangential components of the sources, whereas MEG is mainly sensitive to the tangential components of the sources (Hämäläinen et al., 1993). As a result, in addition to the spikes seen by both modalities, it is not rare to detect EEG spikes where no MEG spikes are visible and vice versa (Iwasaki et al., 2005; Knake et al., 2006; Ramantani et al., 2006; Kakisaka et al., 2013). Spike visible on EEG only are explained by the better sensitivity of EEG to deeper and radially oriented source. Spikes visible on MEG only are explained by the sensitivity of MEG to mainly tangentially oriented sources and less influence of the skull resistivity leading to better SNR of MEG signal for sources in superficial, neocortical areas (Goldenholz et al., 2009; Huiskamp et al., 2010; Kakisaka et al., 2013). It would therefore be important to consider fusion of both modalities even when the spike is detectable on only one of

the two modalities (Zijlmans et al., 2002). With fusion, we could probably improve these conditions where the spike is at low SNR in one of the modality but this was out of the scope of this study and will be considered in further studies. Difference in the EEG and MEG source analysis results can also be explained by the difference in the number of measurement sites between EEG and MEG. Most MEG systems are equipped with more than 100 sensors uniformly distributed around the whole head, which provides high spatial sampling. On the other hand, when recording EEG data only, high density montages involving 64, 128 or 256 channels are needed to ensure reliable EEG source analysis (Lantz and Grave de Peralta, 2003; Babiloni et al., 2009; Brodbeck et al., 2011; Yamazaki et al., 2013). However, most clinical centers commonly use the conventional 10-20 EEG system for recording epileptic patients, which lacks the high spatial sampling required for the improved localization accuracy in EEG (Zelmann et al., 2013).

Analysis of combined EEG and MEG measurements from simultaneous recording was suggested to bring additional information missed by either modalities (Stefan et al., 1990; Fuchs et al., 1998; Iwasaki et al., 2005; Sharon et al., 2007; Babiloni et al., 2009) But, recording simultaneous EEG and MEG data is time consuming to set-up many EEG electrodes and can be associated with some discomfort for the subject wearing the EEG cap inside the MEG helmet, thus limiting the duration of the acquisition. We were able to show that MEEG localization using cMEM was quite robust to the number of EEG electrodes involved, reaching excellent performances (median AUC >0.8 and median SD values <10) even when only 20 EEG electrodes were added to the 272 MEG sensors (**Figure 4.8**). These results suggest that the addition of only 20 EEG electrodes to the 272 MEG sensors, making sure that these electrodes were covering the lower aspects of both temporal lobes, will be sufficient to bring relevant information for the fusion, thus providing localization with good spatial accuracy. However, the example in **Figure 4.7b** and **Figure 4.9** showed that all the 54 EEG electrodes were needed for recovering the deeper aspects of the source even in fusion. This could be explained by the fact that MEG performs poorly in detecting deep source locations in medial areas such as

cingulate gyrus (Molins et al., 2008). Therefore, for most sources only 20 EEG electrodes in the fusion were sufficient but for few other sources the addition of well-placed EEG electrodes might be needed to cover the sites of interest. This raises an important question whether what are the best positions of EEG electrodes such that EEG's information about the deeper and radially oriented sources can be effectively added to the MEG information in fusion. This point will be addressed in further details in a subsequent study but was out of the scope of this one.

4.6.5. Spatio-temporal simulations of realistic IEDs

Assessing neuronal propagation during interictal spikes may take benefit from spatio-temporal source analysis of EEG and MEG data (Hara et al., 2007; Tanaka et al., 2010, 2014). Using dSPM (Shiraishi, Stufflebeam, et al., 2005; Hara et al., 2007) and MNE (Tanaka et al., 2014), previous studies investigated the spatio-temporal source reconstruction of propagated MEG spikes. Although they based their results on averaged spikes localization due to the difficulty in localizing the low SNR individual spikes, it is more reliable to perform single spike localization to recover accurate information on the spike onset and propagation (cf. **Section 4.6.1**). In addition, by combining simultaneously occurring EEG and MEG spikes, the SNR for individual spikes can be increased and complementary information from both modalities will lead to better representation of the propagation patterns (Bast et al., 2004). Therefore, in the present study, simulations of two spatially extended propagating sources, with overlapping time courses, were used to assess the performance of MEEG localization using cMEM. We observed that MEEG localization using cMEM provided the highest detection accuracy for both source 1 and source 2 (**Figure 4.10**). Because of the overlap of topographies of the two sources in EEG, detection accuracy of source 2 was lower than source 1 in EEG localizations for both MNE and cMEM. On the other hand, MEG localizations provided similar detection accuracy for both sources due to smaller overlap between the topographies of the two sources. MEEG localization using MNE behaved similarly to EEG localization in detecting source 2 indicating the influence

of spatial blurring effect of EEG in the fusion. Interestingly, MEEG localization using cMEM showed good performance in separating the two sources with the help of additional key information brought by MEG that was nicely taken into account with the MEM fusion framework (**Figure 4.10** and **Figure 4.12**). This shows that the fusion of EEG and MEG within the MEM framework is able to improve upon the spatial resolution of EEG localization due to the complementarities of the two modalities.

In this study, through Shape Error metric (**Section 4.4.5d**), cMEM reconstructed time courses were evaluated for the first time. cMEM being a non-linear localization procedure applied independently and iteratively on each time sample of the data, the reconstruction of smooth time courses was not obvious, as opposed to MNE that consists in applying a linear projector to the data. While MNE provides excellent accuracy in reconstructing the shape of the time courses of spatio-temporal overlapping sources, it was an important finding that cMEM estimates for MEEG data were able to provide very good accuracy as well (**Figure 4.11**).

The main interest of this study was the fusion of EEG and MEG data within the MEM framework and comparison of cMEM method with MNE as the reference method was sufficient for this study. To address the issue of bias towards superficial sources known in MNE, we also included in our evaluation two noise-normalized variants of MNE: dSPM and sLORETA. Based on the results on static simulations, we concluded that despite the depth weighting property of dSPM and sLORETA, cMEM still provided an overall better spatial accuracy than dSPM and sLORETA, especially in the context of recovering source spatial extent. We did not provide a comparison of the cMEM method with the previously compared Hierarchical Bayesian methods (namely, Independent and Identically Distributed model-IID and spatially Coherent model - COH) as proposing MEEG fusion in this Bayesian framework was not the purpose of the study. However, in a recent paper from our group (Heers et al., 2015), we demonstrated the excellent performance of cMEM when compared to IID and COH, evaluating EEG/MEG source localization of IEDs on 15 patients, using intracranial EEG as a reference. Whereas we are fully aware

that analysis using realistic simulations suffers from some bias, these recent results demonstrated the applicability of our methods on real data. Moreover, following a similar strategy than the one proposed by (Wang and Ren, 2013), we showed that EEG and MEEG source localization using cMEM method was robust to the model-error introduced in the simulation protocol, and especially errors in brain-to-skull conductivity ratios. Currently, studies are in progress (Chowdhury et al., 2014) based on improved simulation paradigms: realistic simulations generated by neural mass model (Cosandier-Rimélé et al., 2010) and comparison of cMEM with other non-linear method such as 4-ExSo-MUSIC (Birot et al., 2011). Different variants of the MEM approach are now available for users as a toolbox (namely, BEst: Brain Entropy in space and time) in the Brainstorm software (Tadel et al., 2011), and the tutorial introducing this toolbox can be found here [9].

4.6.6. Performance of fusion on clinical data

A detailed clinical validation of cMEM fusion was out of our scope and will be considered for future studies. However, we illustrated the behavior of cMEM fusion on two clinical cases. For patient 1, MEEG localization found mainly the propagation of activity from left orbito-frontal to left temporal neocortex when MEG found mainly the orbito frontal and EEG found the temporal neocortex activity. This is interesting to see that we were able to find clear propagation pathway between the frontal lobe and the ipsilateral temporal lobe only when using MEEG localizations. Such reproducible findings on few single spikes suggest a good accuracy of the fusion cMEM method. However, for the purpose of providing clinically useful results, the consensus between many spikes should be certainly investigated. Recently, (Aydin, Vorwerk, Duempelmann, et al., 2014) showed that combined EEG-MEG source analysis reveals the propagation pathways in complete agreement to stereo –EEG (sEEG), while single modality EEG or MEG

[9] http://neuroimage.usc.edu/brainstorm/Tutorials/TutBEst

might only be sensitive to complementary parts of the epileptic activity. A study using Diffusion Tensor Imaging (Lin et al., 2008) described the connection between the anterior temporal lobe and the inferior frontal lobe to be mediated by the uncinate fasciculus (Makris and Pandya, 2009); thus supporting a well-known anatomical substrate for the propagation patterns identified for patient 1. Generally ipsilateral cortical propagation occurred within 30 ms (Zumsteg et al., 2006); which was also what we noticed in the propagation pattern presented in patient 1 (within 26.7 ms). It was shown in (Tanaka et al., 2010) that spatio-temporal analysis of averaged MEG data provides more accurate information on spike propagation than averaged EEG data. This was consistent with our findings in patient 1, even though we did not localize averaged data but we presented the average of six single spike localization results. The propagation pattern was not found by EEG localization but both the primary (orbitofrontal) and secondary (temporal neocortex) source were found in the average of MEG localization results (supplementary **Figure S4.1**). It was shown in (de Jongh et al., 2005) that the SNR of MEG is higher than EEG for frontal areas so MEG yields more spikes than EEG for frontal lobe epilepsy. The lower SNR spikes in EEG for frontal areas may explain why it was difficult to localize the orbito-frontal onset when using EEG only.

For Patient 2, MEEG using cMEM identified mainly a source in the inferior part of the left pre-central gyrus, which was in perfect overlap with the FCD of the patient. On the other hand, EEG and MEG localization identified mainly frontal sources which were probably secondary sources. A source closely related to the FCD was identified with MEG only on single spike localization. However, only MEEG enhanced the generators in the lesion as the primary source with largest amplitude. (Bast et al., 2004) investigated nine patients with localization-related epilepsy and FCD, and showed that it was important to average the EEG and MEG spikes from lesional zone to obtain an accurate localization of the MRI-defined lesion (Bast et al., 2004). (Heers et al., 2012) showed that the localization of averaged interictal MEG spikes was useful in locating subtle MR imaging abnormalities showing peri-insular lesion. (Hisashi Itabashi, 2014) studied six patients with FCD and showed

that source localization of averaged EEG and MEG spikes can confirm the existence of abnormalities associated with FCD based on MR imaging. On the other hand, we showed that localization of single spike of MEEG data found the origin of the spike consistently within the FCD lesion in patient 2. This confirms the advantage of localization of combined EEG and MEG data even in low SNR conditions. This is also in complete agreement with a recent study (Aydin et al., 2015), which investigated the contribution of combined EEG/MEG in comparison to single modality EEG or MEG source analysis of the epileptic activity using a dipole scanning approach. They validated their results with sEEG, where no major dipole cluster was noticeable neither with EEG nor with MEG around the active contacts in sEEG, while there were clear clusters around the active contacts in MEEG. They showed that MEEG localizations were not simply the union of EEG and MEG results but a rather complex interplay of both modalities compensating their relative shortcomings.

4.7. Conclusion

In this paper, we proposed symmetrical fusion of EEG and MEG within MEM framework as a novel method for localizing the onset and propagation patterns of spatially extended generators of IEDs. Effective integration of the complementary information from EEG and MEG in cMEM was demonstrated based on realistic simulations and illustrated on real epileptic data. Overall, for both mono-modal and multimodal data we noticed better performance of cMEM than MNE, dSPM and sLORETA in detecting the spatially extended and propagating sources. Our findings suggest that it is better to perform EEG-MEG fusion when localizing single spikes using cMEM: 1) To yield better recovery of the source spatial extent. 2) To improve the sensitivity to source depth. 3) To represent better the spatio-temporal propagation patterns of the underlying generators of epileptic discharges. We also showed that the addition of only few EEG electrodes brings additional information missed by MEG, in order to allow an optimal EEG-MEG fusion.

4.8. Acknowledgements

This project was funded by studentship from Savoy Foundation, grants from Natural Sciences and Engineering Research Council of Canada (NSERC) and Fonds de la recherche en santé du Québec (FRSQ). The EEG-MEG acquisitions on patients were funded by Canadian Institutes of Health Research (CIHR), Centres of Excellence for Commercialization of Research (CECR) and the American Epilepsy Society award.

4.9. Appendix A

AUC estimation: To assess how a source localization method could be sensitive to the spatial extent of the underlying generator, AUC metric was adapted by (Grova et al., 2006) to fit the context of a distributed source model, in order to take into account that there are quite more inactive dipolar sources than active sources in our simulation schemes.

This detection accuracy index is estimated when the Ground truth is available, where ROC curves are generated by plotting the sensitivity against the false positive detection rate for different detection thresholds, ($\beta \in [0,1]$). Normalized energy for both the estimated and the simulated current distribution were used to quantify the amount of true positive (TP), true negative (TN), false negative (FN), and false positive (FP) for each threshold β.

$$sensitivity(\beta) = TP(\beta)/(TP(\beta) + FN(\beta))$$

$$specificity(\beta) = TN(\beta)/(TN(\beta) + FP(\beta))$$

However, to interpret the area under the ROC curve as a detection accuracy index, one should provide the same number of active and inactive sources to the ROC analysis. Considering the p dipolar sources on the cortical surface, only few dipoles were actually active (p_a) compared to the large number of inactive dipoles (p - p_a). Therefore, selection of same number of inactive sources as the active sources is required. This was done by randomly selecting inactive sources among the p - p_a

sources located within the immediate spatial neighborhood of the simulated source (**AUC_{close}**) or among the local maxima of the reconstructed activity located far from the simulated source **(AUC_{far})**. Final **AUC** index was then computed as a mean of the **AUC_{close}** and **AUC_{far}**.

Chapter 5 Manuscript 2: Complex patterns of spatially extended generators of epileptic activity: Comparison of source localization methods cMEM and 4-ExSo-MUSIC on High Resolution EEG and MEG data

5.1. Context

In chapter 4, we demonstrated the ability of cMEM source localization to accurately reconstruct the spatio-temporal propagation patterns of the underlying generators of epileptic activity based on simple simulation model and on two examples of clinical data. This interesting finding motivated us to further explore the behavior of cMEM on more realistic simulations mimicking complex patterns of epileptic discharges. A fair comparison between EEG and MEG localization entails the use of densely sampled recording channels and realistic forward models during EEG and MEG source analysis (chapter 3). Besides, the performance of cMEM algorithm has never been studied when dealing with high resolution EEG and MEG data or on complex patterns of IEDs. Furthermore, it is essential to compare the performance of cMEM with another advanced source localization algorithm that has also been established for its ability to localize the spatially extended generators of IEDs. In line with this, 4-ExSo-MUSIC (4th order Extended Source Multiple Signal Classification) is one such distributed source localization algorithm that was implemented by the research team UMR INSERM U1099, LTSI (Laboratoire de Traitement de l'Image et du signal) in Université de Rennes 1, France. This led to the next study of this dissertation, which was a collaborative study with the LTSI team. With their expertise (Dr. Isabelle Merlet and Dr. Laurent Albera, the main collaborators for this project) in spatio-temporal simulations based on neural mass

model, we were able to generate fully realistic simulations mimicking different patterns of IEDs.

Therefore, manuscript 2 presents this collaborative study involving a quantitative assessment of cMEM and 4-ExSo-MUSIC using a highly realistic simulation pipeline that combines a biophysical distributed model with a computational neural mass model to generate simultaneous high resolution EEG and MEG signals mimicking normal background and epileptic discharges.

This manuscript was published as (R.A. Chowdhury, I. Merlet, G. Birot, E. Kobayashi, A. Nica, A. Biraben, F. Wendling, J.M. Lina, L. Albera, C. Grova. *Complex patterns of spatially extended generators of epileptic activity: Comparison of source localization methods cMEM and 4-ExSo-MUSIC on high Resolution EEG and MEG data*, NeuroImage, August 2016 (In Press)).

5.2. Abstract

Electric Source Imaging (ESI) and Magnetic Source Imaging (MSI) of EEG and MEG signals are widely used to determine the origin of interictal epileptic discharges during the pre-surgical evaluation of patients with epilepsy. Epileptic discharges are detectable on EEG/MEG scalp recordings only when associated with a spatially extended cortical generator of several square centimeters, therefore it is essential to assess the ability of source localization methods to recover such spatial extent.

In this study we evaluated two source localization methods that have been developed for localizing spatially extended sources using EEG/MEG data: coherent Maximum Entropy on the Mean (cMEM) and 4th order Extended Source Multiple Signal Classification (4-ExSo-MUSIC). In order to propose a fair comparison of the performances of the two methods in MEG versus EEG, this study considered realistic simulations of simultaneous EEG/MEG acquisitions taking into account an equivalent number of channels in EEG (257 electrodes) and MEG (275 sensors), involving a biophysical computational neural mass model of neuronal discharges

and realistically shaped head models. cMEM and 4-ExSo-MUSIC were evaluated for their sensitivity to localize complex patterns of epileptic discharges which includes (a) different locations and spatial extents of multiple synchronous sources, and (b) propagation patterns exhibited by epileptic discharges. Performance of the source localization methods was assessed using a detection accuracy index (Area Under receiver operating characteristic Curve, AUC) and a Spatial Dispersion (SD) metric. Finally, we also presented two examples illustrating the performance of cMEM and 4-ExSo-MUSIC on clinical data recorded using high resolution EEG and MEG.

When simulating single sources at different locations, both 4-ExSo-MUSIC and cMEM exhibited excellent performance (median AUC significantly larger than 0.8 for EEG and MEG), whereas, only for EEG, 4-ExSo-MUSIC showed significantly larger AUC values than cMEM. On the other hand, cMEM showed significantly lower SD values than 4-ExSo-MUSIC for both EEG and MEG. When assessing the impact of the source spatial extent, both methods provided consistent and reliable detection accuracy for a wide range of source spatial extents (source sizes ranging from 3 to 20 cm^2 for MEG and 3 to 30 cm^2 for EEG). For both EEG and MEG, 4-ExSo-MUSIC localized single source of large signal-to-noise ratio better than cMEM. In the presence of two synchronous sources, cMEM was able to distinguish well the two sources (their location and spatial extent), while 4-ExSo-MUSIC only retrieved one of them. cMEM was able to detect the spatio-temporal propagation patterns of two synchronous activities while 4-ExSo-MUSIC favored the strongest source activity.

Overall, in the context of localizing sources of epileptic discharges from EEG and MEG data, 4-ExSo-MUSIC and cMEM were found accurately sensitive to the location and spatial extent of the sources, with some complementarities. Therefore, they are both eligible for application on clinical data.

5.3. Introduction

ElectroEncephaloGraphy (EEG) and MagnetoEncephaloGraphy (MEG) have been widely used as a non-invasive technique to identify brain activation patterns associated with normal or pathological processes. Due to their high temporal resolution, these techniques are particularly appropriate for following the time course of activation during fast transients such as evoked potentials, epileptic discharges or specific oscillatory patterns (Lopes da Silva, 2013). In the particular context of epilepsy, interictal epileptic discharges (IEDs), recorded between seizures with MEG and EEG in the form of spikes, spike and waves, sharp waves, provide important information on the spatial organization of the epileptogenic network, provided that they can be localized accurately. It is now admitted that IEDs recruit a rather large area of cortex in a quasi-synchronous manner. Thus, to be detected on surface recordings, a minimum area of 4−8 cm^2 for EEG (Cooper et al., 1965; Ebersole, 1997a; Merlet and Gotman, 1999; Tao, Baldwin, Hawes-Ebersole, et al., 2007; von Ellenrieder et al., 2014b) and of 3−4 cm^2 for MEG (Hari, 1990; Mikuni et al., 1997; Oishi et al., 2002) has been suggested as activated during IEDs. Therefore, not only is it important to localize the origin of IEDs but also to recover their spatial extent and estimate the temporal course of their activity. This task can become particularly challenging when several distributed regions with highly synchronized activity are simultaneously active or are involved during a propagation process.

To meet this challenge, source localization approaches continue to be developed over the past 40 years and have helped to better define the spatial properties of the regions underlying EEG or MEG transients. The reconstruction of spatially extended cortical sources entails the use of distributed source models, as equivalent current dipole modeling can be misleading for large sources (Kobayashi et al., 2005). Several studies have proposed to localize extended cortical patches using beamformer (Limpiti et al., 2006; Hillebrand and Barnes, 2011), probabilistic approaches based on maximum entropy (Amblard et al., 2004; Grova et al., 2006; Chowdhury et al., 2013), subspace-based approaches (Birot et al., 2011), tensor-

based techniques (Becker et al., 2015), and methods using sparsity in a transformed domain (Ding, 2009a; Zhu et al., 2014). Several of these methods showed sensitivity to source spatial extents when assessed using controlled simulations (Jerbi et al., 2002; Kincses et al., 2003; Limpiti et al., 2006; Ding, 2009a; Cheyne et al., 2010; Huiskamp et al., 2010; Birot et al., 2011; Bouet et al., 2012; Chowdhury et al., 2013; Lina et al., 2014; Becker et al., 2015) and/or when applied on real epileptic activity (Cheyne et al., 2010; Huiskamp et al., 2010; Jung et al., 2013; Zhu et al., 2013; Chowdhury et al., 2015; Grova et al., 2016; Heers et al., 2016). Among them, two approaches, developed separately by our two research teams, have been quantitatively studied for their ability to localize spatially extended sources of epileptic events, based both on simulations and real EEG and/or MEG data. The first method is a probabilistic approach based on maximum entropy, known as coherent Maximum Entropy on the Mean (cMEM), which employs a full brain parcellization model by incorporating two spatial priors: Data Driven Parcellization (DDP) and spatial coherence prior to model locally spatially smooth cortical parcels. Then, based on the state of activation of the parcels, cMEM is able to switch off some parcels while creating contrast of source intensities among other parcels. The method takes advantage of whole cortex parcellization and spatial smoothness constraint to properly recover the spatial extent of sources (Amblard et al., 2004; Grova et al., 2006; Chowdhury et al., 2013; Grova et al., 2016; Heers et al., 2016). The second method is a subspace-based MUSIC-like approach, known as 4-ExSo-MUSIC (4th order Extended Source Multiple Signal Classification), specifically adapted to localize extended sources by exploiting the strong synchronization of dipoles within each extended source (Birot et al., 2011). The use of 4^{th} order statistics in 4-ExSo-MUSIC offers robustness with respect to Gaussian noise and modeling errors. In some recent studies (Chowdhury et al., 2013, 2015; Grova et al., 2016; Heers et al., 2016), it was shown that cMEM is able to recover the spatial extent and the propagation pattern of sources more accurately than Minimum Norm Estimate (MNE) (Hämäläinen and Ilmoniemi, 1994), standardized Low Resolution brain Electromagnetic Tomography (sLORETA) (Pascual-Marqui, 2002), dynamic

Statistical Parametric Mapping (dSPM) (Dale et al., 2000) and various hierarchical Bayesian approaches (Friston et al., 2008). In other separate studies (Birot et al., 2011; Becker, Albera, Comon, Haardt, et al., 2014a), 4-ExSo-MUSIC estimated the spatial extent of generators of epileptic activity with more accuracy than other MUSIC-based approaches, sLORETA, CHAMPAGNE (Wipf et al., 2010), Minimum Current Estimate (MCE) (Uutela et al., 1999), or Mixed Norm Estimate (MxNE) (Ou et al., 2009).

In the present contribution, our first objective was to carefully compare these two methods. To do so, we used a common ground-truth well-controlled simulation environment involving complex patterns of source configurations in particular with respect to the number of sources, their spatial properties, and their level of synchronization. To this end, we used a highly realistic simulation pipeline that combines a biophysical distributed dipole source model with a computational neural mass model (Cosandier-Rimélé et al., 2008) to generate simultaneous EEG and MEG synthetic signals mimicking normal background and epileptic discharges.

Most of the studies that have compared MEG and EEG on clinical data, were acquired using fewer EEG electrodes than MEG sensors (Barkley and Baumgartner, 2003; Malmivuo, 2012; Lopes da Silva, 2013). These studies have demonstrated that MEG localization was more accurate. However, some simulation studies have suggested higher accuracy of EEG localization when an equivalent number of EEG and MEG channels are used (Liu et al., 2002; Song et al., 2015). The advent of dense array EEG caps and of source estimation techniques resulted in a higher spatial accuracy (Ryynanen et al., 2006; Babiloni et al., 2009; Brodbeck et al., 2011; Gavaret et al., 2015). Other studies also demonstrated that improvement in terms of localization can be attained when using a high density scalp electrodes and realistic geometry head models (Lantz and Grave de Peralta, 2003; Wang et al., 2011; Birot et al., 2014; Klamer et al., 2015). Therefore, to get the best of each modality simultaneously, the present study makes use of realistically simulated high resolution EEG (HR-EEG) and MEG data while taking

into account an equivalent number of channels, realistically shaped head model and simultaneous recordings.

The outline of the paper is as follows. First, introduction of the two source localization methods (cMEM and 4-ExSo-MUSIC) is proposed, followed by the description of the realistic simulation dataset. Then, an explanation of the evaluation process and the performance criteria to assess the source localization of both the methods is given. This is followed by the description of the clinical dataset. Then the results, discussion and conclusion are provided.

5.4. Methods and materials

The goal of this study was to compare the performance of the cMEM and 4-ExSo-MUSIC algorithms on different patterns of IEDs seen in HR-EEG and MEG data, mainly to compare the ability of the methods:

- To recover the location and spatial extent of the spatially extended generators of IEDs.
- To identify the propagation patterns exhibited by IEDs.
- To handle multiple sources of IEDs with different levels of synchrony.

5.4.1. Source localization algorithms

a. EEG/MEG inverse solution using distributed source model

It is commonly admitted that the EEG/MEG signals recorded at the head surface mostly reflect the activity of pyramidal cells within the cortex. These activities can be modelled by current dipoles distributed along the cortical surface, and oriented orthogonally to the cortical surface (Dale and Sereno, 1993). Using this anatomical constraint, the relationship between source amplitudes and EEG/MEG measurements can be expressed by the following linear model:

$$\boldsymbol{m}(t) = \boldsymbol{G}\,\boldsymbol{j}(t) + \boldsymbol{e}(t) \qquad (5\text{-}1)$$

where $\boldsymbol{m}(t)$ is a q-dimensional vector of the EEG/MEG signal measured with q=275 MEG sensors or 257 EEG electrodes at time t. $\boldsymbol{e}(t)$ models an additive measurement noise at time t. $\boldsymbol{j}(t)$ is an r-dimensional vector standing for the unknown current density along the cortical surface ($r\approx$8000: unknown dipolar moment amplitudes) at time t. $\boldsymbol{G}$ is the (qxr) lead field matrix obtained by solving the forward problem to estimate the contribution of each dipolar source on the sensors.

To describe cMEM and 4-ExSO-MUSIC that are statistical algorithms, we introduce a random vector **m** (respectively **j** and **e**) to model the τ recorded samples $\{\boldsymbol{m}(t)\}$ (respectively $\{\boldsymbol{j}(t)\}$ and $\{\boldsymbol{e}(t)\}$). According to equation (5-1), **m** can be related to **j** and **e** as follows:

$$\mathbf{m} = \boldsymbol{G}\,\mathbf{j} + \mathbf{e} \tag{5-2}$$

Within the distributed dipole layer, defined as the source space Ω, each dipole is characterized by its location $\rho \in \Omega$ and its current density j(ρ). Thus, to describe the 4-ExSo-MUSIC algorithm (**Section 5.4.1c**) equation (5-2) is reformulated as:

$$\mathbf{m} = \sum_{\rho \in \Omega} \boldsymbol{g}(\rho)\,\mathrm{j}(\rho) + \mathbf{e} \tag{5-3}$$

where j(ρ) is a component of vector **j** representing the activity of a dipole at location ρ and $\boldsymbol{g}(\rho)$ is a column vector of matrix $\boldsymbol{G}$ representing the contribution of a unitary dipole located at ρ to the set of EEG/MEG sensors.

b. cMEM algorithm

In the MEM framework (Amblard et al., 2004), **j** being the r-dimensional continuous random variable that describes the dipole intensities, this variable has the probability distribution $dp(\mathbf{j}) = p(\mathbf{j})d\mathbf{j}$ where $\mathbf{j} \in \mathbb{R}^r$.

To regularize the inverse problem, the MEM framework incorporates prior information on **j** in the form of a reference distribution $d\nu(\mathbf{j})$. Then, the Kullback Leibler divergence or ν-entropy defined by:

$$S_\nu(dp) = -\int_{\mathbf{j}} \log\left(\frac{dp(\mathbf{j})}{d\nu(\mathbf{j})}\right) dp(\mathbf{j}) = -\int_{\mathbf{j}} f(\mathbf{j}) \log(f(\mathbf{j}))\, d\nu(\mathbf{j}) \qquad (5\text{-}4)$$

measures the amount of information brought by the data with respect to the prior $d\nu$, where f is a ν-density of dp defined as, $dp(\mathbf{j}) = f(\mathbf{j})\, d\nu(\mathbf{j})$. Being a pseudo-distance between the reference distribution $d\nu$ and any ν-density dp, this entropy is always negative.

In order to introduce a data fit constraint, let us denote $\mathbb{C}_m$ as the set of probability distributions on **j** that explains the data on average:

$$dp \in \mathbb{C}_m : \quad \mathbf{m} - \left[\boldsymbol{G} \middle| \boldsymbol{I}_q\right] \begin{bmatrix} \mathrm{E}_{dp}[\mathbf{j}] \\ \mathbf{e} \end{bmatrix} = 0 \qquad (5\text{-}5)$$

where $\mathrm{E}_{dp}[\mathbf{j}] = \int_{\mathbb{R}} \mathbf{j}\, dp(\mathbf{j})$ is the mathematical expectation of **j** with respect to the probability distribution dp, $\boldsymbol{I}_q$ is a (qxq) identity matrix.

Then, the MEM solution consists in selecting $d\hat{p}$ in $\mathbb{C}_m$ that maximizes the ν-entropy, thus choosing the distribution fulfilling the data fit constraint that is the closest (in terms of Kullback Leibler divergence) to the reference distribution $d\nu$:

$$d\hat{p} = \mathrm{argmax}_{dp \in \mathbb{C}_m} S_\nu(dp) \qquad (5\text{-}6)$$

Such a regularization framework allows us to estimate the MEM solution through a non-linear optimization of a convex function within a q-dimensional space, iteratively for each time sample. This solution is unique and describes only what we "know": the prior knowledge encompassed in the reference measure $d\nu$, and the measurements $\{\boldsymbol{m}(t)\}$ that define the space $\mathbb{C}_m$ formalizing our data fit constraint (equation (5-5)). During the MEM optimization process, the noise covariance model is estimated as a diagonal matrix with a different value for each channel; thus taking into account the noise levels of each individual channel.

The MEM estimate of the source intensities $\hat{\mathbf{j}}$ is then computed as the mathematical expected value of the distribution $d\hat{p}$:

$$\hat{\mathbf{j}} = \mathrm{E}_{d\hat{p}}[\mathbf{j}] \tag{5-7}$$

Definition of the reference distribution dv **:** MEM relies on its inherent flexibility of introducing constraints or knowledge about the sources through the definition of the reference distribution dv. To do so, we considered brain activity to be organized into *K* cortical parcels, each parcel showing a homogeneous activation state (Amblard et al., 2004). We used a Data Driven Parcellization (DDP) method to perform full parceling of the tessellated cortical surface into non-overlapping parcels (Lapalme et al., 2006). This spatial parcelling is driven by the Multivariate Source Pre-localization (MSP) technique (Mattout et al., 2005), which is a projection method providing a coefficient for each dipolar source characterizing its contribution to the data. For more details on the DDP method please refer to (Chowdhury et al., 2013).

Each cortical parcel *k* is characterized by an activation state S_k, describing if the parcel is active or not. Assuming a collection of mutually independent parcels, the reference distribution dv was defined as a factorization of the joint probability distribution of the *K* parcels:

$$dv(\mathbf{j}) = \prod_{k=1}^{K} \left[\left(1-\alpha_k\right) \delta\left(\mathbf{j}_k\right) + \alpha_k \; \mathcal{N}\left(\boldsymbol{\mu}_k, \boldsymbol{\Sigma}_k\right)\left(\mathbf{j}_k\right) \right] d\mathbf{j} \tag{5-8}$$

where $\alpha_k = Prob\left(\mathrm{S}_k = 1\right)$ is the probability of the k^{th} parcel to be active. $\mathbf{j}_k$ denotes the random vector modeling the intensities of the r_k sources in the k^{th} parcel. δ refers to the Dirac distribution allowing to "shut down" inactive parcels when $\mathrm{S}_k = 0$. $\mathcal{N}\left(\boldsymbol{\mu}_k, \boldsymbol{\Sigma}_k\right)$ is a Gaussian distribution modeling the intensities of the k^{th} parcel when active $(\mathrm{S}_k = 1)$, where $\boldsymbol{\mu}_k$ and $\boldsymbol{\Sigma}_k$ represent the mean and the covariance, respectively, of the r_k sources within the k^{th} parcel. For more details on MEM regularization technique refer to **Appendix A**.

In the present study, we considered the variant of MEM algorithm called coherent-MEM (cMEM) implementation, as described in (Chowdhury et al., 2013). In cMEM, additional constraint of local spatial smoothness in each parcel was

introduced using diffusion-based spatial priors (Friston et al., 2008) in the initialization of the source covariance of every parcel ($\mathbf{\Sigma}_k$ $\{Sigma\}_{k}$). This diffusion-based spatial prior is constructed using the Green's function of the adjacency or spatial connectivity matrix defined over the geodesic cortical surface (Harrison et al., 2007). The mean intensity of every parcel ($\mathbf{\mu}_k$) was initialized to zero. The probability of activation (α_k) of each parcel k was initialized at each time sample as the median of the MSP coefficients of all the r_k sources within the k^{th} parcel. The spatial neighborhood order considered for the parcels has been fixed to a scale of 4, leading to approximately K=200 parcels of size ≈2.5 cm^2. Please refer to (Chowdhury et al., 2013) for further details on the initialization of these parameters.

MEM approach is now available for users as a toolbox (namely, BEst: Brain Entropy in space and time) in the Brainstorm software (Tadel et al., 2011) and the tutorial introducing this toolbox can be downloaded ("Tutorials/TutBEst - Brainstorm," 2015).

c. 4-ExSo-MUSIC algorithm

4-ExSo-MUSIC is a subspace-based method which aims at extending the classical MUSIC method (Schmidt, 1986; Mosher et al., 1992) to the case of distributed sources by means of higher order statistics (Birot et al., 2011). More particularly, the sources to be localized are assumed to exhibit dipoles with highly synchronized activities (Birot et al., 2011). This property is justified by the fact that EEG/MEG signals, to be detectable on scalp, arise from the summation of highly synchronized neuronal assemblies over a spatially extended region.

Then, the EEG/MEG data can be considered as the sum of the epileptic activities arising from the subset $\Theta \subset \Omega$ and normal background activity arising from $\Omega \setminus \Theta$, such that the EEG/MEG vector is represented as follows:

$$\mathbf{m} = \sum_{\rho \in \Theta} \boldsymbol{g}(\rho)\, \mathrm{j}(\rho) + \sum_{\rho \in \Omega \setminus \Theta} \boldsymbol{g}(\rho)\, \mathrm{j}(\rho) + \mathbf{e} = \sum_{\rho \in \Theta} \boldsymbol{g}(\rho)\, \mathrm{j}(\rho) + \boldsymbol{\varepsilon} \tag{5-9}$$

where the sum over Θ models the contribution of the epileptic activity, i.e. the sources of interest while the sum over $\Omega \setminus \Theta$ models the contribution of the background activity, i.e. the sources of non-interest. In addition, let the term $\boldsymbol{\varepsilon}$ model the physiological background and the instrument noise, which can be seen as a Gaussian random vector of unknown spatial covariance and independent from the epileptic sources.

4-ExSo-MUSIC aims at estimating the spatial support Θ of the generators of epileptic activity. 4-ExSo-MUSIC reformulates the spatial support Θ as the union of B circular shaped disks Θ_b, where $1 \leq b \leq B$. The search for this spatial support Θ is actually formulated within a grid containing pseudo-disks of different size over the whole cortical surface. Since the source space is a triangular mesh of the cortical surface, these pseudo-disks of different size were constructed around each vertex on the cortical surface. Each disk was composed of a maximum of 500 adjacent vertices. This set of pseudo-disks of different size for every vertex defines the so-called 4-ExSo-MUSIC grid. The model assumes that all dipolar sources belonging to one disk Θ_b should exhibit the same current density j_b (and consequently the same time course). Then, equation 9 can be reformulated as follows:

$$\begin{aligned} \mathbf{m} &= \sum_{b=1}^{B} \mathrm{j}_b \sum_{\rho \in \Theta_b} \boldsymbol{g}(\rho) + \boldsymbol{\varepsilon} = \sum_{b=1}^{B} \boldsymbol{h}(\Theta_b)\, \mathrm{j}_b + \boldsymbol{\varepsilon} \\ \mathbf{m} &= \boldsymbol{H}(\Theta)\, \mathbf{j}_\Theta + \boldsymbol{\varepsilon} \end{aligned} \tag{5-10}$$

where the b^{th} column vector of the mixing matrix $\boldsymbol{H}(\Theta)$ and the b^{th} component of the source random vector $\mathbf{j}_\Theta = [\mathrm{j}_1, ..., \mathrm{j}_B]^T$ are $\boldsymbol{h}(\Theta_b)$ and j_b, respectively.

Each set of contiguous distinct disks Θ_b represents a so-called Extended Source (ExSo). Moreover, 4-ExSo-MUSIC relies on the assumption that the current densities of the ExSos do not follow a Gaussian distribution, which is an appropriate assumption for most of the signals of interest in EEG/MEG such as

interictal epileptic signals (Nurujjaman et al., 2009). Therefore, the method considers the 4th order cumulants (and more particularly their matrix form called quadricovariance) of **m** to reduce the penalizing effects of the random vector noise $\boldsymbol{\varepsilon}$ (i.e. the background cerebral activity and the instrument noise) that can be seen as a Gaussian and spatially correlated noise. The important property exploited here is that the 4th order cumulant of a Gaussian distribution is zero, therefore one can hypothesize that 4-ExSo-MUSIC would be robust with respect to the presence of background activity and instrumental noise.

Exploiting the linear model proposed in equation 10, the quadricovariance matrix, $\boldsymbol{C}_{4,m}$, of the data can be written as a function of Θ as follows:

$$\boldsymbol{C}_{4,m} = \boldsymbol{H}(\Theta)^{\otimes 2}\boldsymbol{C}_{4,j}\left[\boldsymbol{H}(\Theta)^{\otimes 2}\right]^{T} \tag{5-11}$$

where $\boldsymbol{H}(\Theta)^{\otimes 2}$ is the Kronecker product of the matrix $\boldsymbol{H}(\Theta)$ by itself and $\boldsymbol{C}_{4,j}$ is the quadricovariance matrix of $\mathbf{j}_{\Theta}$. Note that there is no more contribution from the noise $\boldsymbol{\varepsilon}$ since its quadricovariance is zero. Therefore, the 4th order signal subspace of interest, defined as $\text{span}\{\boldsymbol{H}(\Theta)^{\otimes 2}\}$, can be directly estimated from the quadricovariance matrix $\boldsymbol{C}_{4,m}$ since $\text{span}\{\boldsymbol{H}(\Theta)^{\otimes 2}\} = \text{span}\{\boldsymbol{C}_{4,m}\}$.

To do so, the 4th order signal subspace of interest is obtained from an eigenvalue decomposition of $\boldsymbol{C}_{4,m}$. 4-ExSo-MUSIC then exploits the fact that the vector $\boldsymbol{h}(\Theta_b)^{\otimes 2}$ must lie in the 4th order signal subspace computed from $\boldsymbol{C}_{4,m}$.

The spatial support $\Theta = \bigcup_{1\le b\le B}\Theta_b$ of epileptic dipoles was identified by concatenating all the candidates Θ_b such that $\boldsymbol{h}(\Theta_b)^{\otimes 2}$ belongs to the 4th order signal subspace. To do so, the 4-ExSo-MUSIC algorithm consists in scanning the cortex with a grid of disks to estimate the candidates $\boldsymbol{h}(\Theta_b)^{\otimes 2}$ that minimizes the following criterion:

$$\Gamma(\boldsymbol{E}_{4,m}, \boldsymbol{h}(\Theta_b)) = 1 - \frac{\left(\left[\boldsymbol{h}(\Theta_b)^{\otimes 2} \right]^{\mathrm{T}} \boldsymbol{E}_{4,m} \boldsymbol{E}_{4,m}{}^{\mathrm{T}} \boldsymbol{h}(\Theta_b)^{\otimes 2} \right)}{\left\| \boldsymbol{h}(\Theta_b)^{\otimes 2} \right\|_2^2} \qquad (5\text{-}12)$$

where $\boldsymbol{E}_{4,m}$ is the matrix of the eigenvectors associated with the non-zero eigenvalues of $\boldsymbol{C}_{4,m.}$ Providing an exhaustive search to estimate this criterion on every pseudo-disk of the 4-ExSo-MUSIC grid would not be feasible because of computational cost. Therefore, a first scan of the cortex with a coarse grid of disks, for which the size of the disks was fixed to 20, is performed. With this first scan, a region in the cortex is selected according to the corresponding values of the metric. To define this region, the 200 lowest values of the "first-scan-metric" are identified, and the 200 corresponding disks of size 20 are concatenated. Then the original 4-ExSo-MUSIC grid (disk sizes varying from 1 to 500 dipoles) is used but only on this selected region. Finally, the relative contribution of a disk to the 4th order signal subspace (also called metric, as estimated through the second term $\left(\frac{\left(\left[\boldsymbol{h}(\Theta_b)^{\otimes 2} \right]^{\mathrm{T}} \boldsymbol{E}_{4,m} \boldsymbol{E}_{4,m}{}^{\mathrm{T}} \boldsymbol{h}(\Theta_b)^{\otimes 2} \right)}{\left\| \boldsymbol{h}(\Theta_b)^{\otimes 2} \right\|_2^2} \right)$ of equation (5-12)), allowed estimating the most appropriate disk size for every selected vertex. At the end of this second step, every vertex is then associated with a pseudo-disk of specific size (between 1 to 500 dipoles) and a metric value. This metric quantifies the contribution of all the dipoles of the pseudo-disk to the signal subspace.

Finally, the Goodness-Of-Fit (GOF) criterion (equation (5-13)) is used in order to select the optimal concatenation of those pseudo-disks.

$$\mathrm{GOF} = \sqrt{\frac{\sum_t \left\| \mathbf{m}(t) - \mathbf{m}_{\mathrm{rec}}(t) \right\|_2^2}{\sum_t \left\| \mathbf{m}(t) \right\|_2^2}} \qquad (5\text{-}13)$$

where $\{\boldsymbol{m}_{\mathrm{rec}}(t)\}$ corresponds to the data that is reconstructed from the estimated source configuration and $\{\boldsymbol{m}(t)\}$ is the measured data matrix. The source configuration that provides the lowest GOF value is considered the best fit for the

actual ExSo. This provides a binary map of the estimated source, also called the thresholded 4-ExSo-MUSIC map that is stable along time.

The time course of the estimated source configuration was obtained from a least square fit between the mixing matrix $\boldsymbol{H}(\Theta)$ for the estimated source configuration and the measured data $\{\boldsymbol{m}(t)\}$.

Similarly, to all-MUSIC approaches, it is required to indicate the number of underlying ExSos a priori in the 4-ExSo-MUSIC approach. Assuming X as the number of underlying sources expected a priori, the number of underlying sources considered by 4-ExSo-MUSIC was set to $X(X+1)/2$ when the sources were assumed to be correlated and as X when the sources were assumed to be independent.

5.4.2. Evaluation using realistic simulations

In order to evaluate and compare cMEM and 4-ExSo-MUSIC within a controlled environment, realistic simulations of EEG and MEG data were generated based on information regarding the number and position of the EEG/MEG channels during a simultaneous EEG/MEG data acquisition using a 275 channel CTF-MEG system and a HR-EEG EGI system (257 electrodes). The distributed source space consisted in a mesh (8000 vertices) of the cortical surface that was obtained by segmenting the gray-white matter interface from a subject's anatomical MRI using BrainVISA-4.2.1 software[10] (Mangin et al., 1995). Using the OpenMEEG (Gramfort et al., 2011) implementation in Brainstorm software (Tadel et al., 2011), we generated a 3-layer EEG Boundary Element Method (BEM) model consisting of the inner skull, outer skull and the scalp surfaces, with corresponding conductivity values of 0.33:0.0165:0.33 S/m respectively (Ferree et al., 2000; Hoekema et al., 2003; Lai et al., 2005). For the MEG forward problem, we considered a 1-layer BEM model consisting of the inner skull surface, with brain conductivity value of 0.33 S/m.

[10] http://www.brainvisa.info

We used a biophysical distributed dipole source model with a computational neural mass model (Wendling et al., 2000; Wendling, 2005) to generate normal background and epileptic spike-like activity. The reader may refer to (Cosandier-Rimélé et al., 2007, 2008, 2010) for detailed description of neural mass model and of the pipeline used to simulate data. In brief, we assumed a spatio-temporal source model where the neocortical pyramidal neurons were the main contributors of EEG/MEG signals. This source space was modeled by a dipolar layer distributed along the cortical surface, where each dipole corresponded to a distinct neuronal population of the neural mass model (**Figure 5.1A**). Time activities of all dipoles of the source space were generated with the neural mass model in which excitation and inhibition parameters of each neuronal population can be adjusted to obtain either epileptic spikes or background activity (**Figure 5.1B**). With an appropriate setting of coupling parameters between populations, a spatially extended generator exhibiting highly synchronized epileptic activity was constructed. The spatially extended source was made of contiguous triangles manually outlined using a mesh visualization software (Paraview, Kitware Inc., NY, US) (**Figure 5.1C**). Dipoles within the spatially extended source were associated to coupled neuronal populations, tuned to generate highly correlated epileptic activity. The remaining triangles of the mesh were then grouped into 1000 clusters. The dipoles of each cluster were then associated to a neuronal population tuned to generate normal background activity. These populations were not coupled in order to generate uncorrelated background activity. Moreover, when two spatially extended generators were simulated, spike propagation from a population *i* to a population *l* was obtained by assigning the same time course to the two populations and then introducing a propagation delay drawn randomly between 16 and 20 ms (**Figure 5.1B**). According to the scenario considered, we varied the size, location, number of sources or the level of synchronization between neuronal populations and the time delay between populations' activities.

Once the amplitude of each elementary dipole is known the forward problem is applied in order to compute the corresponding EEG and MEG signals (**Figure**

5.1D). Then, the inverse problem consisted in inferring the sources of activity $\{\boldsymbol{j}(t)\}$ based on the simulated measurement at the sensors' level $\{\boldsymbol{m}(t)\}$. Each trial consisted in the simulation of a 10s segment of EEG/MEG data (5120 time samples at 512 Hz) following different simulation schemes. For the inverse problem, in the EEG gain matrix a slightly different value was used for the skull conductivity - 0.0150 S/m instead of 0.0165 S/m.

The following scenarios have been considered. For each scenario, 20 EEG and MEG trials were simulated, each consisting of a new realization for the spiking activity and for the background activity. Consequently, each trial consisted of at least 3 or more spikes simulated within a 10 s window:

1. A single source at 10 different locations: posterior bank of the central sulcus (CS), basal temporal region (BT), mesial orbito-frontal gyrus (OF), supplementary motor area (SMA), inferior parietal region (P), insula, lateral orbito-frontal region, temporal pole, superior temporal region and occipital region. The source size was around 10 cm^2.
2. A single source with different spatial extents at three different locations: posterior bank of the central sulcus (CS), basal temporal region (BT), inferior parietal region (P). The source area was set to 0.5 cm^2, 1 cm^2, 2 cm^2, 3 cm^2, 4 cm^2, 5 cm^2, 7.5 cm^2, 10 cm^2, 20 cm^2, and 30 cm^2.
3. Two sources with synchronous activities: inferior temporal (patch 1) and parietal (patch 2) source of size 10cm^2 each. Time course of dipoles were highly synchronized in each source. In order to mimic two synchronous activities, the dipoles of the parietal source were attributed with the same temporal dynamics as the dipoles of the inferior temporal source.

4. Two sources with propagated activity: inferior temporal (patch 1) and parietal (patch 2) source of size 10cm^2 each. Time course of dipoles were highly synchronized in each source but activities attributed to dipoles of the parietal source were temporally delayed with respect to activities attributed to the dipoles of the

temporal source. The temporal delay was randomly chosen between 16 and 20 ms for each realization of propagating activity.

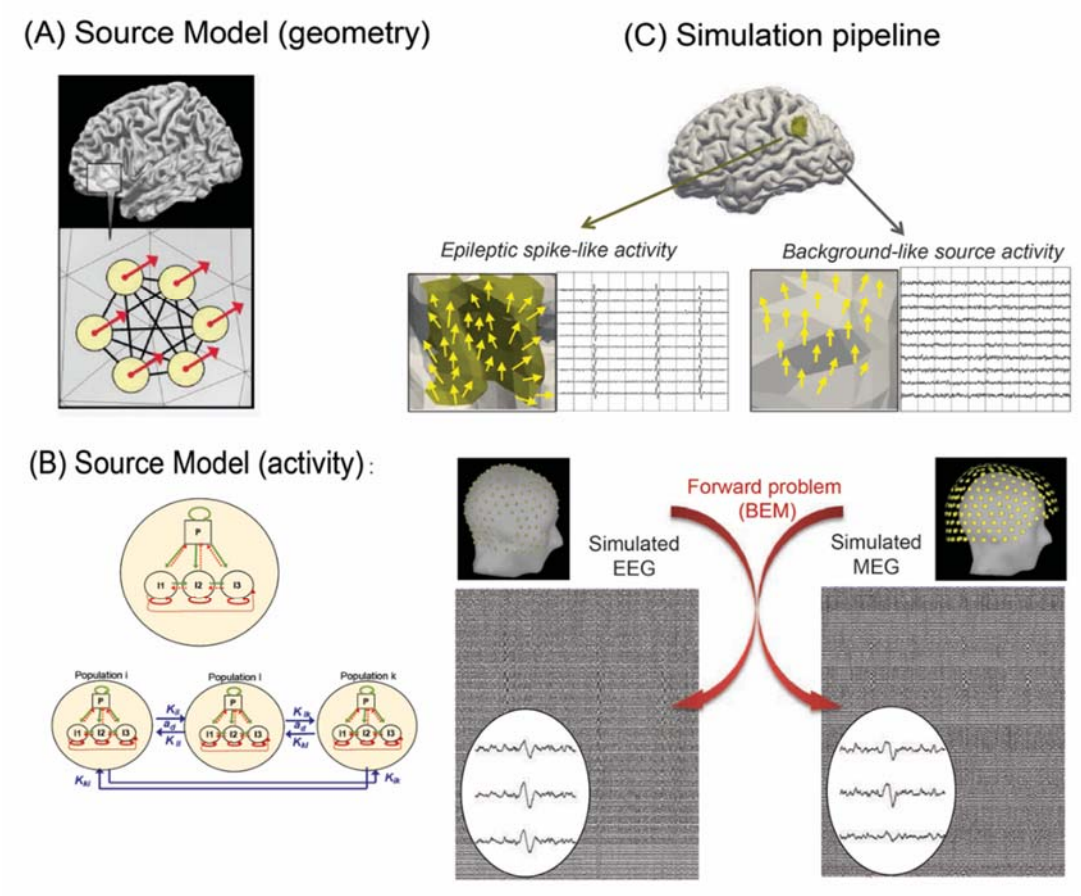

Figure 5.1. Spatio-temporal simulation protocol. (**A**) Source model (Geometry): Distributed source model providing spatial features of the spatio-temporal simulations where the source space was modeled by a dipolar layer distributed along the cortical surface and each dipole corresponds to a distinct neuronal population. (**B**) Source model (Activity): Simulation of temporal features using biophysical computational neural mass model where each neuronal population is made of two subsets of neurons: pyramidal cells (P) and local interneurons (I1, I2, I3). Pyramidal cells receive excitatory input (green arrows) from pyramidal cells of other populations and inhibitory input (red arrows) from interneurons. The interneurons only get excitatory input from the pyramidal cells. A connection from a given population i to a population l is characterized by a parameter K_{il} which represents the degree of coupling, which models the average density of action potentials fired by the pyramidal cells of one population as an excitatory input to the pyramidal cells of another population. Normal background and epileptic spike-like activities were obtained from two different settings of model parameters: excitatory and inhibitory gains in feedback loops, degree and direction of coupling between interconnected populations. These settings are used to simulate the time-course of "focal epileptic sources" (i.e. patches generating epileptic spikes) with surrounding normal background activity. Null coupling but increasing excitation/inhibition ratio generates epileptic spike activities. (**C**) Simulation pipeline: Assigning epileptic activity to the dipoles of the manually

drawn extended source and background activity to all the dipoles on the mesh after grouping them into 1000 clusters. Then, application of the BEM forward model, to obtain simulated EEG and MEG signal.

To analyze these scenarios, first the peak of the spikes was identified and marked on the simulated EEG/MEG signals. In case of very small sources where the signal-to-noise ratio of EEG and MEG signals was very low, the timing of epileptic discharge was detected from the simulated source dynamic within the generator.

In the scenarios 1 and 2, cMEM and 4-ExSo-MUSIC approaches were applied on a window of 500ms around the peak of the averaged EEG and MEG spike (generally 3 or more spikes were averaged for each trial). Therefore, we localized 20 averaged spikes for each of the 10 different source locations. For scenarios 3 and 4, a 500 ms window around the peak of the spike that was extracted from the 10 s of EEG and MEG data, then single spike localization was performed using cMEM and 4-ExSo-MUSIC. For the 4th scenario, since cMEM provides a sample-by-sample result, we could present the source maps at the peak of the first spike and delayed spike. Since, 4-ExSo-MUSIC provides a result over a time interval, we considered a first window involving some background activity to few samples after the peak of the first spike and a second window from the onset of the second spike until few 100 samples after the second peak. For scenarios 1, 2 and 3 we indicated the number of a priori source as 1 (cf. **Section 2.1.1.2**, X=1 for independent source) and for the 4th scenario, we indicated the number of correlated sources ($X(X+1)/2$, where X=2 for 2 correlated sources) a priori to the 4-ExSo-MUSIC method.

All the source localization results using cMEM have been presented after an Otsu threshold, which is obtained by taking the absolute value of the current density at the peak of the spike, normalized to its maximum activity over the whole cortical surface. This normalized map was then thresholded upon the level of background activity, through histogram analysis (Otsu, 1979). 4-ExSo-MUSIC results are presented as a binary map obtained after thresholding the 4-ExSo-MUSIC metric based on GOF measure (cf. **Section 2.1.1.2**).

5.4.3. Evaluation criteria

To characterize the properties of the simulations, the following criteria were used:

(a) Signal-to-Noise Ratio (SNR) of the simulated EEG and MEG signals: this is defined as the standard deviation ratio between the signal around the peak and the background activity.

(b) Cancellation index (*Ic*): This index estimates the amount of overlap between signal patterns of individual sources within an active patch leading to signal cancellation (notably caused by dipolar sources oriented in opposite directions on both walls of a sulcus), as proposed by (Ahlfors et al., 2009).

$$Ic = 1 - \frac{\sqrt{\sum_{i=1}^{q}\left(\sum_{l\in\Phi} \boldsymbol{g}(i,l)\right)^2}}{\sum_{l\in\Phi}\sqrt{\sum_{i=1}^{q}\boldsymbol{g}^2(i,l)}} \qquad (5\text{-}14)$$

where i is the index of summation overall q sensors, l is the index of summation over the set of dipoles in the simulated patch Φ. $\boldsymbol{g}(i,l)$ is the value of the i^{th} row and l^{th} column of the lead field matrix $\boldsymbol{G}$. This index ranges between 0 and 1, Ic=1 indicates full cancellation and Ic=0 indicates no cancellation effect.

In addition, the following two validation criteria were used to compare the source localization results obtained using cMEM and 4-ExSo-MUSIC algorithm for the 4 simulation scenarios. These two criteria were used to assess the detection accuracy and the ability to recover the spatial extent of the generators. To be able to compare the source density map of cMEM with the 4-ExSo-MUSIC metric (which is a probability map), we considered the logarithm of the non-thresholded metric for 4-ExSo-MUSIC. 4-ExSo-MUSIC metric provides a source map that is stable along time and cMEM provides a spatio-temporal source map. For cMEM, we therefore

considered the source map at the main peak (τ_0) of the simulated spike for the following evaluation criteria.

(c) Area Under the Receiver Operating Characteristic (ROC) Curve, AUC: was proposed in (Grova et al., 2006) as a detection accuracy index (between 0 and 1), to assess the sensitivity of a source localization method to the spatial extent of the underlying generator. An AUC value greater than 0.8 was considered a good detection accuracy. The AUC index is assessing towards a Ground Truth the normalized energy of a source map at a specific time sample.

AUC was estimated based on available Ground Truth, whereby, ROC curves were generated by plotting the sensitivity against the false positive detection rate for different detection thresholds, ($\beta \in [0,1]$). Normalized energy for both the estimated and the simulated current density distribution were used to quantify the amount of true positive (TP), true negative (TN), false negative (FN), and false positive (FP) for each threshold β .

However, in such context, ROC analyses are biased by the fact that a source simulation would correspond to quite more negative samples (several thousand sources) than positive ones (few hundred sources). In order to avoid such a bias, we proposed a strategy to consider the same number of active and inactive sources for ROC analysis (Grova et al., 2006). Considering the *r* dipolar sources along the cortical surface, only few dipoles were actually active (r_a) compared to the large number of inactive dipoles ($r - r_a$). Therefore, selection of same number of inactive sources as the active sources was done by randomly selecting inactive sources among the $r - r_a$ sources located within the immediate spatial neighborhood of the simulated source (**AUC_{close}**) or among the local maxima of the reconstructed activity located far from the simulated source **(AUC_{far})**. Final **AUC** index was then computed as a mean of **AUC_{close}** and **AUC_{far}** indices.

In case of simulations involving a single source, the energy at the main peak of the spike was considered.

For the 3rd scenario involving two synchronous sources, the AUC index was estimated separately at the peak of each spike while removing the contribution of the vertices of the second source.

For the 4th scenario involving two propagating sources, as explained in **Section 5.4.2**, the two spikes were extracted separately to localize the sources. Therefore, it was possible to estimate AUC index at the peak of each spike while removing the contribution of the vertices of the second source.

(d) Spatial Dispersion (SD): This index, proposed in (Molins et al., 2008), measures both the spatial spread of the estimated source distribution around the true source location and the localization error between the estimated source distribution and the true source location. Let us denote by $\hat{\boldsymbol{j}}$ the result of the source localization method to be evaluated. Then, $\hat{\boldsymbol{j}}(i,\tau_0)$ represents the amplitude of the current density distribution estimated for a dipolar source *i* on the cortical surface at the main peak of the spike (τ_0).

To measure the SD of this result, we weight the amplitude of all the *r* cortical sources by their minimum distances from the simulated patch using the following formula:

$$\mathrm{SD}(\hat{\boldsymbol{j}}) = \sqrt{\frac{\sum_{i=1}^{r}\left(\min_{l\in\Phi}(\boldsymbol{D}^2(i,l))\hat{\boldsymbol{j}}^2(i,\tau_0)\right)}{\sum_{i=1}^{r}\hat{\boldsymbol{j}}^2(i,\tau_0)}} \qquad (5\text{-}15)$$

where $\min_{l\in\Phi}(\boldsymbol{D}(i,l))$ provides the minimum Euclidean distance between the source *i* and the sources *l* in the simulated patch. Φ denotes the set of indices of the dipoles in the simulated patch and this minimum distance is zero when the source *i* belongs to Φ. SD values close to zero means there is no active source outside the simulated patch. Large SD values could be caused either by the presence of sources far away from the true source that are contributing to the estimated solution

(spurious sources) or by the spatial spread of the reconstructed source around the true extent of the simulated patch.

(e) Shape Error (SE): this is the root mean square of the difference between the normalized simulated current density ($\boldsymbol{jth}$) and the normalized estimated current density ($\hat{\boldsymbol{j}}$). This will assess the accuracy of the reconstructed time courses within the simulated patch. For 4-ExSo-MUSIC, all the dipoles within the estimated source have the same reconstructed time course. This time course was obtained from a least square fit between the lead field matrix for the estimated source configuration and the measured data (**Section 5.4.1c**). Therefore, SE was estimated as follows:

Let us consider $jth(i,t)$ and $\hat{j}(i,t)$, where $i \in \Phi$ and t is the time parameter.

$$\mathrm{SE} = \sqrt{\frac{1}{\tau}\sum_{t}^{\tau}\left(\frac{m(jth_n(t))}{\max_t\left(\left|m(jth_n(t))\right|\right)} - \frac{m(\hat{j}_n(t))}{\max_t\left(\left|m(\hat{j}_n(t))\right|\right)}\right)^2} \qquad (5\text{-}16)$$

with $m(jth_n(t)) = \frac{1}{card(\Phi)}\sum_{i\in\Phi} jth_n(i,t)$ and $m(\hat{j}_n(t)) = \frac{1}{card(\Phi)}\sum_{i\in\Phi}\hat{j}_n(i,t)$.

$card(\Phi)$ is the number of elements in the set Φ. The subscript "$_n$" in jth_n or $\hat{j}_n$ denotes the normalization of the matrix $\hat{\boldsymbol{j}}$ so that its values are between -1 and 1, for example: $j_n(i,t) = {|j(i,t)|}\big/{\max_j(|j(i,t)|)}$. $\max_t$ is the maximum over t time samples.

5.4.4. Application on clinical datasets

Simultaneous recording of HR 257-EEG and 275-MEG was not feasible since the HR-EEG system was available at the Neurological department of the Rennes Hospital in France while the MEG system was available at the Montreal

Neurological Hospital in Canada. Therefore, from each center, we selected one clinical dataset from a patient with intractable focal epilepsy with available Ground Truth information such as intracranial depth EEG (iEEG) findings and MRI visible lesion (Focal Cortical Dysplasia (FCD) in both cases). Patient 1 had a 275-MEG recording and Patient 2 had a 257-EEG recording.

For patient 1, a suspected right orbitofrontal FCD was seen on MRI. This patient underwent a full presurgical evaluation at the Montreal Neurological Hospital and the acquisition was done at the MEG center of Université de Montréal on a 275 channel CTF whole-head MEG system. MEG data were bandpass filtered between 0.3 and 70 Hz after a DC-offset removal, and 60 Hz notch filter was further applied. Interictal spikes were independently visually marked in MEG traces using the DataEditor software (MISL, Vancouver, Canada) by a clinical neurophysiologist (E.K.). A total of 26 MEG spikes were found and averaged. MEG source localization was performed on the averaged spike. iEEG investigation with eight implanted electrodes (10±18 contacts; length: 2 mm, diameter: 0.8mm; 1.5 mm apart, placed intracranially according to Talairach's stereotactic method in the right hemisphere) was further guided by the MEG source localization results within the suspected MRI lesion and revealed a focal ictal and interictal activity in the right lateral orbitofrontal region. The patient provided written informed consent for this study as approved by the Montreal Neurological Institute Research Ethics Board.

Patient 2 also presented a FCD visible on MRI in the left mesial orbitofrontal region, just above the rectus gyrus. This patient underwent a full presurgical evaluation at the Neurological department of Rennes University Hospital, including 257-channels EEG recordings (EGI, Eugene, USA). EEG data were band pass filtered between 0.3 and 100Hz. These data were reviewed for presence of IEDs by the clinical neurophysiologist (I.M.). On these scalp recordings a clear subcontinuous spike activity could be recorded interictally at the most frontopolar electrodes. A total of 85 spikes were extracted away from ocular, muscle or cardiac artifacts, and averaged. Source localization was applied on the averaged spike. During the second phase of his presurgical evaluation, the patient also underwent

intracerebral iEEG recordings with 9 implanted electrodes (10±18 contacts; length: 2 mm, diameter: 0.8mm; 1.5 mm apart) placed intracranially according to Talairach's stereotactic method in the left frontal and temporal region. iEEG revealed a sub-continuous interictal activity, similar in morphology with that observed on scalp EEG, maximal in the contacts located within and around the focal lesion in the left mesial orbito-frontal region but spreads to the cingulate and to the lateral orbitofrontal region. The patient provided written informed consent for the use of his clinical data as requested by the Institutional Review Board of Rennes University Hospital.

For both clinical dataset, we presented source localization results from cMEM, 4-ExSo-MUSIC and from another standard source localization method - sLORETA (Pascual-Marqui, 2002) that is implemented in the brainstorm toolbox (Tadel et al., 2011).

To present the 4-ExSo-MUSIC results, we provided the thresholded 4-ExSo-MUSIC map using the GOF criterion. Both cMEM and sLORETA results displayed over the cortical surface were thresholded at 30% of the maximum amplitude, following a similar approach as proposed in (Heers et al., 2016)**.**

5.5. Results

5.5.1. Evaluation using realistic simulations

The results obtained for the first 5 source locations (CS, BT, OF, SMA, and P) of the first scenario, involving a single spatially extended source, are illustrated on **Figure 5.2**. The results on the remaining 5 source locations have been provided as supplementary figure (**Figure S5.1**). The localization of single 10 cm² sources was accurate (AUC>0.8) and was relatively similar for both 4-ExSo-MUSIC and cMEM, for most locations tested and for both EEG and MEG. EEG and MEG data simulated from these sources exhibited reasonable SNR and Ic values, although the SNR in the case of MEG signals was most of the time slightly lower than that of EEG, except for the SMA and the post-central source (tangential orientations). For

these 10 cm^2 single sources, 4-ExSo-MUSIC performed slightly better than cMEM for deep sources or for sources close to the interhemispheric line (OF and SMA source in **Figure 5.2**). For instance, sources localized with cMEM in the basal temporal region and in the orbitofrontal region were more lateral than their actual location, whereas for the SMA sources, cMEM recovered mainly the most superficial aspects of the generators. On the other hand, cMEM sources were slightly more accurate than 4-ExSo-MUSIC for the CS generator (for EEG mainly) and for the P generator (for MEG mainly). To summarize the differences in performance of the two methods, we pooled together all the 200 source localization results (obtained from the 20 trials of the 10 source locations) and performed non-parametric Wilcoxon signed rank test to compare AUC and SD in cMEM versus 4-ExSo-MUSIC and in EEG versus MEG. We also tested whether the median of AUC distribution was significantly larger than 0.8, since AUC value of 0.8 is usually considered as a good level of detection accuracy (Chowdhury et al., 2013). From these tests, we noticed that overall, 4-ExSo-MUSIC performed statistically significantly better than cMEM for EEG in terms of AUC ($p<0.001$), although both methods provided overall excellent results since they were all showing median AUC significantly larger than 0.8 for both EEG and MEG ($p<0.005$). On the other hand, AUC results for MEG did not show any statistically significant difference between the two methods ($p=0.24$). Based on SD, cMEM exhibited SD values significantly smaller than 4-ExSo-MUSIC for EEG ($p<0.001$) and for MEG ($p<0.005$). In **Figure 5.3**, we provided a plot of AUC values as a function of SNR for all the 200 source localization results. We observed that the low AUC values in EEG and MEG for both cMEM and 4-ExSo-MUSIC were coming mainly from simulations when the source location was deep and the SNR was low. SE values were estimated for these single source activities (provided in **Figure 5.2**) and it was observed that the SE values were slightly lower for 4-ExSo-MUSIC than cMEM when localizing these single source activities, indicating a slightly better reconstruction of the temporal dynamics of the source using 4-ExSo-MUSIC.

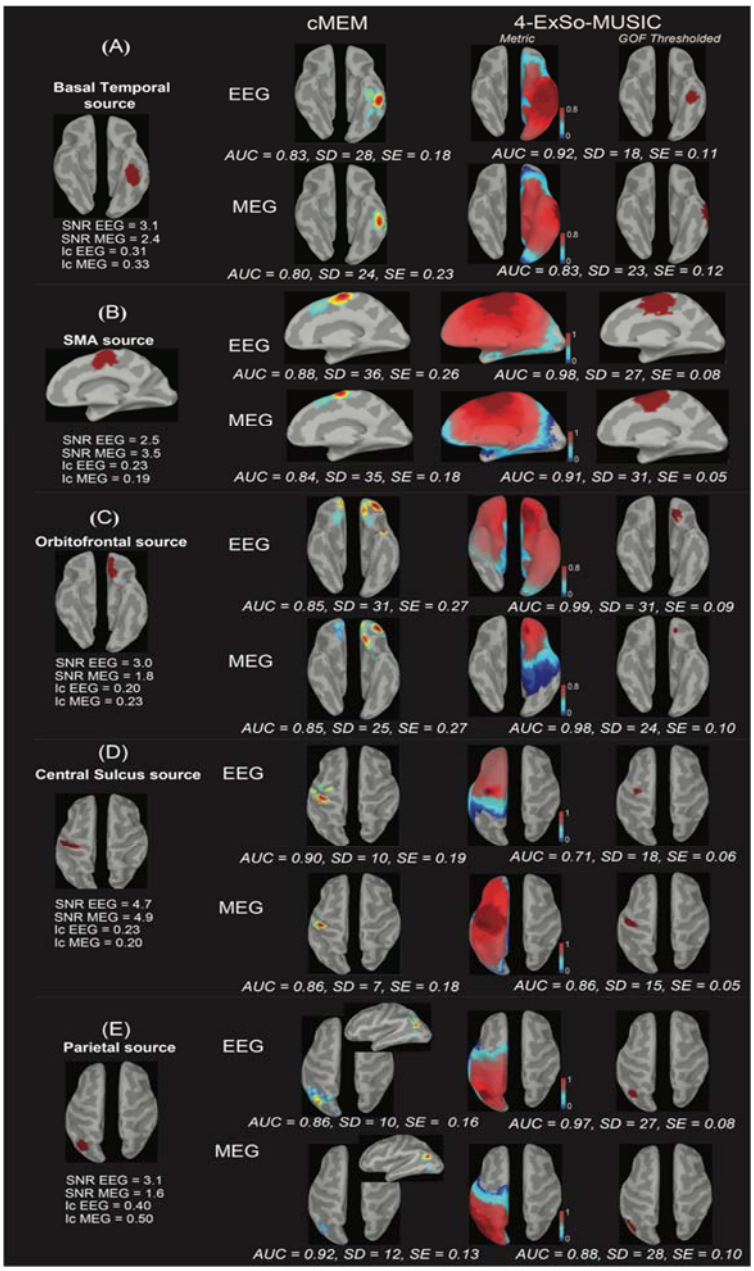

Figure 5.2. Single Source analysis. EEG and MEG source localization results (with their corresponding validation metrics: AUC, SD and SE values) using cMEM and 4-ExSo-MUSIC on simulated sources of spatial extent 10 cm^2 in (**A**) Basal temporal gyrus (BT), (**B**) Supplementary motor area (SMA), (**C**) Orbito-frontal (OF), (**D**) Central sulcus region (CS), and (**E**) Parietal source (P). All the source localization results were displayed over the inflated cortical surface obtained from Brainstorm software toolbox. In this figure, we presented source localization results of cMEM after an Otsu threshold, which is obtained by taking the absolute value of the current density at the peak of the spike, normalized to its maximum activity and thresholded upon the level of background activity (Otsu, 1979). We presented two maps for 4-ExSo-MUSIC results: 4-ExSo-MUSIC metric map and the GOF thresholded binary map to be able to compare between the original and thresholded source maps.

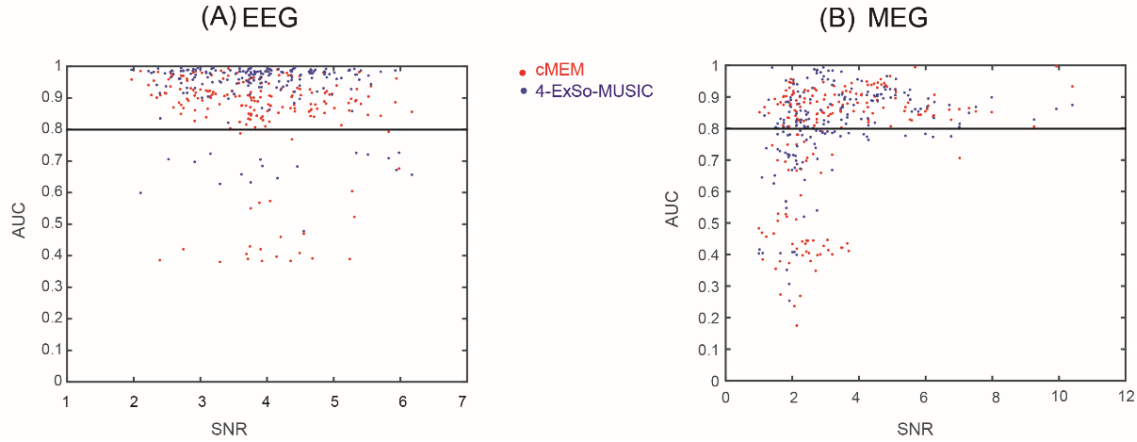

Figure 5.3. Plot of AUC as a function of Signal-to-Noise Ratio (SNR) for all 200 single source localization results pooled together. (**A**) EEG source localization. (**B**) MEG source localization. Color code: cMEM in red color and 4-ExSo-MUSIC in blue. Black horizontal line showing AUC=0.8, considered a good level of detection accuracy.

For 3 of these locations (BT, P and CS), results with respect to the source spatial extent are provided on **Figure 5.4** and **Figure 5.5**. In general, the localization was assessed as accurate (i.e. median AUC value >0.8) when the source area encompassed at least 2cm² for cMEM and 3cm² for 4-ExSo-MUSIC. For EEG and for the BT and P source, small source areas were better retrieved with cMEM while large source areas were better estimated with 4-ExSo-MUSIC. For MEG, both cMEM and 4-ExSo-MUSIC exhibited similar performance levels, with accurate reconstructions for spatial extent larger than 2cm^2 for P and larger than 4cm^2 for BT. For smaller extent (<3cm^2) both methods exhibited large variabilities in their AUC scores (**Figure 5.4**). We noticed from the source localization results visually that both methods notably failed to recover the 0.5cm^2 BT sources from MEG data. The bad performance of 4-ExSo-MUSIC for EEG small sources was due to a wrong localization of the source while the moderately "bad" performance of cMEM for EEG large sources was due to an underestimation of the source spatial extent. Note that in MEG, median AUC values were close but below 0.8, for both methods and for most spatial extents (except slightly better results for extents larger than 7.5 cm²). Actually, in most of those cases, only the most lateral portion of the BT generator was

retrieved whereas most of the deepest aspects were always missed by both methods in MEG. Regarding the CS source, a different pattern was observed. cMEM clearly outperformed 4-ExSo-MUSIC for all sizes except for large sources (20 and 30 cm² sources). This was observed both for EEG and MEG signals.

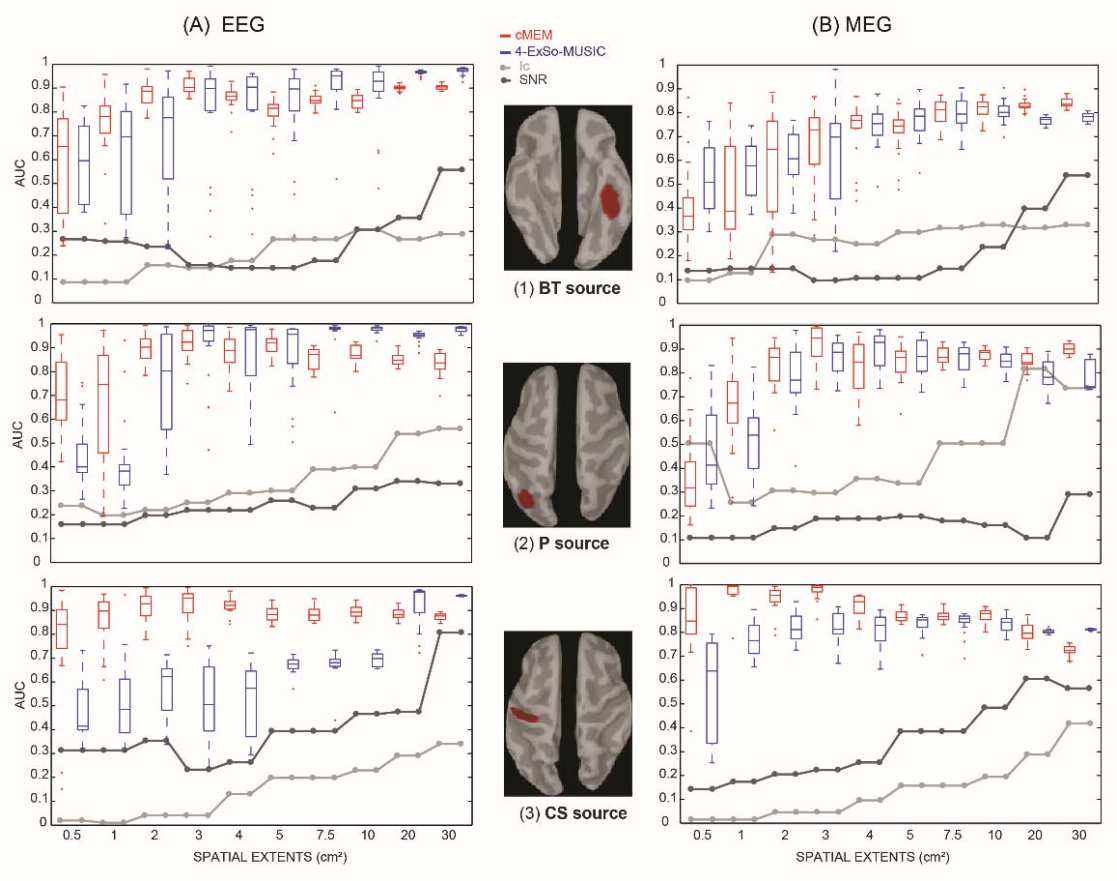

Figure 5.4. Boxplot representation of AUC distribution for three simulated sources (BT, P and CS) at 10 different source spatial extents (0.5 cm², 1 cm², 2 cm², 3 cm², 4 cm², 5 cm², 7.5 cm², 10 cm², 20 cm², and 30cm²) obtained over 20 simulated trials of the same configuration. (**A**) EEG source localization. (**B**) MEG source localization. The middle column represents the simulated source at 10 cm² to display the regions on the cortical surface. Color code: cMEM in red color and 4-ExSo-MUSIC in blue, Cancellation index (*Ic*) in gray ranging between 0 and 1, SNR in black ranging between 0 and 10.

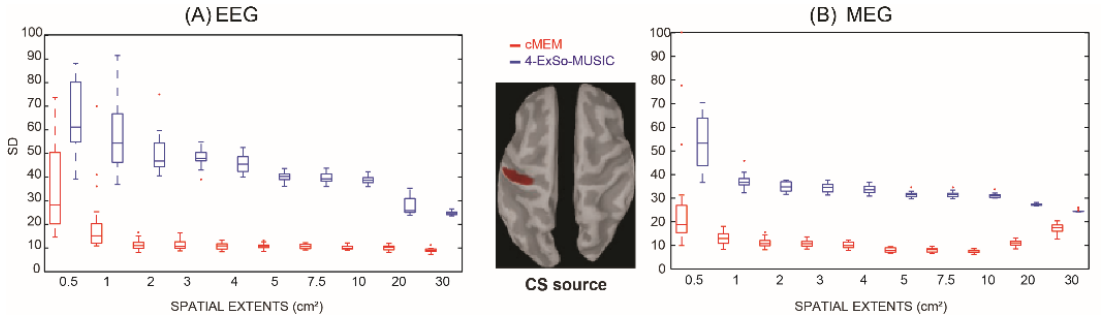

Figure 5.5. Boxplot representation of SD distribution for one simulated source (CS) at 10 different source spatial extents (0.5 cm^2, 1 cm^2, 2 cm^2, 3 cm^2, 4 cm^2, 5 cm^2, 7.5 cm^2, 10 cm^2, 20 cm^2, and 30cm^2) obtained over 20 simulated trials of the same configuration. (**A**) EEG source localization. (**B**) MEG source localization. The middle column represents the simulated source at 10 cm^2 to display the region on the cortical surface. Color code: cMEM in red color and 4-ExSo-MUSIC in blue.

Both EEG and MEG simulated from the post central source we had similar range of SNR and Ic except for the 30 cm^2 source for which MEG signal underwent higher signal cancellation and presented lower SNR than EEG (**Figure 5.4**). There was no clear relationship between SNR or Ic values and the performance of source localization: for instance, SNR values were higher for small BT sources than for the medium ones, while localization accuracy was increased. For the CS MEG source, the SNR gradually increased with the source area, while a trend towards a slight performance decrease was observed. As shown in **Figure 5.5**, SD values were consistently lower for cMEM than for 4-ExSo-MUSIC in the CS region, suggesting that 4-ExSO-MUSIC had a tendency to slightly overestimate the spatial extent, whereas cMEM more likely slightly underestimated the spatial extent. A similar behavior of the SD values was also observed for the BT and P regions (results not shown).

In the presence of two synchronous sources, cMEM retrieved properly both sources. For EEG signals, the spatial extent was slightly underestimated, and for MEG signals the temporal source was anterior to the actual location, while missing the main radial components of this generator. 4-ExSo-MUSIC retrieved the temporal source but largely overestimated its size, and was not able to localize the

second source in the parietal region, neither from EEG nor from MEG data (**Figure 5.6A**).

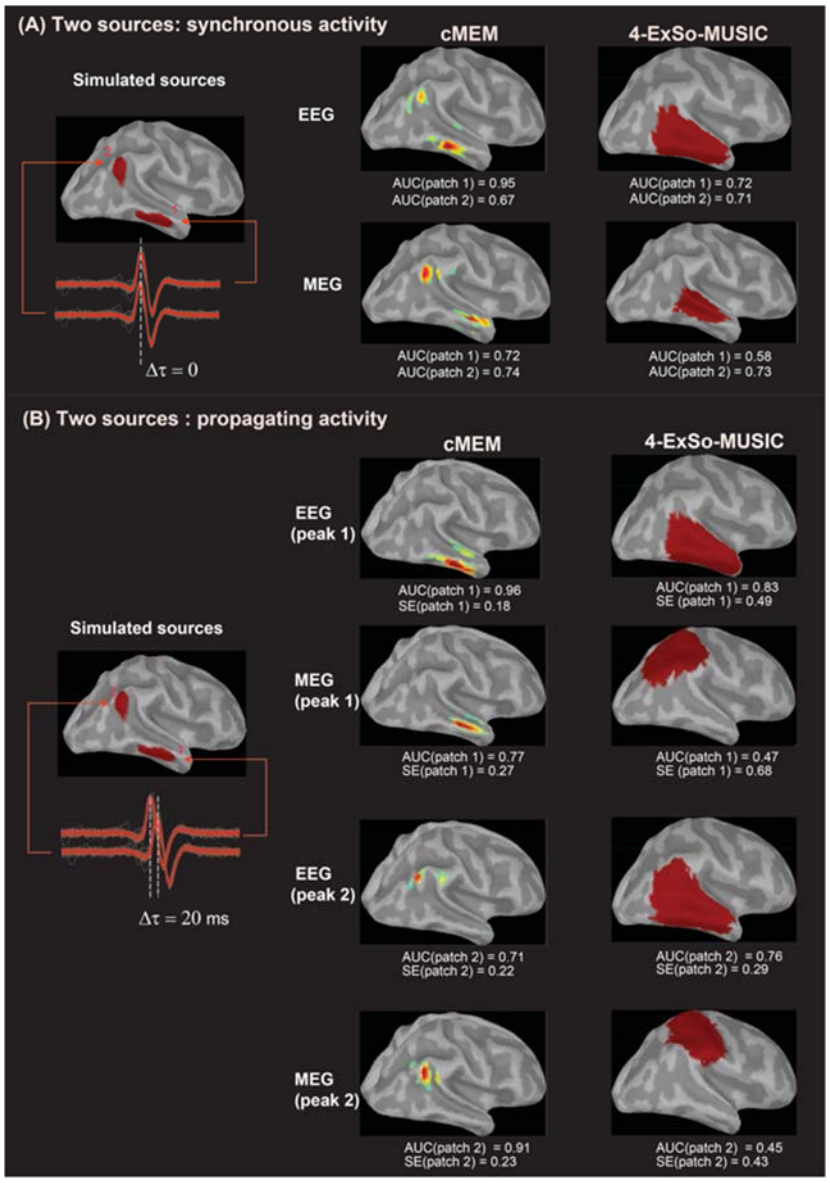

Figure 5.6. Two source analysis: (**A**) Synchronous activities - Simulated sources of spatial extent 10 cm^2 in temporal (patch 1) and parietal (patch 2) region. EEG source localization results (with their corresponding AUC values) using cMEM and 4-ExSo-MUSIC. MEG source localization results (with their corresponding AUC values) using cMEM and 4-ExSo-MUSIC. (**B**) Propagating activity - Simulated sources of spatial extent 10 cm^2 in temporal region at peak 1 and parietal region at peak 2 after 20ms of delay. EEG source localization results (with their corresponding AUC and SE values) using cMEM and 4-ExSo-MUSIC. MEG source localization results (with their corresponding AUC and SE values) using cMEM and 4-ExSo-MUSIC. Here, we presented source localization results of cMEM after an Otsu threshold and for 4-ExSo-MUSIC results the GOF thresholded binary map were presented.

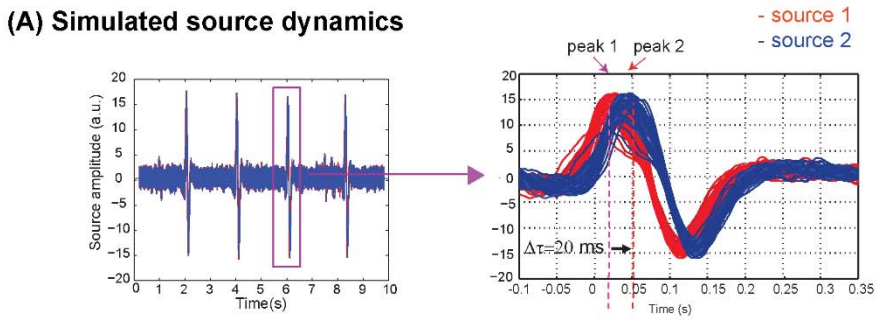
(A) Simulated source dynamics
- source 1
- source 2
peak 1
peak 2
Source amplitude (a.u.)
Time(s)
Δτ=20 ms
Time (s)

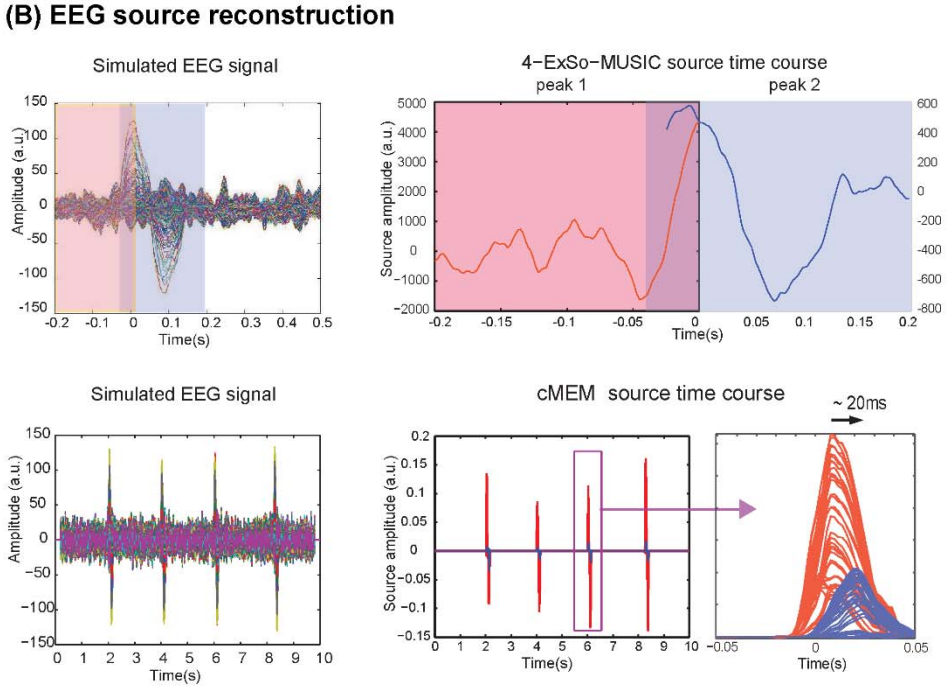
(B) EEG source reconstruction
Simulated EEG signal
4−ExSo−MUSIC source time course
peak 1
peak 2
Amplitude (a.u.)
Source amplitude (a.u.)
Time(s)
Simulated EEG signal
cMEM source time course
~ 20ms
Amplitude (a.u.)
Source amplitude (a.u.)
Time(s)

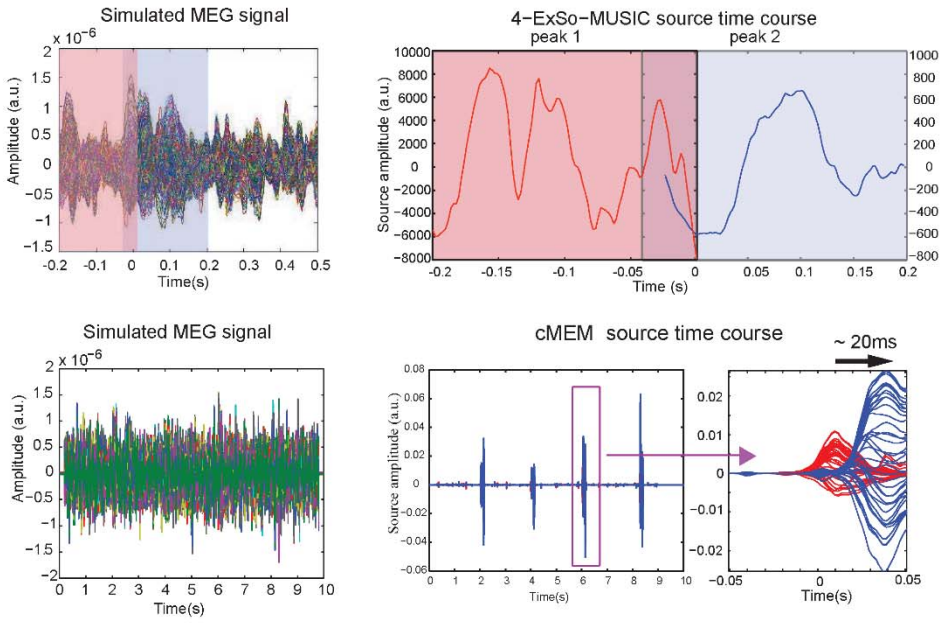
(C) MEG source reconstruction
Simulated MEG signal
4−ExSo−MUSIC source time course
peak 1
peak 2
x 10−6
Amplitude (a.u.)
Source amplitude (a.u.)
Time(s)
Time (s)
Simulated MEG signal
cMEM source time course
~ 20ms
x 10−6
Amplitude (a.u.)
Source amplitude (a.u.)
Time(s)

Figure 5.7. Reconstructed temporal dynamics illustrated for a single trial of the propagating sources presented in Figure 5B. (**A**) Theoretical source dynamics showing the time course of every single dipole of the two epileptic patches generated by the neural mass model in a 10s window consisting of four events (row 1 left) and a 450ms window segment extracted from the 10s window (row 1 right). (**B**) Simulated EEG signal extracted after marking the peaks of the two sources in the propagation pattern (row 2 left), 4-ExSo-MUSIC window for localizing temporal source (peak 1) is in pink box and window for localizing the propagated parietal source (peak 2) is in blue box; (row 2 right) shows the source dynamics reconstructed using 4-ExSo-MUSIC for the temporal and parietal sources in the respective windows; (row 3 left) shows the full 10s window of simulated EEG signal used for cMEM localization; (row 3 middle) shows the source dynamics reconstructed using cMEM for the full 10s window; (row 3 right) shows the zoomed time course reconstructed using cMEM. (**C**) Simulated MEG signal of the propagation pattern (row 4 left), 4-ExSo-MUSIC window for localizing temporal source (peak 1) is in pink box and window for localizing the propagated parietal source (peak 2) is in blue box; (row 4 right) shows the source dynamics reconstructed using 4-ExSo-MUSIC for the temporal and parietal sources; (row 5 left) shows the full 10s window of simulated MEG signal used for cMEM localization; (row 5 middle) shows the source dynamics reconstructed using cMEM for the full 10s window; (row 5 right) shows the zoomed time course reconstructed using cMEM.

When the activity of the second source was delayed by 20 ms to mimic a propagation pattern, the maximum of spikes was first detected on electrodes (respectively MEG sensors) facing the temporal region and then at electrodes (MEG sensors) facing the parietal region for both modalities. From both EEG and MEG data, cMEM localized well the temporal source at the earliest spike peak and the parietal source at the delayed peak (**Figure 5.6B**). Conversely, for EEG signal, 4-ExSo-MUSIC largely overestimated the temporal source at the first peak and the parietal one at the second peak. In that case, the estimated source included both the temporal and the parietal sources. Finally, for MEG signals, 4-ExSo-MUSIC missed both sources. SE values were estimated for these propagating source activity (provided in **Figure 5.6B**) and it was observed that the SE values were lower for cMEM than for 4-ExSo-MUSIC indicating a better reconstruction of the temporal dynamics of the source using cMEM for this scenario. **Figure 5.7** displays the actual and the estimated time course of two sources with propagating activity. In this realization the temporal delay between the two sources was 20 ms. cMEM localization was applied on the full 10s window of the simulated EEG and MEG data. In **Figure 5.7B** and **Figure 5.7C**, we presented the temporal dynamics of the

reconstructed sources. The activity of sources reconstructed from EEG with cMEM reproduced the 20 ms time delay observed in the simulated source signals. Moreover, a clear difference in the amplitude between the first and second source was observed that matched the results reported on **Figure 5.6B**. Indeed, for EEG signals, the source activity reconstructed for the temporal source was stronger than for the parietal source, while for MEG the reverse was observed. 4-ExSo-MUSIC was applied on two separate windows extracted for the two spikes as explained in **Section 2.2**. Since 4-ExSo-MUSIC assumes the same temporal dynamics for all the dipoles within the extended source we were able to reconstruct a global time course for each source from EEG and MEG data (in **Figure 5.7B** and **Figure 5.7C**). In agreement with the results reported on **Figure 5.6B** for 4-ExSo-MUSIC on EEG signal, we noticed that the reconstructed time courses were able to mimic the shape of the spiking activity for the two sources, however, the propagation delay was not well-represented. On the other hand, 4-ExSo-MUSIC on MEG signal failed to localize the two sources, which is also evident from the reconstructed time course that was not able to characterize the temporal dynamics of the simulated sources.

5.5.2. Application on clinical datasets

Figure 5.8 illustrates source localization results obtained from MEG data of Patient 1. As shown in **Figure 5.8A**, this patient was exhibiting almost continuous large amplitude interictal spikes culminating at the level of right frontal MEG sensors. cMEM localized the spikes in the right orbitofrontal region (**Figure 5.8B**). This localization was in agreement with the area identified as the epileptogenic zone according to focal ictal and interictal activity recorded during iEEG investigation (pink outline). A small FCD was also suspected in this region, further confirmed after surgery (right orbitofrontal resection, seizure free for 12 months after the surgery). 4-ExSo-MUSIC also localized the source of MEG spikes in the orbitofrontal region. This localization was contiguous with the iEEG area, but more mesial (**Figure 5.8C**). Results obtained with sLORETA showed a widespread area that included the iEEG outlined region but also involved the mesial aspect of the

orbitofrontal region and the mesio-temporal region (**Figure 5.8D**). Note that additional intracerebral electrodes implanted in temporal regions did not exhibit any epileptic activity.

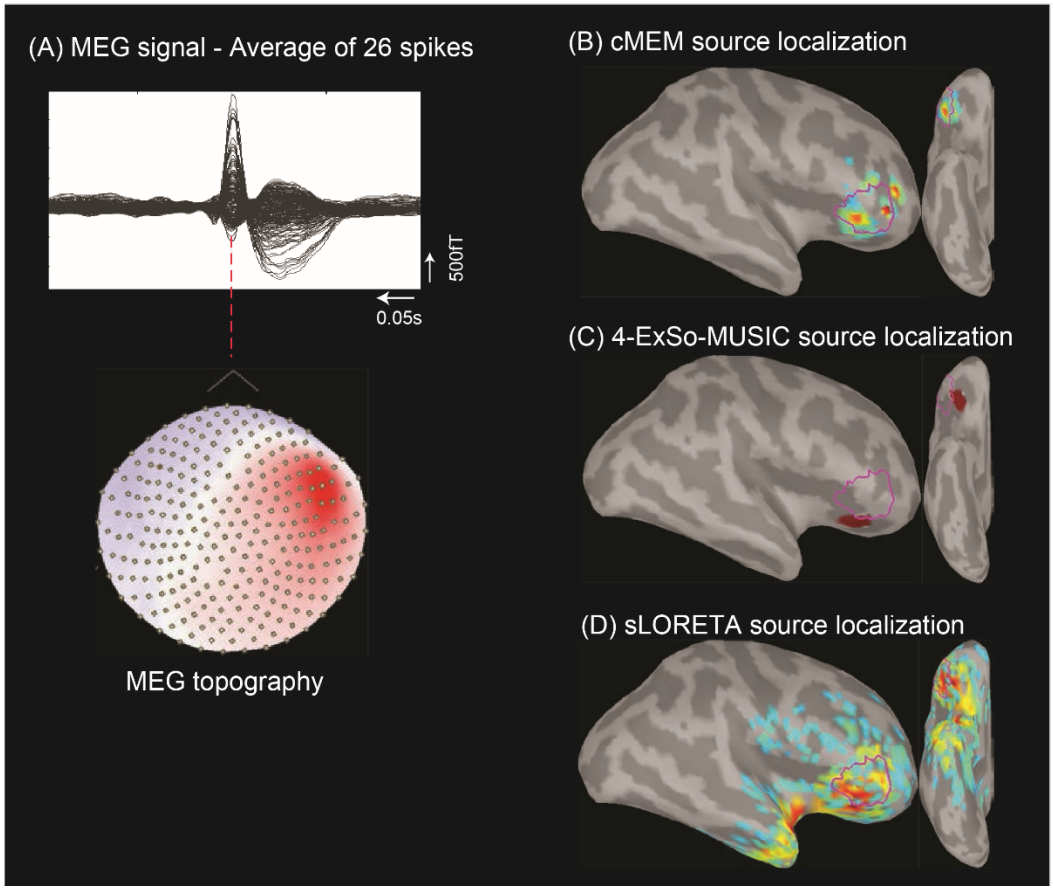

Figure 5.8. Source localization results on MEG data of 26 averaged spikes recorded from patient 1, displayed over the inflated cortical surface. (**A**) MEG signal and topography at the peak of the signal. (**B**) cMEM source localization results thresholded at 30 % of the maximum amplitude, (**C**) 4-ExSo-MUSIC results thresholded using GOF criterion. (**D**) sLORETA results thresholded at 30% of the maximum amplitude. Pink color outline over the cortical surface represents the right orbitofrontal region showing maximal ictal and interictal activity in iEEG recordings.

Figure 5.9 illustrates source localization results obtained from HR-EEG data of Patient 2. This patient had large amplitude interictal spikes recorded at the level of left frontal electrodes (**Figure 5.9A**). cMEM localized the spikes mainly in the left frontal pole and in the lateral orbitofrontal region (**Figure 5.9B**). This localization was more lateral and anterior to the lesion area (FCD) from where subcontinuous

spikes where recorded with iEEG (pink outline). On the other hand, 4-ExSo-MUSIC localized the spikes near the anterior cingulate gyrus, above and deeper than the region identified from iEEG investigation (**Figure 5.9C**). sLORETA localized the source in the left lateral orbitofrontal region with ghost sources (Hauk et al., 2011) located far from the lesion, in temporo-mesial regions notably (**Figure 5.9D**).

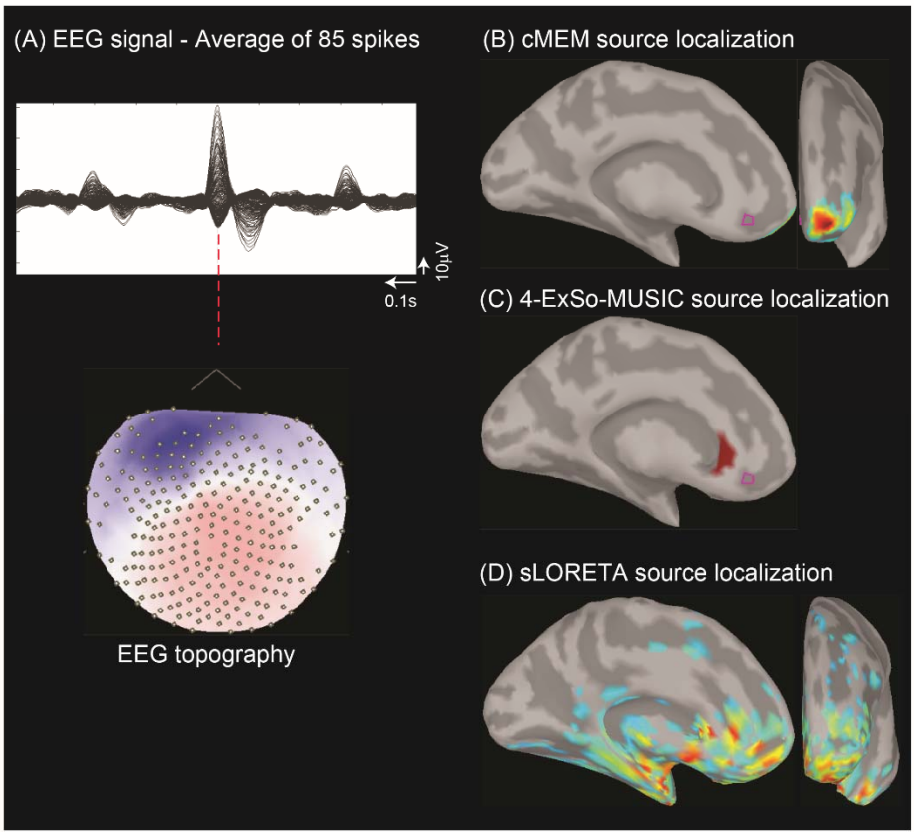

Figure 5.9. Source localization results on EEG data of 85 averaged spikes recorded from patient 2, displayed over the inflated cortical surface. (**A**) MEG signal and topography at the peak of the signal. (**B**) cMEM source localization results thresholded at 30 % of the maximum amplitude, (**C**) 4-ExSo-MUSIC results thresholded using GOF criterion. (**D**) sLORETA results thresholded at 30% of the maximum amplitude. Pink color outline over the cortical surface represents the lesion visible on MRI in this patient.

Table 5.1. Comparison of 4-ExSo-MUSIC and cMEM algorithms.

Algorithm	Advantages	Disadvantages
4-ExSo-MUSIC	1) Sensitive to spatially extended sources 2) Robust to Gaussian Noise 3) Statistical thresholding technique for the source map available	1) High computational complexity 2) Requires a priori knowledge about the number of sources 3) Requires a sufficiently large number of time samples to estimate the data statistics 4) Difficulty in localizing highly correlated extended sources 5) Difficulty in detecting propagation patterns of sources
cMEM	1) Sensitive to spatially extended sources 2) Provides source maps for each time sample 3) Does not need a priori knowledge about the number of sources 4) Ability to shutdown parcels that are not active helps to eliminate false-positives from the solution space 5) Able to localize highly correlated sources with their spatial extent 6) Able to detect propagation patterns of correlated sources	1) Computationally expensive for long data lengths or large number of dipoles in the source space, since the localization requires a non-linear optimization for each time sample 2) Slightly overestimates the size of small sources and underestimates the size of large ones 3) No statistical thresholding technique available for source maps

5.6. Discussion

This study carefully compared the performances of two distributed source localization methods, cMEM and 4-ExSo-MUSIC, in order to assess their ability to localize the different patterns of IEDs, within a realistic simulation environment. While these two methods have been well-established previously for their sensitivity to the spatial extent of the sources of IEDs, it was important to evaluate their behavior on complex spatio-temporal patterns of IEDs such as including multiple sources, propagation patterns, and correlated sources. Both methods demonstrated the importance of factorizing multiple dipole activity within parcels of extended source in order to recover the spatial extent of the sources (Chowdhury et al., 2013; Birot et al., 2011; Heers et al., 2016; Becker et al., 2014b). However, differences between these two algorithms exist both at the level of a priori source model definition and regularization technique. While both methods assume parcellization of extended activity, 4-ExSo-MUSIC strongly relies on the non-Gaussianity of the source activity while cMEM assumes a Gaussian mixture distribution of source activity in its prior model (i.e. in the definition of the reference distribution $d\nu$). However, cMEM inference is actually a Bayesian inference, where the a priori model is used to guide the solution informed by the data. Consequently, even if the Gaussian assumption is not completely fulfilled (cf. non Gaussianity of spiking activity), the inference model can still be valid and applicable. The ability of cMEM model to shutdown parcels that are not active during the regularization process permit to discard false positives in the solution space. On the other hand, the use of 4^{th} order statistics in 4-ExSo-MUSIC helps to eliminate the contribution of the background activity if it is assumed to be Gaussian, while allowing a more accurate reconstruction of the generators of epileptic discharges assumed to be non-Gaussian. These two respective properties of the two algorithms play an important role in providing solutions with an excellent contrast following the true extent of the source and exhibiting less distant spurious activity, unlike most conventional source localization methods such as MNE, sLORETA or dSPM (Chowdhury et al., 2013; Becker et al., 2015; Heers et al., 2016). Note that these more conventional

source localization techniques, do recover accurately the maximum of the activity in most cases but not the spatial extent of the generators. Since 4-ExSo-MUSIC makes use of higher order statistics, the use of longer data sets to reduce the variance associated with estimating the higher order statistics is required. cMEM provides an estimate for each time sample, as long as we have a good estimate of the noise covariance matrix. In terms of computational time, for a reasonable length of the data (~500ms window), 4-ExSo-MUSIC takes only few minutes while cMEM takes around 20 mins to process the data on a linux computer with Intel Core 2 Quad processor at a speed of 2.66 GHz and 8 GB of RAM. On the other hand, 4-ExSo-MUSIC involves computation of large matrices leading to high computational complexity, thus requires high performance processors (**Table 5.1**).

Through this study, we showed that, in most of the considered simulation configurations, both cMEM and 4-ExSo-MUSIC were indeed sensitive to the spatial extent of the generators of IEDs. In previous studies, cMEM was evaluated in MEG on simulated sources with spatial extent ranging between 3 cm^2 and 30 cm^2 (Chowdhury et al., 2013) and 4-ExSo-MUSIC was evaluated in EEG on sources with spatial extent ranging between 0.5 cm^2 and 20 cm^2 (Birot et al., 2011). In the present study, we evaluated the two methods on sources with spatial extent ranging between 0.5 cm^2 and 30 cm^2. Both methods provided consistent and reliable detection accuracy for a wide range of source spatial extents (source sizes ranging from 3 to 20 cm^2 for MEG and 3 to 30 cm^2 for EEG). For both EEG and MEG, 4-ExSo-MUSIC localized the larger sources better than cMEM but failed to localize most small sources. This was also shown in previous studies (Birot et al., 2011; Becker et al., 2014a). For all the three sources (CS, BT, and P), we noticed an overall slightly better sensitivity to the spatial extent of the larger sources on EEG data. This could be explained by the fact that these large sources lead to a higher signal cancellation in MEG than in EEG signals (**Figure 5.4** and **Figure 5.5**). This higher cancellation of MEG signal for the large sources can be justified by the selective sensitivity of MEG to mainly tangential activities (Ahlfors et al., 2010). 4-ExSo-MUSIC performed slightly better than cMEM for deeper sources

and this can be explained by the additional depth weighting applied during the 4-ExSo-MUSIC optimization step through normalization of the lead field matrix (cf. equation (5-12) in **Section 5.4.1c**).

In the presence of two correlated sources (active at the same time or after a delay), 4-ExSo-MUSIC could not separate the two correlated sources. 4-ExSo-MUSIC identified only one patch and largely overestimated its spatial extent in the two cases of two source simulations (**Figure 5.6** and **Figure 5.7**). This can be explained by the fact that during 4-ExSo-MUSIC scan for the 2 correlated sources, the search was performed using a grid constructed for a single source (as explained in **Section 5.4.1c**) which then finds one patch that is largely overestimated. To improve the performance of 4-ExSo-MUSIC for the two sources scenarios, a grid search accounting for all combinations of two sources of two different spatial extents should have been considered. Such a situation would be extremely demanding in terms of computation time and would require some statistical test to assess the number of generators to consider. Note that a similar statistical approach accounting for all possible combinations of 1, 2 or 3 equivalent current dipoles has been proposed in (Bénar et al., 2005) and an F-test was used to infer the number of sources to consider. Such an approach within the context of 4-ExSo-MUSIC, in order to assess the number of sources in addition to the size of each patch, is feasible in theory but not in practice because of computational load. On the other hand, cMEM was able to well-distinguish between the two sources (their location and spatial extent). The difference in the sensitivity of EEG and MEG to the two sources (patch 1 and patch 2) was also visible in the cMEM source reconstruction. While the temporal source was more sensitive to EEG than MEG, the parietal source was more sensitive to MEG than EEG. This explains the larger source amplitude for temporal source than parietal source in EEG source reconstruction using cMEM and vice versa in MEG source reconstruction using cMEM. Even though cMEM is a non-linear estimation of the source amplitude iteratively for each time sample, with no constraint on temporal smoothness, it was interesting to see the temporal dynamics of the sources reconstructed by cMEM exhibiting smooth time course,

mimicking the dynamics of the simulated spike temporally with the two sources peaking at a delay of 20 ms. This ability of cMEM can therefore be particularly interesting when applying methods to identify brain networks using the source time course and perform connectivity along the spike (Ana Coito, 2015). The reconstructed time course using 4-ExSo-MUSIC was reliable as long as the source was well localized. For example, in **Figure 5.2**, the SE values for the reconstructed time course using 4-ExSo-MUSIC was very low indicating that 4-ExSo-MUSIC was able to reconstruct the temporal dynamics of single source activity with high accuracy. On the other hand, for the propagating activity, 4-ExSo-MUSIC found only the strongest source activity (temporal source in EEG and parietal source in MEG), which also explains why the reconstructed time course from 4-ExSo-MUSIC did not contain a clear peak for each of the two source activities at a delay of 20 ms.

In previous studies, 4-ExSo-MUSIC on one side (Birot et al., 2011; Becker et al., 2014b) and cMEM on the other side (Chowdhury et al., 2013, 2015; Heers et al., 2016) were each compared with other standard source localization approaches such as MNE, sLORETA and their variants within the hierarchical Bayesian framework, tensor based methods and methods exploiting sparsity. In this context, and using simulations, cMEM and 4-ExSo-MUSIC proved to be most sensitive to the spatial extent of IEDs. cMEM has been extensively applied on clinical epilepsy data in several studies (Heers et al., 2012; Chowdhury et al., 2015; Grova et al., 2016; Heers et al., 2016). Recently, it was also shown that the accuracy of cMEM could be further increased by exploiting the fusion of EEG and MEG (Chowdhury et al., 2015). In addition, it was also shown that cMEM is well-adapted to the study of complex spatio-temporal patterns such as seizures (Heers et al., 2012). On the other hand, to date, 4-ExSo-MUSIC has only been evaluated in a few epilepsy cases (Becker et al., 2014a). Further work will have to consider larger groups of patients in whom the reliability of results can be evaluated with other investigations such as intracerebral recordings. In the meantime, other methods were proposed to remedy the problem of several correlated sources (Becker et al., 2014b; 2014a; Becker et

al., 2015). Among them an approach that imposes sparsity on the variational map of the sources by characterizing the variations in the amplitude between adjacent dipoles as in (Ding, 2009b) as well as sparsity on the estimated source distribution itself has recently shown promising results (Becker et al., 2014a). Nevertheless, further validation is required in particular regarding the choice of some regularization parameters. In a recent study, Zhu et al., 2014 also showed that variation (V-) and wavelet (W-) based sparse source imaging (SSI) can be combined in order to exploit both the capability of recovering source boundaries (and thus source extents) and of compressing sources for better sparse reconstructions. This method applied on simulations as well as experimental data (language and motor responses), was able to recover the source spatial extents and to distinguish between multiple sources of activity better than the standard MNE and other variations of SSI methods. In a similar context, promising methods have been proposed within the Hierarchical Bayesian modeling (HBM) framework (Lucka et al., 2012; Strobbe et al., 2016). Lucka et al., 2012 proposed a fully-Bayesian inference method that was developed to localize focal sources, to correct depth localization, a well-known source of systematic error of many current density reconstruction methods, and to separate single sources in multiple-source scenarios. Strobbe et al., 2016 proposed a variational Bayesian approach called the multiple sparse volumetric priors (MSVP) to localize distributed sources and demonstrated the potential of a Bayesian approach to estimate the underlying sources of interictal activity. The MSVP approach seems inspired from a previously proposed method called COH-s, which was introduced in Chowdhury et al., (2013). COH-s consisted in a model combining spatially extended parcels (coming from MEM-based parcellization) and smoothness constraint as covariance components within a hierarchical Bayesian model and inference based on restricted maximum likelihood estimate (Friston et al., 2006, 2008). In Chowdhury et al., (2013) we showed that MEM was more robust and reliable than COH-s method especially in regards to the scale of the underlying parcellization. All these recently developed promising approaches should be considered in future comparative work.

One main feature of the present study was not only to compare cMEM and 4-ExSo-MUSIC together but also to quantify their respective ability to retrieve the spatial extent from EEG versus MEG signals. In previous studies, when EEG and MEG source localization were compared on clinical datasets, EEG recordings used a relatively small number of electrodes (typically<64) when compared to MEG (275) (Barkley and Baumgartner, 2003; Malmivuo, 2012; Lopes da Silva, 2013). In such a context, most of these clinical studies demonstrated that source localization from MEG signals was more accurate than EEG. Yet, in line with theoretical studies (Gevins, 1993; Srinivasan et al., 1996, 1998) showing that higher spatial resolution can be obtained with closely spaced electrodes, it has been reported that a clear improvement in terms of localization accuracy can be attained in epileptic patients when EEG is acquired with high density scalp electrodes cap, typically more than 120 electrodes (Lantz and Grave de Peralta, 2003; Holmes et al., 2008, 2010; Brodbeck et al., 2011; Yamazaki et al., 2012, 2013). This is even more true when the data are processed with realistic geometry head models (Wang et al., 2011; Birot et al., 2014) using appropriate brain-to-skull conductivity ratios (Huiskamp et al., 1999; Lantz and Grave de Peralta, 2003; Wang and Ren, 2013) or by calculating the calibrated skull conductivity from EEG/MEG data as recommended by Aydin et al., 2014.

Accordingly, some simulation studies suggested similar level of accuracy of EEG versus MEG source localization for an equivalent number of EEG and MEG channels (Liu et al., 2002; Song et al., 2015). Our results are in agreement with these results. In most simulation scenarios, EEG source localization yielded similar or better results than MEG source localization. The only exception was the case of a source in the wall of the central sulcus, which is a favorable situation for MEG in terms of orientation. Given that these are simulations, we are also dealing with the best case scenario for EEG source localization in terms of the head modeling. Therefore, the results from the simulation studies will always be a bit more in favor of EEG when compared to MEG. Recent comparisons on normal subjects, performed with a comparable number of channels for EEG (257) and MEG (275)

in a motor and sensory task, have also confirmed this trend (Klamer et al., 2015). They demonstrated that EEG localization can reach similar or better accuracy than MEG localization when the same number of channels was considered, provided that an accurate individual EEG head model was used. Both modalities have their pros and cons based on their sensitivity. Therefore, to take advantage of the information from the two modalities, fusion of simultaneously recorded EEG-MEG data should be considered as a relevant option whenever it is possible (Aydin, Vorwerk, Küpper, et al., 2014; Chowdhury et al., 2015). Aydin et al., 2014 showed on real data that a simultaneous analysis of EEG and MEG can take advantage of the fusion information, but it might also need calibrated realistic head models with appropriate conductivities especially for EEG head model. On the other hand, combined EEG-MEG data analysis using cMEM method on simulations have been shown to be robust to the modeling error such as using incorrect skull conductivities (Chowdhury et al., 2015).

In practice, simultaneous EEG and MEG recordings with similar number of EEG and MEG channels is not commonly performed. However, in the particular case of patients with epilepsy, simultaneous recordings would be very important as epileptic spikes recorded at different time might arise from slightly different regions. Therefore, to ensure that strictly the same source arrangement was at the origin of EEG and MEG signals, we conducted our study in the framework of simultaneous simulated EEG and MEG signals, taking into account an equivalent number of channels, and a realistically shaped head model. These simulations were also mandatory to quantify the performance of source localization approaches providing a “Ground Truth” that is otherwise difficult to reach when working with clinical data. In patients with epilepsy, the exact spatio-temporal organization of brain region(s) from where the IEDs arise cannot be defined with certainty. At best, it can be inferred from intracerebral recordings, that are usually not performed simultaneously with scalp EEG or MEG, except on rare occasions (Dubarry et al., 2014) and that have limited spatial sampling. The use of realistic simulation models that can mimic the epileptic generators is therefore a necessary step to validate the

EEG/MEG source analysis techniques. In this realistic simulation framework, it is also necessary to avoid the so-called "inverse crime" (i.e. using the perfectly accurate geometric model for both inverse and forward problem). Therefore, to take this issue into account, we decided to modify slightly the skull conductivity values between the forward model considered for simulations and the one considered to solve the source localization inverse problem. However, we would like to point out that there are other ways to further avoid this so-called inverse crime as suggested in (Lucka et al., 2012), where they used different grids for simulation and source localization. The use of real measured background activity can also be an option, especially in low SNR conditions (Kobayashi et al., 2005; Grova et al., 2006; Chowdhury et al., 2013, 2015). In the present study we decided to consider a realistic biophysical model for simulation, allowing to simulate accurate time courses of synchronized epileptic discharges along the spatial extent of the source as proposed and evaluated in (Cosandier-Rimélé et al., 2007), instead of assuming a uniform simulation profile.

The organization of neural activity in the brain is very complex and the relationship between underlying generators and recorded electro-magnetic signals is difficult to model. The simple static simulation models commonly used are a single dipole (Fuchs et al., 1998; Pascual-Marqui, 2002) or patch of dipoles with uniform activity (Liu et al., 2002; Trujillo-Barreto et al., 2004; Grova et al., 2006; Chowdhury et al., 2013). This patch with uniform activity can be extended to simulate different spatial extents of the source but does not model accurately the individual temporal course of dipoles constituting the patch. The fact that the patch extends in all directions with uniform intensity is not realistic and can be a drawback for MEG and EEG. This bias is expected to have more influence on MEG. Indeed, since MEG is selectively sensitive to sulcal sources when, for instance, a patch including two opposing walls of a sulcus would lead to an increased amount of signal cancellation when exactly the same time course is assigned along the patch (Ahlfors et al., 2009). Therefore, more realistic simulation models are required for modeling epileptic activity. Amongst the most realistic

modeling approaches, neuronal computational models have been proposed. Biologically inspired neuronal mass models (Wilson and Cowan, 1972; Lopes da Silva et al., 1976; Traub, 1979) have been widely used to study and model brain activity. In this context realistic microscopic and macroscopic models have been proposed and evaluated. The macroscopic models, also called "lumped" models, are more adapted to model spatially extended activities by coupling multiple populations of cells. These biologically inspired neuron models can provide accurate description of the temporal activity of epileptic events (Wendling et al., 2000; Wendling, 2005). To describe the spatial features of the extended source, dipolar layer distributed along the cortical surface can be considered where each dipole corresponds to a distinct neuronal population. With this spatio-temporal model, that allows to vary the geometry of the source while keeping a realistic description of the temporal source, signals resembling real epileptic events can be generated at the level of intracerebral contact, EEG electrodes (Cosandier-Rimélé et al., 2007, 2008, 2010) or MEG sensors (Badier et al., 2007). This model provided the ideal framework to evaluate cMEM and 4-ExSo-MUSIC using a common simulation environment for EEG and MEG sources in epilepsy. In particular, in such a realistic framework, we could assess in detail the ability of source localization methods to reconstruct precisely the time course of sources in scenarios simulating propagation patterns.

In order to test the accuracy of cMEM and 4-ExSo-MUSIC on clinical EEG and MEG data, we chose patients for whom the existence of a very focal lesion allows for making strong hypothesis on the origin of epileptic interictal activity. The other interest of choosing patients with focal cortical dysplasia was that sources of interictal activity are meant to stay relatively stable in space (Bast et al., 2004). Therefore, averaging of spikes could be performed with a minimal risk of mixing activities arising from different spatial configurations, and therefore without increasing the spatial smoothness of the source estimates. This is not always the case however, therefore, averaging should be considered cautiously, and the sub-averaging technique proposed by (Aydin et al., 2015) can be considered for

activities whose spatial position changes in a dynamic manner within the epileptogenic tissue. In patient 1, both cMEM and 4-ExSo-MUSIC were able to retrieve a source of IEDs that was in concordance with the iEEG findings and the lesion suggested on MRI, in line with our quantitative MEG/iEEG comparison provided in **Figure 5.2** of (Grova et al., 2016). In this case, cMEM provided better sensitivity to the spatial extent than both 4-ExSo-MUSIC and sLORETA. For patient 2, the result of both methods was slightly away from the small mesial FCD. This result was too lateral for cMEM, and too deep for 4-ExSo-MUSIC. It is interesting to notice however that these two "mislocations" corresponded to brain areas where epileptic spikes were spreading. In this regard, these localizations were not fully consistent with depth recordings but could not be considered as misleading either. In both the clinical cases, sLORETA was able to localize the sources but retrieved also a widespread area, with spurious sources in regions that were not shown to be involved during intracerebral interictal spikes. cMEM and 4-ExSo-MUSIC are therefore good candidates to be used in clinical practice of source localization of epileptic discharges and to guide iEEG implantation, although further validation on more clinical datasets is required but was out of the scope of the present study.

5.7. Conclusion

In this paper, we quantitatively assessed the behavior of two source localization methods, cMEM and 4-ExSo-MUSIC, when localizing complex spatio-temporal patterns of IEDs using simulations of EEG and MEG data generated from biophysical computational neural mass model. While both the methods were studied separately and well-established for their sensitivity to the spatial extent of the generators, our goal was to compare the two methods together on a common ground of well-controlled realistic simulations while taking into account simultaneously recorded HR-EEG and MEG data. Overall, our results demonstrate the eligibility of both 4-ExSo-MUSIC and cMEM for application on clinical data due to their high sensitivity to the location and spatial extent of the generators of

epileptic discharges in EEG and MEG. The superior performance of 4-ExSo-MUSIC when dealing with single source of large signal-to-noise ratio, and superior performance of cMEM when dealing with complex spatio-temporal propagation patterns suggests that the two methods provides interesting complementarities that should be taken into account when localizing clinical data.

5.8. Acknowledgements

This work was supported by a studentship from Savoy Foundation, Canada for the period 2011-2015, NSERC Discovery grant (RGPIN/356610-2013), CIHR (MOP-93614 and MOP-133619), Centres of Excellence for Commercialization of Research (CECR) and the American Epilepsy Society award. The acquisition of the HR-EEG system was supported by a grant from the French Foundation for Research on Epilepsy (FFRE) (2011 annual call).

5.9. Appendix A

MEM regularization: In the MEM optimization (equation (5-4)), the ν-entropy is strictly a convex function that needs to be maximized under constraints, which is equivalent to maximizing an unconstrained strictly concave Lagrangian function. In the Lagrangian function, the Lagrangian parameters κ and $\boldsymbol{\lambda}$ are used to add constraints to the objective function $S_\nu(dp)$, as follows:

$$\begin{aligned} L(dp,\kappa,\boldsymbol{\lambda}) &= -S_\nu(dp) + \boldsymbol{\lambda}^T(\mathbf{m} - \boldsymbol{G}\mathrm{E}_{dp}[\mathbf{j}]) + \kappa(1 - \int dp(\mathbf{j})) \\ L(dp,\kappa,\boldsymbol{\lambda}) &= \int f(\mathbf{j}) \log f(\mathbf{j}) d\nu(\mathbf{j}) + \boldsymbol{\lambda}^T(\mathbf{m} - \boldsymbol{G}\mathrm{E}_{dp}[\mathbf{j}]) + \kappa(1 - \int dp(\mathbf{j})) \end{aligned} \quad \text{(5-A1)}$$

where the first term is the ν-entropy, second term is the data goodness of fit, and the last term expresses the constraint that $dp(\mathbf{j})$ must be a probability distribution. Therefore, the MEM formalism consists in a duality principle where the primal solutions (equation (5-6) and (5-7)) are given as a function of the Lagrange multipliers (equation (5-A1) and (5-A5), respectively).

Therefore, the optimal solution $(d\hat{p}, \tilde{\kappa}, \tilde{\lambda})$ of this optimization problem calculated via the Lagrangian formalism, i.e. $\arg\min_{dp,\kappa,\lambda} L(dp, \kappa, \lambda)$, provides:

$$d\hat{p}(\mathbf{j}) = \frac{e^{\tilde{\lambda}^T G\,\mathbf{j}}}{Z(\tilde{\lambda})} d\nu(\mathbf{j}) \qquad \text{(5-A2)}$$

where $\tilde{\lambda}$ is the maximum of the non-linear optimization of a convex function $D(\lambda)$ in a q-dimensional space, thus accepting a unique solution. In practice, the optimization problem depends only on the parameter λ which is the same dimension as the number of sensors (q).

$$\tilde{\lambda} = \arg\max_{\lambda} D(\lambda) \text{ , where } D(\lambda) = \lambda^T \mathbf{m} - F_\nu(\boldsymbol{G}^T\lambda) - \frac{1}{2}\lambda^T \boldsymbol{\Sigma}_e \boldsymbol{\Sigma}_e{}^T \lambda \qquad \text{(5-A3)}$$

and the normalizing constant in equation (5-A2), $Z(\tilde{\lambda}) = e^{F_\nu(\boldsymbol{G}^T\tilde{\lambda})}$ is the partition function and F_ν is the free energy associated with the reference distribution $d\nu$, defined as the log of the partition function.

$$F_\nu(\xi) = \log \int e^{\xi^T \mathbf{j}} d\nu(\mathbf{j}) \text{ with } \xi = \boldsymbol{G}^T\tilde{\lambda} \qquad \text{(5-A4)}$$

and $\boldsymbol{\Sigma}_e$ is the noise covariance matrix for **e** in equation 1.

It can then be shown that the primal solution in equation (5-7) giving the MEM estimate of the sources' intensities **j** could then be related to the dual solution as the gradient of the free energy F_ν:

$$\hat{\mathbf{j}}_{MEM} = \nabla F_\nu(\xi)\big|_{\xi=\boldsymbol{G}^T\tilde{\lambda}} \qquad \text{(5-A5)}$$

When applied to the reference distribution introduced in equation (5-8), the MEM estimate of the sources in each parcel k can be found to be:

$$\hat{\mathbf{j}}^k_{MEM} = \hat{\alpha}_k[\boldsymbol{\mu}_k + \boldsymbol{\Sigma}_k \boldsymbol{G}_k^T \tilde{\lambda}] \qquad \text{(5-A6)}$$

$$\text{where } \hat{\alpha}_k = \frac{\alpha_k}{\alpha_k + (1-\alpha_k)\exp(-F_{v,k}(\boldsymbol{G}_k^T \tilde{\boldsymbol{\lambda}}))} \tag{5-A7}$$

where $F_{v,k}$ is the free energy corresponding to the k^{th} parcel when active (i.e. S_k = 1), given by:

$$F_{v,k}\left(\boldsymbol{G}_k{}^T \tilde{\boldsymbol{\lambda}}\right) = \boldsymbol{\mu}_k^T \boldsymbol{G}_k^T \tilde{\boldsymbol{\lambda}} + \frac{1}{2}\tilde{\boldsymbol{\lambda}}^T \boldsymbol{G}_k \boldsymbol{\Sigma}_k \boldsymbol{G}_k^T \tilde{\boldsymbol{\lambda}} \tag{5-A8}$$

and $\boldsymbol{G}_k$ is the $(q \times r_k)$ submatrix of $\boldsymbol{G}$ for the k^{th} parcel.

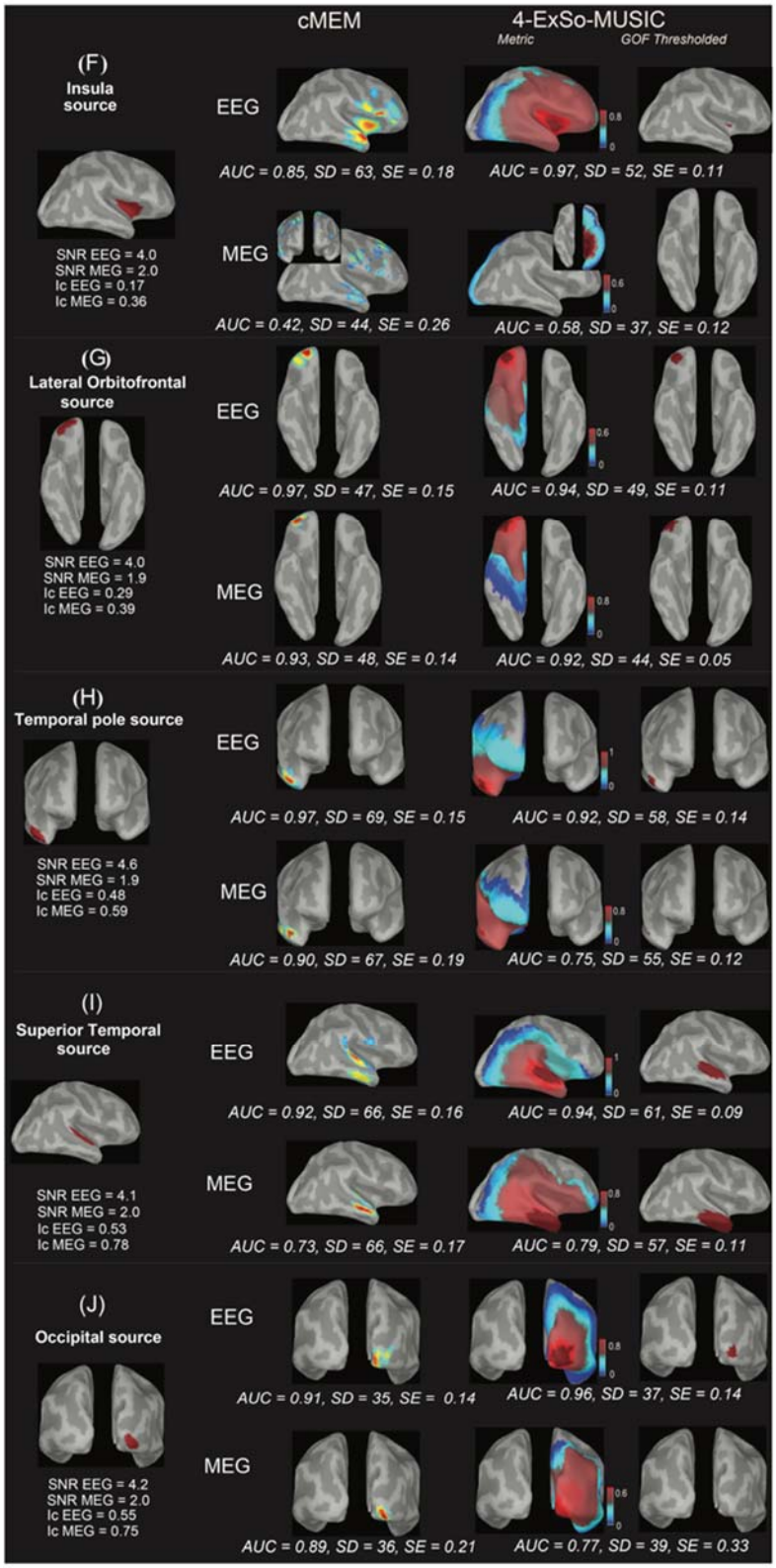
cMEM
4-ExSo-MUSIC
Metric
GOF Thresholded
(F)
Insula source
EEG
AUC = 0.85, SD = 63, SE = 0.18
AUC = 0.97, SD = 52, SE = 0.11
SNR EEG = 4.0
SNR MEG = 2.0
Ic EEG = 0.17
Ic MEG = 0.36
MEG
AUC = 0.42, SD = 44, SE = 0.26
AUC = 0.58, SD = 37, SE = 0.12
(G)
Lateral Orbitofrontal source
EEG
AUC = 0.97, SD = 47, SE = 0.15
AUC = 0.94, SD = 49, SE = 0.11
SNR EEG = 4.0
SNR MEG = 1.9
Ic EEG = 0.29
Ic MEG = 0.39
MEG
AUC = 0.93, SD = 48, SE = 0.14
AUC = 0.92, SD = 44, SE = 0.05
(H)
Temporal pole source
EEG
AUC = 0.97, SD = 69, SE = 0.15
AUC = 0.92, SD = 58, SE = 0.14
SNR EEG = 4.6
SNR MEG = 1.9
Ic EEG = 0.48
Ic MEG = 0.59
MEG
AUC = 0.90, SD = 67, SE = 0.19
AUC = 0.75, SD = 55, SE = 0.12
(I)
Superior Temporal source
EEG
AUC = 0.92, SD = 66, SE = 0.16
AUC = 0.94, SD = 61, SE = 0.09
SNR EEG = 4.1
SNR MEG = 2.0
Ic EEG = 0.53
Ic MEG = 0.78
MEG
AUC = 0.73, SD = 66, SE = 0.17
AUC = 0.79, SD = 57, SE = 0.11
(J)
Occipital source
EEG
AUC = 0.91, SD = 35, SE = 0.14
AUC = 0.96, SD = 37, SE = 0.14
SNR EEG = 4.2
SNR MEG = 2.0
Ic EEG = 0.55
Ic MEG = 0.75
MEG
AUC = 0.89, SD = 36, SE = 0.21
AUC = 0.77, SD = 39, SE = 0.33

Figure S5.1. Single Source analysis. EEG and MEG source localization results (with their corresponding validation metrics: AUC, SD and SE values) using cMEM and 4-ExSo-MUSIC on simulated sources of spatial extent 10 cm^2 in (**F**) Insula, (**G**) Lateral orbito-frontal, (**H**) Temporal pole, (**I**) Superior Temporal region, and (**J**) Occipital region. All the source localization results were displayed over the inflated cortical surface obtained from Brainstorm software toolbox. In this figure, we presented source localization results of cMEM after an Otsu threshold, which is obtained by taking the absolute value of the current density at the peak of the spike, normalized to its maximum activity and thresholded upon the level of background activity (Otsu, 1979). We presented two maps for 4-ExSo-MUSIC results: 4-ExSo-MUSIC metric map and the GOF thresholded binary map to be able to compare between the original and thresholded source maps.

Chapter 6 Manuscript 3: Reproducibility of EEG-MEG fusion source analysis of interictal spikes - relevance in pre-surgical evaluation of epilepsy

6.1. Context

Based on the studies in Chapter 4 and 5, it is well-established that cMEM methodology is eligible for application on clinical data. The MEM-fusion approach presented in Chapter 4 provides a new source analysis framework for combining EEG and MEG, resulting in improved accuracy of IEDs localization. In Chapter 5, we assessed the ability of cMEM to recover accurately more complex propagation patterns of IEDs, when considering either high density EEG or MEG. We showed that cMEM was complementary to 4-ExSo-MUSIC, another probabilistic framework developed to recover the spatial extent of the IEDs sources, with improved performance of cMEM when dealing with complex propagation patterns. To this end, application and validation of MEM-fusion approaches on clinical data and assessing its overall clinical relevance is the main objective of this dissertation.

As explained in **Section 3.4.1**, source localization of single spike offers a good balance between the SNR and spike variability. In Chapter 4, we demonstrated that MEM-fusion was robust to low SNR conditions of single spikes and takes full benefit of the complementarities between EEG and MEG in fusion. Therefore, we propose to study the reproducibility of single spike source localization when combining EEG and MEG data.

We therefore developed and validated a new methodological source analysis pipeline involving clustering of single spike source localization results to provide a consensus map for the most reproducible and clinically reliable source localization results. Therefore, manuscript 3 presents the evaluation of such an approach when applied to a database of 26 patients with focal intractable epilepsy.

This manuscript is in preparation for publication as (R.A.Chowdhury, Pellegrino G., Aydin U., Lina J.M., Dubeau F., Kobayashi E., Grova C. *Reproducibility of EEG-MEG fusion source analysis of inter-ictal spikes - relevance in pre-surgical evaluation of epilepsy*)

6.2. Abstract

Fusion of electroencephalography (EEG) and magnetoencephalography (MEG) using Maximum Entropy on the Mean method (MEM-fusion) provides accurate localization and sensitivity to the spatial extent of the generators of inter-ictal epileptic discharges (IEDs). Our goal is to assess the clinical relevance of single spike source localization (SSSL) using MEM-fusion. We proposed a systematic approach for clustering SSSL results to find the most reliable and consistent source map (consensus map) among the reconstructed single spike sources.

Thirty-four types of IEDs were analyzed from 26 patients with a well-defined epileptic focus. SSSLs were performed on EEG, MEG and EEG-MEG fusion. Consensus maps were estimated using hierarchical clustering in the source space. Qualitative (spike-to-spike reproducibility rate (SSR)) and quantitative (localization error and spatial dispersion) assessments were done using the epileptic focus as clinical reference. The impact of the number of EEG electrodes in fusion was also assessed.

Fusion SSSL provided better results than EEG or MEG alone. Fusion found at least one cluster that was concordant with the clinical reference in all cases and the concordant cluster was always the one involving the highest number of spikes. Fusion yielded highest SSR (EEG = 55%, MEG = 71 %, fusion = 90%) and lowest localization error. Adding only 21 EEG electrodes was sufficient for accurate EEG-MEG fusion.

MEM-fusion with consensus map approach provided an automatic way of finding the most reliable and concordant generators of IEDs. We therefore demonstrated

the pertinence of SSSL using MEM-fusion as a valuable non-invasive tool for pre-surgical evaluation of epilepsy.

6.3. Introduction

Epilepsy is a neurological disorder caused by recurrent seizures and it affects approximately 50 million people worldwide ("WHO | Epilepsy," 2016). Epilepsy surgery offers the possibility of a reduction or elimination of the seizures to drug resistant patients. Candidates for epilepsy surgery undergo an extensive pre-surgical evaluation, which aims at localizing the brain areas where the seizures are generated (epileptogenic focus) and to determine whether surgery is feasible (avoiding any functional loss). Inter-ictal epileptic discharges (IEDs) are spontaneous abnormal neuronal discharges occurring in between the seizures without any clinical manifestations. Their generators usually overlap with the region involved in the seizure onset (Hauf et al., 2012). The localization of the IEDs generator called irritative zone (IZ) is therefore an important marker for the study of intractable focal epilepsy (Bautista et al., 1999; Hufnagel et al., 2000; Ryvlin et al., 2014).

Electroencephalography (EEG) and Magnetoencephalography (MEG) are two non-invasive electrophysiological techniques able to track IEDs at high temporal resolution. They possess specific complementary properties and their combination can be extremely informative in the assessment of the generators of IEDs. Simultaneously recorded EEG and MEG showed that MEG is overall more sensitive to spikes but some spikes could be detected in EEG and not in MEG (Hillebrand and Barnes, 2002; Yoshinaga, 2002; Lin et al., 2003; Iwasaki et al., 2005; Ramantani et al., 2006; Ossenblok et al., 2007; Scheler et al., 2007). This is largely determined by their sensitivity to the orientation of the anatomical sources (Haueisen et al., 2012). MEG is selectively sensitive to sources that are tangential to the skull surface (fissural or sulcal walls) (Hämäläinen et al., 1993). EEG is sensitive to both tangential and radial sources (crest of the cortical gyri) but EEG spikes originating from deeper regions are often obscured by the radially oriented

background ongoing activity, since these generators are located closer to the scalp sensors (Ahlfors et al., 2010). Since the ratio between tangential source and radial sources is approximately 3:1 (Haueisen et al., 2012), MEG is overall more sensitive than EEG (Cohen and Cuffin, 1983). On the other hand, MEG fails to detect deeper cortical sources (such as mesial temporal and deep orbitofrontal cortices) because of the rapid fall of the magnetic field with depth when using axial gradiometers (Mikuni et al., 1997; Oishi et al., 2002; Huiskamp et al., 2010), the lack of direct contact between MEG sensors and skin, and head movements inside the MEG helmet causing noisy data. Therefore, MEG and EEG sources reflect different anatomical aspects of the activated sources because of their relative sensitivities. As a result, epileptic spike detection can be significantly improved by analyzing simultaneously recorded EEG and MEG data; thus taking advantage of the complementarities of the two techniques.

MEG is sensitive to smaller generators than EEG, albeit both techniques require the activity of a brain region to be synchronized over a spatially extended region of several square centimeters in order to result in a signal visually distinguishable from the ongoing background (Cooper et al., 1965; Ebersole, 1997a; Mikuni et al., 1997; Merlet and Gotman, 1999; Oishi et al., 2002; Tao, Baldwin, Hawes-Ebersole, et al., 2007; von Ellenrieder et al., 2014a; Ramantani et al., 2014). EEG and MEG source localization techniques are used to localize the generators of epileptic discharges but the main challenge lies not only in localizing the generators but also accurately recovering their spatial extension. Source localization with the coherent Maximum Entropy on the Mean (cMEM) method has been shown to provide reliable and accurate localization of the sources of EEG and MEG discharges together with their spatial extent along the cortical surface (Grova et al., 2006; Chowdhury et al., 2013, 2015; Grova et al., 2016; Heers et al., 2016).

Spatial resolution of EEG and MEG influences the localization accuracy of source localization. MEG tends to provide higher spatial resolution than EEG due to mainly two reasons. Firstly, EEG scalp potentials are highly attenuated and spatially smeared by the very low conductivity of the skull; whereas MEG is less

distorted by the resistive properties of the skull. This leads to higher sensitivity of EEG to errors in skull modeling while MEG forward problem is more robust in this aspect (Hämäläinen and Sarvas, 1989; Mosher, Leahy, et al., 1999). Secondly, the number of MEG sensors (whole head coverage) when compared to usually considered to EEG system (10-20 or 10-10 system) is typically larger (Ossenblok et al., 2007; Klamer et al., 2015). However, it has been demonstrated that improvement in EEG localization accuracy can be attained when using high density electrodes and realistic geometry head models (Liu et al., 2002; Lantz and Grave de Peralta, 2003; Ryynanen et al., 2006; Wang et al., 2011; Birot et al., 2014; Klamer et al., 2015; Song et al., 2015; Chowdhury et al., 2016). Actually, it has been shown that simultaneously acquired EEG and MEG data are super additive, i.e., their combination provide more information relevant to source localization than the sum of the monomodal information (Pflieger et al., 2000). With the aim to better recover the location and the spatial extent of the generators of IEDs, we previously proposed an EEG-MEG fusion source localization approach using the cMEM framework (hereafter denoted as MEM-fusion) (Chowdhury et al., 2015). Based on simulated data, we showed that MEM-fusion yields higher localization accuracy (more accurate, robust and sensitive to the spatial extent) than monomodal source localizations. In this study, we further evaluate this method on clinical data, proposing a methodology to also assess the reproducibility and reliability of SSSL results.

The first and one of the most crucial steps in source analysis is the spike detection. It is a common practice to visually review EEG/MEG data and to classify and group spikes based on their morphology, topography, and signal-to-noise ratio (SNR). Usually inter-ictal spikes reveal varying morphology and topography, and most single spikes actually show low SNR signals that are highly contaminated by background noise. Therefore, reproducible transient spikes with similar spatio-temporal patterns are usually grouped into distinct categories and averaged to improve the SNR before applying any source localization method (Bast et al., 2004; Hara et al., 2007; Tanaka et al., 2010; Wennberg and Cheyne, 2014). Some studies

also adopted automatic cluster analysis (at sensor level) to align and classify the spikes on the basis of their spatial distribution followed by equivalent current dipole analysis of each cluster average (Van ’t Ent et al., 2003; Ossenblok et al., 2007). Ossenblok et al., (2007) reported that cluster analysis and localization failed in several cases due to either a large variability between single spikes within one cluster or due to strong background activity leading to low SNR cluster averages. Moreover, averaging can also lead to some signal cancellation, which is more likely to filter out source activities that vary slightly over each individual spike (Ahlfors et al., 2009). In this line, Aydin et al., (2015) combined bootstrap techniques and sub-averaging to increase SNR while preserving some of the between spike differences. In order to maintain a balance between the SNR while respecting inherent spike variability, we proposed to consider single spike source localization (SSSL). Moreover, we previously demonstrated the robustness of MEM-fusion in low SNR conditions usually encountered when performing SSSL (Chowdhury et al., 2015). Therefore, we hypothesized that SSSL of combined EEG and MEG data through MEM-fusion can take full benefit of the complementarities between the two modalities to characterize the underlying generators of IEDs.

Following SSSL, we also proposed a new method based on spatial correlation to estimate a consensus map summarizing the most reliable and consistent source maps among the reconstructed single spike sources. The consensus map was used to assess spike-to-spike reproducibility of SSSL results.

Based on combined EEG and MEG data analysis, several studies have indicated that the coverage of the whole head using dense sampling of EEG and MEG channels is crucial to achieve high localization accuracy (Fuchs et al., 1998; Sharon et al., 2007; Chowdhury et al., 2016). We previously demonstrated using simulated data that combining EEG and MEG within the MEM-fusion framework provided accurate results even when only few EEG electrodes were involved (Chowdhury et al., 2015). In the present study, we further evaluate the impact of the number of EEG electrodes to be considered during MEM-fusion on clinical data.

6.4. Materials and methods

6.4.1. Patient selection

This study was approved by the Montreal Neurological Institute (MNI) Research Ethics Board and all procedures were conducted in compliance with the Code of Ethics of the World Medical Association (1964 Helsinki declaration and its later amendments). All patients signed a written informed consent prior to participation in the EEG-MEG acquisition. Among the patients who underwent a simultaneous EEG-MEG recording for pre-surgical evaluation at the MNI, we retrospectively selected those patients fulfilling the following inclusion and exclusion criteria. Inclusion criteria: 1) focal neocortical epilepsy; 2) available ground truth information such as intracranial EEG (iEEG) findings, well-defined epileptogenic lesion, and resection area from epilepsy surgery; 3) good quality anatomical MRI to obtain an accurate segmentation of head surfaces, which is required for realistic individual head modeling; 4) sufficient number of spikes (at least 10 spikes). Exclusion criteria: 1) multifocal or widespread epileptic focus; 2) deep generators; 3) large magnetization artifacts.

Acquisitions were done at the Psychology Department of the University of Montreal from September 2006 until July 2012 and later at Montreal Neurological Institute and Hospital. We selected 26 patients, from whom totally 34 different types of markers involving spikes, spike and wave discharges (spike-wave) and slow waves were marked. It is important to mention that most of these patients who were selected for EEG-MEG investigation consisted in challenging cases from a clinical point of view.

6.4.2. MEG-EEG data acquisition and pre-processing

Simultaneous EEG-MEG recordings were performed using a CTF MEG system (MISL, Vancouver, Canada) with 275 axial gradiometers and 54 EEG electrodes arranged on a cap according to the 10-20 system, plus additional electrodes according to the 10-10 system (F1, FPZ, F2, AF7, AF3, AFZ, AF4, AF8, FT9, FC5,

FC3, FC1, FCZ, FC2, FC4, FC6, FT10, C1, C2, CP5, CP3, CP1, CPZ, CP2, CP4, CP6, P9, P1, P2, P10, PO7, PO3, POZ, PO4, PO8 - Easy-cap, Herrsching, Germany). Note that in the CTF MEG system most of the recordings were done using 272 MEG sensors since 3 channels were bad. Additional electrodes were used to record electro-cardiogram and electro-oculograms. EEG electrode positions and the head shape were digitized using a Polhemus 3D localizer (Colchester, NH). The CTF system is equipped with reference sensors that waere used to calculate synthetic 3rd order gradients to reduce magnetic background interferences. During the acquisition, the head position of the subject was tracked using localization coils placed on three fiducial points (nasion, left and right peri-auricular points). Sampling rates for EEG/MEG acquisitions were either 1200 Hz or 2400 Hz. To minimize head movement, all recordings were done with subjects lying down in a supine position. Recording at rest lasted for 1 hour, with 10 runs of six minutes each. Brainstorm software (Tadel et al., 2011) was used to pre-process EEG/MEG data offline. Data were down-sampled to 600 Hz, synthetic 3rd order gradient noise correction was applied to MEG data, DC-offset was removed, EEG was re-referenced to average montage, and 60 Hz notch filter (and its harmonics) was applied (Heers et al., 2012, 2016). EEG and MEG data were visually inspected and inter-ictal spikes were marked using the DataEditor software (MISL, Vancouver, Canada) by two experienced neurophysiologists (GP and EK). The spikes were marked at their peak. EEG/MEG spikes were further filtered at 0.3-70 Hz bandpass filter (butterworth, 4th order) prior to source localization.

6.4.3. MRI data acquisition, analysis and head modeling

High-resolution anatomical 3T MRI (Siemens Tim Trio 3T scanner) were acquired at the Brain Imaging Center of the MNI, using a T1W MPRAGE sequence (1mm isotropic 3D images, 192 sagittal slices, 256 × 256 matrix, TE (echo time) 52.98 ms, TR (repetition time) 52.3 s). The MRI was processed using BrainVISA-4.2.1

software [11], allowing the segmentation of the surfaces of the skin and the gray-white matter interface which was then used as the source space for source imaging (Mangin et al., 1995). The MRI, the skin surface, and the cortical mesh tessellated from the gray-white matter interface were imported to the Brainstorm software for subsequent processing. MRI-MEG co-registration was performed by applying a surface fitting between the anatomical head shape derived from the MRI and the head points digitized using the Polhemus system at the time of the EEG-MEG acquisition. Individual three-layer Boundary Element Method (BEM) surfaces (inner-skull, outer-skull and skin) were constructed. The EEG and MEG forward models were computed using the OpenMEEG BEM (Kybic et al., 2006; Gramfort et al., 2011) implementation in Brainstorm software, using a three-layer BEM model consisting of the inner skull, outer skull and the scalp surfaces, with conductivity values of 0.33 : 0.0165 : 0.33 S/m, respectively (Ferree et al., 2000; Gonçalves et al., 2003; Hoekema et al., 2003; Lai et al., 2005).

6.4.4. EEG-MEG distributed source localization method

The EEG-MEG inverse solutions evaluated in this study use a distributed sources model where a large number of dipolar sources were distributed along the cortical surface. Considering the anatomical constraint that the orientation of each dipole is fixed perpendicular to the local cortical surface (Dale and Sereno, 1993), the linear relationship between the source amplitude and the measurements is given by:

$$\boldsymbol{M} = \boldsymbol{G}\,\boldsymbol{J} + \boldsymbol{E} \qquad (6\text{-}1)$$

where $\boldsymbol{M}$ is a $q \times \tau$ signal matrix acquired on q EEG/MEG channels at τ time samples. $\boldsymbol{E}$ models the additive measurement noise ($q \times \tau$ matrix). $\boldsymbol{J}$ is a $r \times \tau$

[11] http://www.brainvisa.info

unknown matrix of the current density of the r dipolar sources along the tessellated cortical surface. $\boldsymbol{G}$ indicates the $q \times r$ lead field matrix obtained by solving the forward problem, thus estimating the contribution of each dipolar source on the sensors. The objective of the inverse solution is to estimate $\boldsymbol{J}$ from the measured data $\boldsymbol{M}$ and the estimated lead field matrix $\boldsymbol{G}$.

a. cMEM inverse solution

Every source localization approach consists in solving an ill-posed inverse problem (Baillet and Mosher, 2001). Therefore, some a priori knowledge should be incorporated within a regularization framework in order to estimate a unique solution. In the MEM framework, we consider the amplitude of the sources $\boldsymbol{J}$ to be estimated as a multivariate random variable $\mathbf{j}$ of dimension r, with a probability distribution $dp(\mathbf{j})$. To regularize the inverse problem, the MEM framework incorporates prior information on $\mathbf{j}$ in the form of a reference distribution $dv(\mathbf{j})$ (Amblard et al., 2004). This reference distribution is a realistic spatial model that assumes the brain activity to be organized into K ($K << r$) cortical parcels showing homogenous activation states. This type of spatial clustering is obtained using a Data Driven Parcellization (DDP) technique (Lapalme et al., 2006). This DDP consisted in a region growing approach where the seeds were identified as dipolar source on the cortical mesh more likely to contribute to the data. Such contribution was quantified using a projection method, the Multivariate Source Pre-localization (MSP) technique (Mattout et al., 2005), that provides a probability-like coefficient (MSP score) between 0 and 1 for each dipolar source on the cortical mesh, characterizing the contribution of each source to the data.

In the MEM reference model, a hidden state variable is associated to each parcel in order to model the probability of the parcel to be active. Note that the probability of being active of each parcel was initialized using the median of the MSP scores of all the sources within the parcel. Then, based on the state of activation of the parcels, MEM inference is able to specifically switch these parcels on or off and to estimate a contrast of source intensities within the selected active parcels. cMEM

method, which is a variant within MEM framework, further imposes a spatial smoothness constraint along each cortical parcel in the reference distribution $dv(\mathbf{j})$ (Harrison et al., 2007). Then, the MEM principle aims at estimating the distribution $d\hat{p}(\mathbf{j})$ that maximizes the amount of information brought by the data, with respect to the reference distribution $dv(\mathbf{j})$ (Jaynes, 1957; Amblard et al., 2004). The resulting current density distribution $\hat{\mathbf{j}}_{MEM}$ is estimated using MEM regularization, iteratively for each time sample, as the first moment (or Mathematical expectation) of the distribution $d\hat{p}(\mathbf{j})$, (i.e., $\hat{\mathbf{j}}_{MEM} = \mathrm{E}_{d\hat{p}}[\mathbf{j}]$). For more details on cMEM methodology and implementation please refer to (Chowdhury et al., 2013).

In our previous study (Chowdhury et al., 2013), quantitative assessment of cMEM method demonstrated the benefits of whole cortex parcellization in detecting spatially extended sources. Moreover, EEG-MEG fusion using cMEM (denoted MEM-fusion) has been shown to provide excellent localization accuracy and sensitivity to the underlying spatial extent of the sources (Chowdhury et al., 2015). The MEM-fusion methodology is briefly described in the next section.

b. MEM fusion

The integrated EEG-MEG analysis was performed by the symmetrical fusion of normalized EEG and MEG measurements as follows:

$$\begin{bmatrix} \boldsymbol{M}^{s}_{EEG} \\ \boldsymbol{M}^{s}_{MEG} \end{bmatrix} = \begin{bmatrix} \boldsymbol{G}^{s}_{EEG} \\ \boldsymbol{G}^{s}_{MEG} \end{bmatrix} \boldsymbol{J} + \begin{bmatrix} \boldsymbol{E}^{s}_{EEG} \\ \boldsymbol{E}^{s}_{MEG} \end{bmatrix} \qquad (6\text{-}2)$$

In order to integrate the two modalities efficiently, it was first important to scale them to a common basis since they have different units. To do so, we have applied SNR transformation of the data and the lead field, using the mean standard deviation of their respective background activity ($\boldsymbol{E}_{EEG}$, $\boldsymbol{E}_{MEG}$) for all sensors of a modality (Fuchs et al., 1998; Ding and Yuan, 2013); thus creating unit-less measures of EEG and MEG. The superscript "s" in equation (6-2) represents the scaled data, lead field matrix and noise.

One striking feature of multimodal data fusion within the MEM framework is its ability to incorporate the complementary information provided by EEG and MEG data through the reference distribution $d\nu$. In other words, the probability of activation of each parcel has been initialized by the fusion of the MSP scores obtained from both EEG and MEG data. To integrate the contribution of the sources to either or both the EEG and MEG data, we therefore applied the logical OR operation on the MSP scores of the two modalities:

$$\boldsymbol{MSP}_{MEEG} = \boldsymbol{MSP}_{EEG} + \boldsymbol{MSP}_{MEG} - (\boldsymbol{MSP}_{EEG} \circ \boldsymbol{MSP}_{MEG}) \qquad (6\text{-}3)$$

where $\circ$ denotes the Schur (Hadamard) product of the two matrices leading to element-wise multiplication of their elements. These $\boldsymbol{MSP}_{MEEG}$ scores then further impacted both the estimation of the parcels through DDP and the initialization of their probability of being active, putting forward cortical parcels for which the median of the fusion MSP scores was high. This type of fusion during the definition of the reference model can lead to an efficient way to integrate complementary information from the two modalities. This is a modeling particularity and originality of the MEM model when compared to other fusion approaches. Then starting from this reference model based on the fusion MSP scores, the MEM regularization technique was used to find the MEM solution for fusion data. For more details on the MEM fusion, the reader can refer to (Chowdhury et al., 2015).

6.4.5. EEG-MEG source analysis

Our standard clinical investigation involves averaging spikes with similar morphology and topography to improve the SNR of the EEG/MEG signals and then applying the source localization method (Heers et al., 2014, 2016; Pellegrino, Hedrich, Chowdhury, et al., 2016b). To provide a comparison between standard monomodal EEG and MEG source localization results, we first presented the results from these standard averaged spike EEG/MEG source localizations for all 34 spike types (range, 11 to 287 spikes per type), from 26 patients selected for this

study. cMEM method allows localizing EEG/MEG data in the time domain; thus providing source maps for each time sample. We extracted the spike signals for a window of -100 ms to 100 ms with 0ms being the peak of the spike, whereas a 2 s baseline window was selected for noise covariance estimation. The averaged spike of each marker type was analyzed using monomodal EEG and MEG source localization. In this study, source localization results only at the peak of the spikes were considered.

As explained earlier, SSSL using cMEM method is suitable for retrieving important information available at the individual spike level. Therefore, in this study we have also analyzed the single spikes from each marker type using EEG, MEG and EEG-MEG fusion. Then, we have proposed an approach for clustering all the reconstructed single spike sources to estimate a consensus map. This approach will be described in the next section.

6.4.6. Estimation of consensus map to assess spike-to-spike reproducibility

The purpose of estimating a consensus map was to assess the reproducibility of a reliable and consistent source map across all the reconstructed single spike source maps. To do so, SSSL was first applied and then a similarity index between all source maps based on their spatial correlation was estimated. Later on, the source maps were clustered using a hierarchical clustering approach and the single spike source maps belonging to each cluster were averaged to obtain the averaged source maps (will be further denoted as cluster map). Finally, the most reproducible and reliable cluster map was chosen as the one with highest number of spikes, which will be called a consensus map.

Since SSSLs were applied within a window of -100 ms to 100 ms around the peak of the spike, the consensus map was estimated along a specific window length around the peak of the spike, in order to recover the main spatio-temporal patterns of the spikes. Since we included spikes, spike-waves and slow waves in our

analysis, the window length considered to estimate the consensus map was adjusted accordingly. As per the criteria outlined by Walczak et. al in (Engel et al., 2008), the duration of each transient IEDs should be less than 200ms; a spike has a duration of less than 70ms whereas sharp waves have a duration of 70 to 200ms. Therefore, the chosen window of analysis for estimating the consensus map was 50 ms for spikes and 100 ms for the spike-waves and slow waves.

The procedure for the estimation of the consensus map is described in the following steps:

Step 1. Normalization of the reconstructed source maps

cMEM reconstructed current density distribution, or source maps, obtained for each single spike will be denoted with $\hat{\boldsymbol{j}}$, a $r \times \tau$ matrix, where r is the number of source dipoles and τ is the number of time samples of the selected time window of interest. The mean of the estimated current source density was first subtracted from the source maps to obtain zero-mean maps. Then, source maps were normalized between 0 and 1 using the Frobenius norm as follows, $\hat{\boldsymbol{j}}^n = \left|\hat{\boldsymbol{j}}\right| \Big/ \left\|\hat{\boldsymbol{j}}\right\|_F$. Frobenius norm is the square root of the sum of the square of the coefficients of a matrix. The purpose of this normalization is to retrieve the spatio-temporal shape of all the source maps within a selected window length, thus, to recover similar dynamic patterns.

Step 2. Estimation of the similarity index based on absolute correlation measure

Considering that there were N source maps for each spike type, the absolute correlation measure (a scalar value) between normalized source maps was considered as a similarity index. Considering two normalized source map, $\hat{\boldsymbol{a}}^n(i,j)$ and $\hat{\boldsymbol{b}}^n(i,j)$, the similarity was given by,

$$s(\hat{\boldsymbol{a}}^n, \hat{\boldsymbol{b}}^n) = \sum_{j=1}^{\tau} \sum_{i=1}^{r} (\hat{\boldsymbol{a}}^n(i,j) \; . \hat{\boldsymbol{b}}^n(i,j)) \qquad (6\text{-}4)$$

using element-wise product of the two matrices. Then, the similarity matrix containing the absolute correlation measures between every combination of N source maps was given by $\boldsymbol{S}$, an $N \times N$ matrix with $\boldsymbol{S}(u,v) = s(\hat{\boldsymbol{j}}^n_u, \hat{\boldsymbol{j}}^n_v)$ for u and $v = 1, \ldots, N$.

From this similarity index, a dissimilarity matrix estimated as $\boldsymbol{Đ} = 1 - \boldsymbol{S}$, was introduced to hierarchical clustering purposes.

Step3. Hierarchical clustering of source maps

Given a set of N objects to be clustered, and a dissimilarity matrix $\boldsymbol{Đ}$, we applied hierarchical clustering to indentify clusters of most reproducible spatio-temporal source maps among all SSSL. Hierarchical clustering was applied using the generalized Ward's method (Ward, 1963) of agglomerative clustering; using the Lance-Williams recursive formula (Lance and Williams, 1967) for updating dissimilarities between the clusters (Batagelj, 1988; Marrelec et al., 2015). The clustering was initialized with the dissimilarity values from $\boldsymbol{Đ}$ as the distance between the N objects, which was then followed by updating the cluster distance using Lance-Williams formula (equation (6-5)). For example, considering the disjoint clusters C_i, C_j, and C_k with respective sizes n_i, n_j and n_k, the updated cluster distance can be computed recursively as follows:

$$d(C_i \cup C_j, C_k) = \frac{n_i+n_k}{n_i+n_j+n_k} d(C_i, C_k) + \frac{n_j+n_k}{n_i+n_j+n_k} d(C_j, C_k) - \frac{n_k}{n_i+n_j+n_k} d(C_i, C_j) \quad (6\text{-}5)$$

where $d(C_i, C_j)$ denotes the distance between clusters C_i and C_j and $d(C_i \cup C_j, C_k)$ the distance between the merged cluster (C_i,C_j) and third cluster C_k.

This procedure yields a hierarchy of clusters represented as a binary tree, denoted as a dendrogram. A dendrogram is a tree diagram that shows the nested structure of the partitions and how the various clusters are linked at each level of hierarchy. There is a numerical value (called linkage value) associated with each level of the method where the branches (i.e. clusters) join. This linkage value usually represents

the distance $d(C_i, C_j)$ between the two clusters to be merged. The scale for this linkage value is shown on the vertical axis in Figure 1. Ward's linkage method has been shown to perform well with noisy data, which is in agreement with the analysis of source maps obtained from low SNR single spike localizations. The linkage function provided in the MATLAB R2015 release was used for this implementation.

Mojena's upper tail stopping rule (Mojena, 1977) was then considered for thresholding the dendrogram to infer an optimal classification. Mojena's stopping rule attempts to find the level in the hierarchy implying a significant jump in the dendrogram heights, indicative of the merging of two dissimilar clusters. If d^{h+1} is the linkage value at (h+1) hierarchy level, $\bar{d}$ and α_d are the average and standard deviation of the linkages for h previous levels of hierarchy, respectively. Then, Mojena's stopping rule consists in cutting the tree at the first hierarchical clustering level that satisfies the following rule ($d^{h+1} > \bar{d} + c\alpha_d$), where c is a constant. Mojena suggested a range of value for c, but it has been shown that the value of c can vary depending on the data (Milligan and Cooper, 1985) and was not straightforward to assess. Therefore, Martinez and Martinez, (2004) instead recommended the visual inspection of a break in the evolution of the standardized cluster linkages $\left(\frac{d^{h+1}-\bar{d}}{\alpha_d}\right)$ as a function of the number of clusters, which does not require the estimation of on the constant c. An elbow or a break in the plot should therefore be interpreted as an indication of the number of clusters. This visual approach was used in our study. See **Figure 6.1** for an example where the break at '2' indicates 2 clusters.

Step 4. Generation of consensus map

With the help of the hierarchical clustering, we were able to group the source maps that were spatially similar into clusters. At this stage, we performed an average of the source maps within each cluster to provide a cluster map. This type of averaging helped in avoiding any sort of signal cancellation or loss of information, problems often faced during averaging at the signal level. Finally, we obtained spatio-

temporal cluster maps but for this study we focused only on the results at the peak of the averaged cluster spike. From all of the cluster maps, the one with highest number of spikes representing the most reliable and reproducible source maps was chosen as the consensus map.

6.4.7. Comparison of the consensus map approach on EEG, MEG and fusion data

To evaluate the source localization results obtained from EEG alone, MEG alone and EEG-MEG fusion for every single spike, we considered a qualitative and a quantitative evaluation against the available ground truth, denoted as the clinical reference. Definition of the irritative zone (IZ) as a clinical reference for the source localization results was based on the available clinical information for each patient. This information consisted of (in the order of priority, not all factors were available for every patient): resected region, iEEG ictal and inter-ictal findings, and epileptic lesions such as focal cortical dysplasia (FCD) detected on MRI. Refer to **Table 6.1** for details. Whenever the resection did not lead to seizure freedom, information based on iEEG findings or lesions were considered. Based on such information, two expert neurophysiologists (GP and EK) manually drew the IZ on each patient's MRI based cortical mesh. This clinical reference or IZ was used for both qualitative and quantitative assessment.

a. Qualitative assessment

We visually categorized the cluster maps as either concordant, sub-lobar concordant or discordant with the presumed IZ.

- A cluster map was assessed as concordant with the presumed IZ whenever the vertex of the cluster map exhibiting the maximum source amplitude (source maximum) was inside the IZ.
- A cluster map was assessed as sub-lobar concordant with the presumed IZ whenever the source maximum was within the sub-lobar region of the IZ.

We identified 10 sub-lobar regions per hemisphere based on anatomical atlas (Agirre-Arrizubieta et al., 2009; de Gooijer-van de Groep et al., 2013). These regions consisted in the central, parietal, and occipital lobes; the frontal lobe was divided in the frontal superior, medial, inferior, and fronto-orbital regions; and the temporal lobe into the lateral and mesial regions. The same atlas was used in our previous study and has been illustrated in Figure 2 of that paper (Heers et al., 2012).

- A cluster map was assessed as discordant with the presumed IZ whenever the source maximum was outside the sub-lobar region.

Spike-to-spike reproducibility rate (SSR)

In order to assess the reproducibility of the SSSL results, we proposed an estimation of the spike-to spike reproducibility rate (SSR). This rate was calculated as the total number of single spikes belonging to the concordant cluster divided by the total number of single spikes localized for that specific marker type. This means that all the single spike sources included in the concordant cluster map were considered as reproducible sources.

$$\boldsymbol{SSR} = \frac{\text{No. of single spikes included in the cluster map concordant with IZ}}{\text{Total no. of single spikes localized}} \times 100 \qquad (6\text{-}6)$$

b. Quantitative assessment

Based on the manually drawn clinical reference (IZ), quantitative assessment of the source localization results were also evaluated using the following two metrics:

1. **Minimum distance (Dmin):** minimum Euclidean distance expressed in mm between the source maximum and the presumed IZ. This represents the localization error.
2. **Spatial dispersion (SD):** This metric (Molins et al., 2008) was used in our previous studies based on clinical and simulation data (Heers et al., 2012; Chowdhury et al., 2015; Grova et al., 2016; Heers et al., 2016). It measures both the spatial spread of the estimated source distribution around the IZ

and the localization error between the estimated source distribution and IZ. We weight the amplitude of all the *r* cortical sources by their minimum distance from the set of cortical sources belonging to the IZ. Let us denote $\hat{\boldsymbol{j}}(i,\tau_0)$ as the amplitude of the current density distribution estimated for a dipolar source *i* on the cortical surface at the main peak of the spike (τ_0).

$$\mathrm{SD}(\hat{\boldsymbol{j}}) = \sqrt{\frac{\sum_{i=1}^{r}\left(\min_{l\in\Phi}(\boldsymbol{D}^2(i,l))\hat{\boldsymbol{j}}^2(i,\tau_0)\right)}{\sum_{i=1}^{r}\hat{\boldsymbol{j}}^2(i,\tau_0)}} \qquad (6\text{-}7)$$

where $\min_{l\in\Phi}(\boldsymbol{D}(i,l))$ provides the minimum Euclidean distance between the source *i* anywhere in the cortical surface and the sources *l* in the IZ. Φ denotes the set of indices of the dipoles belonging to the IZ. This minimum distance is zero when the source *i* belongs to Φ. SD values close to zero means that the estimated source was inside the IZ. A high value of SD means there are sources far away from the IZ that are contributing to the estimated solution or that the reconstructed source map was spatially spread around the IZ.

Quantitative assessment using the above two metrics was done to compare the performances of the three modalities. Kruskal-Wallis H test, which is a rank-based non-parametric test, was used to determine if there were statistically significant differences between the three modalities, i.e. if the performance (Dmin or SD) of the SSSL using cMEM was different based on the modality (EEG alone, MEG alone and EEG-MEG fusion). Post hoc comparison tests to determine which of the groups differed from each other were then applied using Dunn's non-parametric pair-wise multiple comparison test. These comparisons were Bonferroni corrected at a significance level of 0.05/3 = 0.0167. Two main questions were addressed in this analysis:

1. *Does fusion provide an overall improved performance when compared to EEG alone and MEG alone?*

   To test this, for each of the modality, we pooled together the metric (SD or Dmin) values obtained for all the clusters including concordant, sub-lobar concordant and discordant clusters from the 34 marker types.

2. *Does the cluster with the highest number of spikes exhibit concordant results with the presumed IZ?*

   To test this, for each modality, we pooled together the metric (SD or Dmin) values for only the cluster with the highest number of spikes from the 34 marker types.

6.4.8. Impact of the number of EEG electrodes in the fusion

In our previous study based on realistic simulations, interestingly we showed that addition of only 20 EEG electrodes to the high density MEG sensors was sufficient to bring additional information missed by MEG in fusion (Chowdhury et al., 2015). To further validate these findings on clinical data, we assessed the impact of fusion source localization on the 34 markers when using either the whole 54 EEG electrodes (following the 10-10 system of electrode placement) and two down-sampled montages involving 32 EEG electrodes and 21 EEG electrodes (following the standard 10-20 system of electrode placement) with the 272 MEG sensors. The application of the consensus map approach (**Section 6.4.6**) applied on the fusion configuration (54 EEG+272 MEG) resulted in a consensus map for each marker type, and the spikes within each consensus map were retrieved from three fusion configurations: 1) 54 EEG+272 MEG, 2) 32 EEG+272 MEG, and 3) 20 EEG+272 MEG. These spikes were further averaged for the three configurations to perform averaged spike source localization.

Markers (Patients)	Surgery	Lesion	iEEG	EEG source localization Averaged spike	MEG source localization Averaged spike
M1 (P1)	N/A	Post central region	N/A		
M2 (P1)	N/A	Post central region	N/A		
M3 (P2)	L OF mesial encephalocele removed	L F	IED: L Hc and L fronto-mesial; Ictal: L OF mesial and L mesial T; F > T		
M4 (P2)	L OF mesial encephalocele removed	L F	IED: L Hc and L fronto-mesial; Ictal: L OF mesial and L mesial T; F > T		
M5 (P3)	Small cortical resection of the RF lobe near its upper convexity	R F parasagittal	IED: R Lesion; Ictal: R Lesion		
M6 (P4)	L mesial F	Normal	IED: Diffuse bil. F L>R; Ictal: Bil. F, max L SMA		
M7 (P5)	L F lesion	L ant. F, parasagittal	IED: L perilesion and lesion, bil. F; Ictal: Bil. F max lesion and perilesion		
M8 (P6)	N/A	R ant.	N/A		
M9 (P7)	R Occ lobe, extension of resection	Normal	IED: R T and post. T and precuneus; Ictal:R pre-cuneus, R Superior Occ		
M10 (P8)	N/A	L Hippocampal malrotation	IED : L mesial T >> R. - Ictal : no focus identified		
M11 (P9)	R OF	R hemimegalencephally	IED: R OF, lat. and ant. Insula, R Am and Hc; Ictal: R OF and ant. Insula, also opercular region		
M12 (P9)	R OF	R hemimegalencephally	IED: R OF, lat. and ant. Insula, R Am and Hc; Ictal: R OF and ant. Insula, also opercular region		
M13 (P9)	R OF	R hemimegalencephally	IED: R OF, lat. and ant. Insula, R Am and Hc; Ictal: R OF and ant. Insula, also opercular region		
M14 (P9)	R OF	R hemimegalencephally	IED: R OF, lat. and ant. Insula, R Am and Hc; Ictal: R OF and ant. Insula, also opercular region		
M15 (P10)	R OF resection	R 0F	IED: ROF, mid F convexity and ant. T neocortex, Ictal: R OF		
M16 (P11)	L sensory hand and face	Normal	IED: L. Post. Rolandic mid convexity; Ictal: L. Post. Sensory cortex		
M17 (P11)	L sensory hand and face	Normal	IED: L. Post. Rolandic mid convexity; Ictal: L. Post. Sensory cortex		
M18 (P12)	R frontomesial	Normal	IED: R Hc>SMA>mid cingulate gyrus>mesial OF; Ictal: R T (ill-defined), R SMA followed by rapid propagation		
M19 (P12)	R frontomesial	Normal	IED: R Hc>SMA>mid cingulate gyrus>mesial OF; Ictal: R T (ill-defined), R SMA followed by rapid propagation		
M20 (P13)	R F lesion	R F	IED: superficial contact SMAa, SMAm or SMAp, R CP; Ictal: R SMA overlapping with structural lesion		
M21 (P14)	N/A	R mesial and ant. F	IED: Bil. F R>L; Ictal: Bil. F R>L, R F or bil. F widespread changes		
M22 (P15)	N/A	Normal	IED:R parasagittal central (deep contacts RSMAP, RCP); Ictal: R parasagittal central		
M23 (P16)	R mid F	R mid F convexity	IED: mid portion R F convexity; Ictal: same contacts		
M24 (P17)	L amygdalohippocampectomy	Cerebral herniation of the L OF region through orbital bone, left hippocampus malrotation	IED:L neocortical and mesial T; Ictal: LT, neocortical and mesial		
M25 (P18)	R F pole	R F pole	N/A		
M26 (P19)	R post. neocortex, Inf. P	Normal	IED: multifocal and widespread T, P ,neocortex, Hc and lingual gyrus; Ictal:diffuse changes and non-localizing		
M27 (P19)	R post. neocortex, Inf. P	Normal	IED: multifocal and widespread T, P ,neocortex, Hc and lingual gyrus; Ictal:diffuse changes and non-localizing		
M28 (P20)	L F resection at the level of the lateral O gyrus	L OF	IED: R mesial T lobe, hippocampus > amygdala, Ictal: likely R mesial T lobe		
M29 (P21)	R ant. T lobectomy	R T hippocampal atrophy and gliosis. L middle cranial fossa meningoencephalocele.	N/A		
M30 (P22)	R ant. T, R OF and and extension in the R OF	L ant. Cingulate OF	IED:L FT(max. ant. Cingulate + T pole), L post. Hc+Am; Ictal: L ant. Cingulate and ant. T		
M31 (P23)	N/A	Bil. Hippocampal atrophy	IED: multifocal temporomesial bil. independent (> R); Ictal: from the R and the L T structures		
M32 (P24)	N/A	L opercular F	N/A		
M33 (P25)	N/A	L F cortex (deep precentral gyrus)	N/A		
M34 (P26)	R OF resection	R OF	IED: R OF; Ictal: R OF		

Table 6.1. Summary of the 26 patients (34 marker types) with details on the available ground truth information from surgery outcome, lesion and iEEG findings. For each of the 34 marker types, the averaged spike source localization results using EEG and MEG data have been provided in the last two columns.
Based on visual inspection, the results that were concordant with the presumed IZ (clinical reference) have been marked in blue color, the sub-lobar concordant results have been marked in orange and discordant results have been marked in gray color.
L: Left, R: Right, T: Temporal, F: Frontal, P: Parietal, Occ: Occipital, O: Orbital, ant.: anterior, post.: posterior, Inf.: inferior, bil.: bilateral, Hc: Hippocampus, Am: Amygdala;

6.5. Results

6.5.1. EEG and MEG averaged spike localization – standard clinical approach

Table 6.1 summarizes the 34 different marker types with details on the available ground truth information. It also lists the results of EEG and MEG averaged spike localization on the 34 markers. Based on the visual assessment, we found 8/34 (23%) cases in MEG and 11/34 (32%) cases in EEG that were discordant with IZ. There were 4/34 (12%) cases that were discordant with IZ in both EEG and MEG. Therefore, neither EEG nor MEG averaged spike localization brought clinically relevant information for 12% of the cases studied.

Consequently, we tried to pinpoint the possible reasons for the failures in the EEG and MEG averaged spike localizations. Some possible reasons were:

- Effect of source orientation or depth – EEG or MEG was not sensitive to the relative orientation and location of the generators.
- Low SNR - data were too noisy, resulting in low SNR conditions even after spike averaging. The reasons for noisy data were either noisy background data or high impedances of the EEG electrodes. Low SNR was noticed also when the patient was not well-positioned inside the MEG helmet resulting in sensors far from the region of interest.
- Spurious localization – Source localization method failed to find the source of interest due to complex source topography.
- Spike Variability – Spikes from different runs were averaged and the variability between the peaks of the individual spikes in EEG was very high.

To summarize the results, one of the most common reason for the failure of source localization (M3, M4, M5, M29, M32, M33 for EEG; M5, M10 and M32 for MEG) was due to the fact that EEG or MEG were not sensitive to the orientation and location of the generators of spikes, especially for generators located in too deep structures. The second common reason was due to low SNR or noisy data (M11, M18, M24 for EEG; M4, M11, M33 for MEG). The SNR was measured as the

standard deviation ratio between the signal around the peak and the background activity. M4, M11, M18 and M33 data exhibited SNRs less than 2. For M24, the impedance between many EEG electrodes and the scalp were very high resulting in noisy EEG signals. Next most common reason for the failure of source localizations was the complex source topographies leading to spurious localizations (M28, M33 for EEG; M9 for MEG). Finally, failure for EEG averaged spike source localization in M16 was due to spike variability. All these reasons clearly indicate the limitations of the standard approach of monomodal averaged spike source localization. In order to overcome such limitations, we proposed to combine SSSL and EEG-MEG fusion.

6.5.2. Application of consensus map approach on EEG alone, MEG alone and EEG-MEG fusion

Figure 6.1 illustrates an example of the application of the consensus map approach on a patient (M23) involving 97 spikes marked on EEG and MEG data. In this patient, the IZ has been marked in the right mid frontal region based on the surgical resection (post-surgical outcome was Engel 1), outlined in green on the cortical surface. In this figure, for each modality, we have presented the dendrogram obtained from Ward's hierarchical clustering method and the plot of the standardized cluster linkages against the number of clusters. The first break in this plot provided the thresholding level in the dendrogram to obtain the number of clusters. For EEG, the first break in the plot was noticed at 2, indicating that there were two distinct clusters among the 97 SSSL results. From the two clusters, cluster 1 containing 26 spikes and cluster 2 containing 71 spikes were both sub-lobar concordant with the IZ (**Figure 6.1A**). For MEG, the first break was noticed at 3 indicating that there were three distinct clusters. From the three clusters, cluster 1 containing 21 spikes was discordant with IZ, presenting a distant source in the left fronto-mesial region. Higher number of spikes were included in cluster 2 (43 spikes) and cluster 3 (33 spikes) that were both concordant with IZ (**Figure 6.1B**).

For fusion, we determined 3 distinct clusters. While the cluster exhibiting the lowest number of spikes (cluster 2 with 15 spikes) presented sub-lobar concordance with IZ, cluster 1 (39 spikes) and cluster 3 (43 spikes) with higher number of spikes were both concordant with IZ (**Figure 6.1C**). Overall, the highest number of spikes presenting concordance with IZ was found in fusion with a total 82 spikes, whereas MEG provided concordance with IZ for 76 spikes. This indicates a higher spike-to-spike reproducibility in fusion when compared to MEG or EEG alone. This suggests that the consensus map providing the most reliable and reproducible source was found as the concordant cluster with the highest number of spikes.

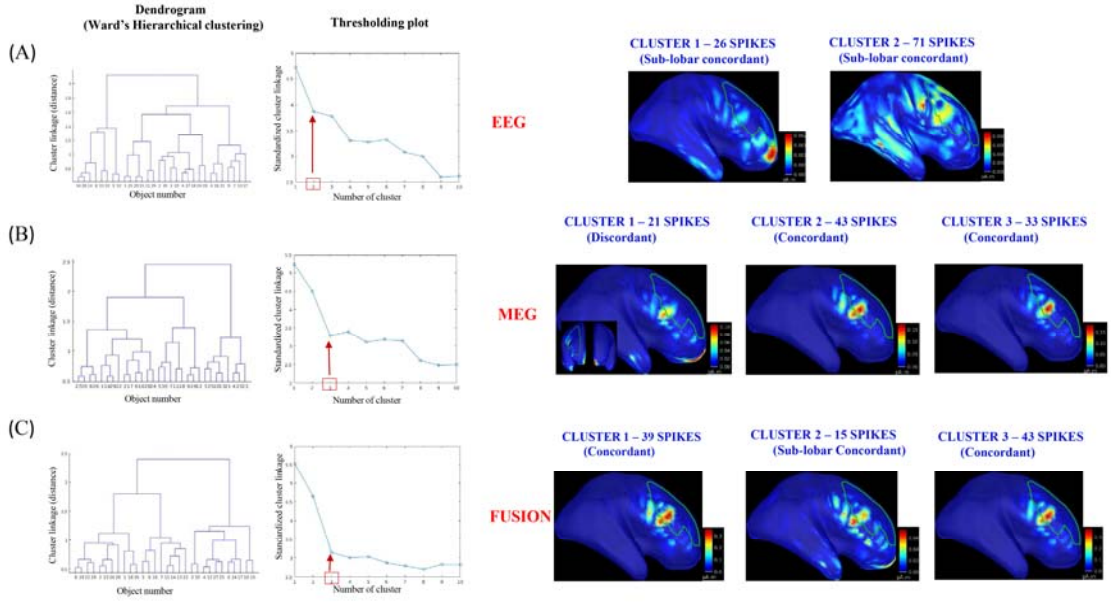

Figure 6.1. Example of consensus map estimation. On a patient (M23) with clinical reference (IZ) located in mid right frontal region, as outlined in green on the cortical surface. A total of 97 spikes have been marked in both EEG and MEG data. Results on EEG, MEG and fusion are presented. Column 1 shows the dendrogram obtained from Ward's hierarchical clustering, x-axis: Object number and y-axis: cluster linkage value. Column 2 shows the plot of the standardized cluster linkage against the number of clusters, red arrow points towards the first break or elbow in the plot indicating the number of clusters; x-axis: number of clusters and y-axis: cluster linkage value. In this plot, only the first 10 hierarchical levels have been shown. The next columns show the cluster maps displayed over the inflated cortical surface obtained through the Brainstorm software toolbox. (**A**) EEG consensus map approach presenting 2 clusters with cluster 1 containing 26 spikes and cluster 2 containing 71 spikes. Cluster 1 and 2 are sub-lobar concordant with IZ. (**B**) MEG consensus map approach presenting 3 clusters with cluster 1 containing 21 spikes, cluster 2 containing 43 spikes and cluster 3 containing 33 spikes. Cluster 1 is discordant with IZ, cluster 2 and 3 are concordant with IZ. (**C**) Fusion consensus map approach presenting 3 clusters with cluster 1 containing 39 spikes, cluster 2 containing 15 spikes

and cluster 3 containing 43 spikes. Cluster 1 and 3 are concordant with IZ. Cluster 2 is sub-lobar concordant with IZ.

6.5.3. Comparison between averaged spike localization and consensus map on single spike localizations

Figure 6.2 illustrates the results of averaged spike source localization and SSSL results using the consensus map approach on a patient (M8), for whom the IZ was identified in the right anterior frontal region with the presence of a FCD in the MRI. In total, 40 spikes were marked. EEG averaged spike localization was successful in localizing the IZ (**Figure 6.2A**). However, MEG averaged spike localization found the source in a sub-lobar region, anterior to the lesion (**Figure 6.2B**). After applying the consensus map approach on EEG, MEG and fusion, we were able to find at least one cluster in all three modalities that was fully concordant with IZ. In all three modalities, this concordant cluster was also the one exhibiting the highest number of spikes (**Figure 6.2 C, D** and **E**).

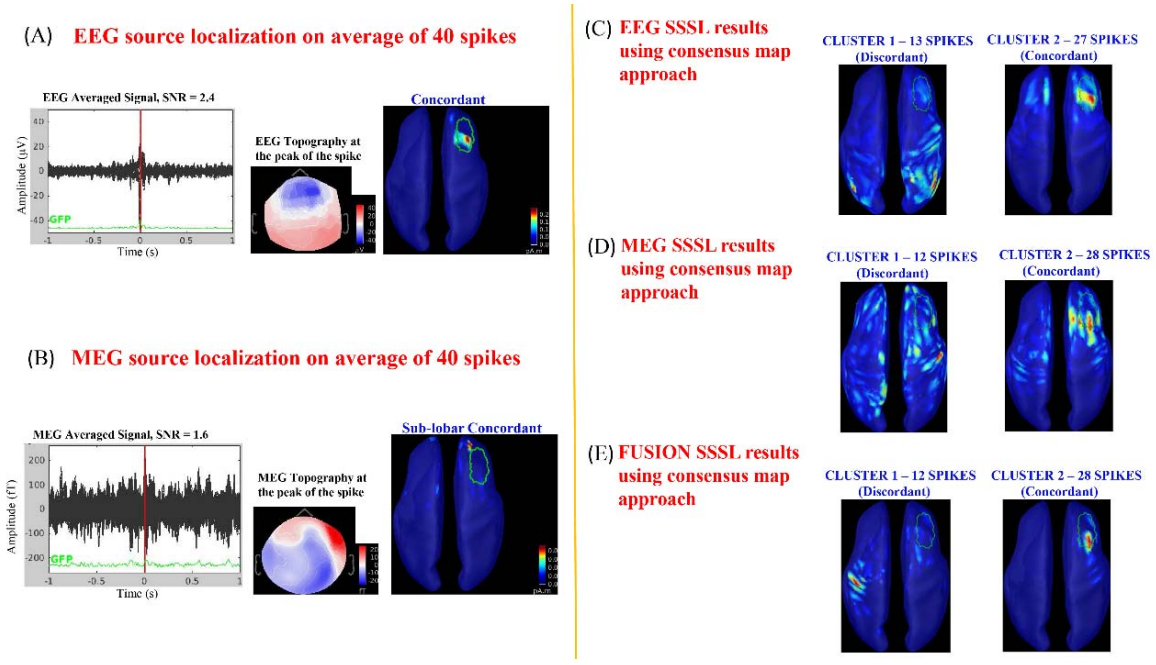

Figure 6.2. Comparison of averaged spike localization results with consensus map approach on the single spike localization results. Example on a patient (M8) with FCD in the right anterior frontal region (IZ), outlined in green on the cortical surface. A total of 40 spikes have been marked

on EEG and MEG data. (**A**) EEG source localization on average of 40 spikes, showing the averaged EEG signal with SNR= 2.4, the topography at the peak of the spike, and the source localization result which is concordant with IZ, presented on the inflated cortical surface. (**B**) MEG source localization on average of 40 spikes, showing the averaged MEG signal with SNR= 1.6, the topography at the peak of the spike, and the source localization result which is sub-lobar concordant with IZ, presented on the inflated cortical surface. (**C**) Consensus map approach applied on EEG single spike source localizations presenting 2 clusters. Cluster 1 containing 13 spikes that is discordant with IZ. Cluster 2 containing 27 spikes that is concordant with IZ. (**D**) Consensus map approach applied on MEG single spike source localizations presenting 2 clusters. Cluster 1 containing 12 spikes that is discordant with IZ. Cluster 2 containing 28 spikes that is concordant with IZ. (**E**) Consensus map approach applied on fusion single spike source localizations presenting 2 clusters. Cluster 1 containing 12 spikes that is discordant with IZ. Cluster 2 containing 28 spikes that is concordant with IZ.

Figure 6.3 illustrates the results of averaged spike localization and SSSL results using the consensus map approach on a patient (M16) who underwent surgical resection of the posterior rolandic mid convexity region (IZ, outlined in green on the cortical surface in **Figure 6.3**). A total of 18 spikes have been marked on EEG and MEG data. EEG averaged spike localization failed to localize the IZ, while MEG averaged spike localization found the source in the sub-lobar region of the IZ. As in previous example, we again noticed that the consensus map approach on single spike localization was able to help finding at least one cluster of spikes that was fully concordant with IZ, indicating the advantage of applying the consensus map approach on single spike localizations over averaged spike localizations. Also, in this case, the other clusters found in the three modalities were sub-lobar concordant with the presumed IZ. The concordant clusters exhibited the highest number of spikes only in EEG (cluster 1 with 11 spikes) (**Figure 6.3C**) and in fusion (cluster 2 with 12 spikes) (**Figure 6.3E**), whereas in MEG only the smallest cluster involving 6 spikes was concordant with IZ (**Figure 6.3D**).

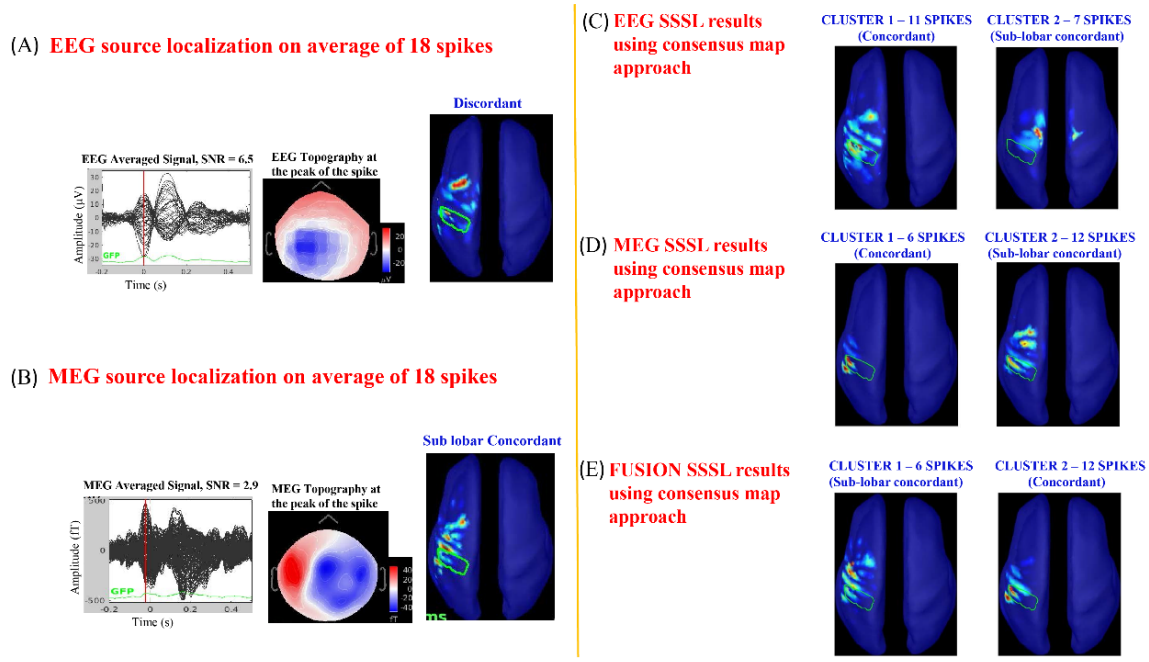

Figure 6.3. Comparison of averaged spike localization results with consensus map approach on the single spike localization results. Example on a patient (M16) with resection in the left posterior rolandic region (IZ), outlined in green on the cortical surface. A total of 18 spikes have been marked on EEG and MEG data. (**A**) EEG source localization on average of 18 spikes, showing the averaged EEG signal with SNR= 6.5, the topography at the peak of the spike, and the source localization result which is discordant with IZ, presented on the inflated cortical surface. (**B**) MEG source localization on average of 18 spikes, showing the averaged MEG signal with SNR= 2.9, the topography at the peak of the spike, and the source localization result which is sub-lobar concordant with IZ, presented on the inflated cortical surface. (**C**) Consensus map approach applied on EEG single spike source localizations presenting 2 clusters. Cluster 1 containing 11 spikes that is concordant with IZ. Cluster 2 containing 7 spikes that is sub-lobar concordant with IZ. (**D**) Consensus map approach applied on MEG single spike source localizations presenting 2 clusters. Cluster 1 containing 6 spikes that is concordant with IZ. Cluster 2 containing 12 spikes that is sub-lobar concordant with IZ. (**E**) Consensus map approach applied on fusion single spike source localizations presenting 2 clusters. Cluster 1 containing 6 spikes that is sub-lobar concordant with IZ. Cluster 2 containing 12 spikes that is concordant with IZ.

In summary, in all three examples illustrated in **Figure 6.1**, **Figure 6.2** and **Figure 6.3**, only in fusion the concordant cluster was always the one exhibiting the highest number of spikes thereby suggesting higher spike-to-spike reproducibility rate in fusion when compared to EEG alone and MEG alone.

6.5.4. Consensus map approach – Qualitative assessment

We performed SSSL on a total of 1435 spikes from 34 marker types. We categorized these 1435 spikes sources into concordant, sub-lobar concordant, or discordant results with the presumed IZ. For instance, all spikes contained in the concordant clusters were categorized as concordant spikes. Similarly, the sub-lobar concordant and discordant spikes were obtained from the sub-lobar concordant and discordant clusters, respectively. **Figure 6.4A** illustrates a pie chart of the percentage of spikes that provided concordant, sub-lobar concordant and discordant results with IZ when considering SSSLs of EEG alone, MEG alone and fusion data. While EEG yielded the lowest percentage of spikes that provided concordant results with IZ (Spike-to-Spike Reproducibility SSR = 55%), MEG performed better than EEG with SSR = 71% of spikes exhibiting concordant results. On the other hand, fusion showed the highest spike-to-spike reproducibility and reliability with 90% of spikes providing concordant results with IZ. This was the case when considering all marker types together. Interestingly, when studying the distribution of SSR values at the level of each marker type (**Figure 6.4B**), we also noticed that overall fusion provided higher SSR when compared to EEG alone or MEG alone. Fusion provided 100% SSR in 18/34 markers, whereas 100% SSR was noticed only in 9/34 markers for MEG and 6/34 markers for EEG. On the other hand, 0% SSR (source localization failure) was observed for 8/34 cases in EEG and 6/34 cases in MEG, whereas for fusion the lowest SSR value 42%. This suggests a high reliability of fusion SSSL results using the consensus map approach when compared to EEG or MEG alone. We noticed that the SSR of fusion was lower than the one observed for either EEG or MEG in only 4/34 markers. Those were marker number 19 (EEG had a higher SSR), 28 (both EEG and MEG had higher SSR), 31 (EEG has higher SSR) and 32 (MEG has higher SSR). Note that the order of the markers was sorted in descending order based on SSR values, therefore, the marker numbers in **Figure 6.4B** do not match with the marker numbers in **Table 6.1**.

With reference to **Section 6.5.1**, we also observed that by applying the consensus map approach on SSSL results, out of 11 cases of averaged spike localizations that

failed in EEG, 9 of them were localized within the IZ and localization remained unsuccessful for 2 of them. Finally, out of the 34, there were 3 additional cases (M10, M26, and M27) that failed to localize the IZ after applying the consensus map approach. In MEG, out of 8 cases for which averaged spike localization failed, 7 of them showed improved localization after applying the consensus map approach; resulting in either concordant or sub-lobar concordant results. Finally, for fusion, we noticed that the consensus map approach improved the localization in 100% of the cases, exhibiting at least one cluster fully concordant with the presumed IZ for each marker type. Note that in 33/34 cases the cluster involving the highest number of spikes was indeed the one concordant with the IZ.

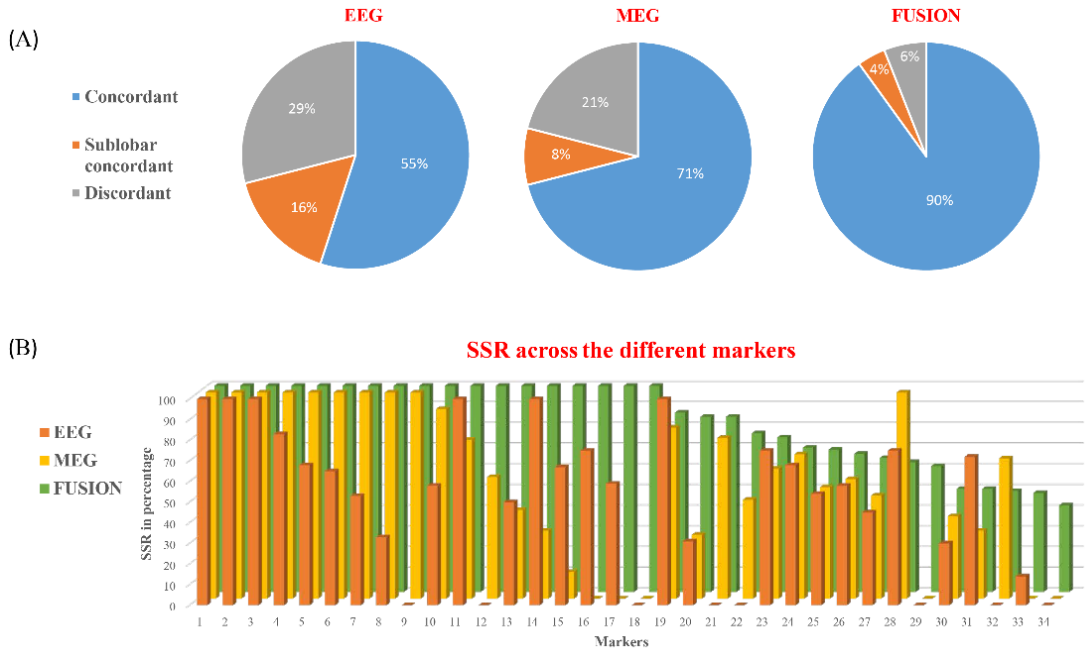

Figure 6.4. Qualitative assessment of consensus map approach. (**A**) Pie charts illustrating the comparison of location of source with respect to IZ in EEG, MEG and fusion single spike localization. The values in the charts represent the percentage of spikes that provided concordant (in blue color), sub-lobar concordant (in orange color) and discordant (in gray color) results in each modality from the total number of 1435 spikes that were localized for 34 marker types. EEG presented 55% spike-to-spike reproducibilty rate (SSR), MEG 71% SSR and fusion presented the highest SSR of 90%. (**B**) Chart comparing the SSR across the three modalities (EEG, MEG and fusion) for each of the 34 marker type. EEG in orange, MEG in yellow and fusion in green color; x-axis: markers type, y-axis: SSR in percentage. At the level of each marker type, fusion provided an overall higher SSR than EEG alone and MEG alone.

6.5.5. Consensus map approach – Quantitative assessment

a. Fusion performed better than monomodal localizations

The first test was to see if fusion provided an improved performance when compared to EEG alone and MEG alone. **Figure 6.5A** shows the boxplot representation of the Dmin values pooled together from all the clusters of the 34 marker types in EEG alone, MEG alone and fusion. We found an overall significant effect of the modality over Dmin values ($H(2) = 10.6$, p=0.005). Post-hoc paired comparison showed that fusion provided significantly lower Dmin than EEG (p=0.004) but neither the differences between fusion and MEG (p=0.054), nor between EEG and MEG (p=0.6) were statistically significant. **Figure 6.5B** shows the boxplot representation of the SD values pooled together from all the clusters of the 34 marker types in EEG alone, MEG alone and fusion. We found an overall significant effect of the modality over SD values ($H(2) = 8.68$, p=0.013). Post-hoc paired comparison showed that fusion provided SD values significantly lower than EEG (p=0.009) but were not significantly different from MEG (p=0.24). We found no statistically significant differences in SD between EEG and MEG (p=0.3).

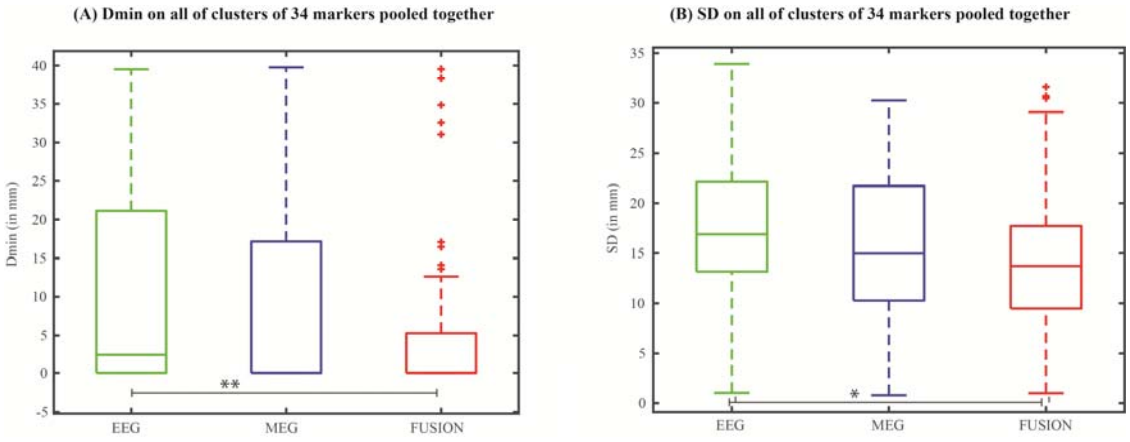

Figure 6.5. Quantitative assessment to compared the performances of monomodal SSSL with fusion SSSL using the quantitative metrics Dmin and SD. Boxplot representation of (**A**) Dmin values and (**B**) SD values pooled together from all the clusters (including concordant, sub-lobar concordant and discordant clusters) of the 34 marker types in EEG alone, MEG alone and fusion. Post-hoc paired comparison: ** represents statistically significant difference with p<0.005; * represents statistically significant difference with p<0.0167.

b. Concordant cluster with highest number of spikes

The second test was to see if the cluster involving the highest number of spikes exhibited a concordant result with the presumed IZ. For fusion, Dmin values were zero for all clusters involving the highest number of spikes (**Figure 6.6A**), except for two clusters: one cluster was sub-lobar concordant (within 3mm distance) with the IZ, and another cluster that was discordant with the IZ. MEG also provided concordant results with IZ for most of the clusters with the highest number of spikes. Only few cases (6/34 cases) provided either sub-lobar concordant or discordant results with IZ. On the other hand, for EEG, the cluster with the highest number of spikes did not exhibit concordant results with IZ in most of the cases (median Dmin≠0). When considering only the clusters with the highest number of spikes, we also found an overall significant effect of the three modalities on Dmin distribution (H(2) = 15.6, p<0.001). Post-hoc paired comparison showed that Fusion provided Dmin values significantly lower thanEEG (p=0.0003) but the differences between fusion and MEG (p=0.364) or EEG and MEG (p=0.03) were not statistically significant. For SD applied on clusters with the highest number of spikes (**Figure 6.6B**), we found no statistically significant effect of the three modalities (H (2) = 5.2, p=0.07).

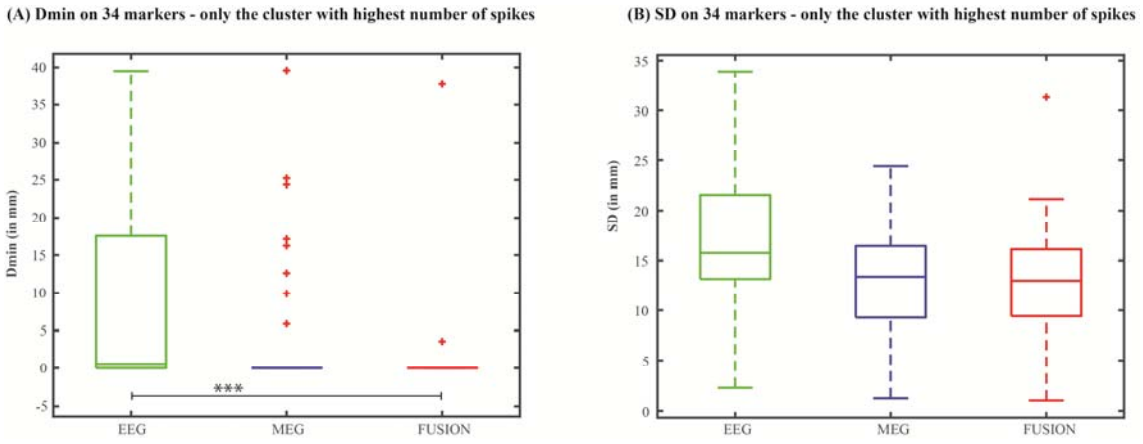

Figure 6.6. Quantitative assessment using the metrics Dmin and SD to find if the cluster with the highest number of spikes exhibited the concordant result with the presumed IZ. Boxplot representation of the (**A**) Dmin values and (**B**) SD values pooled together for only the cluster with

highest number of spikes from each marker type in EEG alone, MEG alone and fusion. Post-hoc paired comparison: *** represents statistically significant difference with $p<0.001$.

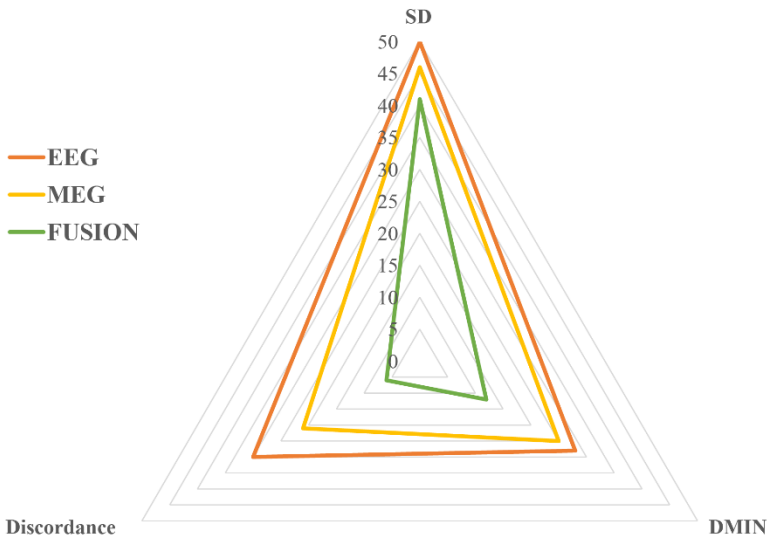

Figure 6.7. Radar chart summarizing the qualitative and quantitative assessment of EEG alone, MEG alone and fusion in terms of the average SD, average Dmin and the percentage of discordant spikes from the 1435 spikes in the 34 marker types. EEG (in orange) with averaged SD = 50mm, Dmin = 28mm and percentage of discordant spikes = 29%. MEG (in yellow) with averaged SD = 46mm, Dmin = 25mm and percentage of discordant spikes = 21%. Fusion (in green) with averaged SD = 41mm, Dmin = 12mm and percentage of discordant spikes = 6%. Fusion has the smallest triangle indicating the advantage of combining EEG and MEG for the localization of inter-ictal spikes.

To summarize the qualitative and quantitative assessments, the radar chart in **Figure 6.7** shows that MEG performed better than EEG by presenting lower SD, lower Dmin, and lower discordance rate but the smallest triangle corresponded to fusion indicating the advantage of combining EEG and MEG for the localization of single inter-ictal spikes.

6.5.6. Impact of the number of EEG electrodes in fusion

We also tested the impact of the three EEG electrode set-up in fusion for all 34 marker types, when applied on averaged signals corresponding to the consensus

map obtained with the complete set up (54 EEG and 272 MEG sensors). Overall, all three configurations achieved similar level of accuracies for most marker types. 33/34 cases presented concordant results with IZ for the 54 EEG+272 MEG set-up (cf. **Section 6.5.5b**). Concordant or sub-lobar concordant results with IZ were found in 31/34 cases (19 concordant) for 32 EEG+272 MEG and in 30/34 cases (21 concordant) for 20 EEG+272 MEG set-up.

Figure 6.8 illustrates two examples (M25 and M8) of the source localization results for the three configurations. **Figure 6.8A** presents the source localization results on a patient (M25) with surgical resection in the right fronto-polar region (IZ, outlined in green in the figure) with an Engel 1A outcome. All three configurations provided sources concordant with the IZ, however, recovered different aspects of the activated cortical patch. **Figure 6.8B**, presents the source localization results on a patient with an FCD in the right anterior frontal region, as outlined in green in the figure. Similar to M25, all three configurations showed concordance with IZ, while being sensitive to different aspects of the activated cortical patch.

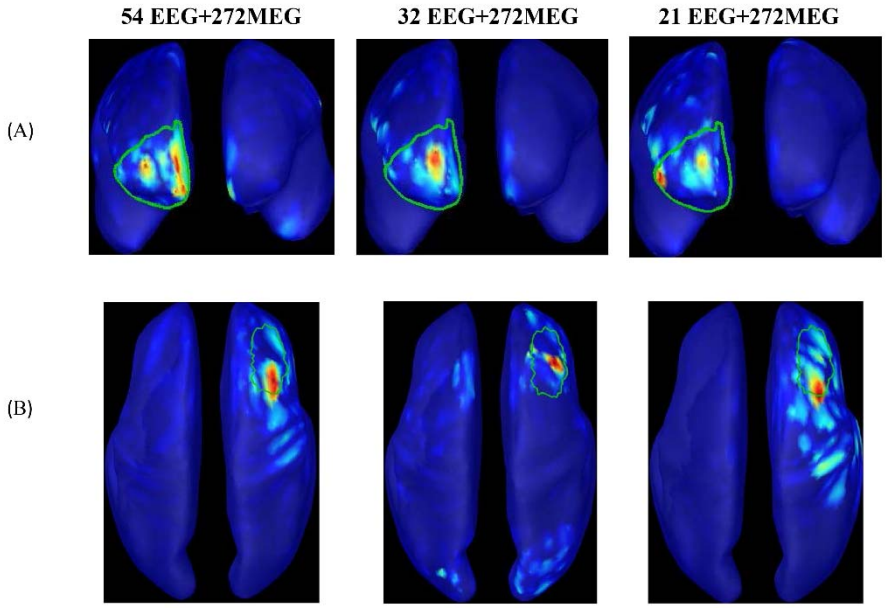

Figure 6.8. Impact of the number of EEG electrodes in fusion – two examples illustrating the performance of the three fusion configurations with different number of EEG electrodes: 1) 54 EEG+272 MEG, 2) 32 EEG+272 MEG, and 3) 20 EEG+272 MEG. (**A**) Source localization results on M25, a patient with surgical resection in the right fronto-polar region (IZ, outlined

in green color) with an Engel 1A outcome. (**B**) Source localization results on (M8), a patient with an FCD in the right anterior region, as outlined in green color. All the three configurations recovered the source that was concordant with the IZ.

6.6. Discussion

The objective of this study was to demonstrate the relevance of EEG-MEG fusion data source analysis for pre-surgical evaluation of epilepsy. The advantage of performing single spike localization of fusion EEG-MEG data is two-folds. Combining EEG and MEG data can help bring additional information missed by either modality, and localizing single spikes can bring important information that may be lost during averaging of the spikes. The advantage of performing single spike localization using MEM-fusion is two folds as well. First, MEM-fusion can provide superior localization accuracy and is sensitive to the spatial extent of the epileptic sources. Second, MEM-fusion is robust to the low SNR conditions of single spike localization (Chowdhury et al., 2015). As opposed to source localization of averaged map providing only one localization result, performing single spike source localization allows building a consensus map to find the most reliable and reproducible source maps. In this study, we proposed and evaluated a systematic approach for clustering single spike source localization results to provide a consensus map. With the application of the consensus map approach on fusion SSSL results, we were able to provide successful localization of the IZ in all 34 markers studied here, where standard monomodal localization of averaged spikes resulted in failures in 8/34 cases for MEG and 11/34 cases for EEG. Moreover, an important finding is that we showed that fusion significantly improved the spike-to-spike reproducibility when compared to monomodal single spike source localizations, i.e., from 55% in EEG and 71% in MEG to 90% in fusion. Finally, we demonstrated that using the consensus map approach on fusion data, the cluster with the highest number of spikes provided consistently concordant

results with IZ; thus providing an automatic way of finding the most reliable, reproducible and concordant source localization result.

With a number of studies (Cohen and Cuffin, 1983; Pflieger et al., 2000; Yoshinaga, 2002; Zijlmans et al., 2002; Pataraia et al., 2005; Bast et al., 2007; Ebersole and Ebersole, 2010; Aydin et al., 2015) having reported the added value of combining EEG and MEG data during source analysis; there are several fusion source localization methods that have been proposed to evaluate the advantage of combining EEG and MEG data. They have been designed using different inverse operators such as the dipole fitting (Diekmann et al., 1998; Fuchs et al., 1998; Huang et al., 2007), beamformer (Hong et al., 2013), minimum norm estimate (Babiloni et al., 2001, 2004) and its noise normalized variant (Liu et al., 2002; Sharon et al., 2007; Molins et al., 2008), sparse source imaging (Ding and Yuan, 2013), and Bayesian approach (Henson et al., 2009b). Most of them were evaluated on simulations of focal activity (Fuchs et al., 1998; Liu et al., 2002; Babiloni et al., 2004; Huang et al., 2007; Ding and Yuan, 2013) or coherent sources (Hong et al., 2013), some were evaluated on experimental data such as auditory responses (Hong et al., 2013), face evoked responses (Henson et al., 2009b), visual evoked responses (Sharon et al., 2007) or responses elicited by electrical median nerve stimulation (Fuchs et al., 1998; Molins et al., 2008) and on epilepsy data (Diekmann et al., 1998). To the best of our knowledge, MEM-fusion seems the only fusion approach designed and evaluated for localizing spatially extended generators of epileptic activity, thus making it more appropriate for this clinical application.

In the context of localizing epileptic activity, single spike source localization of fusion data has been done with a dipole fitting approach, albeit on a small number of patients (6 patients) and with limited MEG/EEG coverage (32 EEG and 22 MEG channels) (Diekmann et al., 1998). The dipole fitting fusion strategy involved mainly one level of fusion, i.e., the symmetrical fusion of normalized EEG and MEG data. At the normalization step, data were weighted by the modality-specific residual variance (obtained after performing dipole fitting on the monomodal data). Consequently, the modality that led to a model with low residual variance was

given a higher weight. However, a lower residual variance does not necessarily locate a source better than the other and it does not guarantee correct source localization (Kobayashi et al., 2005). In the MEM-fusion strategy, symmetrical fusion of EEG and MEG data took place at three levels within the MEM framework. At the first level, the data and the lead field matrices of each modality were normalized by the standard deviation of the respective background activity and then concatenated. The second and third level involved the use of fusion MSP scores for the whole cortex parcellization and for the initialization of the probability of each parcel to be active; which played an important role in combining the complementary information from EEG and MEG in the fusion process (cf. **Section 6.4.4 b**). Reliability of the source localization methods when performing single spike localization is crucial. Wennberg and Cheyne, (2014) studied the reliability of dipole fitting approach when performing single spike localization. They reported that dipole fitting resulted in a scatter of source solutions even when localizing the same single spikes. This was mainly attributed to the limitations in reliability of the dipole fitting method when dealing with low SNR data (Ossenblok et al., 2007). Aydin et al., (2015) also studied the scatter size with respect to SNR by using sub-averages and found that not only the scatter size but also the center of the scatter was affected by the lower SNRs of single spike localizations. In addition, this scattered solution was mainly driven by noise and not necessarily reflecting an extended region. On the other hand, the principle behind the cMEM method attempts to model the spatial extent of the single spike source activity (Chowdhury et al., 2013; Heers et al., 2014; Chowdhury et al., 2015; Heers et al., 2016). In our previous study, we have shown that cMEM method was also robust to distant and spurious sources; which can be attributed to the ability of cMEM method to switch off parcels that are less likely to contribute to the recorded spike signals (Heers et al., 2016). These features of cMEM makes it more suitable for the localization and decomposition of simultaneously active sources; thus providing the possibility to separate spike and background activity. Moreover, the high spike-to-spike

reproducibility rate (90%) in the MEM-fusion (**Figure 6.4**) suggests an excellent reliability of the MEM-fusion single spike source localizations.

Spike averaging has been adopted in most studies (Bast et al., 2004; Hara et al., 2007; Tanaka et al., 2010; Heers et al., 2012, 2014; Wennberg and Cheyne, 2014; Heers et al., 2016) to increase the SNR and improve the reliability of the source localization solutions. However, it is well known that variability of the waveform of individual spikes is not uncommon in epileptic patients (Köhling et al., 2000; Aydin et al., 2015). Therefore, averaging effect is more likely to filter out source activities which slightly varied over each individual spike, by signal cancellation and consequently possible localization errors. Based on the standard averaged spike localizations results (**Section 6.5.1**) obtained in this study, we noticed that in many cases averaging did not increase the SNR nor did it decrease the noisy nature background data; thus resulted in localization errors. We found 11/34 cases in EEG and 8/34 cases in MEG that failed, providing source localization results discordant with the IZ. There were 4/34 cases that were discordant with the IZ in both EEG and MEG. In contrast, after applying the consensus map approach on single spike localization results of these cases, we were able to obtain reliable source solutions for all of them. Applying SSSL and consensus map on EEG or MEG data, we first noticed an overall improvement in the localization accuracy of EEG (discordant – 5/34, sub lobar concordant – 3/34) and MEG (discordant - 1/34, sub lobar concordant – 3/34). This shows that single spike localization can create a balance between the spike variability and SNR, thus indicating that single spike localization is preferable whenever possible. The consensus map approach proposed in this study serves as a new and promising way of overcoming the limitations of averaged spike localizations and extracting the most reliable and reproducible source among the single spike sources. It is also important to emphasize that by applying the consensus map approach on MEM-fusion results, we were able to achieve excellent spike-to-spike reproducibility and reliability for all studied cases. We were able to find at least one cluster that was fully concordant with the presumed IZ, resulting in successful localization in all the 34 cases. Moreover, in 33/34 cases, the cluster

involving the highest number of spikes was indeed the one showing full concordance with the reference.

In the literature, it has been shown that MEG provides a higher localization accuracy than EEG, which is mainly attributed to considerably lower effects of compartments outside the inner skull surface in MEG forward problem and to the dense sampling of MEG sensors (Ossenblok et al., 2007; Vorwerk et al., 2014; Klamer et al., 2015). However, to further improve the localization accuracy of MEG, it is recommended to fuse EEG to the high density MEG to bring the complementary information missed by MEG (e.g. involvment of radial sources or deeper generators). This is exactly what we have noticed in our results. In the quantitative analysis using Dmin, we found lowest localization errors in fusion. Based on SD, we noticed that fusion localizations presented an overall less spatial spread of the solution around the true extent of the source or less spurious activity distant from the true source than EEG. MEG provided comparable spatial dispersion than fusion.

Whole head coverage can be achieved with the high density MEG sensors but MEG can mainly bring information about the tangential component of the underlying neuronal sources. In our previous study (Chowdhury et al., 2015), we suggested that the addition of only 20 or 32 EEG electrodes would be sufficient to bring additional information about the source within an MEM fusion framework. This in turn would help reduce the preparation time required for EEG electrodes set-up during simultaneous EEG-MEG recordings and patient's discomfort inside the MEG helmet. A previous study based on simulations (Babiloni et al., 2004) showed that the use of simultaneous 29 EEG sensors during the MEG measurements carried out with 153 sensors returned an accuracy of the cortical source estimate statistically similar to that obtained by combining 64 EEG and 153 MEG sensors. In the present study we validated the same concept on clinical data showing that the localization accuracy was overall comparable for the three configurations of fusion involving 21, 32 and 54 EEG electrodes combined with 272 MEG sensors.

The consensus map approach provides a spatio-temporal source map, which is well-suited for the study of propagation patterns or other complex epileptic patterns. In our recent study (Chowdhury et al., 2016), we have shown the accuracy of cMEM method on high density EEG and MEG data to localize and characterize the complex patterns of epileptic discharges. Therefore, the combination of consensus map approach with the cMEM algorithm as proposed in this study has future scope for studying the spatio-temporal features of epileptic discharges but this was out of scope of the present investigation.

6.7. Conclusion

The main goal of this study was to assess the clinical relevance of EEG-MEG fusion data source localization as a non-invasive tool for pre-surgical evaluation of epilepsy. We proposed and validated a systematic approach for clustering single spike source localization results at the source level using hierarchical clustering to provide a consensus map for the most reproducible and clinically reliable source localization results. While the consensus map approach brought an improvement in the analysis of monomodal source localization results (when compared to averaged spike localization), it was its combination with MEM fusion that indeed provided successful localization in all cases. MEM-fusion with consensus map yielded excellent spike-to-spike reproducibility and also presented the most consistent and clinically relevant results in the cluster involving the highest number of spikes. The consensus map approach serves as a new and promising method as it is able to overcome the limitations of averaged spike source localization and facilitates an automatic way of extracting the most reproducible and reliable source from clinical data without any ground truth information. In conclusion, we demonstrated that single spike source localization using MEM-fusion with the help of consensus map approach can be used as a valuable non-invasive tool during pre-surgical investigation of patients with epilepsy.

6.8. Acknowledgements

This work was supported by studentship and postdoctoral fellowship from the Savoy Foundation, BioMedical Engineering Excellence award, Natural Sciences and Engineering Research Council of Canada (NSERC) Discovery grant and grant from Canadian Institutes of Health Research (CIHR) (MOP-133619). The EEG-MEG acquisitions on patients were funded by CIHR (MOP-93614), Centres of Excellence for Commercialization of Research (CECR), the American Epilepsy Society award and the FRQS (The Fonds de recherche du Québec – Santé) postdoctoral fellowship. GP was supported by funding from Richard and Edith Strauss Canada Foundation.

Chapter 7 General discussion

7.1. Summary of contributions

To expand the clinical utility of source localization of IEDs during pre-surgical evaluation of epilepsy, it was essential to first develop a source localization technique that can accurately recover the location and spatial extent of the underlying generators of IEDs. In this context, source localization method within the MEM framework have been developed and evaluated through collaborative studies with the team of Dr. J.M. Lina and Dr. Grova (Amblard et al., 2004; Grova et al., 2006, 2016, Chowdhury et al., 2013, 2015; Lina et al., 2014; Heers et al., 2016; Pellegrino et al., 2016a; Pellegrino et al., 2016b).

Following an initial evaluation of MEM performance when localizing the generators of EEG IEDs (Grova et al., 2006), I have been personally involved in the development and validation of a new variant of MEM called cMEM during my Master's thesis project, which set the benchmark for this research and resulted in a first publication in PLoS One journal (Chowdhury et al., 2013). Whereas the main methodological feature was to introduce a local spatial smoothness prior within each parcel of the MEM model, cMEM not only provided the most reliable and accurate localization of the sources when compared to other standard source localization algorithms but also proved to be sensitive to the spatial extent of sources ranging from 3 to 30 cm^2 (Chowdhury et al., 2013). This detailed study also consisted in our first evaluation of cMEM performance when applied to MEG data, comparing cMEM with several methods developed within the hierarchical Bayesian framework (Friston et al., 2008). This was also the first time we reported that the presence of an underlying parcelization model was essential for cMEM to be sensitive to the spatial extent, whereas results were actually stable for different spatial scales of such parcelization. I have also been involved in the implementation

of cMEM method within Brainstorm software (Tadel et al., 2011) as a plug-in toolbox entitled BEst: Brain Entropy in space and time[12].

Following this, the accuracy of EEG and MEG source localization of IEDs using cMEM has been extensively validated and well-established on clinical data through several clinical studies performed in the team and for which I contributed (Heers et al., 2014, 2015; Pellegrino et al., 2016a). First, the spatial concordance between fMRI bold responses and EEG/MEG sources of averaged IEDs reconstructed using cMEM was evaluated (Heers et al., 2014). While, EEG/MEG sources were concordant with the most significant BOLD response in 20 out of 21 patients, there were 3 patients showing only MEG sources and 2 patients only EEG sources concordant with the BOLD responses. In a second study, EEG/MEG sources were compared with iEEG findings on 15 patients (Heers et al., 2015) comparing cMEM with the same hierarchical Bayesian methods introduced in Chowdhury et al., (2013). We showed that MEG sources were concordant with iEEG findings in 73% of the cases whereas EEG sources in 57% of the cases. In these studies, cMEM provided robust, accurate and reproducible results and offered the significant advantage of being sensitive to the spatial extent of the generator to be targeted for invasive EEG or brain surgery.

Parallel to this, I have also been involved in the development of a time-frequency based extension of cMEM called wavelet MEM (wMEM) developed to accurately localize oscillatory/rhythmic activity (Lina et al., 2014). This led to the investigation of non-invasive EEG/MEG source localization of ictal discharges using wMEM, which was compared with ictal iEEG findings as the ground truth information (Pellegrino et al., 2016a). In this study, ictal MEG sources were concordant with iEEG for 90% of the cases and ictal EEG sources were concordant for 64% of the cases. The implications of these studies is that source localization of combined EEG and MEG data within a fusion framework may improve the

[12] BEst plug-in: http://neuroimage.usc.edu/brainstorm/Tutorials/TutBEst

localization accuracy, by taking full benefit of the complementarity between EEG and MEG. An inherent restriction to the analysis of ictal discharges is that simultaneous EEG/MEG recordings are usually only approximately one hour long, so the chances to record seizures are very low. Therefore, combined EEG and MEG localization of IEDs remains an important contribution in the pre-surgical evaluation of epilepsy patients, further confirmed by the fact that in Pellegrino et al., (2016a) we showed that most ictal source localization were actually concordant with IEDs localizations.

The work presented in this dissertation builds on and contributes to work in the field of source localization of IEDs using combined EEG and MEG data, to reliably localize non-invasively the epileptogenic focus during pre-surgical evaluation of patients with epilepsy. Although a number of studies have investigated source localization of combined EEG and MEG data, attention was given mainly to localizing focal activity with no strong focus on recovering the spatial extent of the sources (Diekmann et al., 1998; Fuchs et al., 1998; Babiloni et al., 2001; Liu et al., 2002; Babiloni et al., 2004; Huang et al., 2007; Sharon et al., 2007; Molins et al., 2008; Henson et al., 2009b; Ding and Yuan, 2013; Hong et al., 2013). The MEM-fusion approach developed during this dissertation and described in Chapter 4 addressed this aspect, providing superior localization accuracy and better sensitive to the spatial extent of the epileptic sources than other standard methods such as MNE, dSPM or sLORETA. These characteristics of MEM-fusion along with its robustness to the low SNR condition of single spike localization shown on simulated data allowed to further explore single spike localizations on clinical data.

Chapter 6 presented the evaluation of MEM-fusion on a large cohort of 26 patients with focal epilepsy. In this study, we proposed and clinically validated a pipeline for MEM-fusion source analysis of single IEDs. This pipeline was intended to improve source analysis of IEDs at multiple steps. For instance, the idea of single spike localization of IEDs can overcome the limitations of averaging effect by creating a balance between the SNR of the signal while taking into account the variability between the individual spikes. Moreover, the idea of clustering the

results of single spike localizations through the consensus map approach helped to assess spike-to-spike reproducibility in order to propose reliable and stable source localization results for clinical purposes. On the other hand, performing source localization on one averaged spike would not allow assessing reproducibility and reliability of the results. Overall, in this study we showed that 1) source localization of combined EEG and MEG data helped bring additional information missed by either modality alone, 2) MEM-fusion yielded higher spike-to-spike reproducibility rate than when considering EEG alone and MEG alone, and 3) the cluster with the highest number of spikes provided the most concordant result with clinical reference; thus providing an automatic way of finding the most reliable and reproducible source to be considered for clinical purposes.

Errors in EEG source localization can be reduced by increasing the number of EEG electrodes as well as by the coverage of whole head surface with electrodes (Song et al., 2015). It has been shown in several studies that electrode arrays that approximate the 10-10 system are better than the conventional 10-20 system (Lantz and Grave de Peralta, 2003; Ryynänen et al., 2004) and the improvement in source localization accuracy was noticed for up to 64 channels, higher density EEG systems (128 to 256 channels) were actually more sensitive to noise (Lopes da Silva, 2013). On the other hand, when combining EEG and MEG data within a fusion framework, whole head coverage with dense spatial sampling of sensors can naturally be achieved thanks to whole head MEG device. This raised the question whether how many EEG electrodes should be required in fusion for bringing additional information that is missed by MEG. This was addressed in Chapter 4 through a simulation study, where we have shown that fusion of only 20 EEG electrodes together with 272 MEG sensors was sufficient for providing an optimal EEG-MEG fusion. This was further evaluated on clinical data in Chapter 6, where it was observed that the localization accuracy was similar for fusion of 272 MEG sensors with either 21, 32 and 54 EEG electrodes. Practical implications of using few EEG electrodes during simultaneous EEG-MEG recordings involve reduction

in the preparation time required for EEG electrodes set-up and also reduce eventual patient discomfort inside the MEG helmet.

The performance of cMEM algorithm was carefully compared with several distributed source localization algorithms such as methods implemented within the hierarchical Bayesian framework (IID, COH and multiple sparse prior), standard MNE, dSPM, and sLORETA. It should be noted that none of these methods were actually developed for their ability to recover spatially extended sources. Whereas COH, which consists in combining a minimum norm prior and a spatial smoothness prior within a hierarchical Bayesian model (Friston et al., 2008) could provide accurate results complementary to cMEM (Heers et al., 2015), it should be noted that MNE approaches are actually not sensitive to the underlying spatial extent of the sources as demonstrated in Zhu et al., (2014). Therefore, a fair comparison, in the context of epilepsy, was achieved by comparing cMEM with 4-ExSo-MUSIC as both methods have been well-established for their ability to localize the spatially extended generators of IEDs. Chapter 5 presented the quantitative validation of cMEM and 4-ExSo-MUSIC for their ability to localize complex patterns of IEDs such as propagation patterns and correlated activity. Realistic simulations of simultaneous EEG-MEG data were generated using a biophysical computational neural mass model and realistically shaped head models while taking into account equivalent number of channels in EEG and MEG. Therefore, this study consisted also in our first evaluation of the performance of cMEM on high-density EEG data (256 electrodes). Both cMEM and 4-ExSo-MUSIC localized single spatially extended sources with high accuracy for both EEG and MEG data. However, only cMEM was able to reconstruct accurately complex propagation patterns and correlated activities. Through this study, a complete validation of the cMEM algorithm was achieved, and the eligibility of cMEM for studying the underlying spatio-temporal dynamics of IEDs was demonstrated.

7.2. Future directions

The development of cMEM and MEM-fusion opened new avenues for research and clinical applications. In this section several new directions of research using cMEM or MEM-fusion are summarized.

1. EEG source localization during simultaneous EEG-fMRI recording is possible yet challenging, as the EEG signal is heavily corrupted by MR-induced artefacts. The excellent accuracy of EEG source localization of IEDs using cMEM on high density EEG data has been evaluated in Chapter 5. Moreover, since we demonstrated the robustness of cMEM in low SNR conditions, we assume it should be feasible to study the reproducibility of EEG source localization of IEDs using high density EEG data (256 electrodes) recorded during simultaneous EEG-fMRI session. The main objective of this project currently handled by T. Hedrich (PhD candidate in the lab) is to improve fMRI data analysis from reproducibility and clustering of spike-to-spike source localization results. To assess the feasibility, the results of source localization of high density EEG data recorded outside the MR scanner and inside the MR scanner will be compared. Preliminary results demonstrated the ability of cMEM to provide reproducible results on EEG data recorded both inside and outside the scanner (Hedrich et al., 2016).
2. Results from EEG and MEG source localization of IEDs using cMEM have been used to guide the selection of region of interest for the set-up of optimal montage during prolonged simultaneous recordings of EEG with functional Near Infra-Red Spectroscopy (fNIRS) on patients with epilepsy (Pellegrino et al., 2016b). This study allowed assessing accurately the hemodynamic response elicited by IEDs in term of local fluctuations in oxy and deoxy-hemoglobin fluctuations. Moreover, recent promising results suggested the possibility to apply MEM framework for local 3D reconstruction of fNIRS data from scalp recordings (Cai et al., 2016). These

new results offer the possibility to analyze EEG and NIRS data symmetrically within the MEM-fusion framework.

3. We have already shown that the addition of only few EEG electrodes was sufficient to bring additional information to EEG-MEG fusion for most clinical cases studied in Chapter 6. It raises an important question, whether the few EEG electrodes should be set-up homogeneously along the scalp surface or whether setting them up in a densely sampled montage to cover a pre-defined region of interest would result in improving source localization reliability. This should allow for a further improvement in the spatial resolution of EEG, offering the chance to bring better information regarding deeper or radially oriented sources that are usually missed in MEG.
4. Several recent studies have also suggested that both interictal and ictal activity should arise from the activity of dynamic epileptogenic cortical networks. The epileptogenic network is defined as the area involved in generation and spread of epileptic activity. In case of focal epilepsies, the epileptic activity begins in a spatially localized epileptogenic zone, which further recruits connected areas in a cascade of spreading activity from the central focus outward through both normal and abnormal tissues, to different parts of the brain. Thus, understanding the propagation and maintenance of the functional connectivity and network configurations in complex brain regions in epilepsy may open avenues for improved surgical procedures or even alternative non-surgical treatments, allowing treating the epilepsy as a network rather than as a focus (Wilke et al., 2011; Pittau and Vulliemoz, 2015). To this end, an avenue for research using MEM-fusion to study functional networks involved in insular epilepsy has been initiated by the group of Dr. D. Nguyen at Université de Montréal (Zerouali et al., 2016).
5. Using the MEM-fusion strategy within the time frequency domain, wMEM-fusion has also been developed and it is now being explored for the

localization of sleep spindles within the team of Dr J.M. Lina at Ecole de Technologie Supérieure.

6. According to the study in Chapter 5, cMEM provides an accurate localization and characterization of the spatio-temporal dynamics of IEDs. Furthermore, the proposed consensus map approach can actually provide a spatio-temporal map summarizing most reliable propagation patterns. Therefore, we plan to assess the relevance of MEM-fusion with spatio-temporal consensus maps approach to further investigate the spatio-temporal features occuring during the propagation of epileptic discharges.
7. In a recent study (Pellegrino et al., 2016c), cMEM method has been compared with dipole fitting approach on a large cohort of 49 patients resulting in 340 studies, further demonstrating the superior performance of cMEM method when compared to dipole fitting approach as described in the guidelines of the American Clinical MEG Society (Bagić et al., 2011). This study implies that MEM-based method should definitely complement or even substitute dipole fitting in the daily clinical practice.

Finally, the different variants of MEM including cMEM, wMEM, MEM-fusion, and wMEM-fusion are now freely available for users in the Brainstorm software (Tadel et al., 2011) as a plug-in toolbox namely, BEst: Brain Entropy in space and time (http://neuroimage.usc.edu/brainstorm/Tutorials/TutBEst).

Bibliography

Agirre-Arrizubieta, Z., Huiskamp, G.J.M., Ferrier, C.H., van Huffelen, A.C., Leijten, F.S.S., 2009. Interictal magnetoencephalography and the irritative zone in the electrocorticogram. Brain 132 (11), 3060–3071.

Ahlfors, S.P., Han, J., Belliveau, J.W., Hämäläinen, M.S., 2010. Sensitivity of MEG and EEG to Source Orientation. Brain Topogr 23 (3), 227–232.

Ahlfors, S.P., Han, J., Lin, F.-H., Witzel, T., Belliveau, J.W., Hämäläinen, M.S., Halgren, E., 2009. Cancellation of EEG and MEG signals generated by extended and distributed sources. Hum. Brain Mapp. 31 (1), 140–149.

Ahonen, A.I., Hämäläinen, M.S., Kajola, M.J., Knuutila, J.E.T., Laine, P.P., Lounasmaa, O.V., Parkkonen, L.T., Simola, J.T., Tesche, C.D., 1993. 122-channel squid instrument for investigating the magnetic signals from the human brain. Phys. Scr. T49A, 198–205.

Alarcon, G., Guy, C.N., Binnie, C.D., Walker, S.R., Elwes, R.D., Polkey, C.E., 1994. Intracerebral propagation of interictal activity in partial epilepsy: implications for source localisation. J Neurol Neurosurg Psychiatry 57 (4), 435–449.

Amblard, C., Lapalme, E., Lina, J.-M., 2004. Biomagnetic Source Detection by Maximum Entropy and Graphical Models. IEEE Trans. Biomed. Eng. 51 (3), 427–442.

Ana Coito, G.P., 2015. Dynamic directed interictal connectivity in left and right temporal lobe epilepsy. Epilepsia 56 (2).

Aydin, Ü., 2015. Combined EEG and MEG source analysis of epileptiform activity using calibrated realistic finite element head models.

Aydin, Ü., Vorwerk, J., Duempelmann, M., Kuepper, P., Kugel, H., Wellmer, J., Kellinghaus, C., Haueisen, J., Rampp, S., Stefan, H., Wolters, C., 2014. P806: Effects of spike averaging on EEG, MEG and combined EEG/MEG source analysis of epileptic activity. Clinical Neurophysiology 125, S258.

Aydin, Ü., Vorwerk, J., Dümpelmann, M., Küpper, P., Kugel, H., Heers, M., Wellmer, J., Kellinghaus, C., Haueisen, J., Rampp, S., Stefan, H., Wolters, C.H., 2015. Combined EEG/MEG Can Outperform Single Modality EEG or MEG Source Reconstruction in Presurgical Epilepsy Diagnosis. PLoS One 10 (3).

Aydin, Ü., Vorwerk, J., Küpper, P., Heers, M., Kugel, H., Galka, A., Hamid, L., Wellmer, J., Kellinghaus, C., Rampp, S., Wolters, C.H., 2014. Combining EEG and MEG for the reconstruction of epileptic activity using a calibrated realistic volume conductor model. PLoS ONE 9 (3), e93154.

Babiloni, C., Pizzella, V., Gratta, C.D., Ferretti, A., Romani, G.L., 2009. Fundamentals of electroencefalography, magnetoencefalography, and functional magnetic resonance imaging. Int. Rev. Neurobiol. 86, 67–80.

Babiloni, F., Babiloni, C., Carducci, F., Romani, G.L., Rossini, P.M., Angelone, L.M., Cincotti, F., 2004. Multimodal integration of EEG and MEG data: a

simulation study with variable signal-to-noise ratio and number of sensors. Hum Brain Mapp 22 (1), 52–62.

Babiloni, F., Carducci, F., Cincotti, F., Del Gratta, C., Pizzella, V., Romani, G.L., Rossini, P.M., Tecchio, F., Babiloni, C., 2001. Linear inverse source estimate of combined EEG and MEG data related to voluntary movements. Hum Brain Mapp 14 (4), 197–209.

Badier, J.-M., Cosandier-Rimélé, D., Bénar, C.G., Schwartz, D., Chauvel, P., Wendling, F., 2007. Realistic synthetic background neuronal activity for the analysis of MEG probe configurations. Conf Proc IEEE Eng Med Biol Soc 2007, 2460–2463.

Bagić, A.I., Knowlton, R.C., Rose, D.F., Ebersole, J.S., ACMEGS Clinical Practice Guideline (CPG) Committee, 2011. American Clinical Magnetoencephalography Society Clinical Practice Guideline 1: recording and analysis of spontaneous cerebral activity. J Clin Neurophysiol 28 (4), 348–354.

Baillet, S., Garnero, L., Marin, G., Hugonin, J.-P., 1999. Combined MEG and EEG source imaging by minimization of mutual information. IEEE Transactions on Biomedical Engineering 46 (5), 522–534.

Baillet, S., Mosher, J.C., 2001. and Richard M. Leahy. IEEE Signal Processing Magazine 1053 (5888/01).

Banerji, D., Pauranik, A., 2011. Progress in Clinical Neurosciences. Byword Books Private Limited.

Barkley, G.L., 2004. Controversies in neurophysiology. MEG is superior to EEG in localization of interictal epileptiform activity: Pro. Clinical Neurophysiology 115 (5), 1001â€“1009.

Barkley, G.L., Baumgartner, C., 2003. MEG and EEG in epilepsy. J Clin Neurophysiol 20 (3), 163–178.

Barth, D., Sutherling, W., Engel, J., Beatty, J., 1982. Neuromagnetic localization of epileptiform spike activity in the human brain. Science 218 (4575), 891–894.

Bast, T., Boppel, T., Rupp, A., Harting, I., Hoechstetter, K., Fauser, S., Schulze-Bonhage, A., Rating, D., Scherg, M., 2006. Noninvasive source localization of interictal EEG spikes: effects of signal-to-noise ratio and averaging. J Clin Neurophysiol 23 (6), 487–497.

Bast, T., Oezkan, O., Rona, S., Stippich, C., Seitz, A., Rupp, A., Fauser, S., Zentner, J., Rating, D., Scherg, M., 2004. EEG and MEG Source Analysis of Single and Averaged Interictal Spikes Reveals Intrinsic Epileptogenicity in Focal Cortical Dysplasia. Epilepsia 45 (6), 621–631.

Bast, T., Wright, T., Boor, R., Harting, I., Feneberg, R., Rupp, A., Hoechstetter, K., Rating, D., Baumgärtner, U., 2007. Combined EEG and MEG analysis of early somatosensory evoked activity in children and adolescents with focal epilepsies. Clinical Neurophysiology 118 (8), 1721–1735.

Batagelj, V., 1988. Generalized Ward and Related Clustering Problems, in: In H.H. Bock (Ed.), Classification and Related Methods of Data Analysis. North-Holland, pp. 67–74.

Baumgartner, C., Deecke, L., Stroink, G., 1995. Biomagnetism: Fundamental Research and Clinical Applications. IOS Press.

Baumgartner, C., Lindinger, G., Ebner, A., Aull, S., Serles, W., Olbrich, A., Lurger, S., Czech, T., Burgess, R., Lüders, H., 1995. Propagation of interictal epileptic activity in temporal lobe epilepsy. Neurology 45 (1), 118–122.

Baumgartner, C., Pataraia, E., 2006. Revisiting the role of magnetoencephalography in epilepsy. Curr. Opin. Neurol 19 (2), 181–186.

Baumgartner, C., Pataraia, E., Lindinger, G., Deecke, L., 2000. Magnetoencephalography in focal epilepsy. Epilepsia 41 Suppl 3, S39-47.

Bautista, R.E., Cobbs, M.A., Spencer, D.D., Spencer, S.S., 1999. Prediction of surgical outcome by interictal epileptiform abnormalities during intracranial EEG monitoring in patients with extrahippocampal seizures. Epilepsia 40 (7), 880–890.

Becker, H., Albera, L., Comon, P., Gribonval, R., Merlet, I., 2014. Fast, variation-based methods for the analysis of extended brain sources. Presented at the Signal Processing Conference (EUSIPCO), 2014 Proceedings of the 22nd European, pp. 41–45.

Becker, H., Albera, L., Comon, P., Gribonval, R., Wendling, F., Merlet, I., 2015. Brain-Source Imaging: From sparse to tensor models. IEEE Signal Processing Magazine 32 (6), 100–112.

Becker, H., Albera, L., Comon, P., Haardt, M., Birot, G., Wendling, F., Gavaret, M., Bénar, C.G., Merlet, I., 2014a. EEG extended source localization: Tensor-based vs. conventional methods. NeuroImage 96, 143–157.

Becker, H., Albera, L., Comon, P., Haardt, M., Birot, G., Wendling, F., Gavaret, M., Bénar, C.G., Merlet, I., 2014b. EEG extended source localization: Tensor-based vs. conventional methods. NeuroImage 96, 143–157.

Bénar, C.-G., Grova, C., Kobayashi, E., Bagshaw, A.P., Aghakhani, Y., Dubeau, F., Gotman, J., 2006. EEG-fMRI of epileptic spikes: concordance with EEG source localization and intracranial EEG. Neuroimage 30 (4), 1161–1170.

Bénar, C.G., Gunn, R.N., Grova, C., Champagne, B., Gotman, J., 2005. Statistical maps for EEG dipolar source localization. IEEE Trans Biomed Eng 52 (3), 401–413.

Berg, A.T., Berkovic, S.F., Brodie, M.J., Buchhalter, J., Cross, J.H., van Emde Boas, W., Engel, J., French, J., Glauser, T.A., Mathern, G.W., Moshé, S.L., Nordli, D., Plouin, P., Scheffer, I.E., 2010. Revised terminology and concepts for organization of seizures and epilepsies: report of the ILAE Commission on Classification and Terminology, 2005-2009. Epilepsia 51 (4), 676–685.

Berger, H., 1969. On the electroencephalogram of man. Electroencephalogr Clin Neurophysiol Suppl 28:37+-37+.

Birot, G., Albera, L., Wendling, F., Merlet, I., 2011. Localization of extended brain sources from EEG/MEG: the ExSo-MUSIC approach. Neuroimage 56 (1), 102–113.

Birot, G., Spinelli, L., Vulliémoz, S., Mégevand, P., Brunet, D., Seeck, M., Michel, C.M., 2014. Head model and electrical source imaging: A study of 38 epileptic patients. Neuroimage Clin 5, 77–83.

Bouet, R., Jung, J., Delpuech, C., Ryvlin, P., Isnard, J., Guenot, M., Bertrand, O., Mauguière, F., 2012. Towards source volume estimation of interictal spikes in focal epilepsy using magnetoencephalography. NeuroImage 59 (4), 3955–3966.

Brodbeck, V., Spinelli, L., Lascano, A.M., Wissmeier, M., Vargas, M.-I., Vulliemoz, S., Pollo, C., Schaller, K., Michel, C.M., Seeck, M., 2011. Electroencephalographic source imaging: a prospective study of 152 operated epileptic patients. Brain 134 (10), 2887–2897.

Cacioppo, J.T., Tassinary, L.G., Berntson, G.G., 2007. Handbook of psychophysiology. Cambridge University Press.

Cai, Z., Chowdhury, R.A., Machado, A., Vincent, T., Pellegrino, G., Spilkin, A., Lina, J.M., Grova, C., 2016. NIRS 3D Reconstruction Based on Maximum Entropy on the Mean (MEM). Presented at the fNIRS 2016, Paris, France.

Caton, R., 1875. The electric currents of the brain. British Medical Journal 2, 278.

Chatrian, G.E., Lettich, E., Nelson, P.L., 1985. Ten percent electrode system for topographic studies of spontaneous and evoked EEG activities. American Journal of EEG technology 25 (2), 83–92.

Chauvel, P., Vignal, J., Biraben, A., Badier, J.M., Scarabin, J.M., 1996. , in: Pawlik, G., Stefan, H. (Eds.), Multimethodological Assessment of the Epileptic Forms, chapter Stereoencephalography. Springer Verlag, New York, pp. 80–108.

Cheyne, D., Bakhtazad, L., Gaetz, W., 2006. Spatiotemporal mapping of cortical activity accompanying voluntary movements using an event-related beamforming approach. Human brain mapping 27 (3), 213–229.

Cheyne, D., Lerch, J., Mohamed, I., Ferrari, P., Lalancette, M., Pang, E., 2010. Realistic models of spatially extended cortical activity in MEG. Frontiers in Neuroscience 4.

Chowdhury, R.A., Lina, J.M., Kobayashi, E., Grova, C., 2013. MEG Source Localization of Spatially Extended Generators of Epileptic Activity: Comparing Entropic and Hierarchical Bayesian Approaches. PLoS ONE 8 (2), e55969.

Chowdhury, R.A., Merlet, I., Birot, G., Albera, L., Kobayashi, E., Lina, J.-M., Wendling, F., Grova, C., 2014. Localization of the spatial extent of the generators of epileptic discharges in EEG and MEG: comparison between 4-ExSo-MUSIC and MEM approaches. Presented at the 19th International Conference on Biomagnetism - BIOMAG 2014, Halifax, Canada.

Chowdhury, R.A., Merlet, I., Birot, G., Kobayashi, E., Nica, A., Biraben, A., Wendling, F., Lina, J.M., Albera, L., Grova, C., 2016. Complex patterns of spatially extended generators of epileptic activity: Comparison of source localization methods cMEM and 4-ExSo-MUSIC on high resolution EEG and MEG data. Neuroimage 143, 175–195.

Chowdhury, R.A., Zerouali, Y., Hedrich, T., Heers, M., Kobayashi, E., Lina, J.-M., Grova, C., 2015. MEG–EEG Information Fusion and Electromagnetic Source Imaging: From Theory to Clinical Application in Epilepsy. Brain Topogr 1–28.

Cohen, D., 1968. Magnetoencephalography: evidence of magnetic fields produced by alpha-rhythm currents. Science 161 (843), 784–786.

Cohen, D., 2004. Boston and the History of Biomagnetism. Neurology and Clinical Neurophysiology 114.

Cohen, D., Cuffin, B.N., 1983. Demonstration of useful differences between magnetoencephalogram and electroencephalogram. Electroencephalogr Clin Neurophysiol 56 (1), 38–51.

Cooper, R., Winter, A.L., Crow, H.J., Walter, W.G., 1965. Comparison of subcortical, cortical and scalp activity using chronically indwelling electrodes in man. Electroencephalogr Clin Neurophysiol 18, 217–228.

Cosandier-Rimélé, D., Badier, J.-M., Chauvel, P., Wendling, F., 2007. A physiologically plausible spatio-temporal model for EEG signals recorded with intracerebral electrodes in human partial epilepsy. IEEE Trans Biomed Eng 54 (3), 380–388.

Cosandier-Rimélé, D., Merlet, I., Badier, J.M., Chauvel, P., Wendling, F., 2008. The neuronal sources of EEG: Modeling of simultaneous scalp and intracerebral recordings in epilepsy. NeuroImage 42 (1), 135–146.

Cosandier-Rimélé, D., Merlet, I., Bartolomei, F., Badier, J.-M., Wendling, F., 2010. Computational modeling of epileptic activity: from cortical sources to EEG signals. J Clin Neurophysiol 27 (6), 465–470.

de Curtis, M., Jefferys, J.G.R., Avoli, M., 2012. Interictal Epileptiform Discharges in Partial Epilepsy: Complex Neurobiological Mechanisms Based on Experimental and Clinical Evidence, in: Noebels, J.L., Avoli, M., Rogawski, M.A., Olsen, R.W., Delgado-Escueta, A.V. (Eds.), Jasper's Basic Mechanisms of the Epilepsies. National Center for Biotechnology Information (US), Bethesda (MD).

Dale, A.M., Liu, A.K., Fischl, B.R., Buckner, R.L., Belliveau, J.W., Lewine, J.D., Halgren, E., 2000. Dynamic statistical parametric mapping: combining fMRI and MEG for high-resolution imaging of cortical activity. Neuron 26 (1), 55–67.

Dale, A.M., Sereno, M.I., 1993. Improved Localization of Cortical Activity by Combining EEG and MEG with MRI Cortical Surface Reconstruction: A Linear Approach. J. Cogn. Neurosci 5, 162–176.

Dannhauer, M., Lanfer, B., Wolters, C.H., Knösche, T.R., 2011. Modeling of the human skull in EEG source analysis. Human Brain Mapping 32 (9), 1383–1399.

Dansereau, C.L., Bellec, P., Lee, K., Pittau, F., Gotman, J., Grova, C., 2014. Detection of abnormal resting-state networks in individual patients suffering from focal epilepsy: an initial step toward individual connectivity assessment. Frontiers in neuroscience 8.

Daunizeau, J., Mattout, J., Clonda, D., Goulard, B., Benali, H., Lina, J.-M., 2006. Bayesian Spatio-Temporal Approach for EEG Source Reconstruction: Conciliating ECD and Distributed Models. IEEE Trans. Biomed. Eng. 53 (3), 503–516.

Diekmann, V., Becker, W., Jürgens, R., Grözinger, B., Kleiser, B., Richter, H.P., Wollinsky, K.H., 1998. Localisation of epileptic foci with electric, magnetic and combined electromagnetic models. Electroencephalography and Clinical Neurophysiology 106 (4), 297–313.

Ding, L., 2009a. L1-norm and L2-norm neuroimaging methods in reconstructing extended cortical sources from EEG, in: Engineering in Medicine and Biology Society, 2009. EMBC 2009. Annual International Conference of the IEEE. Presented at the Engineering in Medicine and Biology Society, 2009. EMBC 2009. Annual International Conference of the IEEE, pp. 1922–1925.

Ding, L., 2009b. Reconstructing cortical current density by exploring sparseness in the transform domain. Phys. Med. Biol. 54 (9), 2683–2697.

Ding, L., Yuan, H., 2013. Simultaneous EEG and MEG source reconstruction in sparse electromagnetic source imaging. Hum. Brain Mapp. 34 (4), 775–795.

Dubarry, A.-S., Badier, J.-M., Trébuchon-Da Fonseca, A., Gavaret, M., Carron, R., Bartolomei, F., Liégeois-Chauvel, C., Régis, J., Chauvel, P., Alario, F.-X., Bénar, C.-G., 2014. Simultaneous recording of MEG, EEG and intracerebral EEG during visual stimulation: from feasibility to single-trial analysis. Neuroimage 99, 548–558.

Ebersole, J.S., 1997a. Defining epileptogenic foci: past, present, future. J Clin Neurophysiol 14 (6), 470–483.

Ebersole, J.S., 1997b. Magnetoencephalography/magnetic source imaging in the assessment of patients with epilepsy. Epilepsia 38 (s4), S1–S5.

Ebersole, J.S., 1999. EEG source modeling. The last word. J Clin Neurophysiol 16 (3), 297–302.

Ebersole, J.S., Ebersole, S.M., 2010. Combining MEG and EEG source modeling in epilepsy evaluations. J Clin Neurophysiol 27 (6), 360–371.

von Ellenrieder, N., Beltrachini, L., Muravchik, C.H., Gotman, J., 2014a. Extent of cortical generators visible on the scalp: Effect of a subdural grid. NeuroImage 101, 787–795.

von Ellenrieder, N., Pellegrino, G., Hedrich, T., Gotman, J., Lina, J.-M., Grova, C., Kobayashi, E., 2016. Detection and Magnetic Source Imaging of Fast Oscillations (40-160 Hz) Recorded with Magnetoencephalography in Focal Epilepsy Patients. Brain Topogr 29 (2), 218–231.

Emerson, R.G., Turner, C.A., Pedley, T.A., Walczak, T.S., Forgione, M., 1995. Propagation patterns of temporal spikes. Electroencephalogr Clin Neurophysiol 94 (5), 338–348.

Enatsu, R., Mikuni, N., 2016. Invasive Evaluations for Epilepsy Surgery: A Review of the Literature. Neurol Med Chir (Tokyo) 56 (5), 221–227.

Engel, J., Pedley, T.A., Aicardi, J., 2008. Epilepsy: A Comprehensive Textbook. Lippincott Williams & Wilkins.

Engel, J.J., 1993. Update on surgical treatment of the epilepsies: Summary of The Second International Palm Desert Conference on the Surgical Treatment of the Epilepsies (1992). Neurology 43 (8), 1612–1617.

Engel, J.J., 1996. Surgery for Seizures. New England Journal of Medicine 334 (10), 647–653.

Fangmin Chen, H.H., 2010. Influence of skull conductivity perturbations on EEG dipole source analysis. Medical physics 37 (8), 4475–84.

Feindel, W., Leblanc, R., De Almeida, A.N., 2009. Epilepsy Surgery: Historical Highlights 1909–2009. Epilepsia 50, 131–151.

Fernandes, J.M., da Silva, A.M., Huiskamp, G., Velis, D.N., Manshanden, I., de Munck, J.C., da Silva, F.L., Cunha, J.P.S., 2005. What does an epileptiform spike look like in MEG? Comparison between coincident EEG and MEG spikes. J Clin Neurophysiol 22 (1), 68–73.

Ferree, T.C., Eriksen, K.J., Tucker, D.M., 2000. Regional head tissue conductivity estimation for improved EEG analysis. IEEE Transactions on Biomedical Engineering 47 (12), 1584–1592.

Fisher, R., Saul, M., 2010. Overview of Epilepsy.

Fisher, R.S., Cross, J.H., French, J.A., Higurashi, N., Hirsch, E., Jansen, F.E., Lagae, L., Moshé, S.L., Peltola, J., Perez, E.R., Scheffer, I.E., Zuberi, S.M., 2016. Operational Classification of Seizure Types by the International League Against Epilepsy.

la Fougère, C., Rominger, A., Förster, S., Geisler, J., Bartenstein, P., 2009. PET and SPECT in epilepsy: A critical review. Epilepsy & Behavior, Management of Epilepsy: Hope and HurdlesCritical Reviews and Clinical Guidance 15 (1), 50–55.

Frank, E., 1952. Electric Potential Produced by Two Point Current Sources in a Homogeneous Conducting Sphere. J. Appl. Phys. 23 (11), 1225.

Friston, K., Harrison, L., Daunizeau, J., Kiebel, S., Phillips, C., Trujillo-Barreto, N., Henson, R., Flandin, G., Mattout, J., 2008. Multiple sparse priors for the M/EEG inverse problem. NeuroImage 39 (3), 1104–1120.

Friston, K., Mattout, J., Trujillo-Barreto, N., Ashburner, J., Penny, W., 2006. Variational free energy and the Laplace approximation. NeuroImage 34 (1), 220–234.

Friston, K.J., Penny, W., Phillips, C., Kiebel, S., Hinton, G., Ashburner, J., 2002. Classical and Bayesian Inference in Neuroimaging: Theory. NeuroImage 16 (2), 465–483.

Fuchs, M., Wagner, M., Köhler, T., Wischmann, H.A., 1999. Linear and nonlinear current density reconstructions. J Clin Neurophysiol 16 (3), 267–295.

Fuchs, M., Wagner, M., Wischmann, H.-A., Köhler, T., Theißen, A., Drenckhahn, R., Buchner, H., 1998. Improving source reconstructions by combining bioelectric and biomagnetic data. Electroencephalography and Clinical Neurophysiology 107 (2), 93–111.

Funke, M., Constantino, T., Van Orman, C., Rodin, E., 2009. Magnetoencephalography and magnetic source imaging in epilepsy. Clin EEG Neurosci 40 (4), 271–280.

Gaetz, W., Cheyne, D., 2006. Localization of sensorimotor cortical rhythms induced by tactile stimulation using spatially filtered MEG. Neuroimage 30 (3), 899–908.

Gavaret, M., Maillard, L., Jung, J., 2015. High-resolution EEG (HR-EEG) and magnetoencephalography (MEG). Neurophysiologie Clinique/Clinical Neurophysiology 45 (1), 105–111.

Geddes, L.A., Baker, L.E., 1967. The specific resistance of biological material--a compendium of data for the biomedical engineer and physiologist. Med Biol Eng 5 (3), 271–293.

Genow, A., Hummel, C., Scheler, G., Hopfengärtner, R., Kaltenhäuser, M., Buchfelder, M., Romstöck, J., Stefan, H., 2004. Epilepsy surgery, resection volume and MSI localization in lesional frontal lobe epilepsy. NeuroImage 21 (1), 444–449.

Gevins, A., 1993. High resolution EEG. Brain Topogr 5 (4), 321–325.

Gevins, A., Le, J., Martin, N.K., Brickett, P., Desmond, J., Reutter, B., 1994. High resolution EEG: 124-channel recording, spatial deblurring and MRI integration methods. Electroencephalography and clinical Neurophysiology 90 (5), 337–358.

Global Campaign against Epilepsy, International Bureau of Epilepsy, International League against Epilepsy (Eds.), 2005. Atlas: epilepsy care in the world. Programme for Neurological Diseases and Neuroscience, Department of Mental Health and Substance Abuse, World Health Organization, Geneva.

Goldenholz, D.M., Ahlfors, S.P., Hämäläinen, M.S., Sharon, D., Ishitobi, M., Vaina, L.M., Stufflebeam, S.M., 2009. Mapping the signal-to-noise-ratios of cortical sources in magnetoencephalography and electroencephalography. Human brain mapping 30 (4), 1077–1086.

Gonçalves, S.I., de Munck, J.C., Verbunt, J.P.A., Bijma, F., Heethaar, R.M., Lopes da Silva, F., 2003. In vivo measurement of the brain and skull resistivities using an EIT-based method and realistic models for the head. IEEE Trans Biomed Eng 50 (6), 754–767.

de Gooijer-van de Groep, K.L., Leijten, F.S.S., Ferrier, C.H., Huiskamp, G.J.M., 2013. Inverse modeling in magnetic source imaging: Comparison of MUSIC, SAM(g2), and sLORETA to interictal intracranial EEG. Hum. Brain Mapp 34 (9), 2032–2044.

Gotman, J., 2003. Noninvasive Methods for Evaluating the Localization and Propagation of Epileptic Activity. Epilepsia 44, 21–29.

Gotman, J., Pittau, F., 2011. Combining EEG and fMRI in the study of epileptic discharges. Epilepsia 52 Suppl 4, 38–42.

Gramfort, A., 2009. Mapping, timing and tracking cortical activations with MEG and EEG: Methods and application to human vision (PhD thesis).

Gramfort, A., Kowalski, M., Hämäläinen, M., 2012. Mixed-norm estimates for the M/EEG inverse problem using accelerated gradient methods. Physics in medicine and biology 57 (7), 1937.

Gramfort, A., Papadopoulo, T., Olivi, E., Clerc, M., 2010. OpenMEEG: opensource software for quasistatic bioelectromagnetics. Biomed Eng Online 9, 45.

Gramfort, A., Papadopoulo, T., Olivi, E., Clerc, M., 2011. Forward Field Computation with OpenMEEG. Computational Intelligence and Neuroscience 2011, 1–13.

Grech, R., Cassar, T., Muscat, J., Camilleri, K.P., Fabri, S.G., Zervakis, M., Xanthopoulos, P., Sakkalis, V., Vanrumste, B., 2008. Journal of NeuroEngineering and Rehabilitation. Journal of NeuroEngineering and Rehabilitation 5, 25.

Gross, J., Kujala, J., Hämäläinen, M., Timmermann, L., Schnitzler, A., Salmelin, R., 2001. Dynamic imaging of coherent sources: studying neural interactions in the human brain. Proceedings of the National Academy of Sciences 98 (2), 694–699.

Grova, C., Aiguabella, M., Zelmann, R., Lina, J.-M., Hall, J.A., Kobayashi, E., 2016. Intracranial EEG potentials estimated from MEG sources: A new approach to correlate MEG and iEEG data in epilepsy: Correlation between MEG Sources and iEEG Data for Epileptic Spikes. Human Brain Mapping.

Grova, C., Daunizeau, J., Kobayashi, E., Bagshaw, A.P., Lina, J.M., Dubeau, F., Gotman, J., 2008. Concordance between distributed EEG source localization and simultaneous EEG-fMRI studies of epileptic spikes. Neuroimage 39 (2), 755–774.

Grova, C., Daunizeau, J., Lina, J.M., Benar, C.G., Benali, H., Gotman, J., 2006. Evaluation of EEG localization methods using realistic simulations of interictal spikes. Neuroimage 29 (3), 734–753.

Haas, L.F., 2003. Hans Berger (1873-1941), Richard Caton (1842-1926), and electroencephalography. J. Neurol. Neurosurg. Psychiatr. 74 (1), 9.

Hadamard, J., 1902. Sur les problèmes aux dérivées partielles et leur signification physique. Princeton University Bulletin 13, 49–52.

Hallez, H., Vanrumste, B., Grech, R., Muscat, J., De Clercq, W., Vergult, A., D'Asseler, Y., Camilleri, K.P., Fabri, S.G., Van Huffel, S., Lemahieu, I., 2007. Review on solving the forward problem in EEG source analysis. J Neuroeng Rehabil 4, 1–29.

Hämäläinen, M., Hari, R., Ilmoniemi, R.J., Knuutila, J., Lounasmaa, O.V., 1993. Magnetoencephalography—theory, instrumentation, and applications to noninvasive studies of the working human brain. Rev. Mod. Phys. 65 (2), 413–497.

Hämäläinen, M.S., Ilmoniemi, R.J., 1994. Interpreting magnetic fields of the brain: minimum norm estimates. Medical and Biological Engineering and Computing 32 (1), 35–42.

Hämäläinen, M.S., Sarvas, J., 1989. Realistic conductivity geometry model of the human head for interpretation of neuromagnetic data. IEEE Trans Biomed Eng 36 (2), 165–171.

Hamandi, K., Routley, B.C., Koelewijn, L., Singh, K.D., 2016. Non-invasive brain mapping in epilepsy: Applications from magnetoencephalography. Journal of Neuroscience Methods, Methods and Models in Epilepsy Research 260, 283–291.

Hansen, P.C., 2000. The L-Curve and its Use in the Numerical Treatment of Inverse Problems, in: in Computational Inverse Problems in Electrocardiology, ed. P. Johnston, Advances in Computational Bioengineering. WIT Press, pp. 119–142.

Hara, K., Lin, F.-H., Camposano, S., Foxe, D.M., Grant, P.E., Bourgeois, B.F., Ahlfors, S.P., Stufflebeam, S.M., 2007. Magnetoencephalographic mapping of interictal spike propagation: a technical and clinical report. AJNR Am J Neuroradiol 28 (8), 1486–1488.

Hari, R., 1990. The neuromagnetic method in the study of the human auditory cortex. Auditory Evoked Magnetic Fields and Potentials. Advances in Audiology 6, 222–282.

Hari, R., Parkkonen, L., 2015. The brain timewise: how timing shapes and supports brain function. Phil. Trans. R. Soc. B 370 (1668), 20140170.

Harrison, L.M., Penny, W., Ashburner, J., Trujillo-Barreto, N., Friston, K.J., 2007. Diffusion-based spatial priors for imaging. NeuroImage 38 (4), 677–695.

Haueisen, J., Funke, M., Güllmar, D., Eichardt, R., 2012. Tangential and radial epileptic spike activity: different sensitivity in EEG and MEG. J Clin Neurophysiol 29 (4), 327–332.

Hauf, M., Jann, K., Schindler, K., Scheidegger, O., Meyer, K., Rummel, C., Mariani, L., Koenig, T., Wiest, R., 2012. Localizing Seizure-Onset Zones in Presurgical Evaluation of Drug-Resistant Epilepsy by Electroencephalography/fMRI: Effectiveness of Alternative Thresholding Strategies. AJNR Am J Neuroradiol 33 (9), 1818–1824.

Hauk, O., Wakeman, D.G., Henson, R., 2011. Comparison of noise-normalized minimum norm estimates for MEG analysis using multiple resolution metrics. Neuroimage 54 (3), 1966–1974.

Hedrich, T., Khoo, H.M., Pellegrino, G., Aydin, Ü., Gotman, J., Grova, C., 2016. Combining source localization from high-density EEG and fMRI responses to similar epileptic discharges: a preliminary reproducibility study. Presented at the Annual Meeting of the American Epilepsy Society, Houston, TX, USA.

Heers, M., Chowdhury, R.A., Hedrich, T., Dubeau, F., Hall, J.A., Lina, J.-M., Grova, C., Kobayashi, E., 2015. Localization Accuracy of Distributed Inverse Solutions for Electric and Magnetic Source Imaging of Interictal Epileptic Discharges in Patients with Focal Epilepsy. Brain Topogr 1–20.

Heers, M., Chowdhury, R.A., Hedrich, T., Dubeau, F., Hall, J.A., Lina, J.-M., Grova, C., Kobayashi, E., 2016. Localization Accuracy of Distributed Inverse Solutions for Electric and Magnetic Source Imaging of Interictal Epileptic Discharges in Patients with Focal Epilepsy. Brain Topography 29 (1), 162–181.

Heers, M., Hedrich, T., An, D., Dubeau, F., Gotman, J., Grova, C., Kobayashi, E., 2014. Spatial correlation of hemodynamic changes related to interictal epileptic discharges with electric and magnetic source imaging. Hum. Brain Mapp. 35 (9), 4396–4414.

Heers, M., Rampp, S., Stefan, H., Urbach, H., Elger, C.E., von Lehe, M., Wellmer, J., 2012. MEG-based identification of the epileptogenic zone in occult peri-insular epilepsy. Seizure 21 (2), 128–133.

Henderson, C.J., Butler, S.R., Glass, A., 1975. The localization of equivalent dipoles of EEG sources by the application of electrical field theory. Electroencephalography and Clinical Neurophysiology 39 (2), 117–130.

Henson, R.N.., 2010. Multimodal integration: constraining MEG localization with EEG and fMRI, in: 17th International Conference on Biomagnetism Advances in Biomagnetism–Biomag2010. pp. 97–100.

Henson, R.N., Mattout, J., Phillips, C., Friston, K.J., 2009. Selecting forward models for MEG source-reconstruction using model-evidence. NeuroImage 46 (1), 168–176.

Henson, R.N., Mouchlianitis, E., Friston, K.J., 2009. MEG and EEG data fusion: Simultaneous localisation of face-evoked responses. NeuroImage 47 (2), 581–589.

Hillebrand, A., Barnes, G.R., 2002. A Quantitative Assessment of the Sensitivity of Whole-Head MEG to Activity in the Adult Human Cortex. NeuroImage 16 (3), 638–650.

Hillebrand, A., Barnes, G.R., 2011. Practical constraints on estimation of source extent with MEG beamformers. NeuroImage 54 (4), 2732–2740.

Hisashi Itabashi, K.J., 2014. Electro- and magneto-encephalographic spike source localization of small focal cortical dysplasia in the dorsal peri-rolandic region. Clinical neurophysiology : official journal of the International Federation of Clinical Neurophysiology.

Hoekema, R., Wieneke, G.H., Leijten, F.S.S., van Veelen, C.W.M., van Rijen, P.C., Huiskamp, G.J.M., Ansems, J., van Huffelen, A.C., 2003. Measurement of the conductivity of skull, temporarily removed during epilepsy surgery. Brain Topogr 16 (1), 29–38.

Holmes, M.D., 2008. Dense array EEG: Methodology and new hypothesis on epilepsy syndromes. Epilepsia 49, 3–14.

Holmes, M.D., Brown, M., Tucker, D.M., Saneto, R.P., Miller, K.J., Wig, G.S., Ojemann, J.G., 2008. Localization of extratemporal seizure with noninvasive dense-array EEG. Comparison with intracranial recordings. Pediatr Neurosurg 44 (6), 474–479.

Holmes, M.D., Tucker, D.M., Quiring, J.M., Hakimian, S., Miller, J.W., Ojemann, J.G., 2010. Comparing noninvasive dense array and intracranial electroencephalography for localization of seizures. Neurosurgery 66 (2), 354–362.

Hong, J.H., Ahn, M., Jun, S.C., 2010. Single-Trial Analysis for Empirical MEG Data, in: Supek, S., Sušac, A. (Eds.), 17th International Conference on Biomagnetism Advances in Biomagnetism – Biomag2010, IFMBE Proceedings. Springer Berlin Heidelberg, pp. 163–166.

Hong, J.H., Ahn, M., Kim, K., Jun, S.C., 2013. Localization of coherent sources by simultaneous MEG and EEG beamformer. Med Biol Eng Comput 1–15.

Horsley, V., 1886. Brain Surgery. British Medical Journal 2 (1345), 670.

Huang, M., Aine, C.J., Supek, S., Best, E., Ranken, D., Flynn, E.R., 1998. Multi-start downhill simplex method for spatio-temporal source localization in magnetoencephalography. Electroencephalography and Clinical Neurophysiology/Evoked Potentials Section 108 (1), 32–44.

Huang, M.X., Mosher, J.C., Leahy, R.M., 1999. A sensor-weighted overlapping-sphere head model and exhaustive head model comparison for MEG. Phys Med Biol 44 (2), 423–440.

Huang, M.-X., Song, T., Hagler Jr., D.J., Podgorny, I., Jousmaki, V., Cui, L., Gaa, K., Harrington, D.L., Dale, A.M., Lee, R.R., Elman, J., Halgren, E., 2007. A novel integrated MEG and EEG analysis method for dipolar sources. NeuroImage 37 (3), 731–748.

Hufnagel, A., Dümpelmann, M., Zentner, J., Schijns, O., Elger, C.E., 2000. Clinical relevance of quantified intracranial interictal spike activity in presurgical evaluation of epilepsy. Epilepsia 41 (4), 467–478.

Huiskamp, G., 2008. Interindividual variability of skull conductivity: an EEG-MEG analysis. International Journal of Bioelectromagnetism.

Huiskamp, G., Agirre-Arrizubieta, Z., Leijten, F., 2010. Regional Differences in the Sensitivity of MEG for Interictal Spikes in Epilepsy. Brain Topogr 23 (2), 159–164.

Huiskamp, G., Vroeijenstijn, M., van Dijk, R., Wieneke, G., van Huffelen, A.C., 1999. The need for correct realistic geometry in the inverse EEG problem. IEEE Trans Biomed Eng 46 (11), 1281–1287.

Huppertz, H.-J., Hoegg, S., Sick, C., Lücking, C.H., Zentner, J., Schulze-Bonhage, A., Kristeva-Feige, R., 2001. Cortical current density reconstruction of interictal epileptiform activity in temporal lobe epilepsy. Clinical Neurophysiology 112 (9), 1761–1772.

Ioannides, A.A., Bolton, J.P.R., Clarke, C.J.S., 1990. Continuous probabilistic solutions to the biomagnetic inverse problem. Inverse Problems 6 (4), 523.

Iwasaki, M., Pestana, E., Burgess, R.C., Lüders, H.O., Shamoto, H., Nakasato, N., 2005. Detection of epileptiform activity by human interpreters: blinded comparison between electroencephalography and magnetoencephalography. Epilepsia 46 (1), 59–68.

Jackson, A.F., Bolger, D.J., 2014. The neurophysiological bases of EEG and EEG measurement: A review for the rest of us: Neurophysiological bases of EEG. Psychophysiology 51 (11), 1061–1071.

Jansen, B.H., Rit, V.G., 1995. Electroencephalogram and visual evoked potential generation in a mathematical model of coupled cortical columns. Biol Cybern 73 (4), 357–366.

Jasper, H.H., 1958. Report of the committee on methods of clinical examination in electroencephalography: 1957. Electroencephalography and Clinical Neurophysiology 10 (2), 370–375.

Jayakar, P., Gotman, J., Harvey, A.S., Palmini, A., Tassi, L., Schomer, D., Dubeau, F., Bartolomei, F., Yu, A., Kršek, P., Velis, D., Kahane, P., 2016. Diagnostic utility of invasive EEG for epilepsy surgery: Indications, modalities, and techniques. Epilepsia.

Jaynes, E.T., 1957. Information Theory and Statistical Mechanics. Phys. Rev. 106 (4), 620–630.

Jeong, W., Kim, J.S., Chung, C.K., 2013. Localization of MEG pathologic gamma oscillations in adult epilepsy patients with focal cortical dysplasia. NeuroImage: Clinical 3, 507–514.

Jerbi, K., Mosher, J.C., Baillet, S., Leahy, R.M., 2002. On MEG forward modelling using multipolar expansions. Physics in Medicine and Biology 47 (4), 523–555.

Jette, N., Wiebe, S., 2013. Update on the surgical treatment of epilepsy: Current Opinion in Neurology 26 (2), 201–207.

de Jongh, A., de Munck, J.C., Gonçalves, S.I., Ossenblok, P., 2005. Differences in MEG/EEG epileptic spike yields explained by regional differences in signal-to-noise ratios. J Clin Neurophysiol 22 (2), 153–158.

Josephson, B.D., 1962. Possible new effects in superconductive tunnelling. Physics Letters 1 (7), 251–253.

Jung, J., Bouet, R., Delpuech, C., Ryvlin, P., Isnard, J., Guenot, M., Bertrand, O., Hammers, A., Mauguière, F., 2013. The value of magnetoencephalography for seizure-onset zone localization in magnetic resonance imaging-negative partial epilepsy. Brain 136 (Pt 10), 3176–3186.

Kaipio, J., Somersalo, E., 2005. Statistical and computational inverse problems, Applied mathematical sciences. Springer, New York.

Kakisaka, Y., Alkawadri, R., Wang, Z.I., Enatsu, R., Mosher, J.C., Dubarry, A.-S., Alexopoulos, A.V., Burgess, R.C., 2013. Sensitivity of scalp 10-20 EEG and magnetoencephalography. Epileptic Disord 15 (1), 27–31.

Kincses, W.E., Braun, C., Kaiser, S., Grodd, W., Ackermann, H., Mathiak, K., 2003. Reconstruction of extended cortical sources for EEG and MEG based on a Monte-Carlo-Markov-chain estimator. Hum Brain Mapp 18 (2), 100–110.

Kirsch, H.E., Mantle, M., Nagarajan, S.S., 2007. Concordance between routine interictal magnetoencephalography and simultaneous scalp electroencephalography in a sample of patients with epilepsy. J Clin Neurophysiol 24 (3), 215–231.

Klamer, S., Elshahabi, A., Lerche, H., Braun, C., Erb, M., Scheffler, K., Focke, N.K., 2015. Differences between MEG and high-density EEG source localizations using a distributed source model in comparison to fMRI. Brain Topogr 28 (1), 87–94.

Knake, S., Halgren, E., Shiraishi, H., Hara, K., Hamer, H.M., Grant, P.E., Carr, V.A., Foxe, D., Camposano, S., Busa, E., Witzel, T., Hämäläinen, M.S., Ahlfors, S.P., Bromfield, E.B., Black, P.M., Bourgeois, B.F., Cole, A.J., Cosgrove, G.R., Dworetzky, B.A., Madsen, J.R., Larsson, P.G., Schomer, D.L., Thiele, E.A., Dale, A.M., Rosen, B.R., Stufflebeam, S.M., 2006. The value of multichannel MEG and EEG in the presurgical evaluation of 70 epilepsy patients. Epilepsy Res. 69 (1), 80–86.

Knowlton, R.C., Elgavish, R.A., Bartolucci, A., Ojha, B., Limdi, N., Blount, J., Burneo, J.G., Ver Hoef, L., Paige, L., Faught, E., others, 2008. Functional

imaging: II. Prediction of epilepsy surgery outcome. Annals of neurology 64 (1), 35–41.

Knowlton, R.C., Elgavish, R.A., Limdi, N., Bartolucci, A., Ojha, B., Blount, J., Burneo, J.G., Ver Hoef, L., Paige, L., Faught, E., Kankirawatana, P., Riley, K., Kuzniecky, R., 2008. Functional imaging: I. Relative predictive value of intracranial electroencephalography. Ann. Neurol. 64 (1), 25–34.

Knowlton, R.C., Shih, J., 2004. Magnetoencephalography in epilepsy. Epilepsia 45 Suppl 4, 61–71.

Ko, S., Jun, S.C., 2010. Beamformer for simultaneous magnetoencephalography and electroencephalography analysis. Journal of Applied Physics 107 (9), 09B315.

Kobayashi, K., Yoshinaga, H., Ohtsuka, Y., Gotman, J., 2005. Dipole modeling of epileptic spikes can be accurate or misleading. Epilepsia 46 (3), 397–408.

Köhling, R., Höhling, J.M., Straub, H., Kuhlmann, D., Kuhnt, U., Tuxhorn, I., Ebner, A., Wolf, P., Pannek, H.W., Gorji, A., Speckmann, E.J., 2000. Optical monitoring of neuronal activity during spontaneous sharp waves in chronically epileptic human neocortical tissue. J. Neurophysiol. 84 (4), 2161–2165.

Koles, Z.J., 1998. Trends in EEG source localization. Electroencephalography and Clinical Neurophysiology 106 (2), 127–137.

Körber, R., Storm, J.-H., Seton, H., Mäkelä, J.P., Paetau, R., Parkkonen, L., Christoph Pfeiffer, Riaz, B., Schneiderman, J.F., Dong, H., Hwang, S., You, L., Inglis, B., John Clarke, Espy, M.A., Ilmoniemi, R.J., Magnelind, P.E., Matlashov, A.N., Nieminen, J.O., Volegov, P.L., Zevenhoven, K.C.J., Höfner, N., Burghoff, M., Enpuku, K., Yang, S.Y., Chieh, J.-J., Jukka Knuutila, Laine, P., Nenonen, J., 2016. SQUIDs in biomagnetism: a roadmap towards improved healthcare. Supercond. Sci. Technol. 29 (11), 113001.

Kramer, M.A., Cash, S.S., 2012. Epilepsy as a disorder of cortical network organization. The Neuroscientist 18 (4), 360–372.

Kybic, J., Clerc, M., Faugeras, O., Keriven, R., Papadopoulo, T., 2006. Generalized head models for MEG/EEG: boundary element method beyond nested volumes. Physics in medicine and biology 51, 1333.

Lai, Y., van Drongelen, W., Ding, L., Hecox, K.E., Towle, V.L., Frim, D.M., He, B., 2005. Estimation of in vivo human brain-to-skull conductivity ratio from simultaneous extra- and intra-cranial electrical potential recordings. Clin Neurophysiol 116 (2), 456–465.

Lance, G.N., Williams, W.T., 1967. A General Theory of Classificatory Sorting Strategies 1. Hierarchical Systems. The Computer Journal 9 (4), 373–380.

Lantz, G., Grave de Peralta, R., 2003. Epileptic source localization with high density EEG: how many electrodes are needed? Clinical neurophysiology : official journal of the International Federation of Clinical Neurophysiology 114 (1), 63–9.

Lapalme, E., Lina, J.M., Mattout, J., 2006. Data-driven parceling and entropic inference in MEG. NeuroImage 30 (1), 160–171.

Leijten, F.S., Huiskamp, G., 2008. Interictal electromagnetic source imaging in focal epilepsy: practices, results and recommendations: Current Opinion in Neurology 24 (4), 437–445.

Lew, S., Wolters, C.H., Anwander, A., Makeig, S., MacLeod, R., 2009. Improved EEG source analysis using low resolution conductivity estimation in a four-compartment finite element head model. Hum Brain Mapp 30 (9), 2862–2878.

Limpiti, T., Van Veen, B.D., Wakai, R.T., 2006. Cortical patch basis model for spatially extended neural activity. IEEE Transactions on Biomedical Engineering 53 (9), 1740–1754.

Lin, F.-H., Witzel, T., Ahlfors, S.P., Stufflebeam, S.M., Belliveau, J.W., Hämäläinen, M.S., 2006. Assessing and improving the spatial accuracy in MEG source localization by depth-weighted minimum-norm estimates. NeuroImage 31 (1), 160–171.

Lin, J.J., Riley, J.D., Juranek, J., Cramer, S.C., 2008. Vulnerability of the frontal-temporal connections in temporal lobe epilepsy. Epilepsy Research 82 (2–3), 162–170.

Lin, Y.Y., Shih, Y.H., Hsieh, J.C., Yu, H.Y., Yiu, C.H., Wong, T.T., Yeh, T.C., Kwan, S.Y., Ho, L.T., Yen, D.J., Wu, Z.A., Chang, M.S., 2003. Magnetoencephalographic yield of interictal spikes in temporal lobe epilepsy: Comparison with scalp EEG recordings. NeuroImage 19 (3), 1115–1126.

Lina, J.M., Chowdhury, R., Lemay, E., Kobayashi, E., Grova, C., 2014. Wavelet-Based Localization of Oscillatory Sources From Magnetoencephalography Data. IEEE Transactions on Biomedical Engineering 61 (8), 2350–2364.

Liu, A.K., Belliveau, J.W., Dale, A.M., 1998. Spatiotemporal imaging of human brain activity using functional MRI constrained magnetoencephalography data: Monte Carlo simulations. Proceedings of the National Academy of Sciences of the United States of America 95 (15), 8945–8950.

Liu, A.K., Dale, A.M., Belliveau, J.W., 2002. Monte Carlo simulation studies of EEG and MEG localization accuracy. Human Brain Mapping 16 (1), 47–62.

Lopes da Silva, F., 2013. EEG and MEG: relevance to neuroscience. Neuron 80 (5), 1112–1128.

Lopes da Silva, F.H., van Rotterdam, A., Barts, P., van Heusden, E., Burr, W., 1976. Models of neuronal populations: the basic mechanisms of rhythmicity. Prog. Brain Res. 45, 281–308.

Lucka, F., Pursiainen, S., Burger, M., Wolters, C.H., 2012. Hierarchical Bayesian inference for the EEG inverse problem using realistic FE head models: depth localization and source separation for focal primary currents. Neuroimage 61 (4), 1364–1382.

Lüders, H., Awad, I., 1992. Conceptual Considerations, in: Lüders, H. (Ed.), Epilepsy Surgery. Raven Press publishers, New York, pp. 51–62.

Lüders, H., Comair, Y.G., 2001. Epilepsy surgery. Lippincott Williams & Wilkins.

Luders, H.O., Najm, I., Nair, D., Widdess-Walsh, P., Bingman, W., 2006. The epileptogenic zone: general principles. Epileptic disorders 8, S1.

Makris, N., Pandya, D.N., 2009. The extreme capsule in humans and rethinking of the language circuitry. Brain Struct Funct 213 (3), 343–358.

Malmivuo, J., 2012. Comparison of the properties of EEG and MEG in detecting the electric activity of the brain. Brain Topogr 25 (1), 1–19.

Malmivuo, J.A., Suihko, V., 2001. Effect of skull resistivity on the relative sensitivity distributions of EEG and MEG measurements, in: Engineering in Medicine and Biology Society, 2001. Proceedings of the 23rd Annual International Conference of the IEEE. Presented at the Engineering in Medicine and Biology Society, 2001. Proceedings of the 23rd Annual International Conference of the IEEE, pp. 984–985 vol.1.

Mangin, J.-F., Frouin, V., Bloch, I., Régis, J., López-Krahe, J., 1995. From 3D magnetic resonance images to structural representations of the cortex topography using topology preserving deformations. J. Math. Imaging Vis. 5 (4), 297–318.

Marrelec, G., Messé, A., Bellec, P., 2015. A Bayesian Alternative to Mutual Information for the Hierarchical Clustering of Dependent Random Variables. PLOS ONE 10 (9), e0137278.

Martinez, W.L., Martinez, A.R., 2004. Exploratory Data Analysis with MATLAB, Chapman & Hall/CRC Computer Science & Data Analysis. Chapman and Hall/CRC.

Mattout, J., Pélégrini-Issac, M., Garnero, L., Benali, H., 2005. Multivariate source prelocalization (MSP): Use of functionally informed basis functions for better conditioning the MEG inverse problem. NeuroImage 26 (2), 356–373.

Merlet, I., Gotman, J., 1999. Reliability of dipole models of epileptic spikes. Clinical neurophysiology 110 (6), 1013–1028.

Merlet, I., Paetau, R., García-Larrea, L., Uutela, K., Granström, M.L., Mauguière, F., 1997. Apparent asynchrony between interictal electric and magnetic spikes. Neuroreport 8 (5), 1071–1076.

Michel, C.M., Grave de Peralta, R., Lantz, G., Gonzalez Andino, S., Spinelli, L., Blanke, O., Landis, T., Seeck, M., 1999. Spatiotemporal EEG analysis and distributed source estimation in presurgical epilepsy evaluation. J Clin Neurophysiol 16 (3), 239–266.

Michel, C.M., Murray, M.M., Lantz, G., Gonzalez, S., Spinelli, L., Grave de Peralta, R., 2004. EEG source imaging. Clinical Neurophysiology 115 (10), 2195–2222.

Mikuni, N., Nagamine, T., Ikeda, A., Terada, K., Taki, W., Kimura, J., Kikuchi, H., Shibasaki, H., 1997. Simultaneous Recording of Epileptiform Discharges by MEG and Subdural Electrodes in Temporal Lobe Epilepsy. Neuroimage 5 (4), 298–306.

Milligan, G.W., Cooper, M.C., 1985. An examination of procedures for determining the number of clusters in a data set. Psychometrika 50 (2), 159–179.

Milstein, J.N., Koch, C., 2008. Dynamic moment analysis of the extracellular electric field of a biologically realistic spiking neuron. Neural Comput 20 (8), 2070–2084.

Mojena, R., 1977. Hierarchical Grouping Methods and Stopping Rules: An Evaluation,"The Computer Journal20, 359-363. Comput. J. 20 (4), 359–363.

Molins, A., Stufflebeam, S.M., Brown, E.N., Hämäläinen, M.S., 2008. Quantification of the benefit from integrating MEG and EEG data in minimum l2-norm estimation. Neuroimage 42 (3), 1069–1077.

Morozov, V., 1966. On the solution of functional equations by the method of regularization. Soviet Math. Dokl. 7, 414–417.

Mosher, J.C., Baillet, S., Leahy, R.M., 1999. EEG source localization and imaging using multiple signal classification approaches. J Clin Neurophysiol 16 (3), 225–238.

Mosher, J.C., Leahy, R.M., 1998. Recursive MUSIC: a framework for EEG and MEG source localization. IEEE Trans Biomed Eng 45 (11), 1342–1354.

Mosher, J.C., Leahy, R.M., Lewis, P.S., 1999. EEG and MEG: forward solutions for inverse methods. Biomedical Engineering, IEEE Transactions 46 (3), 245–259.

Mosher, J.C., Lewis, P.S., Leahy, R.M., 1992. Multiple dipole modeling and localization from spatio-temporal MEG data. IEEE Trans. Biomed. Eng. 39 (6), 541–557.

Mouthaan, B.E., Rados, M., Barsi, P., Boon, P., Carmichael, D.W., Carrette, E., Craiu, D., Cross, J.H., Diehl, B., Dimova, P., Fabo, D., Francione, S., Gaskin, V., Gil-Nagel, A., Grigoreva, E., Guekht, A., Hirsch, E., Hecimovic, H., Helmstaedter, C., Jung, J., Kalviainen, R., Kelemen, A., Kimiskidis, V., Kobulashvili, T., Krsek, P., Kuchukhidze, G., Larsson, P.G., Leitinger, M., Lossius, M.I., Luzin, R., Malmgren, K., Mameniskiene, R., Marusic, P., Metin, B., Özkara, C., Pecina, H., Quesada, C.M., Rugg-Gunn, F., Rydenhag, B., Ryvlin, P., Scholly, J., Seeck, M., Staack, A.M., Steinhoff, B.J., Stepanov, V., Tarta-Arsene, O., Trinka, E., Uzan, M., Vogt, V.L., Vos, S.B., Vulliémoz, S., Huiskamp, G., Leijten, F.S.S., Van Eijsden, P., Braun, K.P.J., the E-PILEPSY consortium, 2016. Current use of imaging and electromagnetic source localization procedures in epilepsy surgery centers across Europe. Epilepsia 57 (5), 770–776.

de Munck, J.C., Peters, M.J., 1993. A fast method to compute the potential in the multisphere model. IEEE Trans Biomed Eng 40 (11), 1166–1174.

Murakami, S., Okada, Y., 2015. Invariance in current dipole moment density across brain structures and species: Physiological constraint for neuroimaging. NeuroImage 111, 49–58.

Nakasato, N., Levesque, M.F., Barth, D.S., Baumgartner, C., Rogers, R.L., Sutherling, W.W., 1994. Comparisons of MEG, EEG, and ECoG source localization in neocortical partial epilepsy in humans. Electroencephalogr Clin Neurophysiol 91 (3), 171–178.

Niedermeyer, E., Lopes da Silva, F.H., 2005. Electroencephalography: basic principles, clinical applications, and related fields. Lippincott Williams & Wilkins.

Noachtar, S., Rémi, J., 2009. The role of EEG in epilepsy: a critical review. Epilepsy Behav 15 (1), 22–33.

Nunez, P.L., Srinivasan, R., 2006. Electric Fields of the Brain. Oxford University Press.

Nurujjaman, M., Narayanan, R., Iyengar, A.S., 2009. Comparative study of nonlinear properties of EEG signals of normal persons and epileptic patients. Nonlinear Biomedical Physics 3, 6.

Oishi, M., Otsubo, H., Kameyama, S., Morota, N., Masuda, H., Kitayama, M., Tanaka, R., 2002. Epileptic spikes: magnetoencephalography versus simultaneous electrocorticography. Epilepsia 43 (11), 1390–1395.

Oostendorp, T.F., Delbeke, J., 1999. The conductivity of the human skull in vivo and in vitro, in: [Engineering in Medicine and Biology, 1999. 21st Annual Conf. and the 1999 Annual Fall Meeting of the Biomedical Engineering Soc.] BMES/EMBS Conference, 1999. Proceedings of the First Joint. Presented at the [Engineering in Medicine and Biology, 1999. 21st Annual Conf. and the 1999 Annual Fall Meeting of the Biomedical Engineering Soc.] BMES/EMBS Conference, 1999. Proceedings of the First Joint, p. 456 vol.1.

Oostenveld, R., Praamstra, P., 2001. The five percent electrode system for high-resolution EEG and ERP measurements. Clinical Neurophysiology 112 (4), 713–719.

Ossenblok, P., de Munck, J.C., Colon, A., Drolsbach, W., Boon, P., 2007. Magnetoencephalography is more successful for screening and localizing frontal lobe epilepsy than electroencephalography. Epilepsia 48 (11), 2139–2149.

Oswal, A., Litvak, V., Brown, P., Woolrich, M., Barnes, G., 2014. Optimising beamformer regions of interest analysis. Neuroimage 102, 945–954.

Otsu, 1979. A Threshold Selection Method from Gray-Level Histograms. IEEE Trans. Syst., Man, Cybern. 9 (1), 62–66.

Ou, W., Hämäläinen, M.S., Golland, P., 2009. A distributed spatio-temporal EEG/MEG inverse solver. NeuroImage 44 (3), 932–946.

Ou, W., Nummenmaa, A., Ahveninen, J., Belliveau, J.W., Hämäläinen, M.S., Golland, P., 2010. Multimodal functional imaging using fMRI-informed regional EEG/MEG source estimation. Neuroimage 52 (1), 97–108.

Pascual-Marqui, R.D., 2002. Standardized low-resolution brain electromagnetic tomography (sLORETA): Technical details. Methods and Findings in Experimental and Clinical Pharmacology 24 (SUPPL. D), 5–12.

Pascual-Marqui, R.D., Michel, C.M., Lehmann, D., 1994. Low resolution electromagnetic tomography: a new method for localizing electrical activity in the brain. International Journal of Psychophysiology 18 (1), 49–65.

Pataraia, E., Lindinger, G., Deecke, L., Mayer, D., Baumgartner, C., 2005. Combined MEG/EEG analysis of the interictal spike complex in mesial temporal lobe epilepsy. Neuroimage 24 (3), 607–614.

Pellegrino, G., Hedrich, T., Chowdhury, R., Hall, J.A., Lina, J.-M., Dubeau, F., Kobayashi, E., Grova, C., 2016a. Source localization of the seizure onset zone from ictal EEG/MEG data. Hum Brain Mapp 37 (7), 2528–2546.

Pellegrino, G., Hedrich, T., Chowdhury, R., Hall, J.A., Lina, J.-M., Dubeau, F., Kobayashi, E., Grova, C., 2016b. Source localization of the seizure onset zone from ictal EEG/MEG data. Hum. Brain Mapp.

Pellegrino, G., Hedrich, T., Hall, J.A., Dubeau, F., Kobayashi, E., Grova, C., 2016. Towards new standards for interictal MEG source imaging: comparison between dipole fitting (ECD) and distributed source imaging using coherent Maximum Entropy on the Mean (cMEM), in: submitted. Presented at the Annual Meeting of the American Epilepsy Society.

Pellegrino, G., Machado, A., von Ellenrieder, N., Watanabe, S., Hall, J.A., Lina, J.-M., Kobayashi, E., Grova, C., 2016. Hemodynamic Response to Interictal Epileptiform Discharges Addressed by Personalized EEG-fNIRS Recordings. Front. Neurosci. 102.

Pflieger, M.E., Simpson, G.V., Ahlfors, S.P., Ilmoniemi, R.J., 2000. Superadditive Information from Simultaneous MEG/EEG Data, in: Aine, C.J., Stroink, G., Wood, C.C., Okada, Y., Swithenby, S.J. (Eds.), Biomag 96. Springer New York, pp. 1154–1157.

Phillips, C., Mattout, J., Rugg, M.D., Maquet, P., Friston, K.J., 2005. An empirical Bayesian solution to the source reconstruction problem in EEG. Neuroimage 24 (4), 997–1011.

Phillips, C., Rugg, M.D., Friston, K.J., 2002. Systematic regularization of linear inverse solutions of the EEG source localization problem. NeuroImage 17 (1), 287–301.

Pittau, F., Vulliemoz, S., 2015. Functional brain networks in epilepsy: Recent advances in noninvasive mapping. Current Opinion in Neurology 28 (4), 338–343.

Plonsey, R., Heppner, D.B., 1967. Considerations of quasi-stationarity in electrophysiological systems. Bull Math Biophys 29 (4), 657–664.

Preissl, H., 2005. Magnetoencephalography. Gulf Professional Publishing.

Proposal for revised classification of epilepsies and epileptic syndromes., 1989. . Epilepsia 30 (4), 389–399.

Proposal for revised clinical and electroencephalographic classification of epileptic seizures., 1981. . Epilepsia 22 (4), 489–501.

Pruis, G.W., Gilding, B.H., Peters, M.J., 1993. A comparison of different numerical methods for solving the forward problem in EEG and MEG. Physiol Meas 14 Suppl 4A, A1-9.

Ramantani, G., Boor, R., Paetau, R., Ille, N., Feneberg, R., Rupp, A., Boppel, T., Scherg, M., Rating, D., Bast, T., 2006. MEG versus EEG: influence of background activity on interictal spike detection. J Clin Neurophysiol 23 (6), 498–508.

Ramantani, G., Dümpelmann, M., Koessler, L., Brandt, A., Cosandier-Rimélé, D., Zentner, J., Schulze-Bonhage, A., Maillard, L.G., 2014. Simultaneous subdural and scalp EEG correlates of frontal lobe epileptic sources. Epilepsia 55 (2), 278–288.

Rampp, S., Kaltenhäuser, M., Weigel, D., Buchfelder, M., Blümcke, I., Dörfler, A., Stefan, H., 2010. MEG correlates of epileptic high gamma oscillations in invasive EEG. Epilepsia 51 (8), 1638–1642.

Reynolds, E.H., Trimble, M.R., 2009. Epilepsy, psychiatry, and neurology. Epilepsia 50 (s3), 50–55.

Rosenow, F., Lüders, H., 2001. Presurgical evaluation of epilepsy. Brain 124 (9), 1683–1700.

Rush, S., Driscoll, D.A., 1969. EEG Electrode Sensitivity-An Application of Reciprocity. IEEE Transactions on Biomedical Engineering BME-16 (3), 204–204.

Ryvlin, P., Cross, J.H., Rheims, S., 2014. Epilepsy surgery in children and adults. The Lancet Neurology 13 (11), 1114–1126.

Ryynänen, O.R.M., Hyttinen, J.A.K., Laarne, P.H., Malmivuo, J.A., 2004. Effect of electrode density and measurement noise on the spatial resolution of cortical potential distribution. IEEE Trans Biomed Eng 51 (9), 1547–1554.

Ryynanen, O.R.M., Hyttinen, J.A.K., Malmivuo, J.A., 2006. Effect of measurement noise and electrode density on the spatial resolution of cortical potential distribution with different resistivity values for the skull. IEEE Transactions on Biomedical Engineering 53 (9), 1851–1858.

Scheler, G., Fischer, M.J.M., Genow, A., Hummel, C., Rampp, S., Paulini, A., Hopfengärtner, R., Kaltenhäuser, M., Stefan, H., 2007. Spatial relationship of source localizations in patients with focal epilepsy: Comparison of MEG and EEG with a three spherical shells and a boundary element volume conductor model. Hum Brain Mapp 28 (4), 315–322.

Scherg, M., Bast, T., Berg, P., 1999. Multiple source analysis of interictal spikes: goals, requirements, and clinical value. J Clin Neurophysiol 16 (3), 214–224.

Scherg, M., Von Cramon, D., 1986. Evoked dipole source potentials of the human auditory cortex. Electroencephalogr Clin Neurophysiol 65 (5), 344–360.

Schmidt, R.O., 1986. Multiple emitter location and signal parameter estimation. IEEE Transactions on Antennas and Propagation 34 (3), 276–280.

Schwartz, D., Lemoine, D., Poiseau, E., Barillot, C., 1996. Registration of MEG/EEG data with 3D MRI: Methodology and precision issues. Brain Topography 9 (2), 101–116.

Sekihara, K., Nagarajan, S.S., Poeppel, D., Marantz, A., 2002. Performance of an MEG adaptive-beamformer technique in the presence of correlated neural activities: effects on signal intensity and time-course estimates. IEEE Transactions on Biomedical Engineering 49 (12), 1534–1546.

Sharbrough, F., Chatrian, G.E., Lesser, R.P., Lüders, H., Nuwer, M., Picton, T.W., 1991. American Electroencephalographic Society guidelines for standard electrode position nomenclature. J. clin. Neurophysiol 8 (2), 200–202.

Sharon, D., Hämäläinen, M.S., Tootell, R.B.H., Halgren, E., Belliveau, J.W., 2007. The advantage of combining MEG and EEG: comparison to fMRI in focally stimulated visual cortex. Neuroimage 36 (4), 1225–1235.

Sherwood, L., 2008. Chapter 4: Principles of Neural and Hormonal Communication, in: Human Physiology: From Cells to Systems. Cengage Learning, p. 928.

Shiraishi, H., Ahlfors, S.P., Stufflebeam, S.M., Takano, K., Okajima, M., Knake, S., Hatanaka, K., Kohsaka, S., Saitoh, S., Dale, A.M., Halgren, E., 2005. Application of magnetoencephalography in epilepsy patients with widespread spike or slow-wave activity. Epilepsia 46 (8), 1264–1272.

Shiraishi, H., Stufflebeam, S.M., Knake, S., Ahlfors, S.P., Sudo, A., Asahina, N., Egawa, K., Hatanaka, K., Kohsaka, S., Saitoh, S., Grant, P.E., Dale, A.M., Halgren, E., 2005. Dynamic statistical parametric mapping for analyzing the magnetoencephalographic epileptiform activity in patients with epilepsy. J. Child Neurol. 20 (4), 363–369.

Silva, C., Almeida, R., Oostendorp, T., Ducla-Soares, E., Foreid, J.P., Pimentel, T., 1999. Interictal spike localization using a standard realistic head model: simulations and analysis of clinical data. Clin Neurophysiol 110 (5), 846–855.

Song, J., Davey, C., Poulsen, C., Luu, P., Turovets, S., Anderson, E., Li, K., Tucker, D., 2015. EEG source localization: Sensor density and head surface coverage. J. Neurosci. Methods 256, 9–21.

Speckmann, E.-J., Elger, C., Altrup, U., 2004. Neurophysiological basis of the electroencephalogram, in: Niedermeyer, E., Silva, F.H.L. da (Eds.), Electroencephalography: basic principles, clinical applications, and related fields (5th Edition), chapter 12. Lippincott Williams & Wilkins, Baltimore, pp. 149–163.

Srinivasan, R., Nunez, P.L., Tucker, D.M., Silberstein, R.B., Cadusch, P.J., 1996. Spatial sampling and filtering of EEG with spline Laplacians to estimate cortical potentials. Brain Topogr 8 (4), 355–366.

Srinivasan, R., Tucker, D.M., Murias, M., 1998. Estimating the spatial Nyquist of the human EEG. Behavior Research Methods, Instruments, & Computers 30 (1), 8–19.

Staley, K.J., Dudek, F.E., 2006. Interictal Spikes and Epileptogenesis. Epilepsy Curr 6 (6), 199–202.

Stefan, H., 2009. Magnetic source imaging. Rev. Neurol. (Paris) 165 (10), 742–745.

Stefan, H., Hummel, C., Scheler, G., Genow, A., Druschky, K., Tilz, C., Kaltenhäuser, M., Hopfengärtner, R., Buchfelder, M., Romstöck, J., 2003. Magnetic brain source imaging of focal epileptic activity: a synopsis of 455 cases. Brain 126 (Pt 11), 2396–2405.

Stefan, H., Schneider, S., Abraham-Fuchs, K., Bauer, J., Feistel, H., Pawlik, G., Neubauer, U., Röhrlein, G., Huk, W.J., 1990. Magnetic source localization in focal epilepsy. Multichannel magnetoencephalography correlated with magnetic resonance brain imaging. Brain 113 (Pt 5), 1347–1359.

Stippich, C., 2007. Clinical Functional MRI: Presurgical Functional Neuroimaging. Springer Science & Business Media.

Strobbe, G., Carrette, E., López, J.D., Montes Restrepo, V., Van Roost, D., Meurs, A., Vonck, K., Boon, P., Vandenberghe, S., van Mierlo, P., 2016. Electrical source imaging of interictal spikes using multiple sparse volumetric priors for presurgical epileptogenic focus localization. NeuroImage: Clinical 11, 252–263.

Sutherling, W.W., Crandall, P.H., Engel, J., Darcey, T.M., Cahan, L.D., Barth, D.S., 1987. The magnetic field of complex partial seizures agrees with intracranial localizations. Ann. Neurol 21 (6), 548–558.

Swartz, B.E., Godensohn, E.S., 1998. Timeline of history of EEG and associated fields. Electroencephalography and Clinical Neurophysiology 106 (2), 173–176.

Tadel, F., Baillet, S., Mosher, J.C., Pantazis, D., Leahy, R.M., 2011. Brainstorm: A User-Friendly Application for MEG/EEG Analysis. Computational Intelligence and Neuroscience 2011, 1–13.

Tanaka, N., Hämäläinen, M.S., Ahlfors, S.P., Liu, H., Madsen, J.R., Bourgeois, B.F., Lee, J.W., Dworetzky, B.A., Belliveau, J.W., Stufflebeam, S.M., 2010. Propagation of epileptic spikes reconstructed from spatiotemporal magnetoencephalographic and electroencephalographic source analysis. Neuroimage 50 (1), 217–222.

Tanaka, N., Peters, J.M., Prohl, A.K., Takaya, S., Madsen, J.R., Bourgeois, B.F., Dworetzky, B.A., Hämäläinen, M.S., Stufflebeam, S.M., 2014. Clinical value of magnetoencephalographic spike propagation represented by spatiotemporal source analysis: correlation with surgical outcome. Epilepsy Res. 108 (2), 280–288.

Tanaka, N., Stufflebeam, S.M., 2014. Clinical Application of Spatiotemporal Distributed Source Analysis in Presurgical Evaluation of Epilepsy. Front Hum Neurosci 8.

Tao, J.X., Baldwin, M., Hawes-Ebersole, S., Ebersole, J.S., 2007. Cortical Substrates of Scalp EEG Epileptiform Discharges. Journal of Clinical Neurophysiology 24 (2), 96–100.

Tao, J.X., Baldwin, M., Ray, A., Hawes-Ebersole, S., Ebersole, J.S., 2007. The Impact of Cerebral Source Area and Synchrony on Recording Scalp Electroencephalography Ictal Patterns. Epilepsia 48 (11), 2167–2176.

Tao, J.X., Ray, A., Hawes-Ebersole, S., Ebersole, J.S., 2005. Intracranial EEG Substrates of Scalp EEG Interictal Spikes. Epilepsia 46 (5), 669–676.

Traub, R.D., 1979. Neocortical pyramidal cells: a model with dendritic calcium conductance reproduces repetitive firing and epileptic behavior. Brain Res. 173 (2), 243–257.

Trujillo-Barreto, N.J., Aubert-Vázquez, E., Valdés-Sosa, P.A., 2004. Bayesian model averaging in EEG/MEG imaging. NeuroImage 21 (4), 1300–1319.

Tutorials/TutBEst - Brainstorm [WWW Document], 2015. . URL http://neuroimage.usc.edu/brainstorm/Tutorials/TutBEst

Uutela, K., Hamalainen, M., Salmelin, R., 1998. Global optimization in the localization of neuromagnetic sources. IEEE Transactions on Biomedical Engineering 45 (6), 716–723.

Uutela, K., Hämäläinen, M., Somersalo, E., 1999. Visualization of Magnetoencephalographic Data Using Minimum Current Estimates. NeuroImage 10 (2), 173–180.

Uutela, K., Taulu, S., Hämäläinen, M., 2001. Detecting and correcting for head movements in neuromagnetic measurements. Neuroimage 14 (6), 1424–1431.

Vallaghé, S., Clerc, M., 2009. A global sensitivity analysis of three- and four-layer EEG conductivity models. IEEE Trans Biomed Eng 56 (4), 988–995.

Van ’t Ent, D., Manshanden, I., Ossenblok, P., Velis, D.N., de Munck, J.C., Verbunt, J.P.A., Lopes da Silva, F.H., 2003. Spike cluster analysis in neocortical localization related epilepsy yields clinically significant equivalent source localization results in magnetoencephalogram (MEG). Clinical Neurophysiology 114 (10), 1948–1962.

Van Veen, B.D., Drongelen, W.V., Yuchtman, M., Suzuki, A., 1997. Localization of brain electrical activity via linearly constrained minimum variance spatial filtering. IEEE Transactions on Biomedical Engineering 44 (9), 867–880.

Vega-Hernández, M., Martínez-Montes, E., Sánchez-Bornot, J.M., Lage-Castellanos, A., Valdés-Sosa, P.A., 2008. Penalized least squares methods for solving the EEG inverse problem. Statistica Sinica 1535–1551.

von Ellenrieder, N., Beltrachini, L., Muravchik, C.H., Gotman, J., 2014b. Extent of cortical generators visible on the scalp: Effect of a subdural grid. NeuroImage.

Vorwerk, J., Cho, J.-H., Rampp, S., Hamer, H., Knösche, T.R., Wolters, C.H., 2014. A guideline for head volume conductor modeling in EEG and MEG. NeuroImage 100, 590–607.

Vrba, J., Betts, K., Burbank, M., Cheung, T., Fife, A.A., Haid, G., Kubik, P.R., Lee, S., McCubbin, J., McKay, J., 1993. Whole cortex, 64 channel SQUID biomagnetometer system. IEEE transactions on applied superconductivity 3 (1), 1878–1882.

Vrba, J., Robinson, S.E., 2001. Signal Processing in Magnetoencephalography. Methods 25 (2), 249–271.

Wagner, M., Fuchs, M., Wischmann, H.-A., Drenckhahn, R., Köhler, T., 1996. Smooth reconstruction of cortical sources from EEG or MEG recordings. NeuroImage, Second International Conference on Functional Mapping of the Human Brain 3 (3, Supplement), S168.

Wang, G., Ren, D., 2013. Effect of Brain-to-Skull Conductivity Ratio on EEG Source Localization Accuracy. BioMed Research International 2013, e459346.

Wang, G., Worrell, G., Yang, L., Wilke, C., He, B., 2011. Interictal spike analysis of high-density EEG in patients with partial epilepsy. Clinical Neurophysiology 122 (6), 1098–1105.

Ward, J.H., 1963. Hierarchical Grouping to Optimize an Objective Function. Journal of the American Statistical Association 58 (301), 236.

Wax, M., Anu, Y., 1996. Performance analysis of the minimum variance beamformer. IEEE Transactions on Signal Processing 44 (4), 928–937.

Wendel, K., Väisänen, O., Malmivuo, J., Gencer, N.G., Vanrumste, B., Durka, P., Magjarević, R., Supek, S., Pascu, M.L., Fontenelle, H., Grave de Peralta Menendez, R., 2009. EEG/MEG Source Imaging: Methods, Challenges, and Open Issues. Computational Intelligence and Neuroscience 2009, 1–12.

Wendling, F., 2005. Neurocomputational models in the study of epileptic phenomena. J Clin Neurophysiol 22 (5), 285–287.

Wendling, F., Bellanger, J.J., Bartolomei, F., Chauvel, P., 2000. Relevance of nonlinear lumped-parameter models in the analysis of depth-EEG epileptic signals. Biol Cybern 83 (4), 367–378.

Wennberg, R., Cheyne, D., 2014. Reliability of MEG source imaging of anterior temporal spikes: Analysis of an intracranially characterized spike focus. Clinical Neurophysiology 125 (5), 903–918.

WHO | Epilepsy [WWW Document], 2016. . WHO. URL http://www.who.int/mediacentre/factsheets/fs999/en/

Wilke, C., Worrell, G., He, B., 2011. Graph analysis of epileptogenic networks in human partial epilepsy. Epilepsia 52 (1), 84–93.

Wilson, H.R., Cowan, J.D., 1972. Excitatory and Inhibitory Interactions in Localized Populations of Model Neurons. Biophys J 12 (1), 1–24.

Wipf, D.P., Owen, J.P., Attias, H.T., Sekihara, K., Nagarajan, S.S., 2010. Robust Bayesian estimation of the location, orientation, and time course of multiple correlated neural sources using MEG. Neuroimage 49 (1), 641–655.

Wyllie, E., Cascino, G.D., Gidal, B.E., Goodkin, H.P., 2012. Wyllie's Treatment of Epilepsy: Principles and Practice. Lippincott Williams & Wilkins.

Yamazaki, M., Tucker, D.M., Fujimoto, A., Yamazoe, T., Okanishi, T., Yokota, T., Enoki, H., Yamamoto, T., 2012. Comparison of dense array EEG with simultaneous intracranial EEG for interictal spike detection and localization. Epilepsy Res. 98 (2–3), 166–173.

Yamazaki, M., Tucker, D.M., Terrill, M., Fujimoto, A., Yamamoto, T., 2013. Dense Array EEG Source Estimation in Neocortical Epilepsy. Front Neurol 4.

Yoshinaga, H., 2002. Benefit of combined use of EEG and MEG dipole. International Congress Series 1232, 419–426.

Yu, Q., Yang, W., Wang, Z., Gao, S., Xue, J., Chen, Z., Chen, Y., Wang, F., 2010. [Localization of epileptic foci in frontal lobe epilepsy and its surgical therapy]. Zhonghua Yi Xue Za Zhi 90 (7), 462–465.

Zelmann, R., Lina, J.M., Schulze-Bonhage, A., Gotman, J., Jacobs, J., 2013. Scalp EEG is not a Blur: It Can See High Frequency Oscillations Although Their Generators are Small. Brain Topogr 1–22.

Zerouali, Y., Ghaziri, J., Nguyen, D.K., 2016. Chapter 1 - Multimodal investigation of epileptic networks: The case of insular cortex epilepsy, in: Elsa

Rossignol, L.C. and J.-C.L. (Ed.), Progress in Brain Research, Neurobiology of EpilepsyFrom Genes to Networks. Elsevier, pp. 1–33.

Zhang, Y., van Drongelen, W., He, B., 2006. Estimation of in vivo brain-to-skull conductivity ratio in humans. Appl Phys Lett 89 (22), 223903–2239033.

Zhang, Z., 1995. A fast method to compute surface potentials generated by dipoles within multilayer anisotropic spheres. Phys Med Biol 40 (3), 335–349.

Zhu, M., Zhang, W., Dickens, D.L., Ding, L., 2014. Reconstructing spatially extended brain sources via enforcing multiple transform sparseness. Neuroimage 86, 280–293.

Zhu, M., Zhang, W., Dickens, D.L., King, J.A., Ding, L., 2013. Sparse MEG Source Imaging For Reconstructing Dynamic Sources of Interictal Spikes in Partial Epilepsy: Journal of Clinical Neurophysiology 30 (4), 313–328.

Zijlmans, M., Huiskamp, G.M., Leijten, F.S.S., Van Der Meij, W.M., Wieneke, G., Van Huffelen, A.C., 2002. Modality-specific spike identification in simultaneous magnetoencephalography/electroencephalography: a methodological approach. J Clin Neurophysiol 19 (3), 183–191.

Zumsteg, D., Friedman, A., Wieser, H.G., Wennberg, R.A., 2006. Propagation of interictal discharges in temporal lobe epilepsy: correlation of spatiotemporal mapping with intracranial foramen ovale electrode recordings. Clin Neurophysiol 117 (12), 2615–2626.